Fabrication and Characterization of Nanowires and Quantum Dots for Advanced Solar Cell Architectures

by

Bahareh Sadeghimakki

A thesis
presented to the University of Waterloo
in fulfillment of the
thesis requirement for the degree of
Doctor of Philosophy
in
Electrical and Computer Engineering

Waterloo, Ontario, Canada, 2012

I hereby declare that I am the sole author of this thesis. This is a true copy of the thesis, including any required final revisions, as accepted by my examiners.

Bahareh Sadeghimakki

I understand that my thesis may be made electronically available to the public.

Bahareh Sadeghimakki

Abstract

The commercially available solar cells suffer from low conversion efficiency due to the thermalization and transmission losses arising from the mismatch between the band gap of the semiconductor materials and the solar spectrum. Advanced device architectures based on nanomaterial have been proposed and being successfully used to enhance the efficiency of the solar cells. Quantum dots (QDs) and nanowires (NWs) are the nanosclae structures that have been exploited for the development of the third generation solar cell devices and nanowire based solar cells, respectively. The optical and electrical properties of these materials can be tuned by their size and geometry; hence they have great potential for the production of highly efficient solar cell. Application of QDs and NWs with enhanced optoelectronic properties and development of low-cost fabrication processes render a new generation of economic highly efficient PV devices. The most significant contribution of this PhD study is the development of simple and cost effective methods for fabrication of nanowires and quantum dots for advanced solar cell architectures.

In advanced silicon nanowires (SiNWs) array cell, SiNWs have been widely synthesised by the well-known vapor-liquid-solid method. Electron beam lithography and deep reactive ion etching have also been employed for fabrication of SiNWs. Due to the high price and complexity of these methods, simple and cost effective approaches are needed for the fabrication of SiNWs. In another approach, to enhance the cell efficiency, organic dyes and polymers have been widely used as luminescent centers and host mediums in the luminescent down shifting (LDS) layers. However, due to the narrow absorption band of the dyes and degradation of the polymers by moisture and heat, these materials are not promising candidates to use as LDS. Highly efficient luminescent materials and transparent host materials with stable mechanical properties are demanded for luminescent down shifting applications. In this project, simple fabrication processes were developed to produce SiNWs and QDs for application in advanced cell architectures. The SiNWs array were successfully fabricated, characterized and deployed in new cell architectures with radial p-n junction geometry. The luminescence down shifting of layers containing QDs in oxide and glass mediums was verified. The silica coated quantum dots which are suitable for luminescence down shifting, were also fabricated and characterized for deployment in new design architectures.

Silicon nanowires were fabricated using two simplified methods. In the first approach, a maskless reactive ion etching process was developed to form upright ordered arrays of the SiNWs without relying on the complicated nano-scale lithography or masking methods. The fabricated structures were comprehensively characterized. Light trapping and photoluminescence properties of the medium were verified. In the second approach, combination of the nanosphere lithography and etching techniques were utilized for wire formation. This method provides a better control on the wire diameters and geometries in a very simple and cost effective way. The fabricated silicon nanowires were used for formation of the radial p-n junction array cells. The functionality of the new cell structures were confirmed through experimental and simulation results.

Quantum dots are promising candidates as luminescent centers due to their tunable optical properties. Oxide/glass matrices are also preferred as the host medium for QDs because of their robust mechanical properties and their compatibility with standard silicon processing technology. Besides, the oxide layers are transparent mediums with good passivation and anti-reflection coating properties. They can also be used to encapsulate the cell. In this work, ordered arrays of QDs were incorporated in an oxide layer to form a luminescent down shifting layer. This design benefits from the enhanced absorption of a periodic QD structure in a transparent oxide. The down shifting properties of the layer after deployment on a crystalline silicon solar cell were examined.

For this purpose, crystalline silicon solar cells were fabricated to use as test platform for down shifting. In order to examine the down-shifting effect, different approaches for formation of a luminescence down shifting layer were developed. The LDS layer consist of cadmium selenide- zinc sulfide (CdSe/ZnS) quantum dots in oxide and glass layers to act as luminescent centers and transparent host medium, respectively. The structural and optical properties of the fabricated layers were studied. The concept of spectral engineering was proved by the deployment of the layer on the solar cell.

To further benefit from the LDS technique, quantum efficiency of the QDs and optical properties of the layer must be improved. Demand for the high quantum efficiency material with desired geometry leaded us to synthesis quantum dots coated with a layer of grown oxide. As the luminescence quantum efficiency of the QDs is correlated to the surface defects, one advantage of having oxide on the outer shell of the QDs, is to passivate the surface non-radiative recombination centers and produce QDs with high luminescent quantum yield. In addition, nanoparticles with desired size can be obtained only by changing the thickness of the oxide shell. This method also simplifies the fabrication of QD arrays for luminescence down shifting application, since it is easier to form ordered arrays from larger particles. QD superlattices in an oxide medium can be fabricated on a large area by a simple spin-coating or dip coating methods. The photonic crystal properties of the proposed structure can greatly increase the absorption in the QDs layer and enhance the effect of down shifting.

Acknowledgements

First and foremost I would like to express my sincere gratitude to Professor Siva Sivoththaman. It was an honour to be his student and I greatly appreciate his constant guidance, excellent scientific advices and full support throughout my PhD study. His patience and enthusiasm have always motivated me to work hard and seek perfection in my doctoral research.

I am grateful to Professor Safa Kasap from University of Saskatchewan for accepting to review my work and serve as the external examiner of this thesis. His constructive feedback is greatly appreciated. I am also grateful to the members of my PhD examination committee, Professor M.P. Anantram, Professor Dayan Ban, and Professor Robert Varin for reading my thesis and their time and effort to improve the quality of this thesis.

I am thankful to the Centre for Advance Photovoltaic Devices and Systems (CAPDS) and Giga to Nano (G2N) Lab managers, Joe Street and Richard Barber not only for their invaluable technical assistance but also for creating a friendly and welcoming environment. I am also grateful to all my colleagues. In particular, Mr. Maziar Moradi, Dr. Majid Gharghi, and Mr. Navid M. S. Jahed, have significantly contributed to the outcome of this research through their cooperation and many stimulating discussions. I’m also thankful to my colleagues Mr. Roohollah S. Tarighat, Mr. Behzad Esfandiarpour, Dr. Hassan El-Gohari and Dr. Ehsan Fathi, for their useful discussions. Also, I would like to thank all my friends who have been always there to lend me a helping hand and have supported me during my PhD study at Waterloo.

I would also like to express my appreciation to my dear friends Dr. Arash. A. Fomani and Dr. Maryam Moradi for all their encouragements, supports and thoughtful general or scientific advices throughout my PhD study. They have always believed in me and inspired me to aim higher and move forward.

I am grateful to my caring brother and sisters, Ali, Anoosheh, Ghazaleh and Mahboobeh who stood behind me throughout this journey. They always came to my aid at the time of need.

Finally, I have the utmost gratitude to my parents who unconditionally love me and patiently guide me. They constantly supported me and I cannot be thankful enough for their sacrifices.

Table of Contents

List of Figures

List of Tables

Chapter 1

Introduction

Solar energy is one of the richest and yet least harvested sources of renewable energy. Conventional single-junction semiconductor solar cells only effectively convert 50% of the incident photons with energy close to the semiconductor band gap (E_g). The other 50% of the incident solar spectrum is lost arising from the fundamental limitation of the semiconductor material [1]. Sub-band gap photons ($E<E_g$) that are not able to be absorbed by the semiconducting material of the solar cell are transmitted through the cell. Photons with energy larger than the band gap ($E>E_g$) are absorbed, but the excess energy is not used effectively due to thermalisation of the electrons via non- radiative relaxation of the excited electrons to the conduction band.

Since the short-wavelength photons are mainly absorbed in the top one micrometer of the semiconducting material, optimizing the electronic properties of the front surface of the existing devices is one approach to achieving a more efficient usage of this part of the solar spectrum. Methods to improve the efficiency of absorption on the top surface of the crystalline silicon (c-Si) cells include creation of very narrow top junctions, employing low doping levels, and using very thin window/buffer layers [2]. However, these alterations are difficult and expensive to implement and may have detrimental effects on the overall performance of the device. Although, a conversion efficiency of 24.7% has been reported for the best laboratory scale cell [3], the mas-produced modules exhibit a significantly lower efficiency of 20% for c-Si due to the financial and/or technical reasons.

1.1 Advanced Concepts for Enhanced Efficiency Photovoltaic Solar Cells

Better exploitation of the solar spectrum in the ultra-violet and near-infrared ranges can be achieved by implementation of advanced approaches to create more sophisticated photovoltaic (PV) cells. Such devices commonly referred to as third generation PV devices [4] employ designs such as multi-junction [5], heterojunction [6], intermediate band gap [7], multiple exciton generation [8], hot carriers [9] and up- and down-converter/down-shifter [10] cells. The mechanisms resulting in the enhanced efficiency of PV is mainly occur in nanoscale structures and more importantly in quantum dots (QDs) and nanowires (NWs) with tunable optoelectronic properties [11]. Many of advanced cells are fabricated using expensive vacuum-based quantum dot processing methods that increase the cost of production. However, in recent years, processing methods based on nanocrystal quantum dots have been proposed to lower the cost of fabrication. Of particular interest to cost-effective solar cells is the use of NW based device structures and relative materials processing for producing acceptable efficiencies [12].

In this PhD research two different approaches for developing simple process employing advanced concepts were studied:

Radial p-n Junction Nanowire Solar Cell

In a radial p-n junction (core–shell) nanowire geometry, efficient separation of charge carriers by the coaxial p–n junction [13], as well as efficient light absorption due to light trapping effects [14], results in a high energy conversion efficiency. Nanowire based solar cells have advantages over planar cell structures, especially for use with materials where the bulk recombination rate of carriers is higher. As a result, the radial junction wire array geometry enables a reduction in solar cell material and/or fabrication costs.

Solar Cell with Luminescence Down-Shifting Layer

From the late 1970s, deployment of the luminescence down shifting (LDS) layers on cell devices has been widely proposed as a method for improving the poor spectral response of the solar cells to the short wavelength light. These layers contain highly efficient luminescent materials, embedded in a transparent host medium, where short wavelength photons are absorbed by the luminescent species, and re-emit at a red-shifted wavelength. Internal reflection of the re-emitted photons in the oxide ensures collection of the re-emitted light in the underlying solar cells; which causes the PV device to exhibit a better response. Since luminescence down shifting is a passive approach, it eliminates any interference with the active material of a PV device, which is financially and technically favorable. The method does not add any complication to the production of the existing device.

Practical Challenges Associated with Advanced Concepts

Significant technical hurdles need to be overcomed, before these two technologies compete with first and second generation PV technologies.

For silicon nanowire array fabrication, several techniques are currently being pursued including the bottom-up vapor liquid solid growth (VLS) technique [13] and top-down etching approaches [15] using wet or dry processes either via mask formation or maskless methods.

Recently, semiconductor nanowires grown by the VLS process have been shown to be a highly promising material for photovoltaic devices [16]. Owing to their single-crystalline nature, they have potential for high performance solar modules. However, it was found that in the VLS process, gold, which was used as the catalyst and is a deep level trap in silicon, is incorporated within the bulk [17] and outer surface of the nanowires [18] during growth and the subsequent cooling. Consequently, radial junction solar cells fabricated using gold-catalyzed silicon nanowire arrays and single nanowires all reported low V_{oc} of 130–300 mV[19], suggesting that residual gold impurities may have negatively impacted the performance of the devices. The second most approach for the silicon nanowire formation involves deep reactive ion etching (DRIE) following the mask formation on the crystalline substrate using the electron beam lithography technique. Although this method is useful for producing silicon nanowires with desired geometry, it is also not beneficial for cost effective devices. In addition, the sidewall residues resulting from the DRIE process needs to be removed which adds a critical step to the process.

Vertical silicon nanowires (SiNWs) array fabricated by maskless reactive ion etching (RIE) can be exploited in radial p-n junction PV cells. This method is advantageous, as it is a simple and cost effective process. Due to the surface damage resulting from the RIE process, an important step in the fabrication process by etching is a gentle cleaning of the wire arrays after the formation step. Both etching and cleaning parameters should be precisely adjusted to avoid further diffusion of the ions inside the wires while maintaining the shape of the wires. However, the diameter, spacing and shape of the NWs are difficult to be precisely control using this method. Recently, a technique known as natural lithography has exploited arrays of chemically synthesized nanospheres as masks for patterning the NWs with desirable sizes and shapes. The advantage of this approach is that nanospheres can assemble into close-packed arrays. Simple coating techniques such as dip coating or spin coating are usually used to prepare single or multiple layers of nanospheres, which is quick and cost-effective. The spacing and diameter of the NWs can also be tuned by nanosphere particle size and by etching [20].

Despite the great advances, the current status of SiNW PV devices is far from satisfactory; and the laboratory efficiencies are much lower than the theoretical limits. Up to now, the conversion efficiency of the fabricated photovoltaics based on coaxial NW arrays, grown by VLS, have been far from the simulation limits, with the highest reported efficiency of ~0.5% [21]. Some of the problems may include charge carrier trapping at the NW surfaces, low p-n junction interface quality, insufficient control of dopant distribution across the NWs, high contact resistances, un-optimized NW dimensions, poor NW density and alignment. In addition, although single-nanowire devices have demonstrated better efficiencies, controlled and cost-effective process schemes for the fabrication of large-scale solar modules, that use highly dense and ordered arrays of single-crystalline NW arrays, have not been demonstrated [22].

In order to justify the application of the luminescence down shifting method, the gains from the increased response of the cell to the new spectrum have to compensate for additional losses originating from two sources: the host material and the luminescent species. The main physical processes that take place are as follows:

- Absorption from the host material
- Emission at less than unity luminescence quantum efficiency (LQE) from the luminescent species
- Re-absorption from the luminescent species due to partial overlapping of their absorption and emission bands
- Losses through top and side planes of the layer, as luminescent light is not exclusively emitted towards the cells' direction and
- Increased reflection due to the introduction of an additional interface

The LDS concept has been demonstrated through extensive theoretical studies [23] and simulation results [24]. However, in the early experiments the theoretical estimations was not perfectly reached [25] due to the limitations arising from the inadequacy of the properties of the available materials at the time. The most important of these were the inadequate photostability [26] and the low luminescence quantum efficiency of the organic dyes that were dominantly used as the luminescent species. The low absorption coefficient and narrow absorption band of the dye molecules were other factors that limited the effectiveness of the LDS layer [27]. Rare-earth ions also exhibit extremely low absorption coefficients [28]. Polymeric host materials such as ethylene-vinyl acetate (EVA) [29], poly- methyl methacrylate (PMMA) [30], polyvinyl butyral (PVB) [31], and polyvinyl acetate (PVA) [25] have been widely used; however the absorption of the encapsulation materials limited the cell response on some scale. In some cases the luminescence quantum efficiency of the luminescent materials decreases after inclusion in a matrix. In addition, the proportion of emitted photons that escaped from the top plane was quantified to the range of 12.5% for the case of the air and a material with refractive index of 1.5. Side plane losses are strongly dependent on the dimension of the LDS layer. Thin large area sheets will lose a smaller fraction of photons through the sides than thicker ones with a smaller area.

Modern materials exhibit higher luminescence quantum efficiencies and better photostability. Research in this field was strengthened recently through the development of the QDs. QDs have been proposed by many authors for use as luminescent species instead of organic dye molecules. QDs are nanometer-size semiconductor crystals, of which the emission wavelength can be tuned by their dimensions, as a result of quantum confinement [32]. The high brightness, stability and quantum efficiency are the advantages of QDs with respect to organic dye molecules [33]. Furthermore, QDs have much broader absorption bands in contrast to the small-band absorption of dye molecules. Potentially and theoretically, the deployment of QDs in luminescent shifting layers could lead to relative increase in efficiency. The luminescence properties of QDs are sensitive to surface interactions, and the degree of surface passivation was shown to be a crucial parameter in determining their luminescence quantum efficiency. Close-packed nanocrystal superlattices ordered over a large area produce a media with a great potential to deploy as down shifter layers on the solar cells for efficiency enhancement. Also, oxide and glass mediums [34] are extensively considered as host material and their great potential is reviewed for a wide range of PV technologies.

Worthy to be noted, according to the results of the research that has been done so far on the luminescence down shifting, due to the limitation of the materials available, only a slight gain via the LDS is predicted. Due to the high surface-to-volume ratio of the quantum dots the luminescence quantum efficiency of these particles is significantly related to the quality of the surface. Safe, simple, and large-batch syntheses with high yields is required for better understanding of nucleation, growth, and the role that surfactants, ligands, additives, and reagent impurities play a major role during quantum dot nanocrystal synthesis, in order to better control the nanocrystal morphology and the luminescence quantum efficiency. Continued research and development is required to improve the quantum dot's quantum efficiency and lower the process cost.

1.2 Motivations and Objectives

Despite the great progress achieved in the field of single nanowire cells, there are still many issues associated with SiNWs array cells that limit their efficiency and need to be addressed through device structure engineering and fabrication process development. Although solar cell technology based on crystalline silicon is well-established with 90% of the market share; the efficiency of this type of cell is low in the short wavelength and long wavelength range of the spectrum. Approaches to achieve high efficiency crystalline silicon devices in a simple and cost-effective manner are of great interest. Hence, there is a strong need for technology development and proof of the concepts.

Development of simple, feasible and cost effective approaches to fabricate radial p-n junction silicon nanowire array cells is the objectives of this doctoral study. In depth investigation and experimental work have been also performed to spectrally engineer the solar spectrum for better exploitation in the short wavelength range using a luminescence down shifter layer on crystalline silicon solar cells.

In order to simplify the fabrication process of PV devices based on silicon nanowire arrays and to decrease the production cost of solar cells, two approaches were investigated based on etching. Chapter 3 presents the methodology for fabrication of SiNWs by simple maskless reactive ion etching.

The size, pitch and surface quality of the silicon nanowires can be controlled precisely in an etching process, utilizing nanosphere crystals as a mask. SiNWs, with larger diameters, can be produced using this method, which in turn allows for better cleaning of the surface damage arising from the etching and diffusion processes, with minimal chance of nanowire structural damage. Also, the reduced surface-to-volume ratio in silicon nanowires with large diameter results in lower surface recombination velocity. The size of the NWs can also be tuned by further processing through oxidation and etching.

In Chapter 5, the feasibility of the formation of SiNWs array cells, with radial p-n junction, are addressed by employing the fabricated SiNWs. The first architecture incorporates ordered, upright, crystalline p-Si nanowire arrays, formed on silicon substrate using maskless reactive ion etching as core, and conformal thin films of phosphorous doped amorphous silicon deposited by plasma enhanced chemical vapor deposition as emitter. Low temperature deposition of thin films for shell formation is advantageous, as it provides core-shell structures with less recombination centres. In the second architecture, a method combining microsphere lithography and reactive ion etching were developed for fabrication of ordered arrays of single crystalline SiNW arrays. A major advantage of this fabrication strategy is the ability to produce high-density, single-crystalline silicon nanowire arrays on a crystalline silicon substrate with fine geometric control without relying on epitaxial growth and complicated mask formation methods. Conformal transparent contact layers were formed by sputtering to planarize the sample and facilitate the formation of metal fingers. NW arrays do not require complex contacting as that of a single nanowire. The fabricated silicon nanostructures also have great potential for use as luminescence centers for down shifting. Moreover nanowire array geometry is beneficial for light trapping enhancement.

In order to better understand how the geometrical structure of the NWs affects the charge separation, theoretical simulations are performed, in COMSOL multiphysics, which is capable of solving drift-diffusion equations in 3 dimensional cylindrical coordinates. For this purpose, space charge density and electric fields, across the junction for a single core-shell wire and for different doping levels of p and n regions are investigated for conformal and non-conformal contacts. These studies provide further insights to improve the design and the materials in order to benefit from the implementation of SiNW array cells by enhanced efficiency in a cost effective manner.

In order to practically employ the concept of spectral down shifting in a simple and potentially inexpensive way, the feasibility of performance improvement of the crystalline solar cell by employment of simple luminescent down shifting architectures was explored. The LDS layer is comprised of cadmium selenide/zinc sulfide (CdSe/ZnS) quantum dots, with absorption in ultra-violet and emission in visible-near infrared range, embedded in transparent oxide and spin-on-glass mediums. As the luminescence down shifting is extensively correlated to the luminescence quantum efficiency of the quantum dots and the structure of the layer, a synthesis method for the formation of silica coated quantum dots is presented, aiming to effectively passivate the surface non-radiative recombination centres, and provide well-ordered quantum dot arrays over a large area with enhanced optical properties. Development of a technology for fabrication of a crystalline silicon solar cell is presented in Chapter 6. The fabricated cells were used to study the luminescence down shifting effect. The fabrication and characteristics of the solar cells with down shifting layer and silica coated QDs synthesis are described in Chapter 7 and Chapter 8, respectively.

The major objectives of this PhD study are summarized as follows:

- Development of simple and scalable processes based on reactive ion etching for the fabrication of silicon nanowire arrays. The silicon nanowire arrays will be utilized as a medium with enhanced optoelectronic properties including anti reflection coating, luminescence, and carrier separation.
- Development of simple approaches based on reactive ion etching and thin film deposition to fabricate radial p-n junction silicon nanowire array solar cells.
- Theoretical study on a radial junction core-shell silicon nanowire to investigate the effect of nanowire geometry and the doping levels of p/n regions on the charge separation.
- Development of simple approaches for deployment of a luminescence down shifting layer containing quantum dots in transparent layers, on crystalline silicon solar cells and to experimentally prove the concept of spectral engineering for better exploitation of solar spectrum in short wavelength range.
- Development of a synthesis method for formation of silica coated quantum dots, to provide control on the quantum dots' surface, and to experimentally prove the enhancement in luminescence quantum efficiency.
- To obtain ordered arrays of quantum dots over large area with enhanced optical properties.

1.3 Thesis Outline

Chapter 1: Introduction

In Chapter 1, silicon nanowire array cells and the luminescence down shifting method is briefly introduced to motivate the reader and to illustrate the demand for future research on these subjects. Some drawbacks of existing technology of both concepts are also pointed out.

Chapter 2: Approaches for Next Generation Photovoltaic Devices

Chapter 2 provides a review of the advanced photovoltaic concepts that potentially can yield high efficiency cells. In particular, spectral engineering in the form of the luminescence down shifting method and silicon nanowire array cells are comprehensively discussed. The former provides a high efficiency cell with less complication added to the existing cell, while the latter technology has great potential to improve the efficiency at a lower cost.

Chapter 3: Development of a Maskless Etching Process for Fabrication of Sub-wavelength SiN_x Structures and SiNW Array

Chapter 3 describes fabrication and characterization of silicon nitride (SiN_x) sub-wavelength structures and SiNWs formed by maskless reactive ion etching on silicon substrate. Results are also presented on dimensional control, surface passivation, detachment and further manipulation of the structures. The process parameters were optimized and their impacts on the synthesis process are discussed. The structural characteristics of the fabricated wires are studied. The surface properties of the wires after cleaning are analyzed. Optical properties of the fabricated structures are examined by the spectroscopic reflectance and photoluminescence measurements. The potential of the fabricated silicon nitride nanostructure for use as a template for the etching of the silicon substrate, are addressed. Reduced reflectance and the photon conversion ability of the fabricated nanostructures are verified.

Chapter 4: Simplified Process for Periodic Arrays of Silicon Nanowires

A simple and scalable method for fabrication of periodic arrays of SiNWs using colloidal crystals is reported in Chapter 4. The monolayers of colloidal silica nanospheres are formed on the silicon substrate by spin-coating and utilized as a template for subsequent patterning of sub-500 nm silicon nanowire array using reactive ion etching. The effects of plasma process parameters on the material synthesis are studied. The resulting sub-wavelength-structured arrays exhibit excellent broadband antireflective properties; which is promising for developing antireflection coatings for crystalline silicon solar cells.

Chapter 5: Radial p-n Junction SiNW Solar Cells: Modelling and Fabrication

The fabricated silicon nanowires are employed in fabrication of radial p-n junction silicon nanowire array cell architectures, with the conformal emitter planarized with transparent conductive oxide layers, for use as passivation and top electrode contact. The fabrication methodology and device characteristics of the fabricated cells are then presented in Chapter 5. The simulation results on the diode characteristics of the fabricated device, dependence of the depletion region depth on doping level at the p and n regions, and the distribution of the electric field across the junction for conformal and non-conformal contacts, are discussed. The nanowire array geometry also results in reduction in reflection loss and enhancement in the cell efficiency.

Chapter 6: Base Technology Development for Crystalline Silicon Solar Cells

The experimental details of the developed base technology for crystalline silicon solar cell fabrication which is used as a benchmark for future advanced solar cell designs are presented in Chapter 6. The crystalline silicon solar cell is fabricated replacing all conventional furnace processes with two low thermal budget rapid thermal process steps and a spin coating from spin-on-diffusion sources. The junction and the cell characteristics are reported. Optical confinement via random surface texturing is also discussed.

Chapter 7: Quantum Dot Layer for Luminescence Down-Shifting

The feasibility of performance improvement of the fabricated crystalline silicon solar cells by deployment of the planar luminescence down shifting layers containing cadmium selenide-zninc sulfide (CdSe/ZnS) quantum dots incorporated in oxide or spin-on-glass mediums is explored in Chapter 7. Attempts on the formation of the luminescence down shifting layer, in simple and potentially inexpensive ways, and deployment of the layer on top of the cell are presented. The experimental verification of the spectral down-shifting of the incident photons, are reported. The luminescence down shifting layer is only optically coupled to the cell. This is technically and potentially preferred as the introduced method does not add any complication to the production of PV cells using existing technologies.

Chapter 8: Synthesis of Silica Coated QDs for Spectral Engineering

Growth of an oxide layer on the CdSe/ZnS quantum dots, to form Cdse/ZnS/SiO_2 (core/shell/shell) nanoparticles using a chemical synthesis method, is presented in Chapter 8. The structural and photoluminescence (both steady state and lifetime) properties of the fabricated core/shell/shell structures are presented. The excitonic emission and decay of the synthesized nanoparticles are studied using a liquid nitrogen cryostat in the 77K-300K range. Experimental and theoretical decay lifetime analyses are also performed on the particles to better understand their excitonic lifetime behaviors. This study provides a better control on the quantum dot surface. Signatures of enhanced photoluminescence properties show the potential of the method to possibly provide quantum dots with improved luminescence quantum efficiency. In addition, it provides larger size nanoparticles that can be potentially self-assembled easier than smaller particles. Close-packed quantum dot superlattices in an oxide medium, ordered over a large area, can produce a media with great optical potential to deploy as down-shifter layers on the solar cells, for efficiency enhancement.

Chapter 9: Conclusions and Future Work

Finally, Chapter 9 concludes the contributions of the doctoral research in the development of feasible approaches for fabrication of radial p-n junction silicon nanowire array cells, and luminescence down shifting layers for spectral engineering.

Chapter 2

Literature Survey

Approaches for Next Generation Photovoltaic Devices

The sun provides earth with as much energy every hour as human civilization uses every year. If a small fraction of sunlight, captured by PV devices, could turn it straight into electricity, there would be no need to emit greenhouse gases from any power plant. However, due to the mismatch between the solar spectrum and the semiconductor material band gap (E_g) a primary proportion of the sum power is lost. Over the past three decades, new concepts have been investigated by many research groups, providing possibilities for the conventional solar cell to overcome this problem and thus enhance the cell conversion efficiency (η) at an even lower cost. These new pathways have shown great promise in the progress of photovoltaic technology. In this review these concepts were briefly discussed through new material properties and advanced device architectures.

2.1 Shockley–Queisser Limit for Crystalline Si Solar Cell

Currently, one of the major limits for the efficiency improvement of solar cells is ascribed to the spectral mismatch between the incident solar photon spectrum and the band gap of semiconductor on which the PV device is fabricated. For photons with energy higher than the band gap, the excess energy is transformed into kinetic energy of the electron–hole (e^--h^+) pairs, and subsequently converted to heat (known as lattice thermalization loss). For photons with energy lower than the band gap, the energy cannot be absorbed by the solar cell (known as sub-band gap transmission loss). Lattice thermalization and sub-band gap transmission contribute to >50% of the total losses (see Fig. 2.1). Therefore, the band gap energy of the semiconductor establishes a fundamental upper limit for the conversion efficiency of the PV device, known as the Shockley–Queisser limit [35]. The maximum thermodynamic conversion efficiency in a single-threshold bulk absorber was calculated to be about 31% under standard air mass 1.5 global (AM1.5G) [36] and 43.9% under concentrated solar illumination [35].

2.2 Approach to Ultra-high Efficiency Cell

To reduce spectral mismatch losses, two basic solutions might be adopted: designing a novel solar cell to better use the solar spectrum, or modifying the solar spectrum to better match the solar cell. The fabricated solar cells are known as “Third-Gen PV” [11]. The first route has been applied in constructing

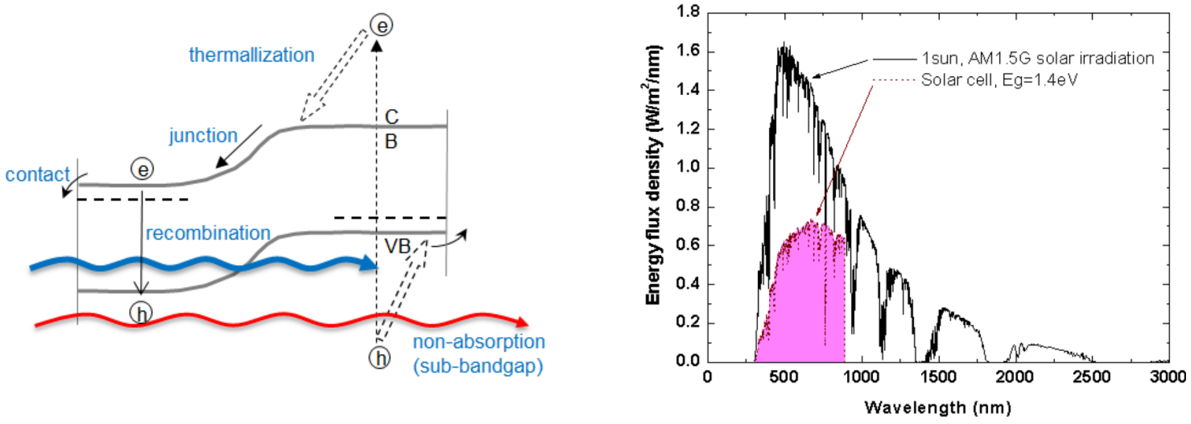

(a) (b)

Figure 2.1 a) Loss mechanisms in single junction devices, b) Solar irradiation spectrum of AM1.5G, 1 sun and energy utilization spectrum by a single junction cell with an energy bandgap of 1.4 eV [37].

the multi-junction solar cells, multi-exciton generation (MEG) cells [38,39], hot carrier (HC) solar cells [40,41] and multiband and impurity band solar cells [11]. Up-and-down conversion on the other hand has been utilized for spectral engineering [10,42]. These concepts utilize the photons with energy higher and lower than the semiconductor band gap. They are also considered as leading concepts that are mainly obtained with quantum dots (QDs) for high efficiency cells. Silicon nanowire (SiNW) array cells have also been widely proposed for low cost, high efficiency advanced solar cell architectures. It was attempted within this survey, to give an overview of recent efforts directed at utilizing nanocrystal (NC) QDs and NWs to produce low cost and/or high efficiency advanced solar cell architecture designs. In order to exploit their promising optoelectronic properties within these advanced device structures, understanding basic physics and inter-nanostructures coupling is necessary.

2.2.1 Nanocrystal QDs

Colloidal semiconductor NCs are promising functional materials with quantum confinement effect properties that hold immense potential for low-cost processing and high-efficiency solar energy conversion. Their low price process makes them advantageous over that of vacuum based techniques such as molecular beam epitaxial (MBE) for QD formation. Recent progress obtained over the last three years, regarding relatively efficient solar cells based on semiconductor NCs, provides ample incentives to continue investigating NCs as active components in both 2nd and 3rd generation solar cells. Some issues need to be addressed to enable the highest efficiency and lowest cost solar cells via colloidal NCs. Safe and simple large-batch syntheses with high yields and tight control over surface properties, size-dispersion, and morphology are required. We also need a better understanding of the factors that influence efficient NC coupling and transport within NC assemblies. Scalable fabrication of robust devices is also vital.

2.2.2 Multi-Junction Solar Cells

One approach to reduce the thermalization loss and increase efficiency above the 31% limit has been to use a stack of cascaded multiple p–n junctions, separated by tunnel junctions with descending band gap values along the direction of the incident light such that higher energy photons are absorbed in the higher band gap semiconductors and lower energy photons in the lower band gap semiconductors; this reduces the overall heat loss. Such cells are generally called tandem or multi-junction solar cells [43].

In practice, multi-junction solar cells using compound semiconductors have been successfully developed. They typically are implemented in III-arsenide and phosphide systems with 2-4 band gaps, taking advantage of the tunability of band gap energies and lattice constants with the compositions of III-V compounds. A typical structure of a triple junction solar cell with current world record efficiency is shown in Fig. 2.2.a. In this case the top cell is made of Gallium Indium Phosphide (GaInP) (E_g= 1.89 eV), the middle cell is Gallium Arsenide (GaAs) (E_g = 1.42 eV) and the bottom cell is Germanium (Ge) (E_g = 0.67 eV) with tunnel junctions in between, to match the currents between each cells [44]. The three absorb different portions of the solar spectrum, as demonstrated in the quantum efficiency plot of Fig. 2.2.b, depicting excellent coverage of the sun's spectrum.

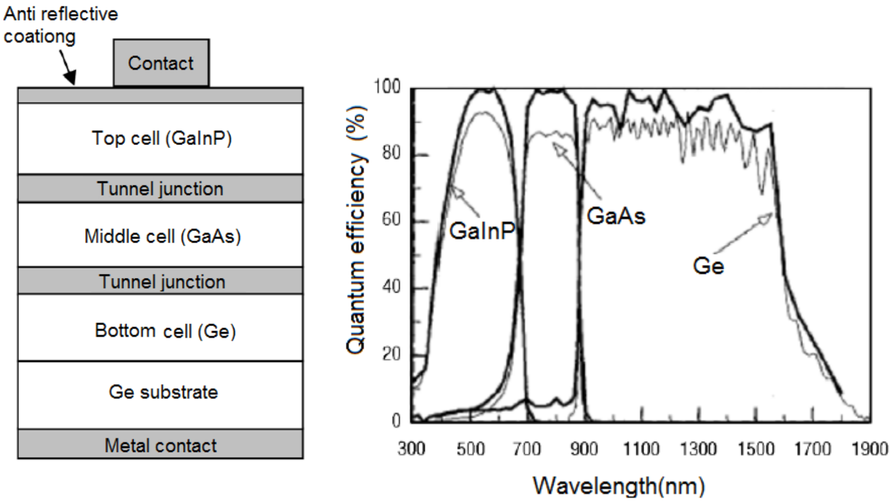

(a) (b)

Figure 2.2 a) A typical structure of a triple junction solar cell, b) Quantum efficiency curve of the cell [45].

It has been theoretically shown that the ultimate conversion efficiency of a tandem cell with an infinite stack of band gaps at one-sun intensity increases to about 66% and reaches 85% under maximum concentration of sunlight [46]. Actual efficiencies of about 32% have been reported in laboratory-scale PV cells with two tandem p–n junctions; and a world-record of 40.7% (under 240 sun illumination) efficiency has recently been demonstrated by Boeing Spectrolab Inc. using a structure containing a 3-junction device [47]. Work towards four and even six band gaps is in progress. The theoretical efficiency for four junctions is reported as 71% under maximum concentration [46]. Although the tandem cell efficiencies are very impressive, their cost is very high (>$7W_p$). The multi-junction cells were originally developed for space applications, where efficiency is of prime importance whereas cost constraints are less stringent.

Implementing the multi-junction solar cell technology for terrestrial applications has also been investigated using concentrated systems in solar power stations, where small area is necessary [44]. The cell cost can be kept low in spite of the expensive materials needed to make it, because only a small area is needed. However, this is at the expense of increased system complexity. Using cheaper material is an alternative approach to making cost-effective, high-efficiency PV modules based on tandem cells. Some researchers have proposed to use multi-layered Si quantum dot arrays to create an all Si-based multi-junction solar cell [11]. The concept is novel, in that it uses Si QDs of increased diameter with depth into the structure. The band gap tunability of Si QDs in an oxide matrix has been demonstrated by showing a photoluminescence (PL) energy shift as a function of dot size, which occurs due to the quantum confinement effect [11]. The main challenge here is to achieve sufficient regularity of the quantum dots in order to achieve the required charge transport properties.

2.2.3 Multi-exciton Generation Solar Cells

In the Shockley–Queisser analysis, the biggest loss factor limiting the conversion efficiency is that the absorbed photon with energy above the semiconductor band gap creates electrons and holes with a total excess kinetic energy equal to the difference between the photon energy and the band gap. Such charge carriers are termed “hot electrons and hot holes”. In such a case, additional energy from high energy photons is converted to thermal energy of excitons due to energy conservation and through electron–phonon scattering and subsequent phonon emission, as the carriers relax to their respective band edges and equilibrate with the phonons (see Fig. 2.3). This thermal energy will not be harvested by a conventional PV device, thus will be wasted. It is logical to propose new approaches so that the excess energy of the high energy photons can be harvested more efficiently.

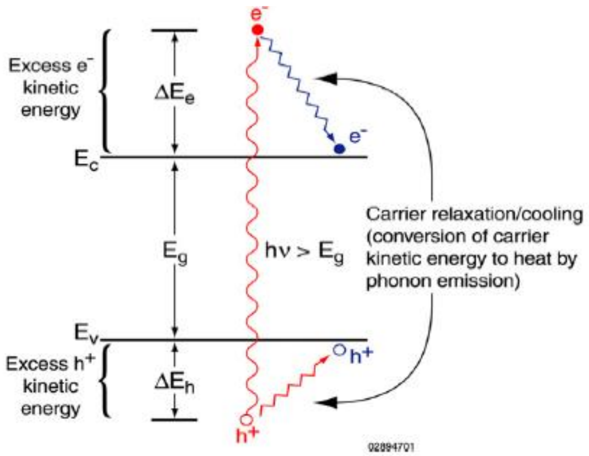

Figure 2.3 Hot carrier relaxation in semiconductors [40]

It has been shown that a single, absorbed high energy photon can generate two or more electron-hole pairs; thereby potentially increasing the output electrical current of the solar cell. This process occurs in all semiconductors, though in bulk the efficiency of the process is very low and termed impact ionization (II) [48]. In semiconductor QDs, the e^{-}-h^{+} pairs become correlated because of the spatial confinement and thus exist as excitons. Therefore, the formation of multiple excitons in quantum dots is labeled as multiple exciton generation by some authors; other authors prefer to use the term carrier multiplication (CM). In 1978, Nozik first proposed, theoretically, [40] that conversion efficiencies above 31% in single band gap solar cells could be achieved by capturing the excess energy of e^{-}-h^{+} pairs created by the absorption of solar photons larger than the band gap before these high energy e^{-}-h^{+} pairs converted their excess kinetic energy to heat (see Fig. 2.4.a) [40]. In order to achieve the higher photovoltages, the rates of photogenerated carrier separation, transport, and interfacial transfer across the semiconductor interface, must all be fast as compared to the rate of carrier cooling [40]. To achieve a higher photocurrent via MEG, the rate of impact ionization (Γ_{II}) must be greater than the rates of carrier cooling ($\Gamma_{cooling}$), electron transfer (Γ_{ET}) of hot electrons, and the Auger recombination processes (Γ_{Auger}). Also, the rate of electron transfer of cooled electrons must be faster than the radiative recombination rate ($\Gamma_{radiative}$) and Γ_{Auger} (see Fig. 2.4.b) [49].

Theory of MEG in Quantum-confined NCs

Semiconductor nanocryastals (NCs) provide a regime where carrier multiplication could be greatly enhanced through impact ionization (II) [38, 40]. II is an Auger-type process whereby a high energy exciton, created in a semiconductor by absorbing a photon of energy ($h\nu=2E_g$), relaxes to the band edge

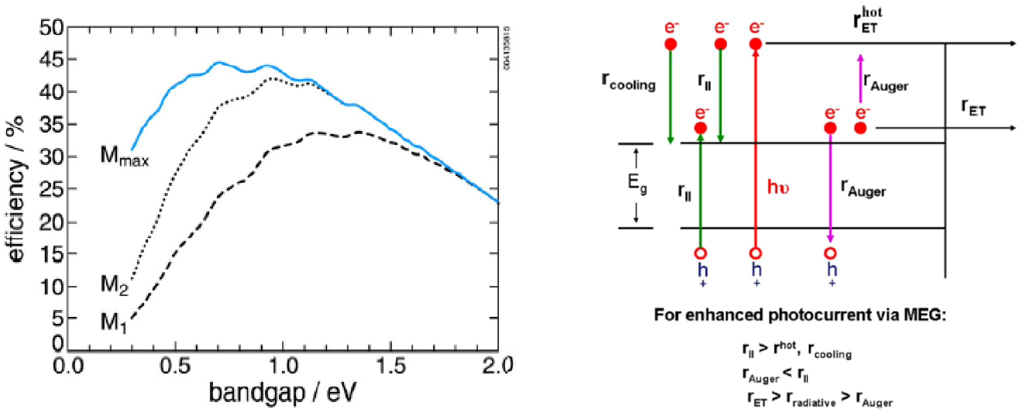

(a) (b)

Figure 2.4 a) Maximum thermodynamic power conversion efficiency with no solar concentration as a function of band gap for different carrier multiplication values per photon absorbed (M). M_1 is the Shockley–Queisser result with 1 e^--h^+ pair/photon, M_2 is the result for 2 e^--h^+ pairs/photon, and M_{max} is the maximum multiplication possible from the solar spectrum. About 95% of the efficiency gain with carrier multiplication is obtained with generating just 2 e^--h^+ pairs/photon. b) Dynamical channels for photoinduced hot electron–hole pair [50].

via energy transfer to a valence band electron. As a result of this energy transfer process two excitons are formed for one absorbed photon (see Fig. 2.5.a). Thus, this process converts more of the high photon energy portion of the solar spectrum into usable energy. Auger recombination (AR), the opposite of II, is a process in which an exciton recombines via energy transfer to an electron (or hole) that is excited to a higher energy state (see Fig. 2.5.b). Because of restrictions imposed by energy and momentum conservation, AR is inefficient in bulk materials. However, several theoretical models explain the enhancement of MEG in quantum confined NCs. The process is intensively under discussion, but has mainly attributed to the coherent superposition of degenerate single and multi-exciton states coupled by interparticle Coulomb interactions due to three-dimensional carrier confinement [51]. As depicted in Fig. 2.5.c, immediately following high photon-energy excitation (hν > $3E_g$), highly excited excitons form in some NCs. A fraction of these undergo II to create biexcitons (n_{xx}), while others simply cool to the band edge, remaining as single excitons (n_x). Biexcitons that form via II, next undergo AR to produce a single excitonover a long time. Fig. 2.5.d represents time resolved data in which carrier populations are monitored.

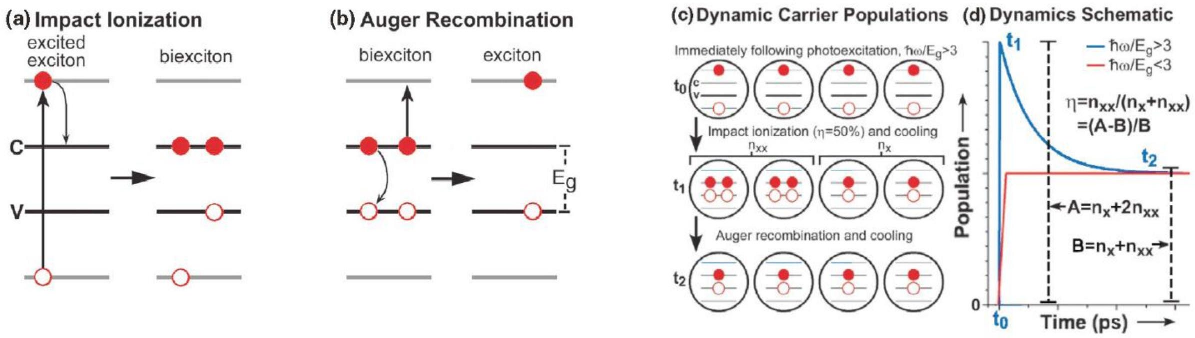

Figure 2.5 a) II and b) AR processes, c) Dynamic of MEG, d) Representative time resolved data [52].

MEG in Bulk Semiconductors

The creation of more than one e^--h^+ pair per absorbed photon has been recognized for over 50 years in bulk semiconductors; it has been observed in the photocurrent of bulk p–n junctions such as Si, Ge, PbS, PbSe, PbTe, and InSb [53,54]. However, II in bulk semiconductors is rather inefficient because of competing decay channels for the photogenerated electron-hole pairs, such as phonon-assisted cooling, which is extremely fast. Also, the threshold photon energy for II exceeds that required for energy conservation alone because, in addition to conserving energy, crystal momentum (k) must also be conserved. It has been shown that the rate of II becomes competitive with phonon scattering rates only when the kinetic energy of the electron is many times the E_g [48,55]. For important PV semiconductors like Si, which is overwhelmingly dominant in the PV cells in use today, this means that impact ionization does not become significant until the incident photon energy exceeds 3.5 eV, an ultraviolet energy threshold, that is beyond the photon energies present in the solar spectrum. Hence, this large blue shift of the threshold photon energy for II in semiconductors prevents materials such as bulk Si and GaAs from yielding improved solar conversion efficiencies [48].

MEG in Semiconductor QDs

In contrast to bulk semiconductors with low MEG quantum efficiency, Klimov and co-workers [56] recently demonstrated that in semiconductor QDs the MEG can be very efficient and the threshold photon energy for the process to generate two electron–hole pairs per photon can approach values as low as twice the threshold energy for absorption (the absolute minimum to satisfy energy conservation); this effect allows the threshold to occur in the visible (VIS) or near infra-red (NIR) spectral region. In fact, such a scenario can be realized in QDs due to their discrete energy levels that greatly slow down the energy dissipation process (Fig. 2.6.a,b) [57]. This arises because the energy separation between quantized levels in QDs can be many times the typical phonon energy. In order for the high-energy electrons and holes in higher excited quantized states to cool, by relaxing from a given quantum level to the next lower level, simultaneous multi-particle scattering events are required to satisfy energy conversion, which becomes highly improbable with increasing numbers of phonons emitted. Furthermore, crystal momentum need not be conserved because momentum is not a good quantum number for three-dimensionally confined carriers. According to the Heisenberg uncertainty principle the well-defined location of the electrons and holes in the nanocrystal makes the momentum uncertain.

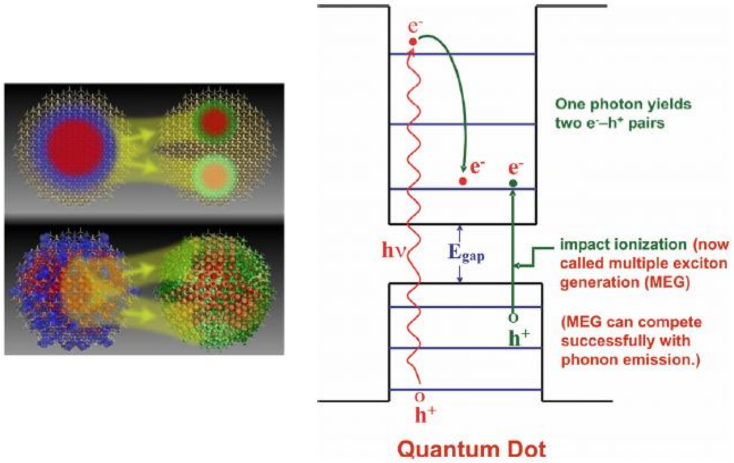

(a) (b)

Figure 2.6 a) The top image is a conceptualized MEG process while the bottom shows an actual exciton and biexciton [58], b) MEG in quantum dots with discrete energy levels [38].

MEG have been detected using several spectroscopic measurements including transient absorption (TA) spectroscopy, time-resolved photoluminescence (TRPL), terahertz (THz) spectroscopy and quasi continuous wave (CW) spectroscopy [59]. The evidence of MEG process has been reported by several groups [60]. Very efficient MEG has been reported in semiconductor QD materials including PbSe, PbS [59], PbTe [61], CdSe [62], InAs [63], InP QDs [60] and Si [64]. In experiments conducted with InP [65], PbSe and PbS [66] QDs, the cooling time of hot electrons increased by a factor of about 10 (from 200–300 fs to 2–3 ps) when inhibiting the Auger cooling channel. The slowed relaxation/ cooling of hot excitons via phonon emission allows other channels for relaxation, such as MEG, to become competitive and even dominant in QDs**.** Schaller and Klimov first reported a carrier multiplication energy threshold (ECM), the minimum photon energy necessary to achieve multi-exciton generation, for the formation of two or more excitons in PbSe NCs, 4-6 nm in diameter, to be more than 3 times the NCs band gap energy ($h\nu_{th}>3E_g$) [59]. They reported a quantum yield (QY) value of 218% at $3.8E_g$; QYs above 200% indicated the formation of more than two excitons per absorbed photon. Ellingson et al. have reported a quantum yield value of 300% for 3.9nm diameter PbSe QDs at photon energy of 4 times the QDs band gap, indicating the creation of three excitons per photon for every photo-excited QD [66]. More striking news of a 700% QE in 2006 was reported by Schaller et al. for PbSe QDs [67], indicating that it is indeed possible to multiply the number of excitons to 7 for a single absorbed photon [59]. It was shown that efficient MEG also occurs in PbS (see Fig. 2.7.a) and in PbTe nanocrystals [66]. Fig. 2.7.b presents the MEG QYs for Si QDs rising much more rapidly toward a QY of 3.0 at 3.5E_g and the threshold is at about 2.4E_g; this is to be compared to a threshold of 3.5E_g for bulk Si and a QY of only 1.4 at 4.5E_g.

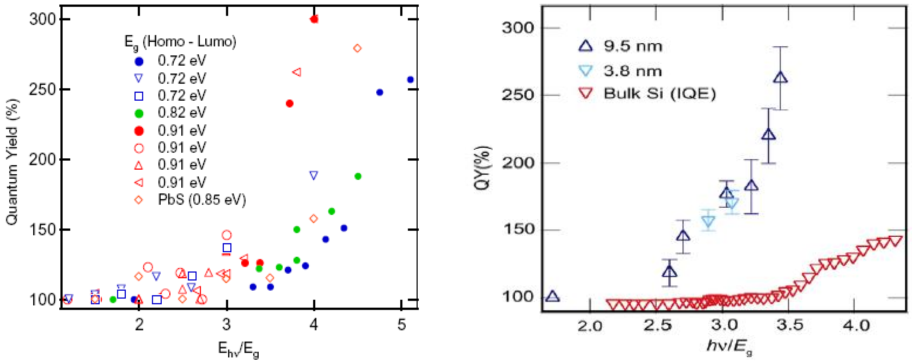

(a) (b)

Figure 2.7 a) MEG QY vs ratio of photon energy to QD band gap ($E_{h\nu}/E_g$) for a) three PbSe QD sizes and one size PbS QD (dia. = 3.9, 4.7, 5.4 nm and 5.5 nm, respectively, and E_g = 0.91, 0.82, 0.73 eV, and 0.85 eV, respectively) [66], b) 9.5 nm and 3.8 nm diameter Si QDs and bulk Si [64].

Successful ECM reduction down to ~2E_g has recently been observed utilizing momentum spread, small electron-to-hole mass ratio (m_e/m_h) and stronger exciton-exciton Coulomb coupling in InAs QDs [67]. To utilize the initial free energy after MEG occurs, the e^--h^+ pairs must be separated on a time scale, faster than the multiexciton lifetime; and extracted before free-carrier recombination.

Detailed balance limit calculations for solar cell efficiency with multiple carrier excitations have been calculated by Hanna and Nozik [68]. These calculations show that such processes fundamentally change the efficiency limit, as compared to the Shockley–Queisser limit, in a manner that the ‘‘ultimate’’ conversion efficiency can increase to 66% from 44% for a band gap below 1 eV, assuming ECM ~ 2E_g .

Photocurrent in MEG Devices

To date, the MEG in QDs has been mostly observed based on indirect spectroscopic methods. Few investigators have specifically looked for photocurrent >1 in a device design capable of utilizing MEG. This would require that in the QD device the time scale, for exciton dissociation, charge separation, and charge transport, be much faster compared to exciton recombination. However, in all optoelectronic QD devices, non-radiative recombination channels, arising from the charge delocalization and increased density of surface trapping and recombination sites, limits the charge extraction of the dissociated excitons. All the losses in the device such as reflection, transmission, scattering, re-radiation, absorption in the non-QD elements of the device structure and the non-radiative recombination channels are required to not exceed the increase in exciton population created through MEG. Law et al. [69] and Mora-Sero et al. [70], developed an approach to determine signatures of MEG in internal quantum efficiency (IQE) calculated from measured external quantum efficiency (EQE) within the device. Kirchartz and Rau modelled the I–V characteristics of idealized NC-based solar cells that can exhibit MEG [71]. They presented values of the carrier mobility and extraction rates needed in order to realize the benefits of MEG. However, there is still not an established device fabrication technology, since the charge separation and charge transport are a challenge.

2.2.4 Hot Carrier Solar Cells

As discussed in the previous section, electron–hole pairs generated in conventional solar cells, via absorption of photon energies above the semiconductor band gap, lose energy by cooling down from their initial energetic ‘‘hot’’ position to the band edges, by optical phonon emission. The hot carrier thermalization occurs in a very short period, in the range of picoseconds. If thermalization losses in solar cells can be avoided, significant improvement in efficiency can be obtained. Hot carrier (HC) solar cells attempt to minimize this loss by extracting carriers at elevated energies in a narrow range, requiring a substantial delay in carrier cooling in the hot carrier absorber (HCA) and energy selective carrier extraction by an energy selective contact (ESC) (see Fig. 2.8.a) [72]. The output voltage is given by the difference in the chemical potential of extracted carriers minus carrier cooling during extraction.

Minimum extraction time is required in HC devices. This is underlined by recent findings, where the optimum ratio of time constants for HC retention and HC thermalization is τ_{re}/τ_{th} ~1/10 [73]. Cold carriers in the external contacts are not supposed to cool the hot carriers to be extracted. In this case the design of contacts is a major challenge. The contacts should be able to extract hot carriers from the solar cell at selective energy levels. Contacts based on resonant tunnelling using quantum dots have been proposed [74].

General Carrier Cooling Dynamics

Carrier cooling in bulk semiconductors occurs within 10–100ps (see Fig. 2.8.b). Electron–electron interaction sets in by elastic scattering, leading to energy re-normalization for hot electrons, or to impact ionization. AR, the reverse process, is a no-loss mechanism as the energy released re-heats the free electron. Energy re-normalization leads to a Fermi–Dirac electron population and lattice thermal equilibrium. Local electrostatic lattice distortion, due to electron–optical phonon interaction, yields

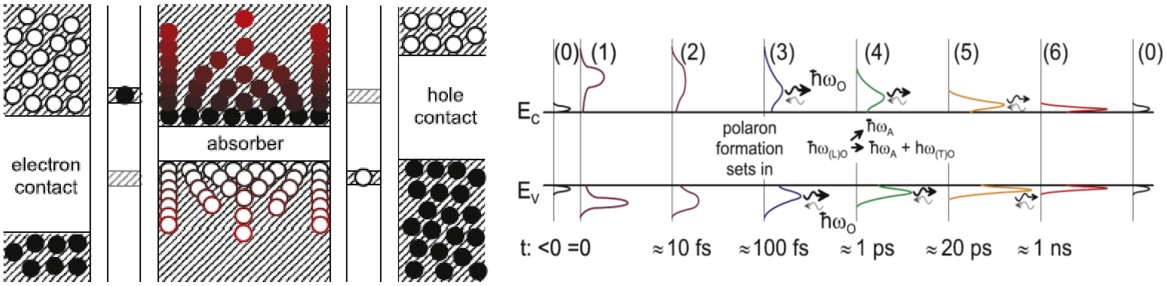

(a) (b)

Figure 2.8 a) Schematic of HC solar cell, b) carrier cooling kinetics in bulk semiconductor: Thermal equilibrium(0); immediately after optical generation (1); carrier–carrier scattering, impact ionization, re-normalizations, Fermi–Dirac statistics (2); optical phonon emission (3); decay of optical into acoustic phonons (4); further phonon emission (5), to thermal equilibrium, by carrier recombination (6) [75].

optical phonons, thus electron energy loss by optical phonon emission. Optical phonons decay further into acoustic phonons. Acoustic phonons re-heat free electrons that yield to direct (radiative) and indirect Hall–Shockley–Read (HSR) recombination. Photons generated by the former can be re-absorbed by ground state transitions or by free carrier re-absorption. HSR recombination is at least three orders of magnitudes lower than electron cooling.

Energy Selective Contacts

Energy selectivity is given by energy selective level (ESL), beyond which all electrons are reflected back into the HCA. Carriers cool with very low entropy production during extraction, losing some energy at the macroscopic contact in order to avoid back-diffusion (see Fig. 2.9.a-left). ESLs with sharp transitions minimize cooling during extraction. Quantum wires and wells show stronger carrier cooling by continuous electronic density of state (DOS) in a lateral ESC direction [76]. Highest energy selectivities are obtained by QDs (see Fig. 2.9.a-centre) or atomic impurities (see Fig.2.9.a-right). ESLs formed by atomic impurities do not suffer from size deviations like QDs. Iso-valent impurities form a neutral ESL mini-band with low electron exchange-correlation interaction. Such an ESL position depends less on its occupancy and is more robust for carrier transport.

Dopant at highly doped regions in conventional solar cells accelerates cooling by acting as scattering centres. A heavily n-doped semiconductor with wide band gap works as a buffer layer and removes the states into which minorities (holes) can tunnel (see Fig. 2.9.b).

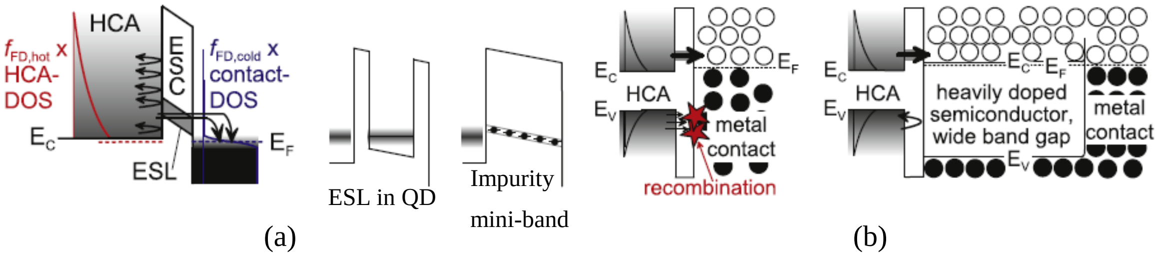

(a) (b)

Figure 2.9 a) ESC and ESL formation, b) Spacer layer of heavily n-doped semiconductor removes allowed states for minorities, reflecting them back into HCA [75].

Working Principle and Device Behavior

The processes in HC solar cells providing a steady-state HC population with HC extraction into macroscopic contacts are shown and briefly described in Fig. 2.10.a. Fig. 2.10.b shows the typical current density (J)-voltage (V) behavior of the HC solar cell; describing how this technology pushes the power flux and efficiency of a single-junction device beyond the thermodynamic limit (See dot-dashed black line in the figure). A photon flux of 1000 Suns, AM1.5, yielded conversion efficiencies of 55%, assuming feasible, yet unachieved carrier thermalization times of t_{th}=1ns [73].

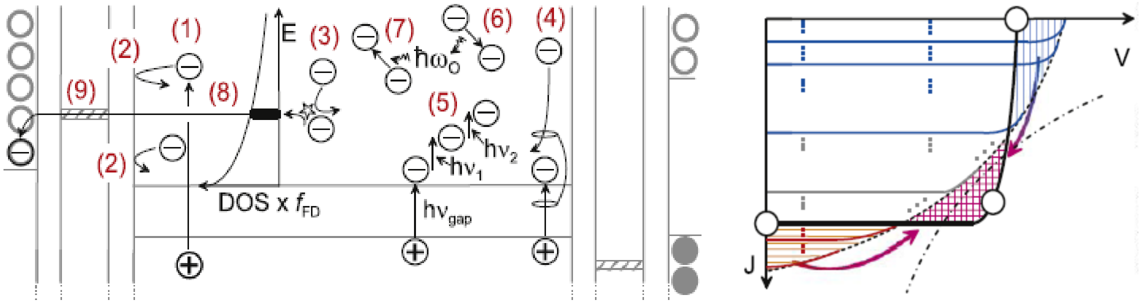

(a) (b)

Figure 2.10 a) HC solar cell with mechanisms of changing electron energy: hot exciton generation (1), reflected electrons at ESC (2), energy re-normalization by electron–electron scattering, refilling DOS subject to carrier extraction (3), impact ionization (4), free electron re-absorption of sub-band gap photons (5), optical phonon emission (6) and re-absorption (7), quasi-ballistic transport (8), energy selective tunnelling from HCA (9) , b) Qualitative JV-behavior of HC cell [75].

2.2.5 Impurity Photovoltaic Effect and Intermediate Band Solar Cells

Another leading concept that can be obtained with quantum dots for high efficiency cells is the impurity level PV (IPV) or intermediate band (IB) solar cell which can be considered as a form of up-conversion. The intermediate energy levels or bands give rise to multiple energy gaps, suitable for absorbing photons of a wide energy range, such that low energy photons can be absorbed in a two-photon process that promotes charge carriers to the conduction band.

The IPV concept can be exploited by two-step generation via impurity states within the band gap to utilize sub-band gap photons and therefore enhance solar cell performance (see Fig. 2.11.a) [77,78]. The challenge is to find a suitable host wide band gap semiconductor combined with a sufficiently radiatively efficient impurity. The IB solar cell is characterized by the existence of a narrow band within the main band gap (see Fig. 2.11.b). The states of closely spaced QDs, when finely tuned, yield an intermediate band. Three transitions, available in both systems, enable the device to better match to the solar spectrum.

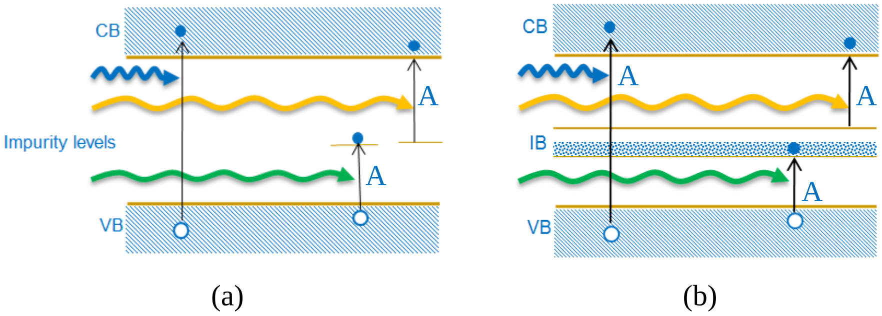

Figure 2.11 Schematic diagram showing absorption of above-band gap and sub-band gap photons through (a) impurity level, (b) intermediate band; showing the valence band (VB), intermediate band (IB), and conduction band (CB), transitions between these bands (A).

To date, very few bulk materials have been shown to possess such intermediate states. One of these is the ZnCdTe system demonstrated by Yu et al. using a combined high energy oxygen implantation and laser recrystallization process [79]. Other materials have been studied theoretically, but not demonstrated experimentally. Sub-band gap photons can be absorbed by quantum wells (QWs) or QDs with narrower band gap incorporated in the original PV material [80]. The carriers or excitons generated in the QWs/QDs can thermally escape onto the conduction band, for electrons or valence band for holes, to contribute to the total photocurrent enhancement, ideally maintaining the photovoltage of the original material. Photocurrent enhancement for a GaAs solar cell with InGaAs/GaAs multi-quantum wells (MQWs) relative to a GaAs cell without MQW in the IR region was observed [81]. Experimental work has been carried out using InAs quantum dots embedded in GaAs to form an effective intermediate band structure, which is being pursued by Luque and co-workers, showing promising initial results. The prototype cells have also been fabricated [82].

The limiting solar cell efficiency for single impurity level and single intermediate band gap is reported to be above 63 % [7,10], which is the same as the limiting efficiency of a stack of three solar cells.

However, the advantage in IPV and IB concepts is that the same material is used throughout and the interconnection between cells occurs automatically, thus this approach has great promise.

2.2.6 Up/Down Conversion & Down-shifting

To reduce the energy losses including lattice thermalization loss and sub-band gap transmission loss, spectral modification through down-shifting (DS), down-conversion (DC) as well as up-conversion (UC) of photons is regarded as an effective route.

In a typical solar cell, high-energy photons are excited well beyond the conduction band edge, where they are mostly lost due to interaction with phonons (thermalization). Down-shifting is aimed at absorbing these high-energy photons and shifting them to lower energies, through a relaxation process, to a lower energy state (see Fig 2.12.a). It is a process, where the QY is always less than or equal to unity. The fundamental mechanism of down-conversion is the absorption of high energy photon, with relaxation into intermediate states within the band gap, emitting two lower energy photons (see Fig. 2.12.b); thus its QY exceeds one provided that the non-radiative losses can be prevented. On the contrary, up-conversion is to generate one higher energy visible or NIR photon from at least two lower energy photons [83]. The typical mechanism of up-conversion involves absorption of sub-band gap light into an intermediate state, followed by further absorption of a second photon to the conduction band edge. The excited charge carrier then relaxes back to the valence band edge, emitting a single higher energy photon (see Fig. 2.12.c).

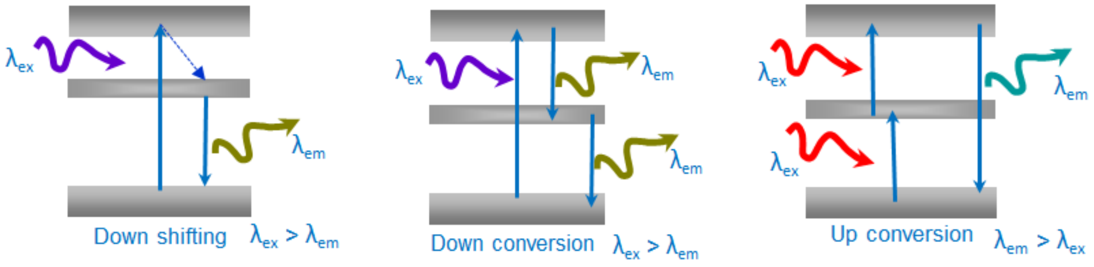

(a) (b) (c)

Figure 2.12 Fundamental mechanisms for a) down-shifting, b) down-conversion and c) up-conversion.

Multiple mechanisms, including various energy transfer schemes from a state associated with the luminescent materials to those associated with the host lattice, have been identified for DS, DC and UC. In Fig. 2.13 photon conversion processes for *lanthanide* ions (Ln^{3+}) ions are illustrated. The simplest Ln^{3+} DS processes are resonant radiations, in which a photon of a particular wavelength is absorbed and an equivalent photon is immediately emitted. More common processes occur when Ln^{3+} ion undergoes non-radiative transitions. The generated photon is red-shifted, as it loses its energy referring to Stoke-shifting (see Fig. 2.13.a). The reported NIR DC processes are generally based on two kinds of mechanisms, i.e., the second-order cooperative energy transfer (ET) and the first-order stepwise ET. One incident high energy photon is absorbed by one donor ion and then the energy is transferred to two neighbor Ln^{3+} acceptors either simultaneously (ET) (see Fig. 2.13.b) or in a consecutive manner (stepwise ET) (see Fig. 2.13.c), yielding two low energy photons with theoretical QY of 200%, assuming no non-radiative losses is presented. The stepwise ET mechanism is effective only when the donor has a suitable intermediate state to assist the two-step sequential ET to the acceptors.

UC processes are mainly divided into three categories: excited state absorption (ESA), energy transfer up-conversion (ETU) and photon avalanche (PA). All these processes involve the sequential absorption of two or more photons resulting in the population of a higher excited state where up-conversion emissions occur. In the case of ESA, the incident excitation photons are successively absorbed by a single Ln^{3+} ion, as shown in Fig. 2.13.d. The excitation in ETU is realized through energy transfer between two neighouring ions and populates the metastable state E1 where each ion absorbs a phonon of the same energy (see Fig. 2.13.e). One of the ions promotes to the upper emitting state E2 in a non-radiative energy transfer while the other ion relaxes back to the ground state G. The dopant content, which determines the mean distance between the neighouring ions, has a strong impact on the UC efficiency of an ETU process. In a PA process as shown in Fig. 2.13.f, cross-relaxation (CR) ET between the excited ion and a neighouring ground state ion occurs, leading to the occupation of both ions at the intermediate state E1. Circularly, these two ions can populate the E2 state again, to further intrigue cross-relaxation and promote exponentially the population of E2 state by ESA, finally producing a strong UC emission like an

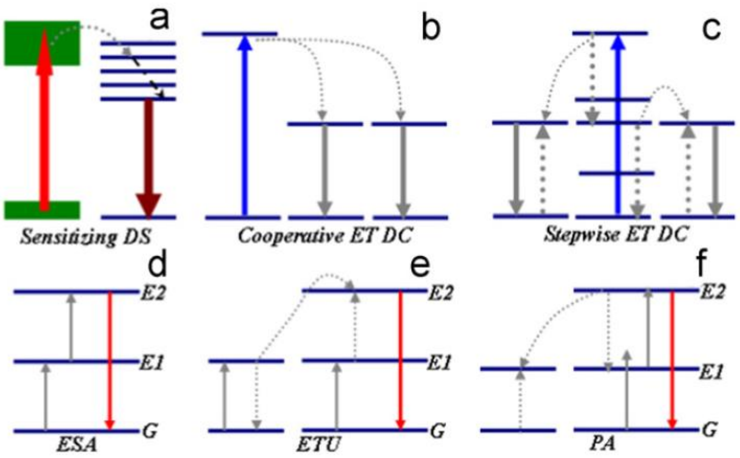

Figure 2.13 Schematic illustrations of photon conversion processes for Ln^{3+} ions through multiple ET mechanisms: a) down-shifting, b, c) down-conversion, d-f) up-conversion, The dotted, dashed–dotted and full arrows represent energy transfer, non-radiative relaxation and photon absorption/ emission processes, respectively [84].

avalanche process. Among three UC processes, ETU has mostly been used to offer highly efficient UC, since it is instant and pump power independent [85].

Spectral modification aims at converting the solar spectrum via luminescence to match the absorption properties of the PV devices. This is fundamentally in contrast to other concepts of third generation solar cells, which require major change in the structure of the device. Consequently, spectral modification can be treated as an optical process alone, just by adding layers on top or at the bottom of conventional cells, and dissociated from the actual operating physics of the PV devices. This is attractive because one can keep the assets of the existing solar cell technology. As a result, photon conversion materials can be applied to the existing first and second-generation PV devices. The typical coupling of a solar cell with a photon conversion layer is schematically illustrated in Fig. 2.14. The material layer performing the down-conversion/down-shifting operation should be placed at the top of the cell, where light is entering the cell. The material layer performing the up-conversion operation should be placed at the bottom or rear side of the cell with a reflector. Here, the unabsorbed low-energy photons will be converted into high-energy photons and the reflector will send them back into the solar cell to be absorbed.

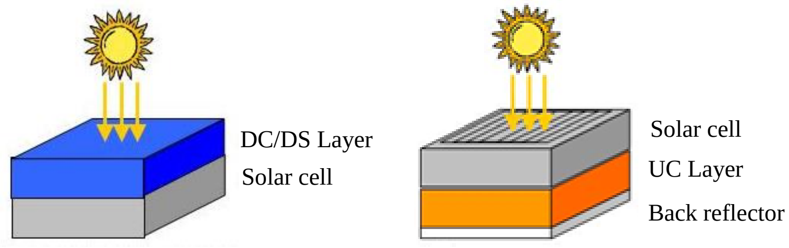

(a) (b)

Figure 2.14 Coupling of a solar cell with a) DS or DC and b) UC layers [85].

Noticeably, DS may raise the efficiency of the solar cell by converting one higher energy photon into a lower energy one that is more efficiently absorbed by the cell, but it could never be used to break through the Shockley–Queisser limit. Whereas, DC and UC processes are capable of increasing the solar cell efficiency beyond this limit. Using DS, the energy losses originating from surface recombination, Auger effect and HSR recombination are reduced in the cell. This results in an increased spectral response of the solar cell at higher energies. A higher number of photons and additional electron–hole pairs are generated in the DC or UC layer, which would result in an increase of short circuit current and efficiency of the solar cell. Theoretical studies based on detailed-balance calculations predict a maximum conversion limit of 36.6% and 37.4% for an ideal DC and UC layer, respectively, under non-concentrated sunlight irradiation [10, 42].

The feasibility of gaining from DS through some simple, cost effective design architectures was examined in this work. Hence, this process is reviewed here in more detail, where the properties of the available materials are considered.

Grade of Effectiveness of the Luminescent Down-shifting (LDS) Layer

Any potential gains to be made by the shifting of the spectrum will have to compensate for additional interactions with the light passing through the LDS layer, resulting in extra loss mechanisms, before offering an overall improvement. The extent of these losses is strongly dependent on the material and the thickness of the sheet, as discussed in the following sections.

Host Material

In order to maximize the benefits from the LDS method, the host material must exhibit high transmittance and low scattering, particularly in the region where the cell's response is high. It also needs to provide an optimum environment for the dissolving of the luminescent species with the thermal and photostability. Given that highly transparent materials are naturally desirable for PV applications, the thickness of the luminescent layer is critical. Thin sheets of polymers such as polymethyl methacrylate (PMMA) [23, 24, 86] or polyvinyl acetate (PVA) [25], inorganic crystalline materials such as aluminum oxide (Al_2O_3) [2] or calcium fluoride (CaF_2) [87], oxide/glasses [88-90], organic molecule silicates (ORMOSIL) [91] and organic paint thinners [92], seem to fulfill these requirements.

Polymeric and glass materials can exhibit high transparency in the visible region of the spectrum, adequate resistance to heat and humidity variations, and high mechanical strength [93]. The PV industry has extensive experience in the use of cover glasses and polymeric materials, especially polyethylene vinyl acetate (EVA) copolymer, which is the standard encapsulant used for wafer-based Si solar cells [29]. On the other hand, photo-degradation under extended UV exposure is a major issue for polymeric materials that can be addressed by utilizing UV stabilizers and absorbers [29, 93]. Inorganic crystalline materials exhibit high transparency for the whole spectrum and long photostability [2]. They are, however, expensive and difficult to process and thus, unlikely to be considered as an option on a commercial basis. As host materials, polymers, oxides and glasses appear to be the most attractive choices due to the good optical properties that they exhibit, along with ease of processing and low cost.

Luminescent Materials

The luminescent species introduce the most significant additional losses resulting from the addition of an LDS layer. Non-unity luminescent quantum efficiency (LQE) gives rise to energy loss from the excited luminescent species by non-radiative relaxation. Re-absorption losses are significant, especially in the cases of QDs [28] and of some organic dyes, particularly if high concentrations are used [94]. Additional loss mechanisms are due to the isotropic profile of luminescence. The photons emitted towards the top or the sides of the LDS sheet with an angle of incidence smaller than the critical angle will escape. The rest will be internally reflected and transmitted towards the cell.

The luminescent species used for LDS ideally needs to exhibit: (i) unity LQE, (ii) a wide absorption band in the region where the external quantum efficiency (EQE) of the cell is low, (iii) a high absorption coefficient, (iv) a narrow emission band, coinciding with the peak of the cell EQE, and (v) good separation between the absorption and emission bands in order to minimize losses due to re-absorption. Low cost materials with prolonged photostability are also of great interest. A large number of luminescent materials have been investigated for LDS and can be separated into three main categories: QDs [89,95, 96], organic dyes [23, 24,97] and rare-earth ions [98-102].

QDs are nanosize semiconducting crystals with tunable absorption/emission bands, according to their size. They exhibit a wide absorption band, high emission intensity, relatively good photostability [103]. On the other hand, they result in high re-absorption losses due to their large overlap of absorption and emission bands, exhibit relatively poor LQE and they remain generally expensive [28].

Organic dyes exhibit relatively high absorption coefficients as defined by the Beer-Lambert law [24] close to unity LQE and are easy to process in polymeric matrices [104]. Their drawbacks are narrow absorption bands and relatively significant re-absorption losses [105]. Several dyes can be mixed within one layer in order to improve their absorption bandwidth and to expand their Stokes-shift [106] . Their photostability, over prolonged periods of UV exposure, remains questionable in many cases.

Rare-earth ions exhibit high LQE, but have extremely low absorption coefficients [107]. The latter can be improved slightly by increasing concentrations and thickness, or by using the more promising approach of an antenna structure with much higher absorption properties. [108].

Fluorescent organic dyes are currently the most promising luminescent species, due to their high LQEs and absorption coefficients, ease of processing in polymeric matrices and relatively low cost. While, QDs are attractive due to their tunable absorption/emission bands and their wide absorption band, continued research and development is required to improve their LQE and lower the cost.

Effect of Different Spectra

The spectral energy distribution, of the incident spectrum to a cell, is of great importance for the gains to be obtained by the LDS method. This is because there is more gain when more photons are available to be shifted in the first place and thus contribute to the cell’s output. LDS will therefore result in higher gains under blue-weighted spectra. Naturally the AM1.5 diffused spectrum in absolute figures will give the smallest gains, since it has the smallest energy flux, but it offers the largest improvement in relative terms. It gives three-fold improvement in the device output as compared to AM1.5D [96,108]. The AM0 gives the second best improvements. AM0 spectrum exhibits a 50% greater improvement in comparison to AM1.5G [109]. It should be noted, that at extra-terrestrial and/or diffuse conditions, LDS -results in cell performance enhancement in terms of conversion efficiency and not necessarily of absolute output power, which primarily depends on the power density of the illuminating spectrum. The consequence of the LDS analyses depends strongly on the choice of incident spectrum. This should always be taken into consideration for the analysis of results; and reports should refer clearly to the illuminating spectrum.

Advantages of the Luminescence down shifting method

As the LDS is a passive approach, the optimization of the LDS layer can be done independently from the cell, imposing no additional difficulties, other than the engineering of the layer itself. The cost of the luminescent species itself is considered negligible in comparison to the overall cost of the module (for instance in the case of a Si-based device). Si wafer-based devices are commonly encapsulated with sheets of cover glass and some polymers at the front and rear. The inclusion of luminescent species in these materials can simplify, even more, the fabrication method. LDS can also be utilized to prevent UV-induced photodegradation [27], reduce electron-hole pair thermalization [109] and finally present the PV modules through coloration. This technology is commercially feasible for the UV blocking layers or encapsulating material needed in polymer-based devices.

To date, efforts in down-conversion have been successful using bulk materials and with limited success when using nanostructures; with attempts using Si nanocrystals [89,110] and QDs [96] being the main approaches. PL-based enhancement of CdTe thin film solar cells has been demonstrated using bulk crystals [111]. Several schemes have been proposed for photon conversion to lower energies using nanostructures. So far very few materials have shown quantum efficiency greater than one [108]. It has been demonstrated, by fabricating silicon NCs in dielectric layers to be put on the top of the cell to work as an anti-reflective coating (ARC), which additionally provides quantum efficiency enhancement in the ultra violet (UV) range. Svrcek et al. attempted to implement such a scheme by forming Si quantum dots in a spin-on-glass (SOG) layer deposited on top of a standard Si solar cell [89]. They observed a small enhancement in quantum efficiency at short-λ, however, the overall efficiency was not enhanced. This was attributed to losses associated with non-radiative recombination at surface states due to incomplete surface passivation. The basic down-converting properties of silicon nanostructures have also been studied; and similar to the above report, show a dependence on passivation [112]. De la Torre et al. fabricated Si NCs in SiO_x and SiN_x matrices for this purpose. Fig. 2.15.a exhibits the photocurrent intensity as a function of photon energy from Si NCs dispersed in a SiO_x matrix. It shows increased absorption at high excitation energy as compared to the reference sample (without SiO_x layer) [110].Another way to achieve spectral down-conversion is using quantum dots as photoluminescent converters, as has been shown, for example, with CdSe QDs by van Sark et al. [113]. Calculations showed an expected relative efficiency improvement of 10% for npp^+ multicrystalline Si (mc-Si) solar cells based on experimental absorption and luminescence data of 4.3 nm diameter CdSe QDs. However, experimental verification of such an improvement was not shown.

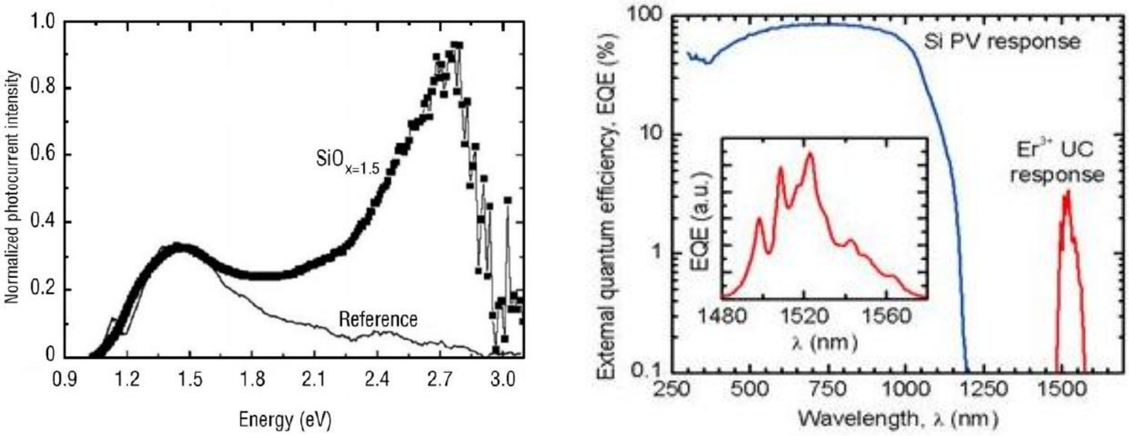

Figure 2.15 a) DC in Si nanocrystals dispersed in a SiO_x matrix [110], b) Measured EQE of a Si cell with a $NaYF_4$:20%Er^{3+} UC layer [114].

Up-conversion has been demonstrated by putting $NaYF_4$:20%Er^{3+} at the rear of the cell (see Fig.2.15.b). [93]. There have also been recent demonstrations of the use of micron scale and nanoscale phosphor particles to enhance the quantum efficiency of a solar cell by UC [115]. Recent work on nanoparticle based up-converters has shown that the luminescence efficiency is in the order of 1% and is strongly influenced by particle size and annealing conditions. One of the principal issues with such nanoscale size particles is the loss in efficiency associated with non-radiative recombination at the surface, as the size of the particles is decreased. It has also been shown that two IR photons, absorbed by a vitroceramic doped with certain rare earth, could emit one visible photon[116]. This concept was proven for a GaAs cell, showing power output from IR incident light [117]. The upper limit of cell efficiency with an up-converter was estimated to be 48% and 63% under 1 sun and 46,200 suns, the geometrical concentration limit, respectively [10].

2.2.7 Enhanced Absorption through Plasmonic Effects

The final mechanism associated with nanoparticles (NPs) to be discussed is plasmonic. The absorption of a given wavelength photon can selectively be enhanced using surface plasmon (SP); defined as the collective oscillation known as surface plasmon polarities (SPPs) of free electrons at the metal surface [118,119]. In metallic NPs these SPPs are resonant at frequencies that are size and shape dependent [120,121]. The plasmon excitation is possible when the size of the metallic particles at the surface is much smaller than the photon wavelength. This principle is particularly suited for absorption of long wavelength photons (>700 nm).

Metal nanoparticles placed on solar cell surfaces can act as "antennas" to collect the incident light with their large extinction cross section near the surface plasmon resonance and then scatter the incident light into a wide range of angles to increase the optical path length in the thin absorber layer (see Fig. 2.16.a). High optical scattering rates over absorption rates can be obtained for noble metal particles to minimize absorption loss by properly choosing particles' diameters in the 20-100 nm range. By placing a metallic layer at the bottom of a photovoltaic layer, as schematically depicted in Fig. 2.16.b, incident sunlight is coupled into surface plasmons, propagating at the semiconductor/metal interface via subwavelength-size grooves to increase the optical path by switching the light direction from normal to lateral [122,123].

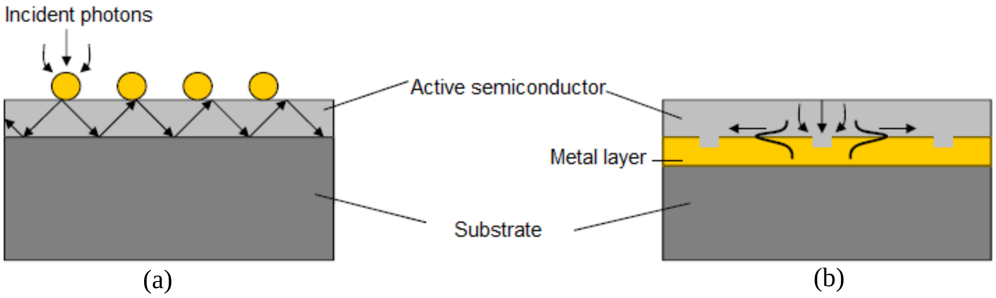

Figure 2.16 Schematic cross section of plasmon-enhanced solar cell structure with (a) metal nanoparticles on top and (b) back metal layer with grooves [131].

Plasmon waveguides consisting of closely spaced silver (Ag) nanoparticles with diameters around 30 nm have been experimentally observed to guide electromagnetic energy over distances of several hundred nanometers via near-field particle interactions [124]. The surface plasmon can improve the absorption of light in thin film cells by local electromagnetic field enhancement, where due to economic reasons, less material is used, which in many cases is not sufficient for complete absorption of the solar spectrum [125 ,126]. Schaadt and co-workers showed that when 20–100 nm gold (Au) NPs are placed on top of a standard Si p–n junction (see Fig. 2.17.a), the short-circuit current can be improved by a few percent, at wavelengths associated with SPP resonant frequency (see Fig. 2.17.b). The optimum size distribution for absorption of the solar spectrum by plasmonic nanoparticles has been calculated by Cole and Halas [121]. At or near the plasmon resonance wavelengths, increases in photocurrent response of 50-80 % or more, relative to that of the Si p-n junction diode, have recently been demonstrated [127] (see Fig. 2.17.c).

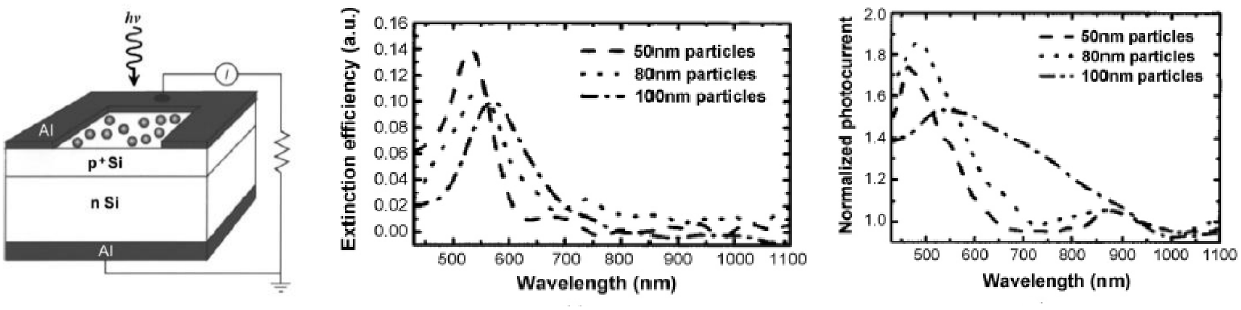

(a) (b) (c)

Figure 2.17 a) Schematic of the structures used to demonstrate the plasmonic concept, b) extinction efficiency of NPs and c) photocurrent enhancement as a function of wavelength for different metal nanoparticle size [127].

Ag NPs have also been applied to silicon solar cells and showed an absorption enhancement of between 7 and 16 times, in the wavelength range of 1050–1200nm [127]. Yu and co-workers further showed enhanced photocurrent effects in a-Si-based thin film cells; and also that the concentration of NPs played a strong role in the observed photocurrent enhancement [128]. Optimum concentration of NPs enhances the light scattering, and above this concentration the particles reflect too much light. The trade-off between the absorption length and the carrier diffusion length exists in III-V semiconductor compound solar cells. A couple of groups have experimentally studied optically-thin GaAs solar cells with arrays of sub-λ-size metal particles on top; and observed enhancement in photocurrent, particularly in the NIR region and even in overall cell efficiencies [129]. Several research groups have observed photocurrent enhancement for Si cells by using NPs on the rear side [127,130]. Applications of such plasmonic metal nanoparticles to other types of solar cells, such as dye-sensitized solar cells and organic solar cells, have also been reported [131]. The plasmon-induced absorption enhancement by metallic back structures would only occur significantly for strongly absorbing or direct band gap semiconductors, accounting for the ohmic loss in the metals. Silicon, which is a weak absorber, has a much lower energy absorption fraction [131]. Enhanced absorption in SP can also be utilized to improve the efficiency of up-conversion and down-conversion materials and devices.

2.2.8 Nanowire Approaches

The potential of the semiconductor NW PV devices for lower cost and greater energy conversion efficiency, as compared to conventional thin films and crystalline solar cells, have recently attracted much interest in the PV industry. These structures consist of single or high density arrays of Si wires [13,132] with diameters ranging from approximately 50 nm to 10 µm, with axial or radial p-n junction formed on the wires.

NW Synthesis Methods

Nanowire solar cell fabrication consists of three key steps including: nanowire synthesis, junction formation and contacting.

Many research studies are now dedicated to nanowire synthesis [133-135]. Vapor-liquid-solid (VLS) mechanism is one of the most common techniques used in NW solar cells. Vertical nanowire is grown with the proper substrate, precursor, temperature, catalyst, and concentration; and ordered nanowire array is obtained by catalyst patterning. However, it has been found that the Au catalyst used in conventional SiNW VLS growth, introduces an impurity state in band gap, deteriorating minority carrier lifetime and device performance.

Alternatively, patterned etching is a top-down approach that involves a lithography step followed by an etch step. Approaches, such as electron beam lithography (EBL)**,** nanoimprint, nanosphere assembly, anodic alumina and block copolymer formation, are mainly considered for the initial lithography step [136-138]. Directional, substrate-selective etching methods such as deep reactive-ion etching (DRIE) or metal-assisted chemical etching are used to make the NW patterns [139].

The nanosphere assembly patterning approach is particularly useful, as it provides an excellent control on the nanowire's diameter and pitch, simply by choosing the appropriate sphere diameter and etch time, prior to the substrate etch step [20]. Silica and polymer spheres can be synthesized with a wide range of diameters (100–1000 nm). Using Langmuir-Blodgett (LB), dip-coating, spin coating and roll-coating methods, nanospheres charge delocalization can be assembled over large areas [140,141]. Anodic alumina and block copolymer templates can access much smaller pattern dimensions (10–100 nm) and have been used to fabricate nanowires with diameters of ∼10 nm [142]. Fig. 2.18 shows the nano wire array cell fabricated with nanosphere lithography and DRIE.

Approaches for Dopant Introduction

Dopants can be introduced by diffusion or by depositing a thin film over the original nanowire [143,144]. In the case of diffusion, if the time is too long or the temperature too high, the benefits of the radial junction can be completely lost, due to formation of recombination centres in the wire. In thin film deposition, the shell can be single crystalline if grown epitaxially, but more often it is polycrystalline, in cost effective processes. Fig. 2.19.a shows a schematic of a SiNW array cell with a crystalline *n*-Si nanowire core and the polycrystalline *p*-Si shell. The secondary electron microscopy (SEM), transmission electron microscopy (TEM) and high resolution transmission electron microscopy (HRTEM) exhibited in Fig. 2.19.b, Fig. 2.19.c and Fig. 2.19.d respectively; demonstrate dense wire packing with vertical alignment, single-crystalline core and the polycrystalline Si shell.

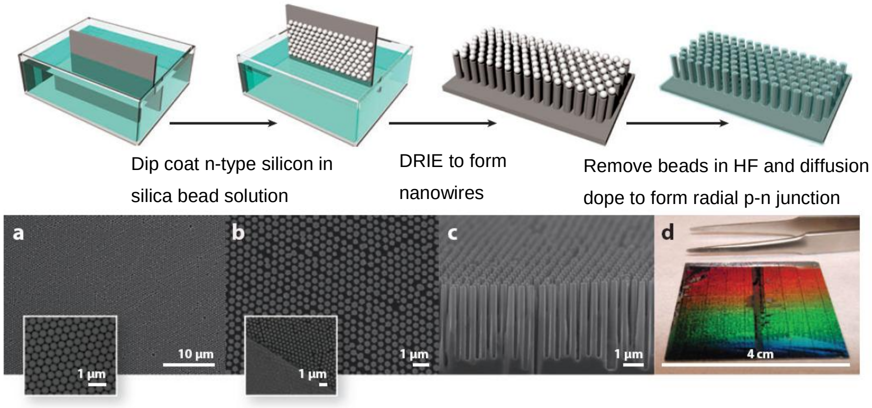

Figure 2.18 Schematic(top) and (a-c) Scanning electron microscopy of NW array solar cell fabricated by bead assembly and DRIE, (d) Tilted optical image of 36 silicon nanowire radial p-n junction solar cell arrays from panel a (bottom) [140].

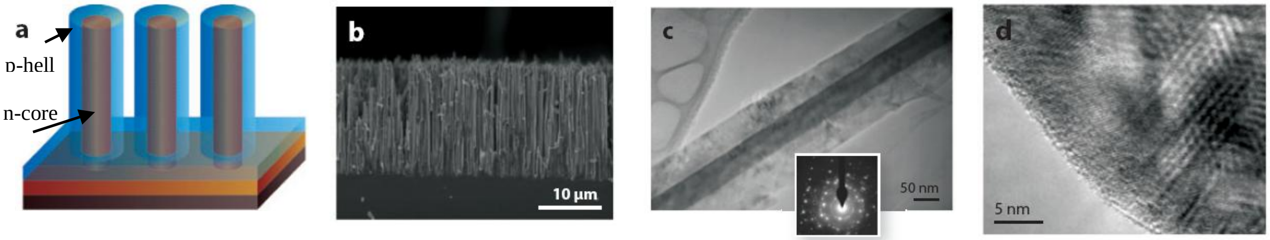

Figure 2.19 a) Schematic core-shell NW array cell design, b) SEM image of completed device with dense and vertically aligned NW arrays, c) TEM image showing single-crystalline n-Si core and polycrystalline p-Si shell: inset is the electron diffraction pattern, d) HRTEM image from the edge of the core-shell nanowire showing nanocrystalline domains [15].

With the VLS method, both in-situ or ex-situ doping approaches can be used to form the junction [145,146]. The former has the advantage of being able to occur at lower temperatures while, ex-situ doping decouples the growth, doping time and temperature. One important advantage of the etching technique over VLS is that the doping level has already been set in the starting wafer, which allows for more precise control over the material parameters and simplifies the material characterization.

Most commercially available solar cells, including silicon (both crystalline and amorphous), gallium arsenide, and high-efficiency multi junction cells, use a homojunction to separate carriers [147]. Measuring the dopant concentration in nanowire systems is significantly more difficult than in bulk wafers or thin films and sophisticated methods are required.

Challenges Associated with Contact Formation

EBL and photolithography are usually used to form contacts on single NW solar cells. Multiple lithography and etch steps are required for the radial junction (core-shell) structures, so that electrons and holes can be extracted separately [146,148]. Nanowire array contacting schemes are typically similar to those of planar thin-film solar cells. The bottom or top contact must be transparent to allow light to come through, and the other contact is usually made of reflective metal. Uniform deposition techniques such as sputtering or electrodeposition techniques can be used to obtain conformal transparent conductor coatings and continuous metal finger grids on high-aspect-ratio structures. This can be challenging, as it often requires a much thicker layer that results in transparency loss in the layer [140]. If the junction is made by deposition, the shell diameters can expand to the point at which they planarize the structure and simplify the contacting scheme.

In any solar cell, there are many sources of loss that must be minimized. The steps required to convert light to electricity are photon absorption, exciton creation, exciton separation to free carriers and carrier collection by the electrodes. Using nanowires instead of wafers or thin films provides opportunities to minimize losses in each step at lower costs.

Charge Separation Mechanism

Conventional thin film and crystalline PV devices rely on the generation and separation of electron-hole pairs with an internal electric field. Among different factors, the absorption efficiency of the material and the minority carrier lifetime, often determine the energy conversion efficiency [149]. As exhibited in Fig. 2.20, radial p-n junction wire geometry is potentially able to improve the efficiency, by decoupling of the direction of light absorption from that of electron-hole pairs separation and collection [150]. This type of structure is particularly advantageous when the thickness of the device is comparable to the optical absorption depth and the radius of the wire is approximately equal to the minority carrier diffusion length, which therefore provides a pathway to improve the efficiency of solar cells with short bulk minority carrier lifetimes. Under such circumstances, the optical generation of carriers is significant in the entire device thickness and the three dimensional structure facilitates the efficient electron-hole pair's separation and collection.

Single-nanowire solar cell measurements verified an efficiency increase of a factor of approximately five, for radial versus axial *p-n* junctions, due primarily to an improved photocurrent (see Fig. 2.21) [12]. The increased photocurrent must come partly from enhanced absorption and partly from IQE, which measures charge separation and collection efficiency. Due to large surface-to-volume ratio of NWs and

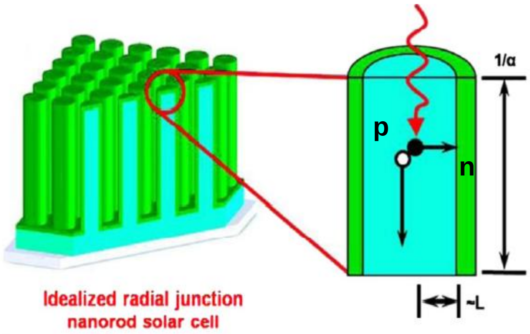

Figure 2.20 Schematic cross sections of radial p–n junction nanorod solar cell and a single nanorod: In this device, geometry light is absorbed in the axial direction while charge carriers are collected in the radial direction. Diffusion length (L) can be short in this design [150].

high surface recombination of Si [151], the axial junction Si NW PV devices showed relatively low efficiency [12]. Nevertheless, core-shell structure with radial p–n junction demonstrated improved carrier collection efficiency and improved conversion efficiency up to 3.4% at 1 sun illumination and 4.8% at 8 sun condition.

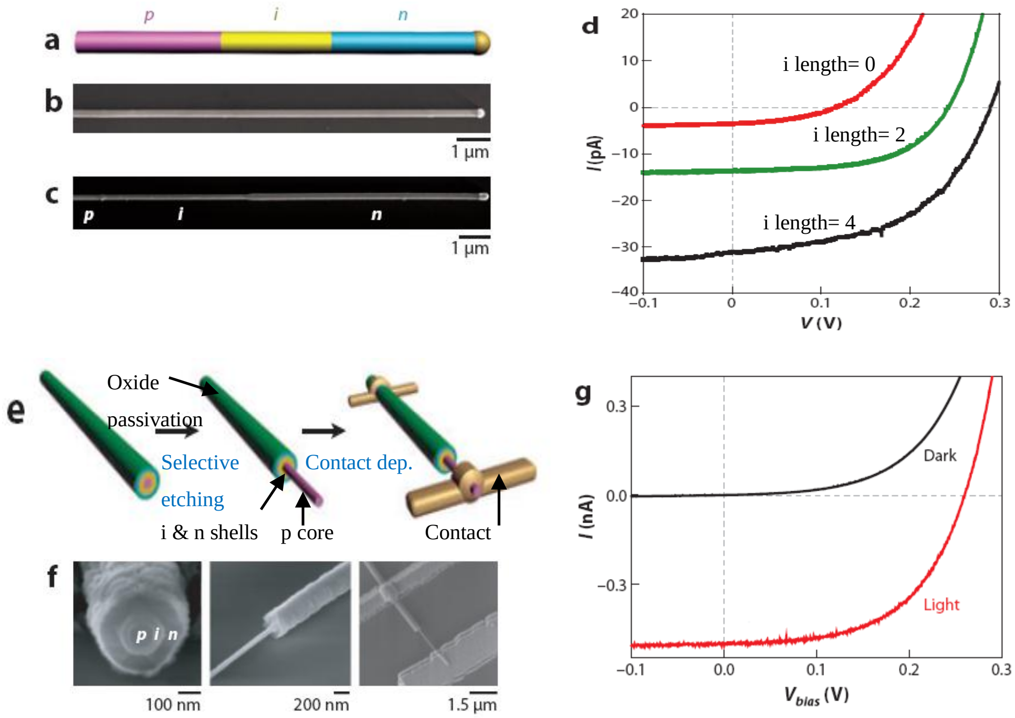

Figure 2.21 a) Schematic and b-c) SEM images of an axial p-i-n silicon nanowire, d) Light I-V characteristics enhanced by increasing the intrinsic layer (i) length: illumination intensity is 100 mW cm^{-2}, AM1.5G, e) Schematics of radial p-i-n junction device fabrication, f) SEM images corresponding to the schematics in panel [12] e, g) Dark and light I-V curves of a typical radial p-i-n junction device [144].

An increase in efficiency, from approximately 0.5% to nearly 6%, by increasing the interpenetration of cadmium sulfide nanowires into a constant thickness cadmium telluride thin film, has been shown by Fan et al. [136] (see Fig. 2.22 **)**. This verifies the enhanced charge separation-collection in radial geometries. Fig. 2.22.a indicates that the carrier extraction efficiency increases dramatically with nanopillar (NPL) length, as expected when the minority carrier diffusion length is considerably smaller than the film thickness. The improved absorption with longer NPLs due to the periodic light-trapping effects cannot account for the order-of-magnitude efficiency improvement. Additionally, the longer nanopillars will have increased interface_recombination, which will reduce the efficiency. Device physics simulations, which consider recombination but not light-trapping effects, qualitatively agree with the experimental results (see Fig. 2.22.b). SRH recombination in NPL cells for devices with no NPL embedded in cadmium telluride and an NPL embedded height (H) of 900 nm were compared through simulation (see Fig. 2.22.c,d). The space charge and carrier collection region is significantly enlarged when *H* = 900nm; thus, the total carrier recombination loss is greatly reduced.

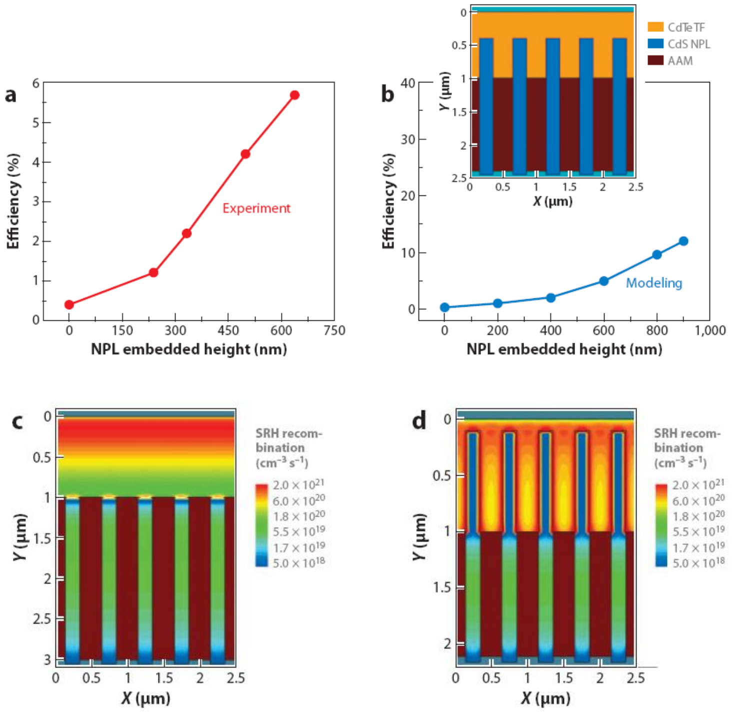

Figure 2.22 Effects of the NPL geometric configuration on device performance, (a) Experimental and (b) Theoretical simulation of the NPL cell efficiency as a function of H: (Inset) Schematic diagram of the NPL cell used for the simulation. Visualization of SRH recombination in NPL cells with (c) H = 0 nm and (d) H = 900 nm [136].

Optical Confinement

Tapered nanowire arrays (nanocones) with tips much smaller than the wavelength of light act as a graded index medium given by the weighted average of the material and air; which leads to greatly enhanced absorption compared with planar samples over a broad wavelength and angle range[152]. Garnett and Yang [140] did the light-trapping measurements on ordered Si arrays with different lengths and found a strong enhancement in absorption when nanowire length increased (see Fig. 2.23). The strong dependency on nanowire length may come from inefficient coupling to photonic crystal and waveguiding modes for short nanowires. Optical simulations performed by Zhu et al. [153] showed that periodic nanocones with aspect ratios approaching 1 can effectively couple light into waveguiding modes within ana-Si solar cell. They found strong absorption enhancement, through the measurements, that was in agreement with the simulations. The device's exceptional short-circuit photocurrent density (J_{sc}) of 17.5 mA cm^{-2} is above that of the world record a-Si solar cell, although the efficiency is much lower due to V_{oc} and *FF* losses [154]. Kelzenberg et al. [155] also found absorption enhancements above the randomized scattering limit in periodic arrays of SiNWs. A number of other papers also report that periodic arrays show enhanced absorption [156]. Studies have further reported greatly reduced reflection with tapered and untapered nanowires made of different semiconductor materials [157, 158].

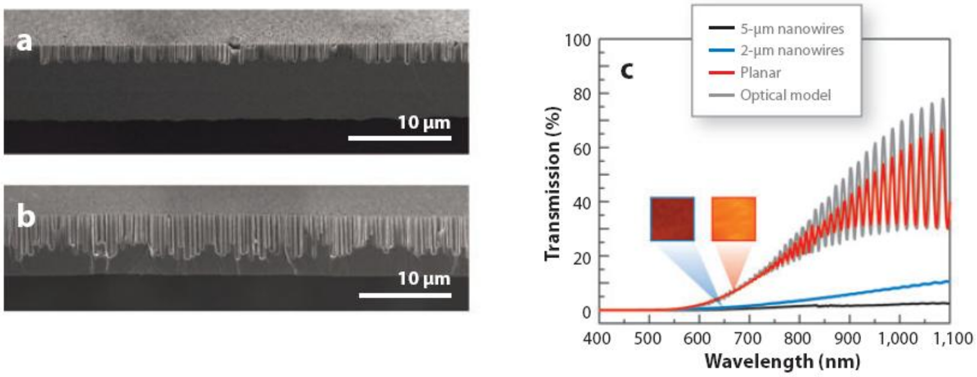

Figure 2.23 a) 2-μm and b) 5-μm SiNW arrays fabricated by etching, c) transmission spectra of thin silicon window structures before etching (red), after etching to form 2-μm (blue) and 5-μm (black) NWs and planar control sample (grey): Insets are backlit color images of the membranes before and after etching. There is a large intensity reduction and redshift in the transmitted light after the nanowires are formed, suggesting strong light trapping [140].

Single Nanowire PV Device

A series of innovatory works on single NW PV devices has been done, in which core-shell and axial p–n/p–i–n junctions were realized on SiNWs for PV devices [12]. Kelzenberg et al. [159] utilized copper

(Cu) to catalyze Si micro wire (MW) growth, and fabricated single-wire radial p–n junction solar cells with amorphous silicon and silicon nitride surface passivation coatings. Fig. 2.24 demonstrates a single NW PV device with a combination of radial and axial carrier collection.

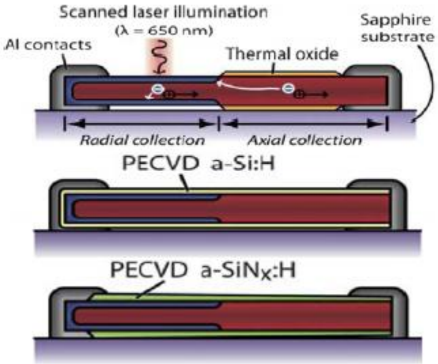

Figure 2.24 Single NW PV device with a combination of radial and axial carrier collection scheme: (a) Schematic of wires without surface passivation (top) and with surfaces passivated by a-Si:H (middle) and a-SiN$_x$:H (bottom), [159].

Nanowire, Microwire and Nanopillar Array Approaches

Single NW PV solar cells can potentially be used to drive the nanoelectronic components [144]. On the other hand, arrays of these nanomaterials are needed for large scale PV generation. To date, a number of works on nanowire, microwire and nanopillar (NW/MW/NPL) array-based PV devices using Si, indium phosphide (InP), cadmium sulfide (CdS), GaAs, zinc oxide (ZnO), etc., as active materials, have been reported [138,142,157]. These structures have been fabricated with several approaches, including VLS growth [135,137], dry/wet etching [160,161], etc. Efficiency of the Si wire array PV device fabricated by VLS was projected to be 17.4%, as shown in Fig. 2.25 [159]. This work pointed out a future direction for high efficiency Si wire solar cells.

Top down etching has been widely used to fabricate Si wire arrays for PV devices. An efficient SiMW radial junction solar cell fabricated by simple one-step photolithography, dry etching, and intermediate temperature deposition processes has recently been reported (see Fig. 2.26.a) [162]. It showed efficiency up to 7.2% and 11% underAM1.5G illumination by passivating the top surface and p–n junction with thin, conformal a-SiN:H and intrinsic poly-Si films, respectively. The SEM image of a typical hybrid SiMW-planar solar cell with vertically aligned SiMWs is shown in Fig. 2.26.b. This cell exhibited a maximum efficiency of 11% with V_{oc} of 0.580V, J_{sc} of 29.2 mAcm $^{-2}$, and FF of 0.649 (see Fig 2.26.c).

Cho et al. have reported InP NPL solar cells with highly abrupt and heavily doped emitter layers [160].

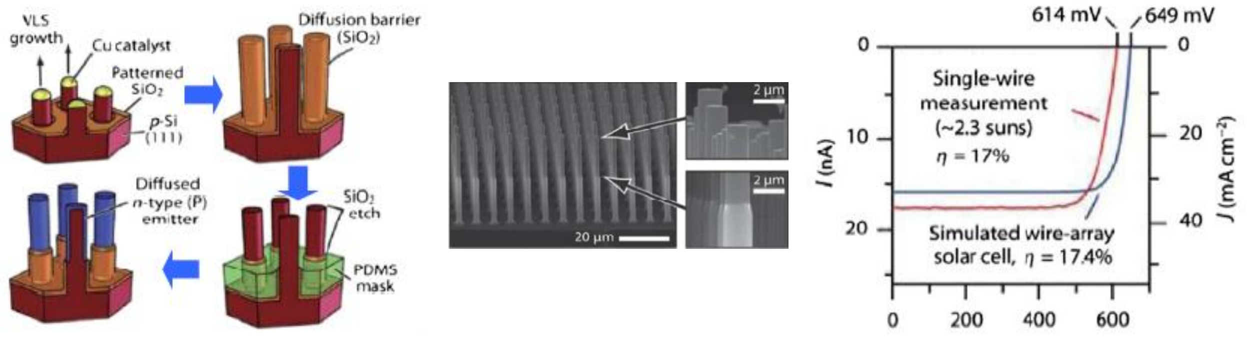

(a) (b) (c)

Figure 2.25 a) Fabrication process scheme of Si wire array solar cells, b) SEM images of an MW array grown by VLS, c) predicted efficiency and J–V characteristics of the wire-array solar cell [159].

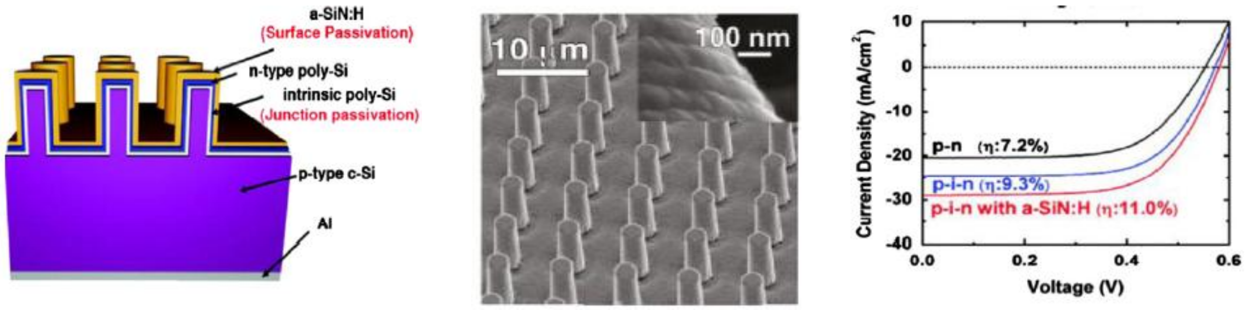

(a) (b) (c)

Figure 2.26 a) Schematic of the hybrid SiMW-planar solar cells, b) SEM images of the hybrid SiMW–planar solar cells fabricated by etching: Inset shows that the coating of the poly-Si layers and the a-SiN:H layer are uniform, c) Illuminated J–V curves of the hybrid SiMW-planar solar cells with three different structures [162].

The fabrication process involves silica microsphere lithography followed by a two-step reactive ion etching (RIE) and conformal surface n-doping (see Fig. 2.27.a).The indium tin oxide (ITO) was sputtered and annealed using rapid thermal annealing as the top contact. Fig. 2.27.b shows the SEM image of a fully fabricated cell. Efficiency of 8.1%, with a V_{oc} of 0.54 V, J_{sc} of 25mAcm^{-2} and FF of 60% were obtained for the InP NPL cells underAM1.5G illumination (see Fig. 2.27.c).

2.3 Remaining Challenges and Future Outlook

In this survey, it was highlighted that under ideal conditions and full solar concentration, where non-

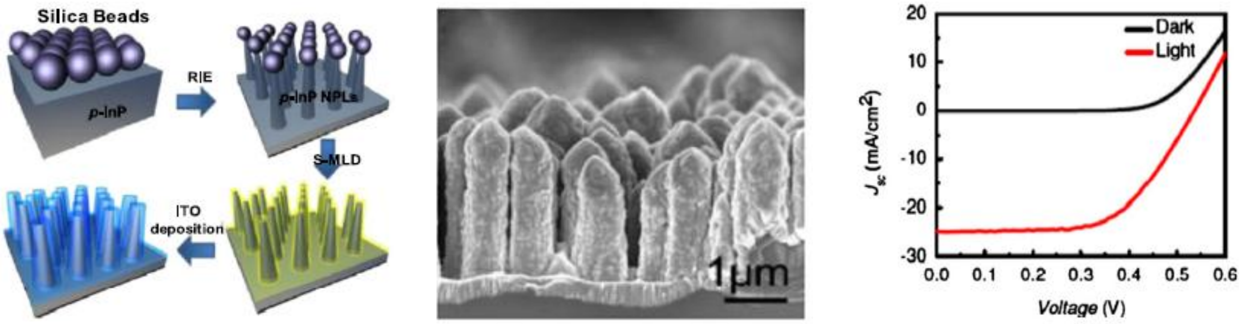

(a) (b) (c)

Figure 2.27 a) Fabrication process of InP NPL array solar cells using microsphere lithography and etching, b) SEM images of NPLs coated with ITO (100nm thick), c) Photovoltaic J–V characteristics of InP NPL solar cells [160].

silicon materials are included, the 3rd generation PV results in above 60% efficiency (see Fig. 2.28.a). However there are some serious technical challenges which limit the estimated theoretical efficiency in practice.

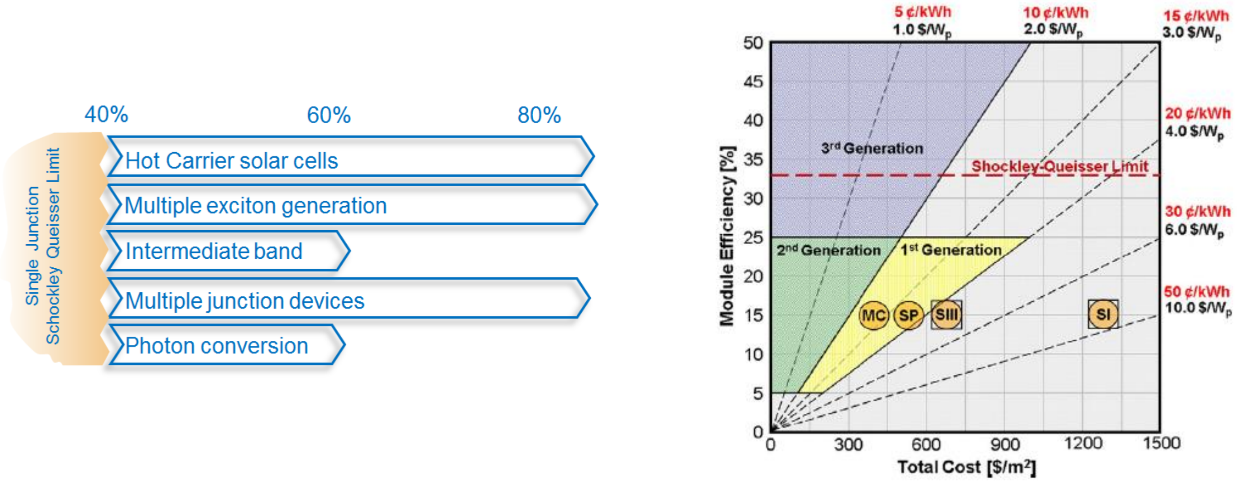

Figure 2.28 a) Pathways to future ultra-high efficiency devices, b) The cost of electrical power from photovoltaic systems is shown as a function of the total upfront cost and the module power conversion efficiency. MC, SP, SIII, and SI are the manufacturing cost, average selling price, installed cost for a utility scale system, and installed cost for a residential system, respectively [163].

Cost and suitability for terrestrial applications:

Multi-junction solar cell technology is not expected to seize a large market, as it is complex and thus expensive, and not well suited to terrestrial applications where the variable spectral content of sunlight causes current mismatch problems.

Lack of clear understanding of underlying physics and practicality:

NC QD based solar cells have not yet been shown to benefit from HC effects, such as MEG or hot carrier extraction. To date, no reports claim an absence of MEG in lead salt NCs; however variations in the reported efficiencies are cause for concern, which mainly depend on the NC size and the surface chemical treatment. It has not yet been determined what the relative contributions of reduced quantum confinement vs. surface chemistry on MEG efficiency are.

A better understanding of how NC surfaces affect the electrical properties, carrier dynamics, inter-NC electronic coupling and MEG efficiency, is clearly needed in order to design systems that harness MEG with very high efficiency. Also, slowed carrier cooling mechanism has a long history in literature and is controversial. Furthermore, the absorption, charge separation/conversion, and transport mechanisms in nanostructured solar cells are not well understood. Defect passivation is anther critical issue that must be addressed, since the very high surface area of nanostructure solar cells will lead to a large surface recombination velocity. Nevertheless, there needs to be more research on these topics, to obtain a more complete picture of the conversion and transport physics that can be subsequently applied to practical improvements in nanostructure-based solar cell performance.

Limitations by quantum dot materials and manufacturability:

The key technical challenges for the IB concept include the relatively low absorption cross section of the QDs, potentially significant non-radiative recombination in such materials, charge transport, and manufacturability issues, have limited the performance and hindered demonstration of the full potential of intermediate bands in a practical manner and must be addressed by further research.

Limited material options:

In up/down-conversion and down-shifting systems, due to limitation of the materials available, only slight gain via these concepts is predicated. In general, improving the performance of a converter and hence a converter composite cell system, will require careful engineering of the band structure, associated transition rates, and defects**.** The breakthrough in this field will be finding suitable material with high LQE, as well as suitable designs which minimize the absorption and reflection in the layer. The metal NPs with plasmon effect can also be used to improve the efficiency of UC, UC and US materials by enhanced absorption. The challenge here remains in finding material with plasmon resonance in the UV-NIR range.

In addition, these new cells, based on such nanoscale materials, will be competing against improving conventional and 2nd Generation technology. They will have to be robust and yield long lifetimes without significant degradation due to environmental factors such as oxygen and moisture. Further, the entire device fabrication must be scalable in a similar fashion.

Nanowire devices, especially when they incorporate a radial junction, can realize efficiencies comparable to those of planar devices at a much lower cost by use of a small amount of abundant, nontoxic, low-cost material. Despite the tremendous promise offered by nanowire solar cells, some challenges include: surface and interface recombination, surface roughness, mechanical and chemical stability, fine morphology, doping control, nanowire array uniformity, and synthetic scalability must be addressed before the benefits can be realized commercially.

Although great progress has been made in most of these areas, advanced solar cell concepts are still in their infancy and more work is needed. Meeting these challenges will require significant funding, much human creativity, and dedicated research. However, the pay-off for these efforts could revolutionize the PV market by producing low-cost high-efficiency solar cells utilizing Third Gen PV that yield electricity at less than \$1/W_p (see Fig. 2.28.b). In addition, the rapid improvements in efficiency and the potential for cost reductions far below planar limits certainly warrant further research into nanowire solar cells.

Chapter 3

Development of a Maskless Etching Process for Fabrication of Sub-wavelength SiN_x Structures and SiNW Array

Antireflection coatings (ARCs) are keys to enhance the photon collection in photovoltaic solar cells. One well-known, and industrially applied, but somewhat narrowband ARC, in silicon-based solar cells, is the silicon nitride (SiN_x) thin film. However, if sub-wavelength structures of SiN_x can be formed and deployed on Si, it leads to much improved broadband antireflection properties [164,165]. In the first part of this Chapter, a simple and maskless process is demonstrated; which employed a reactive ion etching (RIE) technique in carbon tetrafluoride (CF_4) chemistry, for the top-down fabrication of SiN_x nanostructures on SiN_x thin films pre-formed by plasma-enhanced chemical vapor deposition (PECVD). Silicon nitride nanostructures with diameters of 20-50nm and a height of 30-400nm are obtained. The formation mechanism of SiN_x nanostructures, the process controllability, and the dependence of their shape and size on plasma process conditions is investigated. It is also shown that the fabricated nanopillar array can be used as a template to form nanostructures on the underlying Si substrate surface; using a less aggressive plasma etch chemistry, sulfur hexafluoride (SF_6), with less polymeric residue on the sidewalls of the fabricated nanostructures [166]. Scanning electron microscope (SEM) and energy-dispersive x-ray spectroscopy (EDX) are used for structural and surface analysis. Spectroscopic reflectance measurements performed on single/double layers reveal a low reflectivity over a broad range of photon spectrum. The spectral reflectivity of the fabricated structures is also analytically calculated by assigning an effective refractive index to the sub-wavelength layer, as well as adopting experimentally obtained wavelength-dependent refractive indices for Si and SiN_x. Excellent fits are obtained between the analytical calculations and experimental data.

In the second part of this Chapter, technology development and characterization of SiNWs for advanced PV are presented. SiNWs have tunable optical properties for deployment on photovoltaic devices, in such a way, that the optical window of the overall device is widened. In addition to functioning as passive components to enhance the optical performance of cells, they can be used as active carrier generators by exploiting in SiNWs array cells. Formation of SiNWs by a maskless, highly anisotropic RIE process is first described; then the effect of plasma process parameters on both the shape and size of the wires is discussed. Next, results are presented on the dimensional control, surface passivation, detachment and further manipulation of the nanostructures. Different schemes for passivation of the surface bonds, to be accomplished without damaging the order, uniformity, and shape of the wires, are presented. SEM, transmission electron microscope (TEM), high resolution transmission electron microscope (HRTEM), EDX and x-ray photoelectron spectroscopy (XPS) are used for the structural and surface analysis. The result of photoconductive decay (μ-PCD) lifetime measurement shows that rapid thermal oxidation of Si nanowires leads to degradation of the lifetime; while with PECVD silicon nitride passivation, the lifetime is improved. The spectroscopic reflectance measurement shows optical reflection of the SiNWs is considerably reduced, as compared to the polished silicon. Photoluminescent (PL) properties, which are studied in the passivated/non-passivated nanostructures for use in PV; and the photon conversion ability, of some of the fabricated structures, are verified.

3.1 Concept for the Experimental Approach

Dry etching is composed of plasma and plasma-generated methods employing energetic gas molecules, ions, and/or free radicals to remove surface materials from the wafer. The basic goal of any etch process is to reproduce the image of a mask with a high degree of integrity. For the small geometries, which are now common in semiconductor processing, this can only be achieved by providing precision sidewall slope control.

For a good etch process, the etch must be uniform across the wafer, from wafer-to-wafer, from run-to run; and it needs to be highly selective against etching the masking material and the materials underlying the film being etched. The process should also leave no residual particulate, or chemical film contamination, on the wafer. Furthermore, it should not produce any electrical damage in the film material or the finished device; and it should provide precision control of the edge profile for the remaining material. Finally, the process should have high throughput with low material costs.

Isotropy, anisotropy and etch selectivity are the important etching characteristics. Where the sputter etching suffers from lack of selectivity, chemical gasification is usually isotropic. Inhibitor-enhanced chemistry is a method used to create enough selectivity between the mask and the substrate material. It is an ion-enhanced process, which is a combination of chemical processes that enhances the chemical reactions at the surface of the processed sample by ion bombardment. In this method, applying plasma generates etchant species. The etchant species and radicals are formed through collisions between energetic free electrons and gas molecules. For, example, Fluorine atoms merely react with silicon substrate and form SiF_4, a gas which is volatile. It also involves an inhibitor that passivates the surface and is not exposed to ion bombardment by formation of a protective layer or polymer film. The ion bombarding flux prevents the inhibitor layer from forming or clears as it forms, exposing the surface to the chemical etchant. Where the ion flux does not fall, the inhibitor protects the surface from the etchant. Inhibitor precursor molecules include CF_2, CF_3, CCl_2, and CCl_3 molecules, which can deposit on the substrate to form fluoro- or chloro- carbon polymer films. The substrates and etchants in this mechanism would react spontaneously and etch isotropically, if it were not for the inhibitor species. The inhibitors form very thin film on vertical surfaces that see little or no ion bombardment. The film acts as a barrier to etchant and prevents attack on the sidewalls, thereby making the process anisotropic. However, the disadvantage of this method is damage inflicted on the surface by impinging ions. Damage includes: introduction of defects or dislocations into the lattice, formation of dangling bonds on the surface and partial dislocation of a surface compound.

RIE is a plasma etch process; based on a combination of the chemical activity of reactive species generated in the plasma, with physical effects caused by ion bombardment. When substrates to be etched are positioned on the powered electrode of a parallel plate reactor, a reactive ion etching is configured. The powered electrode size is significantly smaller than the ground electrode, which is typically the chamber itself. A negative dc bias is generated on the sample electrode, usually by applying RF power to the electrode. The RF operating frequency of the RIE system relates to the energy required to move the ion through the dark space regions of the glow discharge. If the frequency is in the range of 13.56 MHz, the ions need several RF cycles to migrate through the dark space region between the wafer surface and the plasma. If the frequency is reduced to 100 – 450 kHz, the ions can cross the dark space in a small percentage of the RF cycle time. This will allow the ions to strike the wafer surface with higher energies. Therefore, the equipment design must obtain an energy balance between etching and possible damage or charging of the wafer surface. During RIE, the electrode and the samples placed on it are thus exposed to

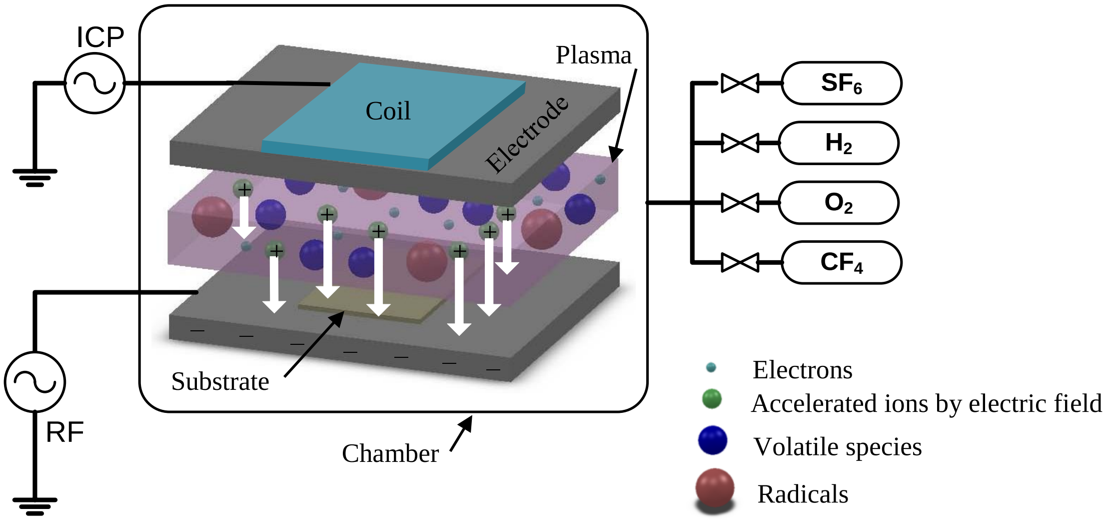

Figure 3.1 Generation of etchant species in plasma.

the bombardment of energetic positive ions (see Fig. 3.1). The RIE mode facilitates directional movement of ionized species at high rates toward the wafer. The RIE etch system configuration facilitates improved control of anisotropic etch parameters. RIE uses lower pressures, higher ion and electron energy levels, and higher electrode voltages than standard planar plasma etching.

The primary processes occurring in an RIE process can be summarized as: (i) active species generation, (ii) formation of dc bias for ion acceleration, (iii) transport of plasma generated reaction intermediates, from the bulk of the plasma to the surface of the material being etched, (iv) adsorption, (v) reaction, (vi) desorption of volatile reaction product and (vii) pump-out of volatile reaction product. These steps are demonstrated in Fig. 3.2.

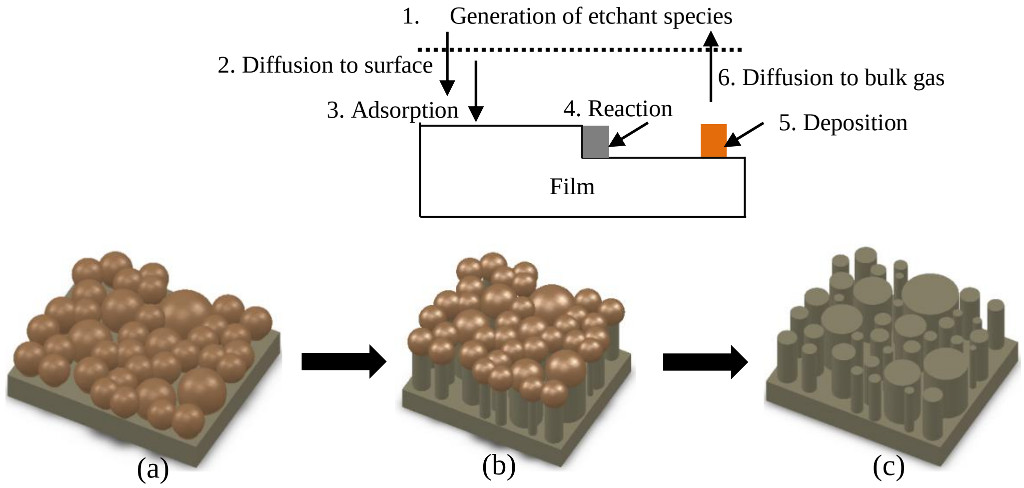

Diffusion of radicals to the surface -adsorption

Diffusion of ions to the surface adsorption-chemical/physical reaction-desorption

Residual cleaning

Figure 3.2 Primary processes occurring in an RIE process

An etching process is sufficiently explained by the etchant-unsaturated species model. For example, the corresponding reactions in a CF_4 plasma are:

$$2e + CF_4 \rightarrow CF_3 + 3F + 2e \qquad (3.1)$$

$$F + CF_2 \rightarrow CF_3 \qquad (3.2)$$

$$nCF_2 + \text{surface} \rightarrow (CF_2)_n \qquad (3.3)$$

$$4F + Si \rightarrow SiF_4 \qquad (3.4)$$

If the main reaction path is (3.2), the result will be recombination. If the main reaction path is (3.3), the result will be polymerization (see Fig. 3.2.a). If the main reaction path is (3.4), then the result will be etching (see Fig. 3.2.b). Fig 3.2.c shows the resultant features after cleaning. Because of the non-uniform formation of the carbon chains on the surface, during the plasma etching process, a distribution of size over the etched features is expected. Gas-phase additives can dissociate and react with unsaturated species, changing the relative concentration of a species and the reaction paths.

3.2 Formation of Sub-wavelength SiN_x Structures using a Plasma Etching Process

Uniformly distributed vertical SiN_x sub-wavelength structures were obtained using a plasma etch process of Si wafers, in a Trion Phantom II with an 8 inch bottom electrode, coupled to a 13.56 MHz RF generator. A polished <100> silicon wafer was cleaned with 2% HF to remove the native oxide. A layer of 400nm thick SiN_x was deposited on the cleaned wafer by the PECVD technique. The sample was then etched by RIE, with a bias power of 150w, for the formation of silicon nitride nanopillars using a gas mixture of CF_4:H_2, with a flow rate of 20:60 (sccm) respectively. The morphology of the fabricated nanopillars was analyzed by SEM. The reflectance of the SiN_x nanostructures was measured using a LAMBDA 1050 PerkinElmer UV/Vis spectrophotometer.

3.2.1 Effects of Plasma Conditions on the Shape of the Nanostructures

The effects of the plasma parameters on the shape of the nanostructures were examined. Two samples shown in Fig. 3.3 were etched using the same plasma power of 150w and an etching time of 30s, but processed under different self-bias voltages and pressures. The shape and size of the etched SiN_x were compared. After etching at a self-bias voltage of 400V and pressure of 250mTorr, the pillars did not completely form on the silicon nitride layer as shown in Fig. 3.3.a. However, by increasing the self-bias voltage and decreasing the pressure, upright, densely packed and uniform pillars were formed. The size of the pillars was small at this stage. Fig. 3.3.b shows the pillars formed on the SiN_x layer after etching at 750V and 20mTorr.

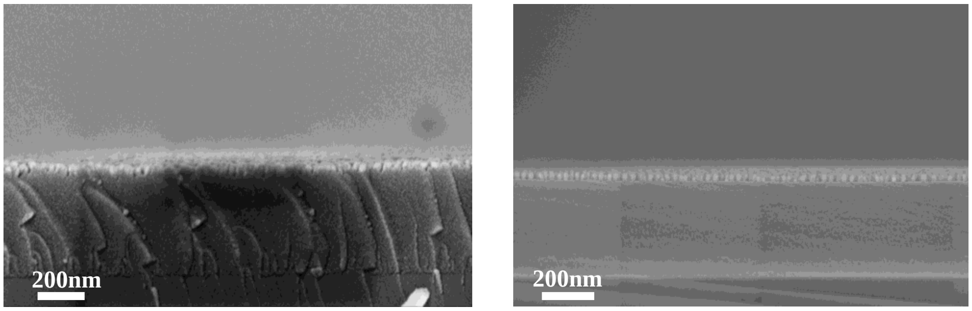

(a) (b)

Figure 3.3 Effects of plasma parameters on the shape of SiN_x nanopillars: etching at a) self-bias voltage of 400V 250mTorr, b) self-bias voltage of 750V and pressure of 20mTorr

The SEM image in Fig. 3.4.a shows that the length of the fabricated silicon nitride nanopillars formed on the SiN_x layer are 120nm, with a diameter of 20nm, after RIE etching at a plasma power of 150w (750V/20mTorr) using a gas mixture of CF_4:H_2, with flow rate of 20:60 (sccm) respectively for 90s. The structure's height increased as the etching cycle increased (see Fig. 3.4.b). Because the sizes of the carbon chains, formed on the surface during the plasma etching process, were not uniform, it was expected to see a distribution of size over the pillars. The size of the fabricated pillars was measured to be in the 20-50nm range depending on the time of the etching. Using the data in Fig. 3.4.b, the etch rate of the silicon nitride was calculated to be about 1.3nm/s.

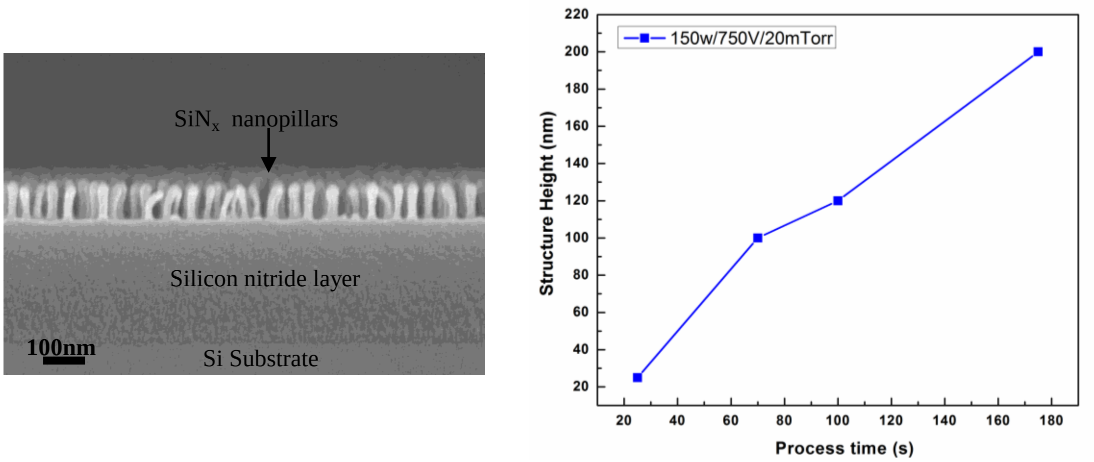

(a) (b)

Figure 3.4 a) SEM image of the silicon nitride layer etched for 90s under plasma process condition of 150w/750V/20mTorr/(60sccm:20sccm) H_2:CF_4 b) Effects of etching cycle on silicon nitride

3.2.2 Effect of Hydrogen Content on the SiN_x Etching

The result shows that hydrogen slowed down the nitride etching and made the formation of nanopillars possible. The chemical reaction of fluorine (F) atoms in fluorocarbon polymers, formed on the silicon nitride surface with a nitrogen (N) atom in the silicon nitride layer, was high enough to consume the fluorocarbon polymer masks and make them unstable during etching. As shown in Fig. 3.5.a, the silicon nitride layer etched before formation of any nanostructures of nitride, when no hydrogen was used. The incorporation of H_2 led to the generation of hydrogen radicals, which decreased the reaction between F and N atoms; hence the hydro-fluorocarbon polymer chains could form on the silicon nitride surface, and resist being removed during the etching cycle; thus leading to formation of silicon nitride nanopillars (see Fig 3.5.b). Comparing the EDX results, for these two samples, shows a higher atomic percentage of nitrogen for the samples etched with a mixture of CF_4:H_2.

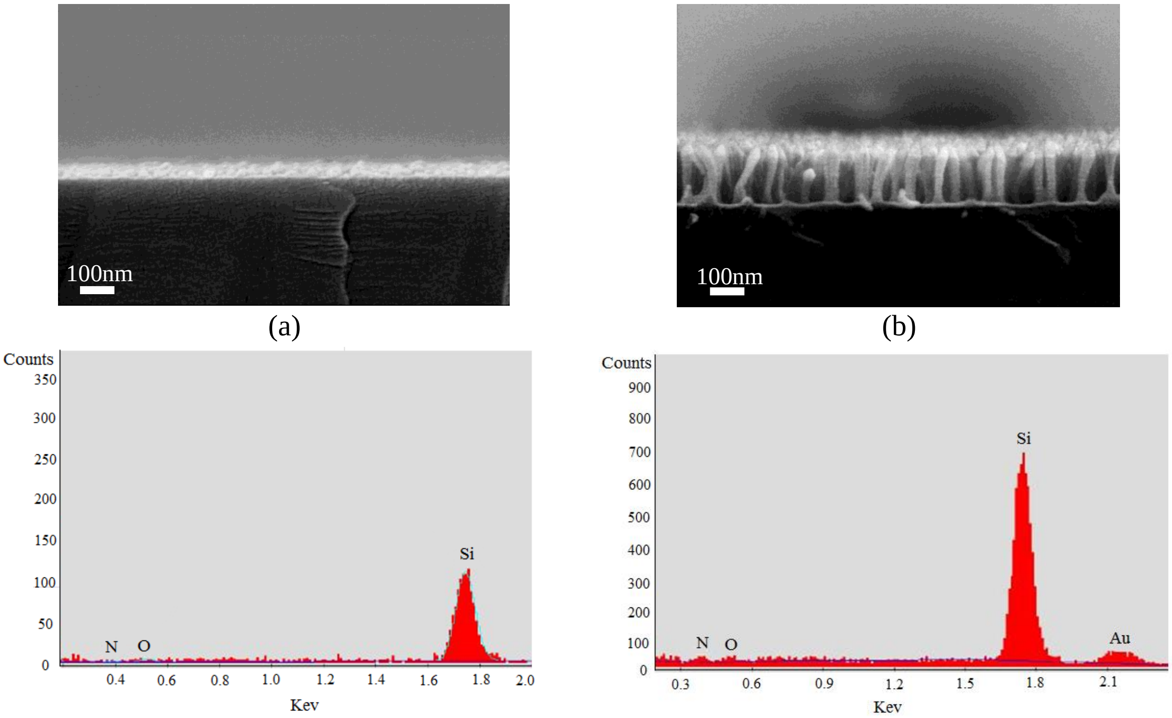

(a) (b)

(c) (d)

Figure 3.5 SEM images of the silicon nitride sample etched for 180s under plasma conditions of 150w/20mTorr/750v using (a) 20sccm CF_4 (b) (60sccm:20sccm) H_2:CF_4

3.2.3 Optical Characterization of Antireflective Sub-λ SiN_x Nanostructures

Spectroscopic reflectance measurements were performed on SiN_x nanostructures in a LAMDA 1050 PerkinElmer UV/Vis spectrophotometer. The result, demonstrated in Fig. 3.6, reveals a lower reflectivity of fabricated structures, over a broad range of photon spectrum, with respect to the Si wafer. The interference patterns in the reflectance spectra of samples, prepared in shorter etching cycles (30s-215s), are due to the fact that the SiN_x structure consists of both SiN_x thin film and SiN_x nanopillars; so-called double-layer (DL) structure. The number of maxima and minima decreases, with an increase of the etching time from 30s to 300s. As the etching time increases to 300s, the pillars cover the entire SiN_x layer, hence the interference patterns disappear.

3.2.4 Analytical Study of Spectral Reflectivity of Fabricated SiN_x Nanostructures

The spectral reflectivity of the fabricated structures (see Fig. 3.7.a) has been analytically calculated by assigning an effective refractive index to the sub-wavelength layer. An experimentally obtained wavelength-dependent refractive index of Si and SiN_x is adopted in the calculations instead of a constant refractive index. The outcome is compared with the experimental observations (see Fig. 3.7.b). The

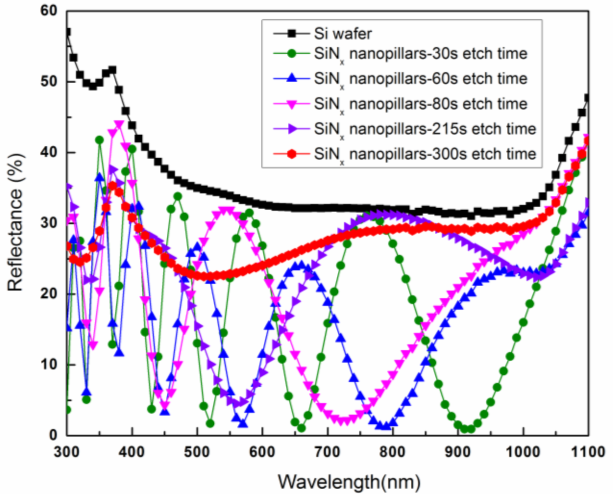

Figure 3.6 Total reflectance of SiN$_x$ nanopillars/ SiN$_x$ double layer structures.

wavelength-dependent refractive index of each layer is obtained by employment of an empirical formula [Eq. (3.1)]. The constants are obtained by fitting the curve with the experimental data. Having the reflectance, the wavelength-dependent refractive index [Eq. (3. 2)] is calculated.

$$R = A\lambda^5 + B\lambda^4 + C\lambda^3 + D\lambda^2 + E\lambda + F \qquad (3.\ 1)$$

$$n = \frac{1+\sqrt{R}}{1-\sqrt{R}} \qquad (3.\ 2)$$

The effective refractive index of the SiN$_x$ pillar layer is calculated utilizing the following equation:

$$n_{piillar} = \sqrt{\frac{(1-f+fn_{\mathrm{SiNx}}^2)(f+(1-f)n_{SiNx}^2)+n_{SiNx}^2}{2(f+(1-f)n_{SiNx}^2)}} \qquad (3.\ 3)$$

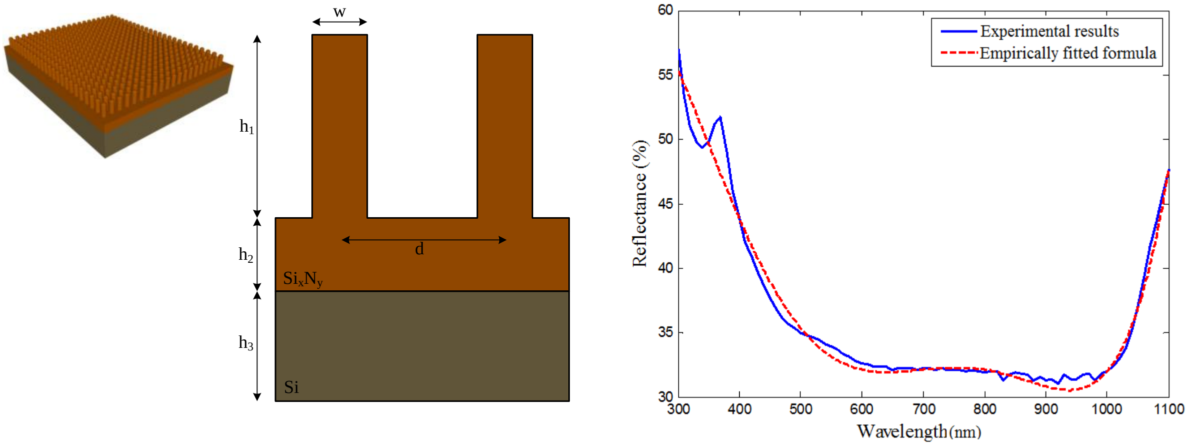

(a) (b)

Figure 3.7 a) Geometrical schematic used for the modelling, b) Spectral reflectivity of Si layer: experimental (solid) and empirically fitted formula (dotted line).

Where,

$$f = \frac{\pi w^2}{4d^2} \tag{3. 4}$$

Having the refractive indices of all three layers, the fundamental optics laws are employed to calculate the total reflectance (see Fig. 3.8.a). Excellent fits are obtained between the analytical calculations and experimental data (Fig. 3.8.b).

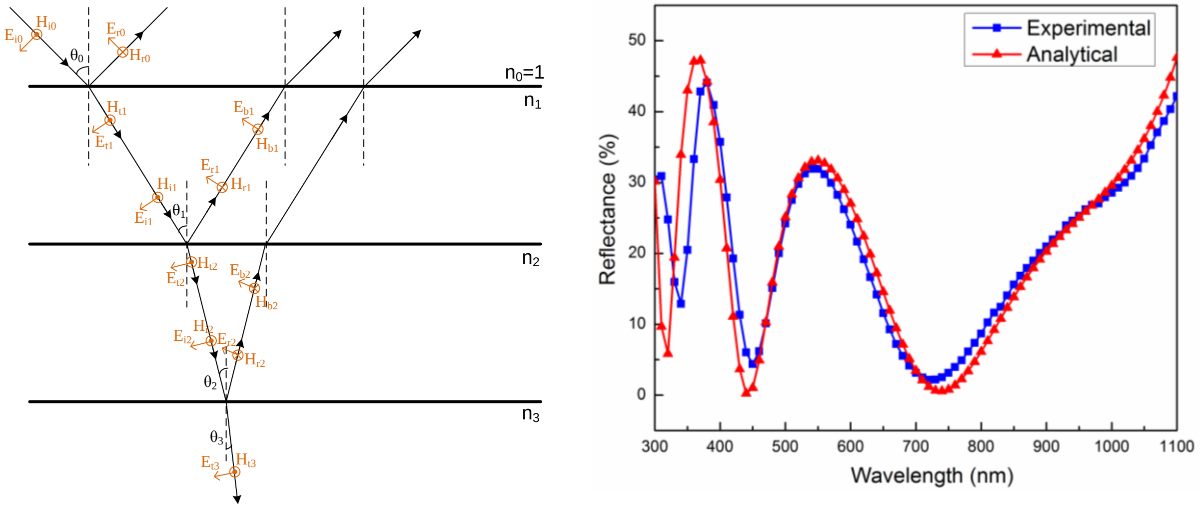

(a) (b)

Figure 3.8 a) Fundamental optics laws employed to calculate the total reflectance b) Spectral reflectivity: experimental and analytical

3.2.5 Application of SiN_x Nanostructures as a Template for the Formation of Nanostructures in Silicon

By further etching, at controlled gentle plasma conditions, the silicon nitride nanostructure patterns can be transferred to the underlying silicon substrate. The schematic diagram, in Fig. 3.9.a, exhibits the SiN_x film deposited on a window of a cell device. Fig. 3.9.b shows a double layer ARC structure after etching

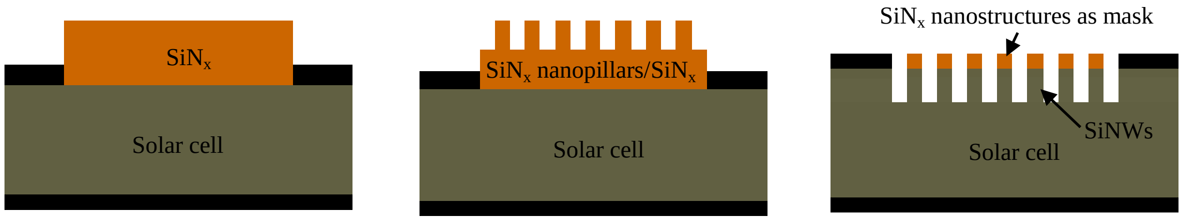

(a) (b) (c)

Figure 3.9 a) Solar cell with a) ARC layer, b) Double layer ARC structure, c) SiNWs formed by pattern transfer from SiN_x nanostructures to silicon

halfway through the silicon nitride layer. Fig. 3.9.c demonstrates the patterns of SiN_x nanostructures being transferred to the underlying silicon substrate.

Etching the silicon substrate, using the same conditions as outlined above for the nitride layer, was continued. The resultant structure is shown in Fig. 3.10.a. However, it is possible to use the silicon nitride nanostructures, as a mask for the formation of Si nanostructures, by switching to the inductively coupled plasma (ICP) power during silicon etching in order to decrease the etching rate of the SiN_x mask. Total reflectance from the SiNWs, after transferring the SiN_x nanopatterns to underlying silicon at different etching cycles, is exhibited in Fig. 3.10.b.

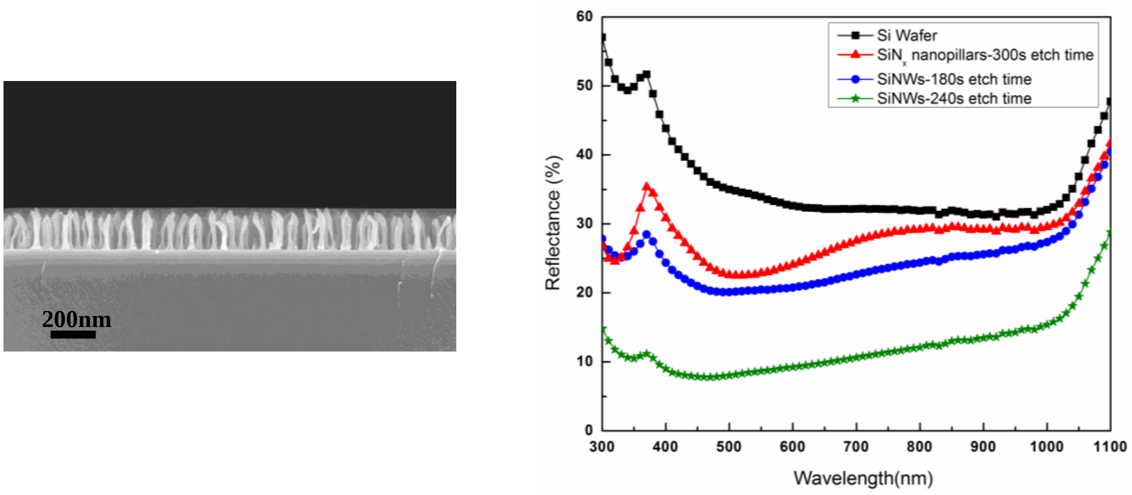

(a) (b)

Figure 3.10 a) Transferred SiN_x nanopatterns to the underlying silicon substrate after 240s etching, under process conditions of 150w/20mTorr/750V/(60sccm:20sccm) H_2:CF_4, b) Total reflectance from the SiNWs at different etching cycles

This method can be utilized when the SiNWs are being used as an active part of the device. Self-aligned selective emitter solar cell structures, with photoluminescent silicon nanowire, can be formed using this approach. As seen in the schematic, in Fig. 3.11.a, and the corresponding SEM image in Fig. 3.11.b, the wires form on the Si wafer after consumption of about 1μm of the Si wafer, which is not desirable, as these wires form at a risk of losing junction where the diffusion has not been deep enough. Formation of silicon nitride nanostructures prevents the undesirable consumption of Si substrate (see Fig. 3.9.c).

3.3 Formation of SiNWs using a Plasma Etching Process

A plasma etching process was also developed for fabrication of crystalline silicon nanowoires. The fabrication methodologies, structural and optical characteristics of the wires were discussed.

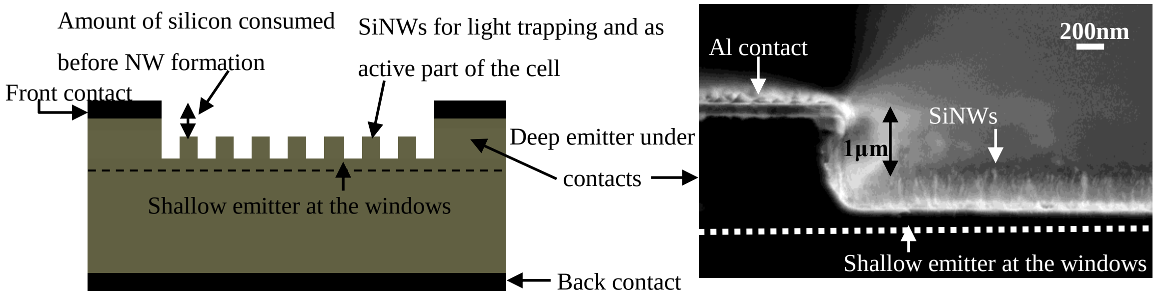

(a) (b)

Figure 3.11 Self-aligned selective emitter solar cell structure with photoluminescent SiNW

3.3.1 Fabrication of Crystalline Silicon Nanowires

Uniformly distributed vertical Si nanowires were obtained using a plasma etch process of Si wafers with CF_4 reactant, in a Trion Phantom II with an 8 inch bottom electrode, coupled to a 13.56 MHz RF generator. P-type wafers were cleaned in an RCA1 solution, dipped in 1-2% hydrofluoric acid and rinsed in deionized (DI) water, before being loaded into the RIE chamber. CF_4 was used as a reactant gas at a flow rate of 25sccm. Plasma pressure varied over a wide range from 10 to 100 mTorr; and the bias value changed from 400V up to 1200V. By controlling the process conditions, including plasma parameters such as gas chemistry, pressure, self-bias voltage and etching duration, vertical needle-like Si nanowires can be formed on the Si substrate. Using the appropriate C/F ratio, in orine chemistry C, adsorption dominated over etching by F, making fluorocarbon polymerization possible on the surface. High aspect ratio structures can be obtained, as the self-organized carbon polymer masks were stable enough during the etching cycle. As demonstrated in the schematics in Fig. 3.12, the NWs or conic nanostructures can be obtained after formation of the carbon polymer masks, etching and cleaning steps; depending on the plasma parameters used during the etching process. As will be discussed in more detail in Section (3.3.2), the high aspect ratio wires are obtainable at intermediate plasma conditions (see Fig. 3.12.a). Whereas, the cone-like structures were the result of etching under intense plasma, when high self-bias voltage or plasma pressure was applied; and the size of the carbon masks reduced during the prolonged etching (see Fig. 3.12.b). The layer of carbonate compounds on the sidewalls can also be removed by gentle plasma cleaning. The results of the cleaning process will be discussed in Section (3.3.2).

3.3.2 Effect of Plasma Process Parameters on Nanowire Geometry

The shape and size of these nanostructures mainly depends on a trade-off between the etching capacity and directionality of the RIE process. The plot, shown in Fig. 3.13.a, and the SEM image in Fig. 3.14.a, both reveal that at intermediate self-bias voltages (600V-1000V) the nanostructures have a wire shape;

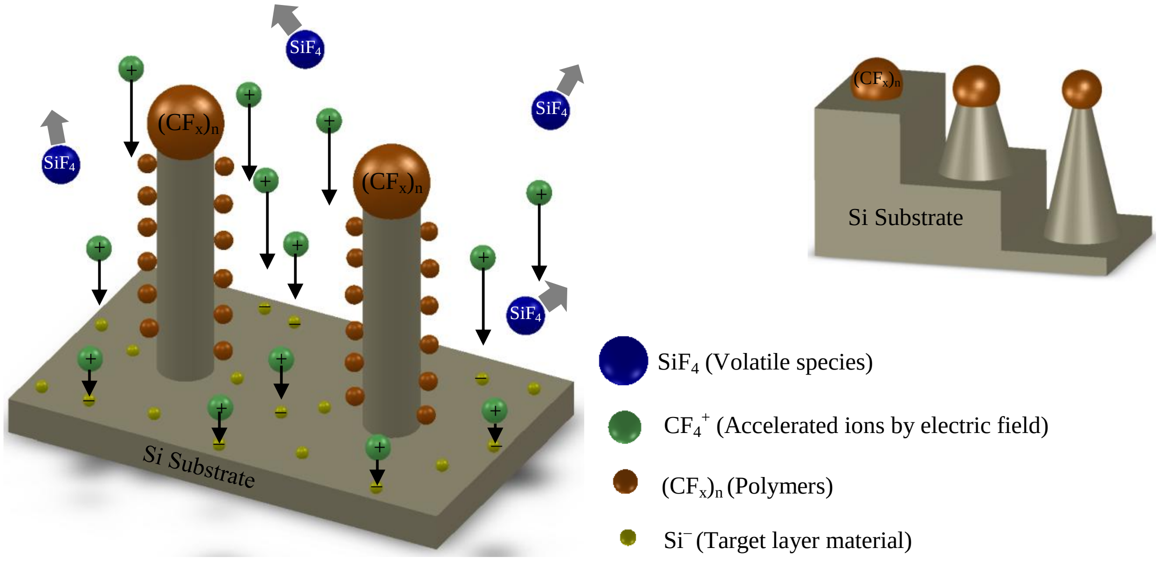

(a) (b)

Figure 3.12 Schematic diagrams showing formation of a) needle-like wires with carbonate compounds on the sidewalls and b) cone-like nanostructures by reducing the mask size during etching

and their height increases as the etching rate increases at higher pressures. The plot also shows that the structures turn pyramid-like at 100 mTorr, where chemical plasma etching capability is higher than the energetic ions directed to the sample, resulting in etching the randomly formed polymer masks and forming cone-like nanostructures. The sidewalls of the wires formed at high pressure conditions are not as smooth as the sidewalls of the samples etched at lower pressures. High self-bias voltages (>800V) result in longer wires, mainly at a pressure lower than 60mTorr, however this leads to highly porous, delicate structures (see Fig. 3.14.b). Sidewall damage increases at higher self-bias voltages (>1000V) leading to conic structures. The plot also indicates that the cone-like structures form at low self-bias voltages (<600V) (see Fig. 3.14.c).

High pressure conditions (>50mTorr) enlarge the etching rate at a risk of over-etching the carbon polymer mask and deforming Si nanowires. As soon as the tips of the cones start to form needles, as the base is etched down, the fluorine species laterally consumes the top part of the wires, back to the sharp cone peaks. At lower pressures, the structures turn into wires and the height of the wires increases, by increasing the self-bias voltage to about 800V (see Fig. 3.13.b, 3.14.d).

By using intermediate plasma conditions, high-aspect-ratio wires are obtainable at longer etching cycles. Upright silicon nanowires were obtained at an 800V plasma self-bias voltage and pressure of 10 mTorr. At a voltage of 600V, longer etching time is required, to obtain needle-like structures (see Fig. 1.13.c).

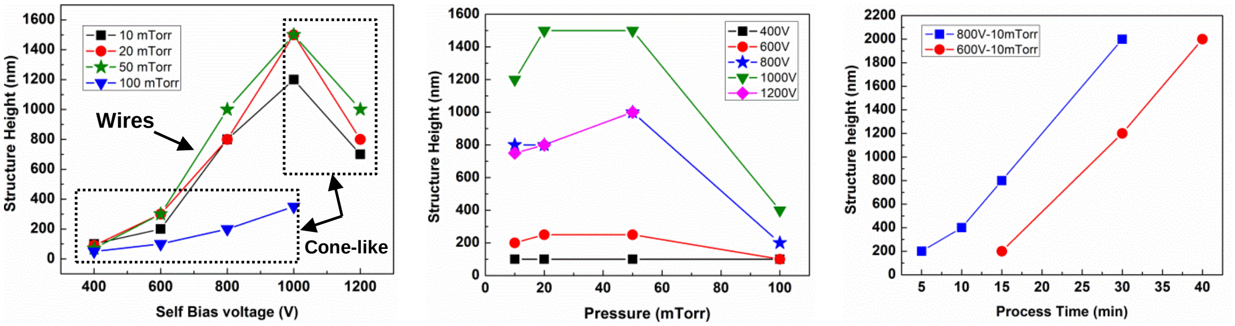

(a) (b) (c)

Figure 3.13 Effect of plasma process parameters: (a) self-bias voltage, (b) plasma pressure and (c) etching cycle on nanowire geometry

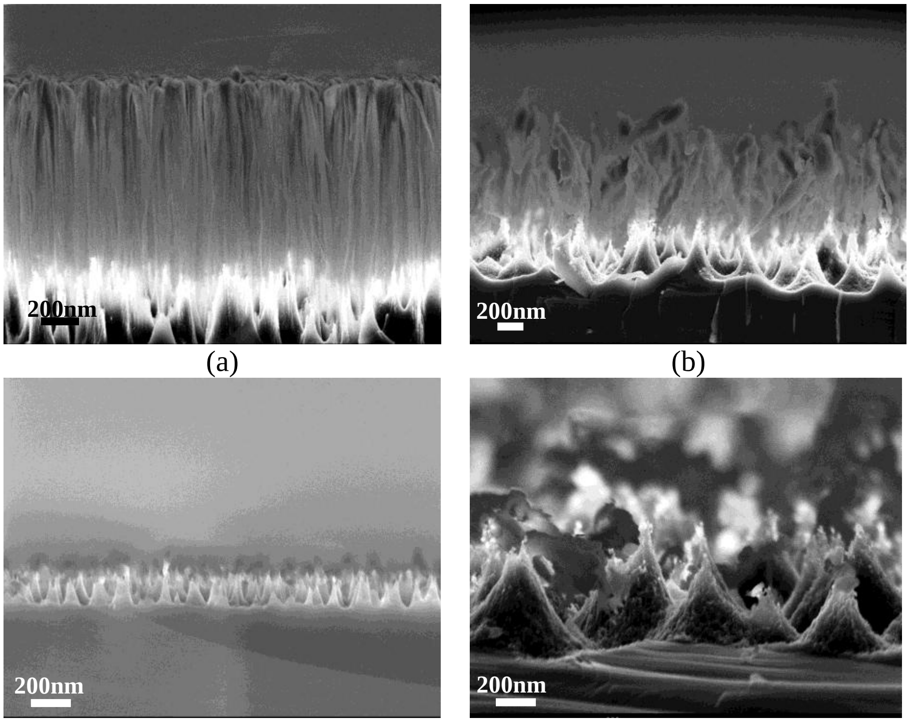

(a) (b)

(c) (d)

Figure 3.14 SEM images of silicon nanostructures formed after 900s etching at (a) 800V-10mTorr, (b) 1000V-10 mTorr, (c) 400 V-10 mTorr (d) 1000V, 100mTorr

TEM images in Fig. 3.15.a, show a cluster of Si nanowires, seated on the carbon copper grid, by drop casting of a solution containing SiNWs. TEM images in Fig. 3.15.b and Fig. 3.15.c, exhibit a magnified view of a part of Fig. 3.15.a, consisting of a cluster of nanowires and a single wire respectively. Fig. 3.15.d and 3.15.e are the HRTEM image of a single NW and a group of them respectively. Fig. 3.15.d demonstrates that NWs, with diameters less than 50nm, are obtainable using the illustrated etching method. Further, the crystalline orientation of fabricated NWs is clearly observable in both of the high resolution images. Intensity variation, in the HRTEM images of Si nanowires, is a result of the cross-cutting of different crystalline planes and thickness variation across the nanowire due to the circular nature of the wire (see Fig. 3.15.f). The sharp dots, in the dark diffraction pattern of this image, are an indication of the crystal nature of the NWs (see inset in Fig. 3.15.f).

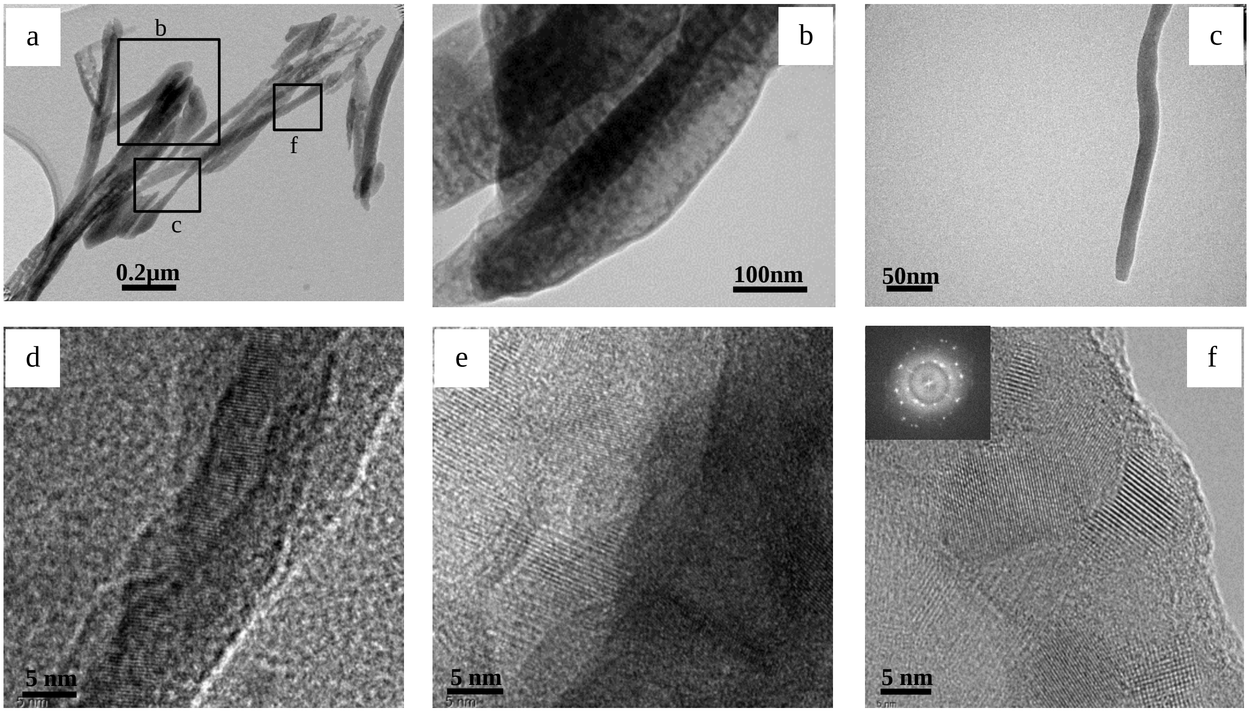

Figure 3.15 TEM image of a) cluster of SiNWs seated on the carbon copper grid by drop casting, b) magnified image of a group of SiNWs and a c) single wire. HRTEM image of a single SiNW, with diameter which is less than 50nm and its crystalline orientation, e) crystalline orientation of agglomerated wires, f) intensity variation as a result of the cross-cutting of different crystalline planes and thickness variation across the nanowires. Inset is the dark diffraction pattern.

3.3.3 Formation of SiNWs over the <111> Crystalline Planes

In another approach, the Si nanowires formed on the <111> crystal orientations, pre-formed by the wet etching of a Si wafer in a potassium hydroxide (KOH) solution. Fig. 3.16.a, shows a top view of pyramid structures formed on the Si substrate. In a wet etch process, a solution consisting of 1 wt% KOH and 7 vol% IPA, at 70°C, was used to form the pyramids with 100% coverage of a 3 inch silicon wafer. The plasma etching condition, as described in Section (3.3.2), was introduced on this textured surface, to form wires on the <111> planes. Fig. 3.16.b indicates the nanowires have been formed on these planes. Fig. 3.16.c and Fig. 3.16.d, are the low and high magnification cross section views of the resultant nanostructured surface. This double-textured structure can improve the light-trapping in the solar cell by reducing the reflectance.

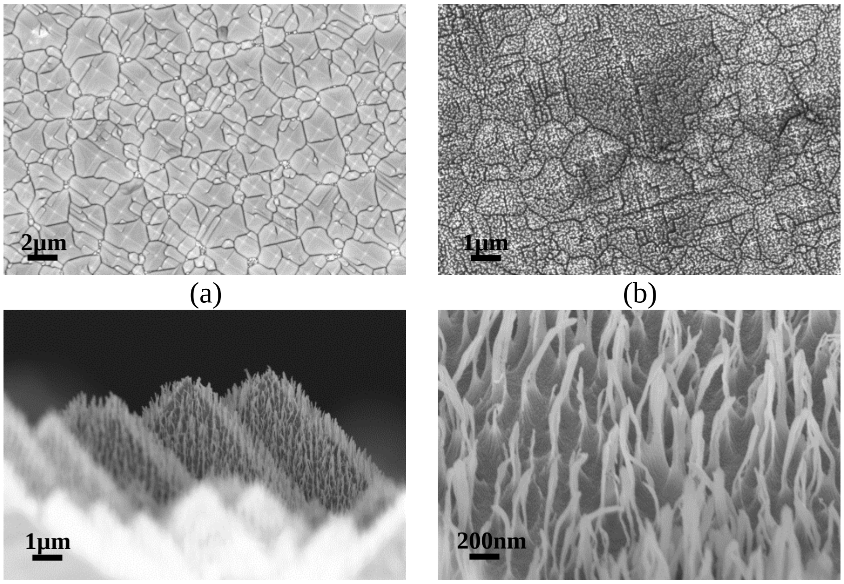

(a) (b)

(c) (d)

Figure 3.16 a) Pyramid structures formed on the Si substrate by wet etching. Formation of the wires on the <111> planes, b) top view and c, d) low/high magnification cross section view

3.3.4 Surface Analysis of the SiNWs

A thin, amorphous layer formed on the sidewalls of silicon nanostructures during the dry etch process, due to a combination of native oxide, polymer deposition and RIE damage. Carbon, fluorine and oxygen

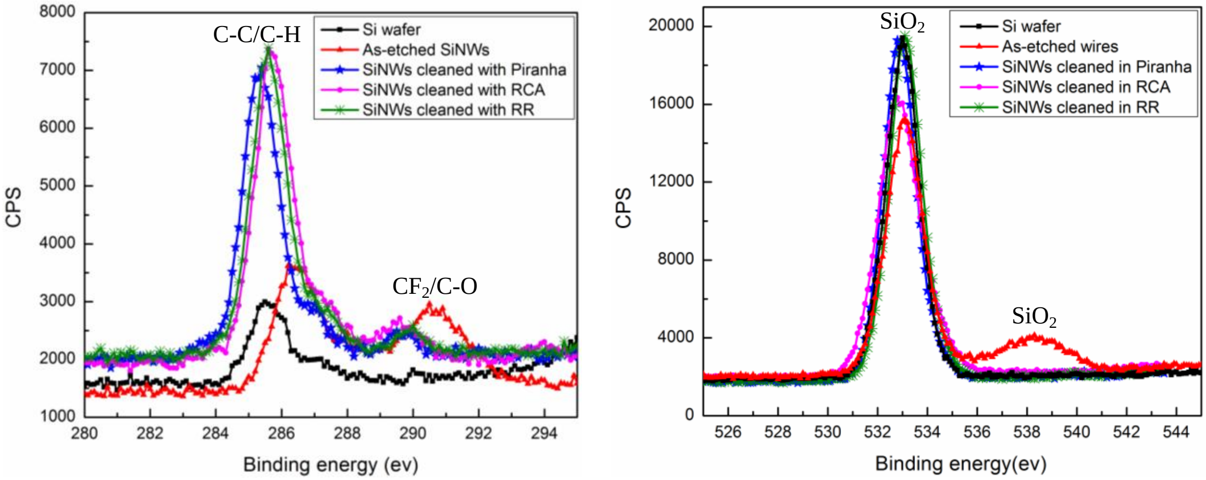

(a) (b)

Figure 3.17 XPS analyses on arrays of Si nanowires: percentage atomic concentration of the a) carbonate compounds and b) oxide component, after wet cleaning

were detected on the sidewalls of the Si nanowires in XPS analyses. In order to clean the sidewalls caused by the RIE damage, solutions of Piranha, RCA and removal residue (RR) were used. XPS analyses demonstrate that the carbonate compounds (see Fig. 3.17.a) and oxide layer (see Fig. 3.17.b) deposited on the sidewalls of the wires during the etching were removed after the wet etching process.

Isotropic etching, under ICP conditions, was also used to remove carbonate compounds/oxide layers from the sidewalls of the Si nanowires. SF_6:O_2 gases were introduced into the chamber at flow rates of 80:30 (sccm) respectively. The etching was performed for 5 min. using plasma power of 400w; and ICP: DC bias voltages of 500:100 (V) respectively at 50mTorr. XPS analyses in Fig. 3.18.a, showed a reduction in content of CF_2 and carbonate compounds (peak shown at binding energy of 290ev) after isotropic etching in SF_6:O_2 plasma. The peaks which appeared at a binding energy of 537ev, correspond to oxide components on the sidewalls was disappeared at this cleaning process condition (see Fig. 3.18.b). In another process, a mixture of $H_{2:}O_2$ gases were introduced into the chamber, at flow rates of 27:6 (sccm) respectively, using the same plasma process conditions. The oxide layer was removed using this chemistry; however, no change was observed for the carbonate compounds before and after etching under this plasma. O_2 plasma with the flow rate of 50sccm, was utilized, using the plasma condition as described earlier. The O_2 plasma was not as reactive to the oxide layer as it was to carbon and polymers. However, the plasma condition used here did not successfully remove carbon contaminations. Worthy to be noted: the peaks appearing at the binding energy of 285ev and 533ev, correspond to the carbonate compounds and native oxide layers, that formed on the surface by leaving samples in air.

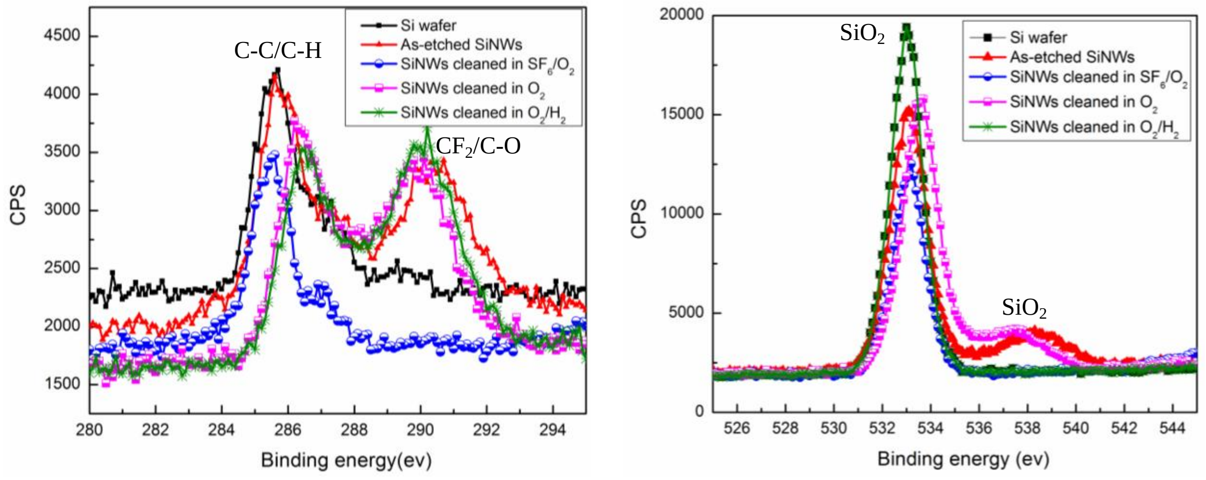

(a) (b)

Figure 3.18 XPS analyses on arrays of Si nanowires: percentage atomic concentration of the a) carbonate compounds, and b) oxide component, after dry cleaning

The TEM images in Fig. 3.19 visualize how the NWs look, before and after cleaning, at SF_6:O_2 plasma. The wires are cleaner after the dry etch process.

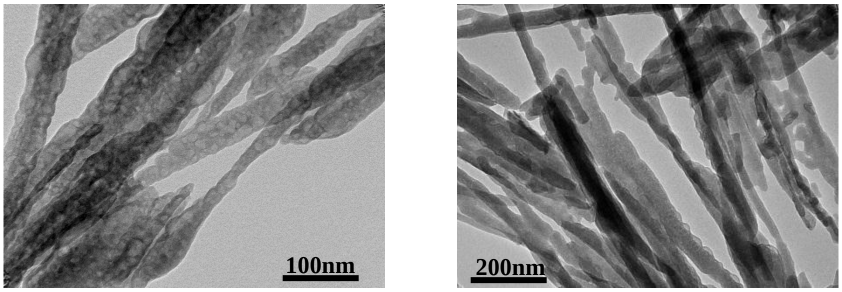

(a) (b)

Figure 3.19 SiNWs a) before and b) after dry cleaning in SF_6:O_2 plasma

The XPS results of dry cleaning processes of arrays of wires, using SF_6:O_2 gas chemistry and wet cleaning processes in RCA solutions are compared in Fig. 3.20. In situ, EDX analysis, in a TEM chamber on single wires, was also performed; and the results for as-etched wires, wires cleaned with dry etch

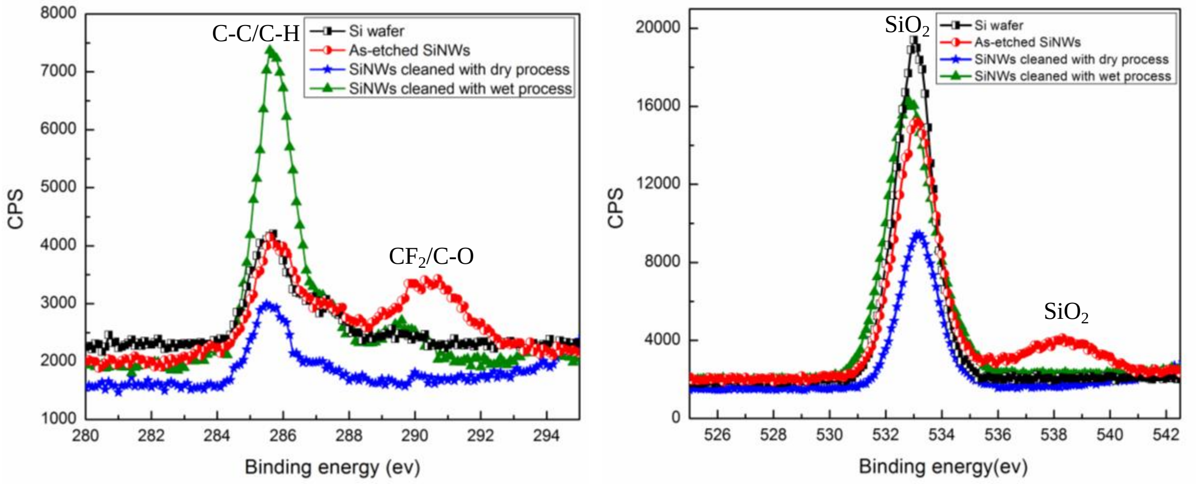

(a) (b)

Figure 3.20 Comparison of XPS analyses on dry and wet cleaning of arrays of Si nanowires: a) carbonate compounds and b) oxide component

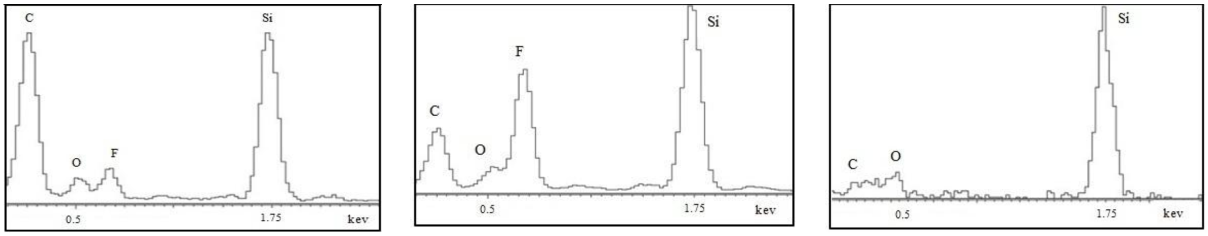

(a) (b) (c)

Figure 3.21 EDX spectrums: (a) as-etched wires (b) wires after dry cleaning (c) wires after wet cleaning

process under SF_6:O_2 plasma and wires cleaned using a wet etch process with RCA solution, are compared (see Fig. 3.21).

From the results, as shown in Fig. 3.20.a,b, Fig. 3.21.a,b, and the SEM micrograph shown in Fig. 3.22.a, it can be concluded that the dry process removes undesirable oxide and organic compound layers from the sidewalls, without damage. From the SEM image it is obvious that the wires are slightly bent to the sides. The wet process fully cleans the wires, but it is likely to destruct the structures (see Fig. 3.20.a,b and Fig. 3.21.c and SEM micrograph in Fig. 3.22.b). The SEM micrograph, in Fig. 3.22.b, shows the wires are completely damaged after the wet etching process.

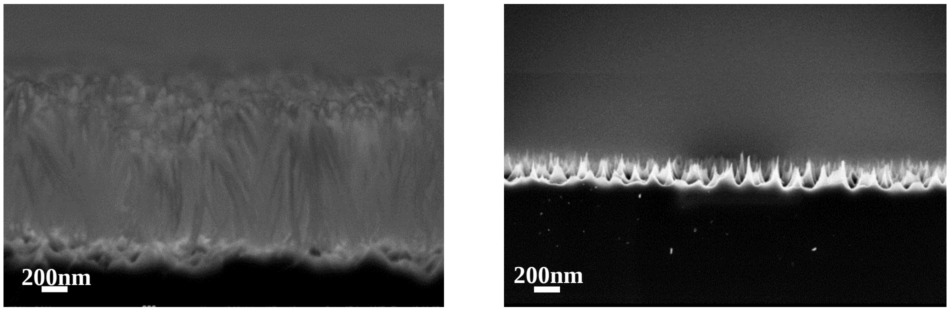

(a) (b)

Figure 3.22 SiNWs after a) dry and b) wet cleanings

3.3.5 Surface Passivation of SiNWs by Oxidation

A high temperature, rapid thermal process (RTP) was developed to oxidize the SiNWs, in order to passivate and reduce the wire diameter. In addition to an excellent Si/SiO_2 interface, diameter control was achieved; which is crucial to reaching diameters where quantum confinement can take place. Surface

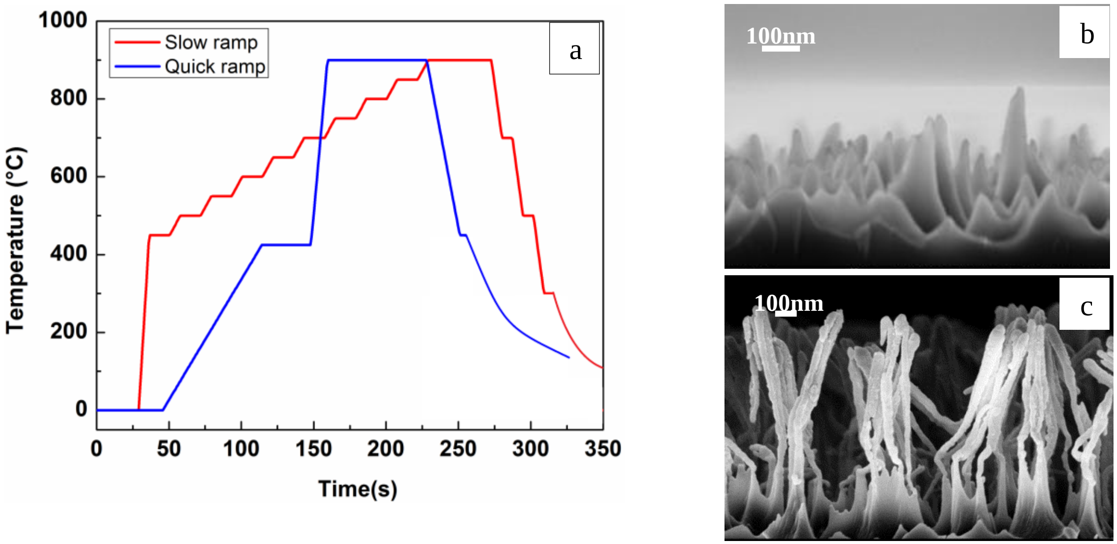

Figure 3.223 a) RTP profiles used to oxidize SiNWs. SEM images of oxide-passivated nanowires using b) quick and c) slow ramps

passivation is also essential for the luminescent studies; and for device applications where the nanowires function as luminescent converters.

An RTP process was used at 900°C, under oxygen, to oxidize the wires. Fig. 3.23.a, shows two RTP profiles used to oxidize Si nanowires. Ramp up/down slopes are critical parameters in both controlling the oxide growth and avoiding breaking of the nanowires. The use of the quick RTP ramp resulted in undesirable structures as shown in Fig. 3.23.b. By increasing the number of ramp steps and hold times, as well as the cooling steps, the annealing process was slowed down; this led to oxidation of the wires in a controlled manner. Using this annealing condition, the shape of the wires was maintained, during the high temperature annealing. Fig. 3.23.c, shows the SEM micrograph of the 1μm wires after oxidation, using a slow ramp profile under 4sccm oxygen for 60s. The images indicate that some wires bent, during the high temperature process, but the structure shapes were preserved and not damaged. However, exposure to high temperature resulted in density reduction and uniformity loss. The wires were also oxidized at 60s and 120s oxidation cycles. No significant difference in the shape of the wires was noted, as the wires oxidized either at short or long oxidation cycles.

TEM and HRTEM were used to study the size, core-shell and crystalline structure of the oxidized wires. In Fig. 3.24.a, the TEM images of a cluster of oxidized wires are shown. As demonstrated in the magnified image in Fig. 3.24.b, these wires are fairly long (about 2μm) and their diameters are about 25nm. The core crystalline part, with darker contrast, is distinguishable from the amorphous oxide skin in Fig. 3.24.c. The core-shell structure is also clearly shown in the inset image. Bending is because of the interaction of the nanosize structures and the electron beam. The HRTEM image, in Fig. 3.24.d, indicates an axial crystalline core structure. The lattice structure of the crystalline part is clear. This image also shows that the core size is 10nm; and the amorphous shell with an oxide nature is about 10nm on each side. The diffraction image shows the combination of the rings and dots, as an indication of the presence of both the amorphous shell and crystalline core structures (see inset in Fig. 3.24.d).

An in situ EDX analysis on the oxidized wires, during characterization of particles with TEM, was obtained (see Fig. 3.25.a). The result reveals a high percentage of atomic concentration of oxygen at the shell of the structure, after oxidation, while the silicon percentage is higher at the core. The result from the XPS analyses compares the oxidized Si wires to the as-etched wires and silicon wafer as shown in Fig. 3.25.b. The SiO2 peak intensity was improved for the oxidized wires.

3.3.6 Surface Passivation of SiNWs by PECVD Silicon Nitride

In a process variation, a low-temperature (300°C) surface passivation method was also developed for Si nanowires. The wires were passivated by silicon nitride coating in a PECVD process using a silane/ammonia gas system at 150 mTorr and a plasma power of 25 w. The optimized process resulted in

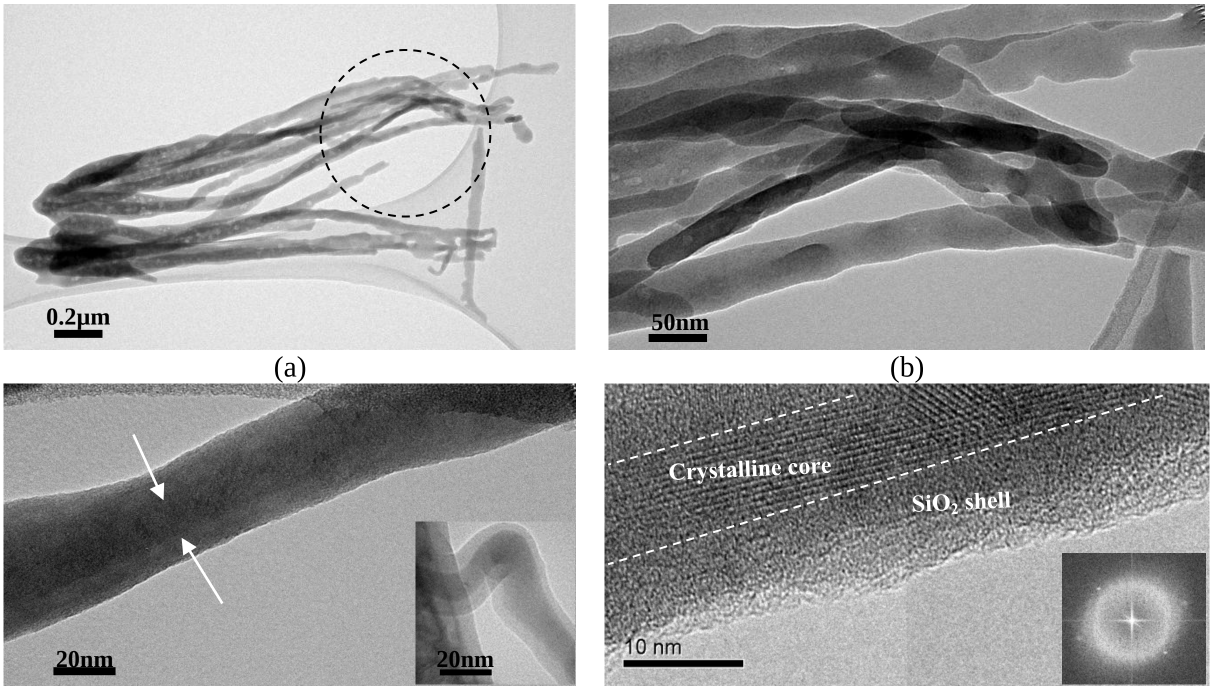

(a) (b)

(c) (d)

Figure 3.24 a) TEM image of cluster of oxidized SiNWs detached from the Si wafer and seated on the TEM carbon grid, (b) magnified view of 25nm core-shell wires, (c) 25nm core/shell SiNW. The core is distinguishable from the shell in the inset image, (d) HRTEM image with the lattice structure of the core and amorphous shell. Inset is the diffraction pattern.

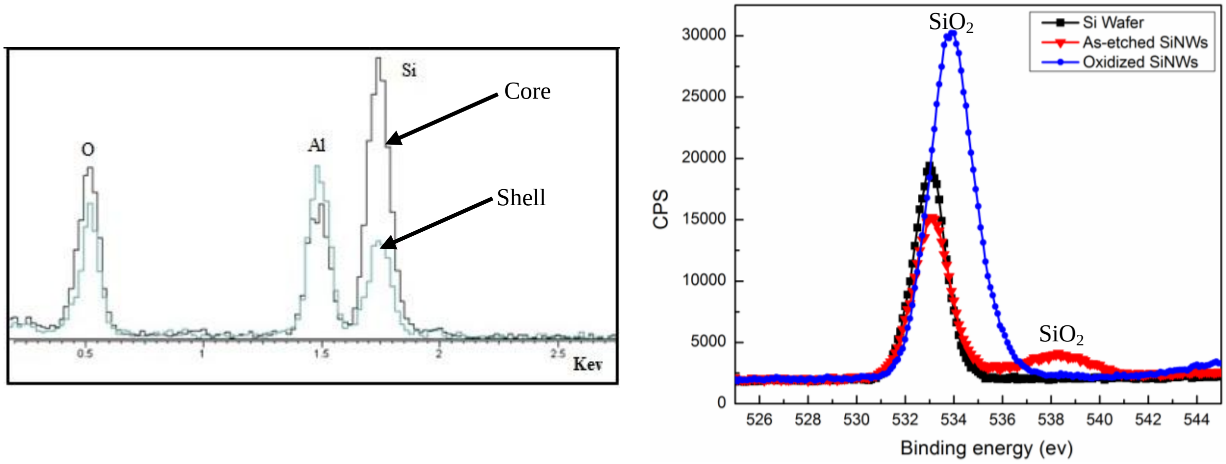

(a) (b)

Figure 3.25 a) EDX and b) XPS analysis on the oxidized NWs.

a highly conformal deposition; and a SiN_x thin layer covered the sidewalls of the nanowires, without damaging or bending the structures (see Fig. 3.26.a). It also appeared that the nitride passivation resulted in robust structures, which benefits wires with further processing and manipulation, as will be seen in

Section (3.3.7). The Fig. 3.26.b, presents the upright, densely packed SiN_x coated wires; and the inset is a magnified view for more clarification.

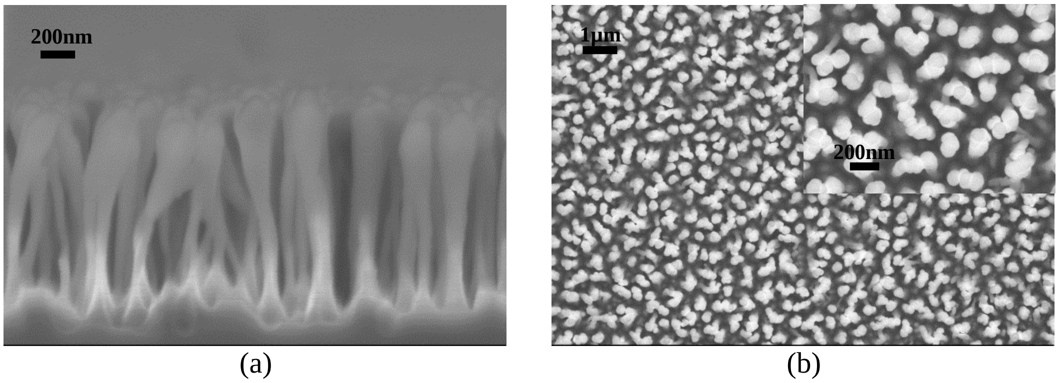

(a) (b)

Figure 3.26 a) cross section and b) top view image of nanowires covered with a thin layer of PECVD silicon nitride: inset is the magnified image.

The TEM images exhibited in Fig. 3.27 indicate the core-shell NW structures, fabricated by conformal coverage of the SiNWs, with a thin layer of PECVD silicon nitride. The image, in Fig. 3.27.a, shows a group of detached wires from the substrate seated on the TEM copper grids. The magnified image, in Fig. 3.27.b, shows the core-shell wire, with a core size of 25nm and a thin shell of about 10nm. The shell is also completely distinguishable from the core, having a lower contrast. In Fig. 3.27.c, the diffraction contrast, between the amorphous nitride skin and the crystalline core, is clear. Different crystalline planes can also be recognized with high-low contrasts in the core; as well as, in some regions, these planes crossing resulted in crystalline zones. The diffraction pattern, shown as an inset in Fig. 3.27.c, belongs to the entire structure; wire covered with amorphous silicon nitride. The rings are due to the presence of amorphous shell and the dots are as a result of the crystalline core structure. The HRTEM image, in Fig. 3.27.d, demonstrates the lattice structure of the core. Different crystalline planes exist on the outer surface of the silicon wires. Crystalline orientations, at some sites and zone areas, can be recognized from the micrograph. This is evidence of the presence of crystalline structures at the entire core, even though in some sites this crystallinity is present in low contrast.

3.3.7 Surface Passivation of SiNWs Using Spin on Glass

In another process variation, a commercially available spin on glass film (SOG) was spin-cast onto the upright nanowires, thus (partially or fully) burying them into an oxide film, while providing surface passivation. This was achieved subsequent to an RTP thermal treatment, which improved the oxide quality and also helped to further tune the dimensions.

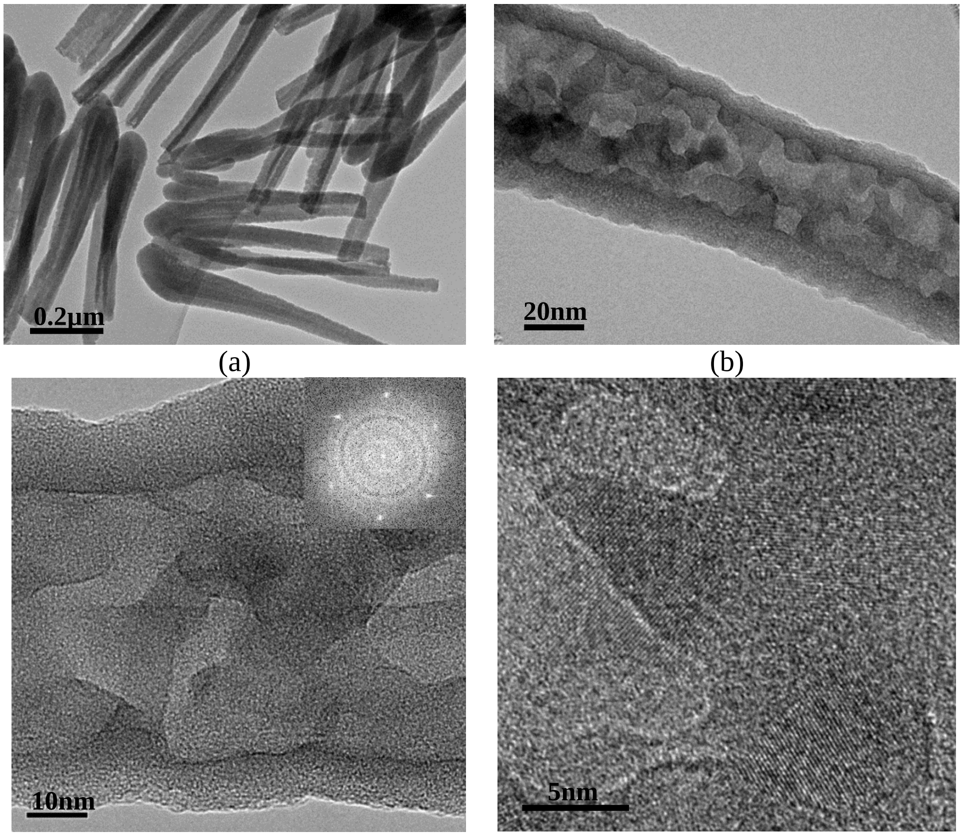

(a) (b) (c) (d)

Figure 3.27 a) TEM image of conformal coverage of the Si nanowires with PECVD silicon nitride film, b) magnified image of a single core-shell wire with 25nm Si core and 10nm SiN_x shell, c) magnified image of the same structure showing different crystalline planes on the Si core and the amorphous nature of the SiN_x shell. The inset is the diffraction pattern of the core-shell structure, d) HRTEM image of the core showing the lattice structure of the crystalline part.

SEM images in Fig. 3.28.a show several wires bending and joining to form clusters after spinning at 1000 rpm for 30s, and subsequent annealing at 850ºC, under oxygen. It was realized that fast spin resulted in the formation of large clusters, which finally transformed into pyramid-like structures. Reducing the spin speed to 550 rpm resulted in conformal coverage and low damage of the wires after 30s (see Fig. 3.28.b). As shown in Fig. 3.28.c,d, by using a bilayer deposition of the SOG at this spin speed, full coverage of the 1µm wires in the SOG was achieved. Fig. 3.28.e shows the top view of the nanowires buried in the SOG layer. The inset is the magnified view of the same structure for clarification. The tips of the wires are clear in this image. The subsequent annealing process improved the material quality of the SOG layer both mechanically and optically. It also made the SOG layer uniform and crack-free, by stress release, as a result of the annealing. The annealing further made the glass layer reach an oxide level which is optically transparent; and improved the light-trapping inside the structure by providing the desired refractive index matching. The dimension of the Si nanowires embedded in the matrix could be controlled as well, due to consumption of the silicon during oxidation.

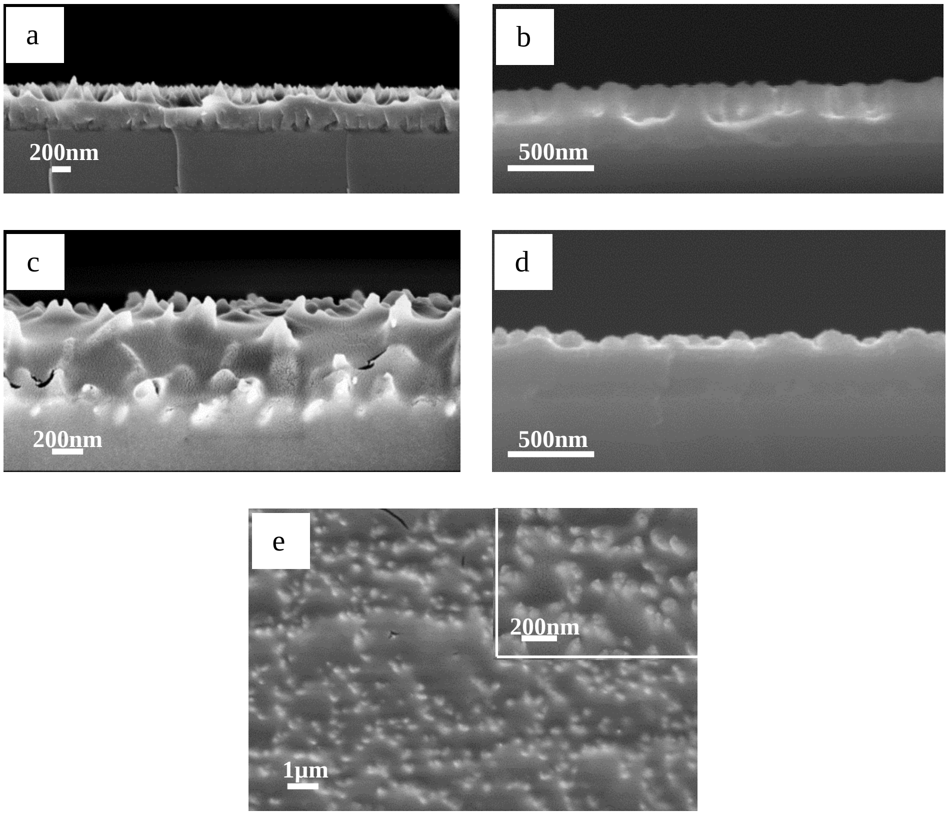

Figure 3.28 a,b) Partially and c,d) fully buried nanowires in a spin-cast SOG layer, c) top view of the fully buried wires in SOG: the inset is the magnified image.

In some of the experiments, the wires that were subjected to the spin-cast process were pre-coated with PECVD SiN_x films, in order to make them mechanically robust. Fig. 3.29.a reveals that at a high spin speed of 1500 rpm, a thin layer of glass film formed on top of the wires pre-coated with silicon nitride, where the wires were completely buried underneath. Although this condition resulted in poor step coverage, it is appropriate for planarization; as well as having a porous structure under the glass layer with promising optical properties for solar cell applications. This structure can be used as a medium with graded index properties. In addition, absorption of incident light reduced in the thin glass film. A slower spin speed of 800 rpm was still not optimized; as can be seen in Fig. 3.29.b, it resulted in many voids. A lower spin speed of 650 rpm for 30s resulted in a conformal layer of SOG forming on the SiN_x layer (see Fig. 3.29.c). Multiple spin-cast steps using the latter spin parameters could also be applied to fully bury the wires (see Fig. 3.29.d,e).

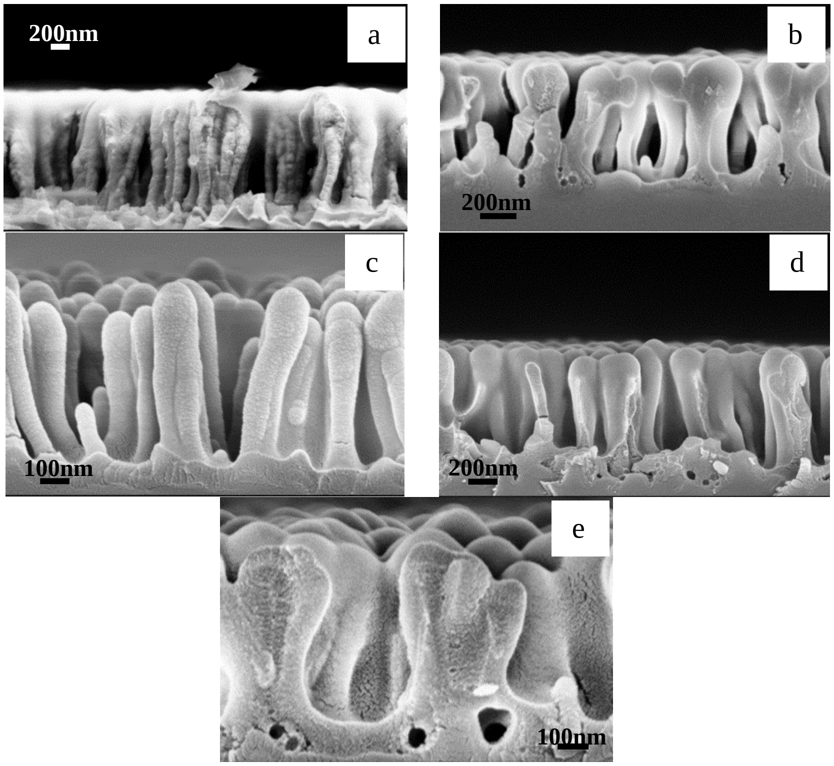

Figure 3.29 SiNWs pre-coated with PECVD SiN$_x$, subjected to spin-cast process of SOG for 30s at spin speed of a) 1500 rpm b) 800 rpm c) 650 rpm, d, e) Low and high magnification images of the wires after two depositions using the spin parameters in (c) to fully bury the wires in SOG

The TEM images in Fig. 3.30.a show the wires embedded in SOG after the post annealing treatment. Some wires were bent during the spin step or TEM sample preparation. Fig. 3.30.b exhibits a single wire embedded in SOG. The HRTEM image in Fig. 3.30.c shows the crystalline structure of the single wire having a higher contrast, with respect to the amorphous oxide matrix in which it embedded; as well, crystallite cites appeared in the SOG layer after the high temperature annealing process. The film-

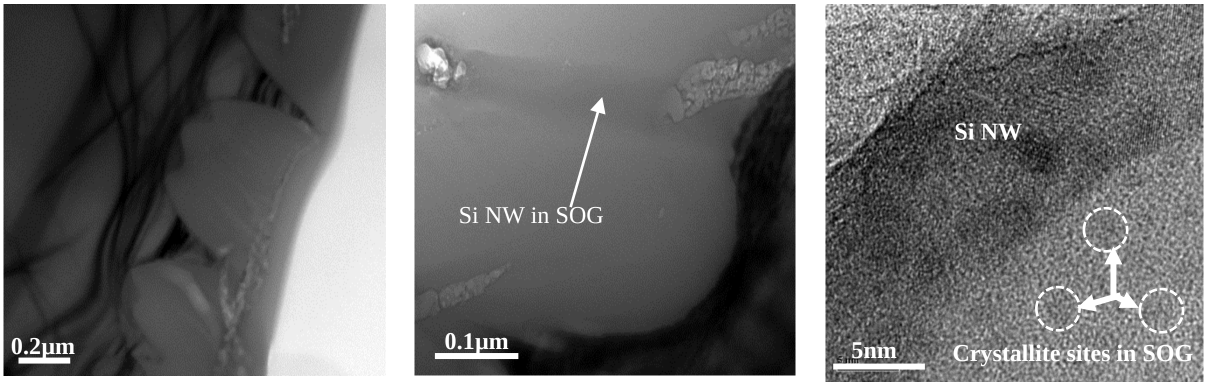

(a) (b) (c)

Figure 3.30 TEM images of a) arrays of wires and b) single wire embedded in SOG c) HRTEM image of a wire in an SOG matrix

embedded nanowires can also be used to form cylindrical p-n junctions for advanced devices, if dopant-containing polymers are introduced. This will be discussed in Chapter 5.

Detachment of SiNWs and Embedment in SOG

In the next phase of the development of nanoscale structures for PV, a methodology was devised to detach the nanowires in order to manipulate them for further deployment. Nanowires were detached by sonicating the wafer on which the nanowires formed, in a solution of HPLC[1] methanol with ammonium hydroxide declustering [167]. SEM images of the detached nanowires using this method are shown in Fig. 3.31.a,b. The nanowires can also be detached from the wafer by scratching, as shown in Fig. 3.31.c. The extracted NWs were further used for structural characterization (TEM) and for embedment as spin-cast oxide/polymeric films. The silicon wafer could be used repeatedly in plasma dry processes, for nanowire formation, after every detachment cycle and a subsequent cleaning process.

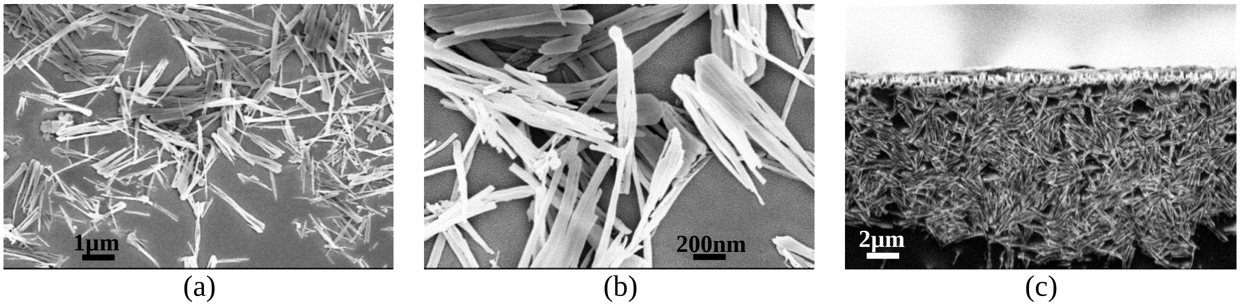

Figure 3.31 Nanowires detached by a,b) sonication; low and high magnifications,respectively and c) scratching

Detached SiNWs, obtained by sonication of the wafers, were incorporated in an SOG spin-cast solution and fully embedded in an oxide matrix by subsequent annealing in oxygen ambient at 850ºC. Such solutions can be used to fabricate self-supporting SiNW/oxide thin films of various concentrations. The crystalline orientation of the SiNWs embedded in an oxide matrix is clearly observable in the high resolution TEM images in Fig. 3.32. As shown in Fig. 3.32.a to Fig. 3.32.c, the shape and density of the crystallite sites varied, when moving from the regions close to the substrate, to the top part of the layer. The crystalline dot-shaped sites are attributed to the crystallization of the silicon materials in the SOG solution. The EDX analysis shows silicon and oxygen contents in the layer (Fig. 3.32.d). High quality oxide matrices, with a high concentration of Si nanowires, are desirable, to act as passivation and luminescent down shifter (LDS) respectively. The LDS concept is discussed in Chapter 7.

---

[1] high performance liquid chromatography

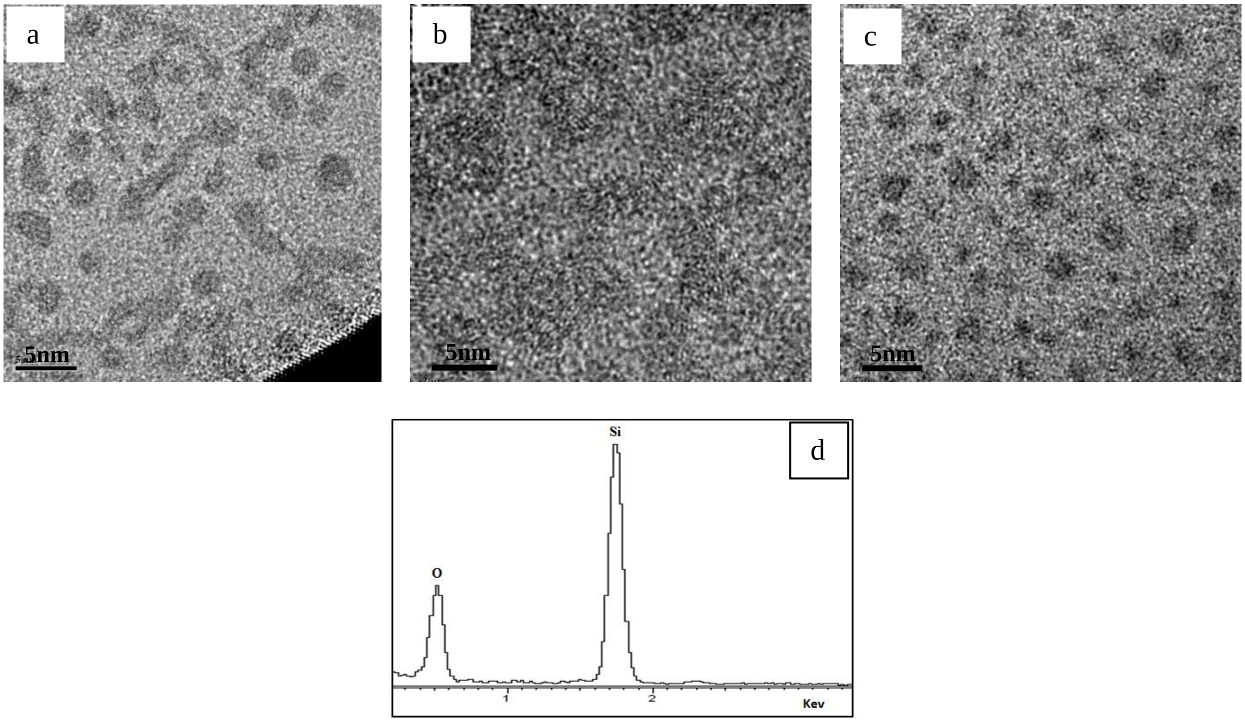

Figure 3.332 The crystallite sites in an oxide matrix containing SiNWs after annealing at 850°C a) close to the substrate, b) middle and c) top part of the layer, d) EDX analysis of the layer

Access to the Substrate by Etching the SOG through the Top

In addition to PV applications, electroluminescence devices based on silicon nanostructures, can be made after planarization of the nanowires and top electrode formation [168]. After the nanowires were planarized in SOG, dry etching processes were applied to remove the SOG from the tips of the buried NWs. In the RIE process, an SF_6:H_2 gas mixture with a flow rate of 50:10 (sccm) respectively; and a ratio of 5, was used to remove the oxide layer at the plasma pressure, self-bias voltage and power of 50mTorr, 150V and 124w respectively. Fig. 3.33.a, displays the top view of the buried wires underneath the SOG, after 1min etching at this plasma condition. The image indicates that the wires are starting to protrude from the SOG layer. Fig. 3.33.b shows that by continuing the etching to 5 minutes, more tips protrude from the SOG. From the image it can be seen that this etching condition is quite monotonous and the density of the wires sticking out of the SOG is considerable. It also indicates that the tips of the bunch of wires are attached after protruding from the SOG. This is a result of the spin coating process, which leads to the cluster formation of nanowires by bending during the rotation, as discussed earlier in section 3.3.7.

In another approach, the layer with SF_6:H_2 was etched for 1min, using the same conditions used in the previous approach, following an etching in a CF_4:O_2 gas mixture, with the flow rates of 75:30 (sccm) respectively and a ratio of 2.5 at the plasma pressure, self-bias voltage and power of 50mTorr, 525V and

124w, respectively, for 4min. As shown in Fig. 3.33.c the tips of the wires protrude from the SOG. The etch process seems to be homogenous over the large area, as shown in the SEM image, however the etching rate is slower than the former process. When comparing Fig. 3.33.b with Fig. 3.33.c, one sees that the pillars stick out from the SOG farther for the sample etched under SF_6:H_2 and under the same etching cycle. An alternative etching process was also developed by using CF_4:O_2 gas mixture at the plasma condition, as discussed previously for this plasma chemistry (see Fig. 3.33.d). Further, when comparing the density of the pillars protruding from the SOG in Fig. 3.33.b with Fig. 3.33.d, it can be concluded that the etch rate in the latter process is less, than when using CF_4:O_2 as the etching gas. It can be seen that the density of the wires is higher for the sample etched under SF_6:H_2 with the same etching cycle.

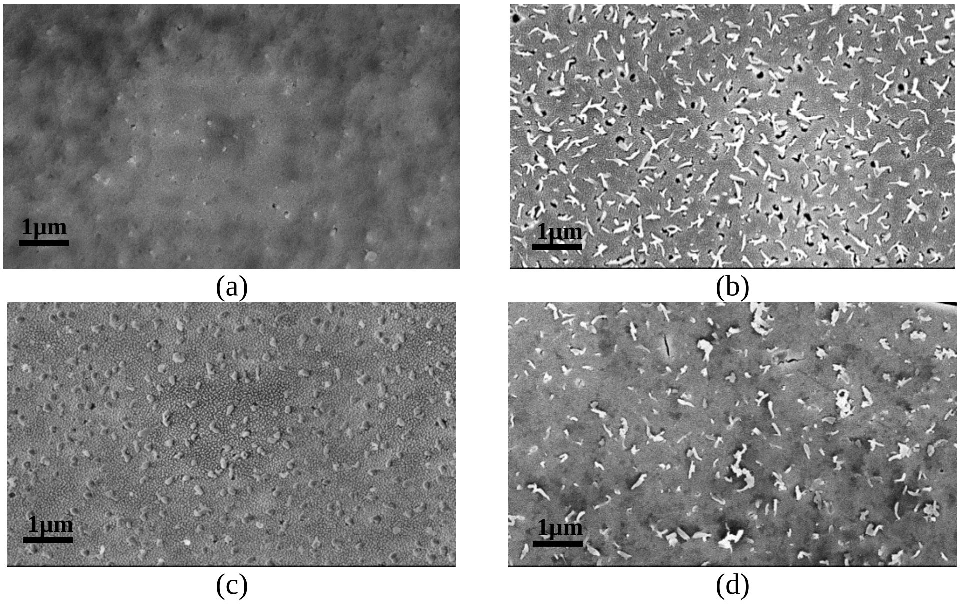

Figure 3.33 a) wires protrude from the SOG after a) 1min etching in SF_6:H_2, b) 5min etching in SF_6:H_2, c) 1min etching in SF_6:H_2 followed by 4 min etching in CF_4:O_2, d) 5min etching in CF_4:O_2

3.3.8 Carrier Lifetime Analysis of Passivated and Non-passivated SiNWs

In order to study the electronic properties of the fabricated nanowires, the lifetime of the passivated/non-passivated structures were measured by the µ-PCD technique, using SEMILAB. The results show that rapid thermal oxidation of SiNWs results in the degradation of their electronic properties; while with silicon nitride and SOG passivation, the electronic properties of the nanowires were improved (see Fig. 3.34).

3.3.9 Optical Characterization of the SiNWs

In order to study the optical properties of the fabricated nanowires, reflection and photoluminescence measurements were performed. The obtained results are discussed in this section.

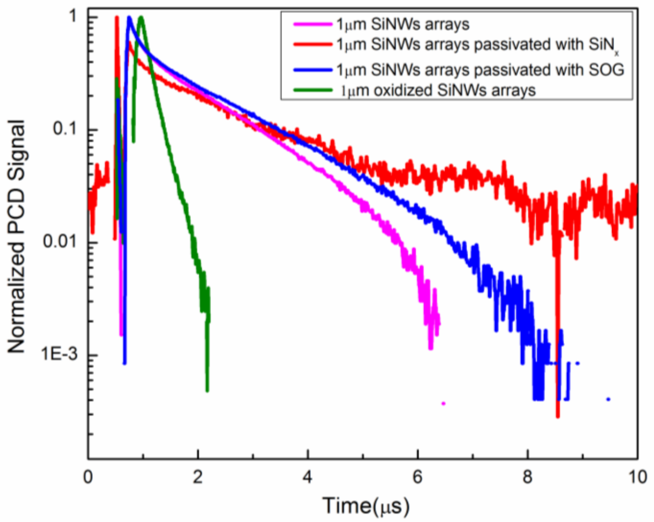

Figure 3.34 Carrier lifetime analyses of passivated/non-passivated SiNWs

Reflectance of Passivated and Non-passivated SiNWs

Photovoltaic devices can benefit from nanostructures through reduced reflection. The reflectance of the passivated/non-passivated silicon nanowires was investigated by a LAMDA 1050 PerkinElmer UV/Vis spectrophotometer. The obtained results as shown in Fig. 3.35 indicate that the optical reflection of the silicon considerably decreased in the nanowires. The reflection of 500nm long wires is shown in this figure. It was seen that the reflectance dramatically reduces as the length of the wires increases. The reduction in the reflectance of the wires after coverage with SiN$_x$, SOG, SiN$_x$/SOG and after oxidation was also seen. The lowest reflectance is obtained by conformal coverage of the wires with SiN$_x$ followed by embedment in an SOG layer.

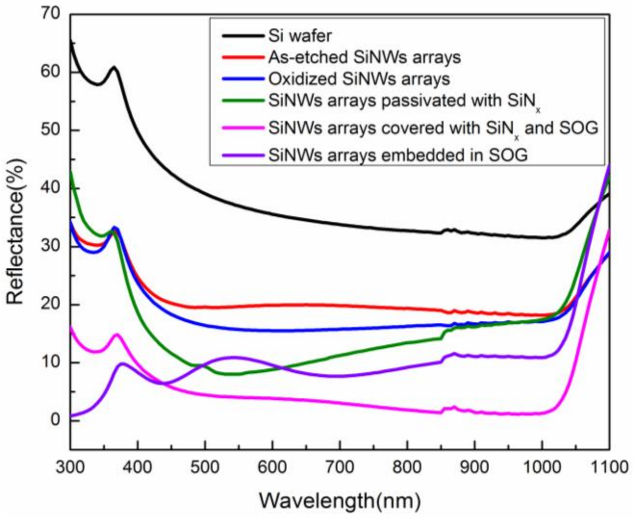

Figure 3.435 Reflectance of the passivated/non-passivated SiNWs

Photoluminescence of Passivated and Non-passivated SiNWs

As-formed Si-nanowires, oxidized wires, wires with nitride skin and silicon NWs embedded in SOG were illuminated, at an excitation wavelength of 300nm in an Edinburgh photoluminescence system, to investigate the photoluminescent properties of the fabricated structures. The experiment set-up involved a Xenon lamp and a double monochromator with a photomultiplier (PMT) detector to record the emitted photons. To verify that the signal was originating from the sample, a filter with cut-off wavelength at 340nm was used. The intensity and photoluminescence peak position can be seen in Fig. 3.36.

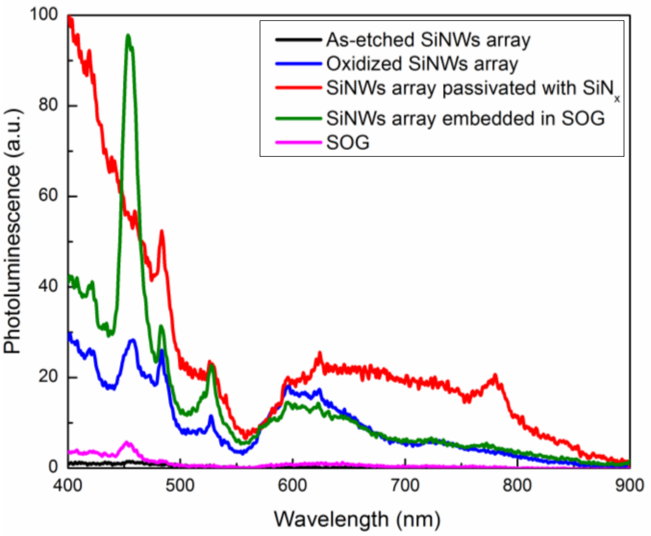

Figure 3.36 Photoluminescence of the passivated/non-passivated SiNWs at 300nm excitation wavelength.

Depending on the size of the wires, the photoluminescence of SiNWs can be tuned from the near infrared to the ultraviolet. Both quantum confinement and surface passivation determine the electronic states of the Si nanostructures [169,170]. Numerous models treat low structural dimensions, as well as high surface-to-volume ratios, to include quantum confinement, surface states, and defects in the oxide or nitride matrices; and explain the entire PL from the nanostructures [171].

The similarity between the PL spectra of nanowires and PL spectra of porous silicon layers suggests that the same mechanism that is responsible for light emission from porous Si, is also responsible for emission from nanowire samples.

It is seen that each PL spectrum consists of bands in 450nm and 520nm. The passivated wires also consist of 650nm and 700-800nm PL bands. The origin of each peak appearing at this stage is not clearly recognizable due to the overlapping of the peaks relevant to different phenomena. The origin of the 450nm peak in PL spectrum might be related to surface conditions such as residual dangling bonds, surface stress and/or strain, and Si oxide defects at the surface [172]. The PL peak at 520nm might be a result of the recombination within localized band tail states, existing below the optical band gap in $SiO_{x,}$ created on the sidewalls of the wires. Another possible explanation is that hydrogen-related species formed on the surface sidewalls [173]. The 650nm band is usually caused by non-bridging oxygen-hole centers in SiO_2 [174]. The 700-800nm band can be due to quantum confinement [175]. The observed broad PL signal is attributed to the wide range of size distribution of silicon nanowires, which is typical of the preparation method. The low quantum efficiency of the Si nanowires is attributed to the loss associated with nonradiative recombination at surface states, due to incomplete surface passivation. The PL properties of silicon nanowires similar to the developed structure that has been studied so far, also show a strong dependence on passivation [113]. A better understanding of the origin of the PL in Si nanostructures needs to be gained. Also, preparation of small particles would be of interest, in order to provide quantum confined related PL peaks. Extensive PL characterization on Si nanowires has been done. The observed PL of the SiNWs is weak. In order to continue investigation of this phenomenon on the nanowires, measurements need to be done under laser excitation in future experiments.

3.4 Conclusions

Silicon nitride sub-wavelength structures were fabricated on silicon substrate using the maskless RIE technique. The reflection properties of the structures were explored through spectroscopic measurements and modelling. The experimental results show that the SiN_x nanostructures and the non-etched SiN_x layer can be engineered to act as a graded index ARC. Excellent fits were obtained between the analytical calculations and experimental data. These structures can result in lower surface recombination velocity as compared to silicon nanostructures, if the aim of fabrication of such structures is trapping the incident light more efficiently. Also, silicon nanostructures with desired shape, dimensions and pitches can be fabricated by utilizing SiN_x nanostructures as templates.

Also, uniformly distributed vertical Si nanowires were obtained by a simple maskless plasma etching process. High-temperature RTP and low-temperature PECVD processes were developed for passivation as well as size reduction of SiNWs. Incorporation of fabricated SiNWs in glass matrices to form a luminescent down-shifter layer was also presented. Structural, surface and optical properties of the NWs were studied. The µ-PCD lifetime measurement shows that when the wires were passivated with PECVD SiN_x and SOG it results in lifetime improvement. Spectroscopic reflectance measurements confirm the reduced reflection of the nanostructures. The photon conversion ability of the fabricated structures was also verified by PL. The low quantum efficiency of the Si nanowires was attributed to the loss associated with nonradiative recombination at surface states due to incomplete surface passivation. The results from such characterization methods are vital in optimizing the film preparation and deployment methodologies for solar cells in such a way that the optical window of the overall device is widened. In addition to serving as passive components to enhance the optical performance of the solar cells, these fabricated SiNWs can be used as active carrier generators in new type devices. The simplicity, repeatability, and scalability of the developed processes have strong potential for use in deployment on photovoltaic device architectures.

Chapter 4

Simplified Process for Periodic Arrays of Silicon Nanowires

In this chapter a simple and scalable method for fabrication of arrays of silicon nanowires using colloidal crystal as mask is proposed. Silica nanospheres of about 500nm diameter were assembled by spin coating into close-packed colloidal crystals over a large area. Using the colloidal crystals functioning as masks, a reactive ion etching (RIE) process was developed to successfully form arrays of NWs on silicon substrates. Effects of plasma etching process conditions on the shape of the nanowires are discussed.

4.1 Candidate Material for Nanosphere Mask

Nanowire array geometry has been shown to be beneficial for new generation of PV device architecture. For many of the advanced PV applications, the diameter, spacing and shape of the nanowires need to be precisely controlled. Also the nanowire arrays should be fabricated over a large area with high throughput and low cost. While the known methods of vapor-liquid-solid synthesis and solution chemistry synthesis have poor control on the array arrangement, electron beam lithography based methods are considered expensive for PV applications. Moreover, the use of Au as the nanowire growth catalyst in the VLS method is of particular concern because Au is a deep level trap in silicon which negatively impacts the performance of the devices [176].

Natural lithography that exploits arrays of chemically synthesized nanospheres as masks for patterning different shapes of nanoparticles and pillars can be an alternative approach for nanowire fabrication [177-179]. The advantage of this approach is that nanospheres can assemble into close-packed arrays. Langmuir-Blodgett (LB), dip coating and roll coating are the methods that have been used for nanosphere assembling [140,141]. Spin coating is a simple and cost effective method for layer formation. However, there is not much reported on the spin coating method for assembling the nanospheres. The spacing and diameter can then be tuned simply by changing the size of the nanospheres [180,181]. Silica and polymer spheres can be synthesized with a wide range of diameters (100-1000nm). Anodic alumina and block copolymer templates can produce much smaller particle diameters (10-100nm). Nanowires with diameters of about 10nm have been fabricated using these particles [142]. Silica and polystyrene nanospheres can be used for the formation of wires with bigger diameters.

In this chapter, fabrication of 500nm SiNW arrays, using natural lithography and etching, was presented. Silica nanospheres were assembled over a 4cm^2 silicon wafer by spin coating forming the template to create large-area periodic silicon NWs in an etching process in an O_2:SF_6 plasma. The silica nanospheres are preferable as they don't remain polymeric residue on the surface.

The fabricated NW arrays provide promising opportunities for improved efficiency in photovoltaics. These nanostructures have tunable electro-optic properties that can be beneficially engineered for PV devices. They can be used as electrically active layers leading to advanced device structures with the band gap of the base material effectively tuned enhancing the cell collection efficiency [15,182].

4.2 Concepts for Experimental Approach

The passivation compounds (deposition of silicon fluoride oxide (SiF_xO_y) on the sidewalls from low energy compositions) and etching periods (ion-induced etching from high energy composition) have to be optimized in order to obtain vertical sidewalls. In addition, at a fluorine-based discharge, the silica etch rate is less than silicon due to the fact that the silica is chemically inert and needs high energy ions.

The competition between the F and O attacks of a Si surface may schematically be written for pure fluorine and oxygen fluxes, respectively. The etch rate of the SiO_xF_y material produced according to Eq. (4.1) depends strongly on ion bombardment energy and the F/O flux ratio. The overall Si surface response can be controlled from high rate etching Eq. (4.2) to oxide growth Eq. (4.3) by adjusting these parameters.

$$\mathrm{Si} + x\mathrm{F} + y\mathrm{O} \longrightarrow \mathrm{SiF}_x\mathrm{O}_y \qquad (4.1)$$

$$\mathrm{Si} + 4\mathrm{F} \longrightarrow \mathrm{SiF}_4 \text{ (etching)} \qquad (4.2)$$

$$\mathrm{Si} + 2\mathrm{O} \longrightarrow \mathrm{SiO}_2 \text{ (passivation)} \qquad (4.3)$$

The surface chemistry including low energy composition (deposition) and high energy composition (etch) in an appropriate plasma condition lead to the desired etched profile. In this work, it has been observed that a high proportion of oxygen gas in an O_2:SF_6 plasma, results in anisotropic selective etching of silicon. In other words, anisotropic etching can be achieved by controlling the amount of sidewall passivation, by mixing a ratio of O_2/SF_6. Oxygen atoms released into the discharge increase oxygen to a fluorine ratio in the plasma and shift the overall reaction towards deposition of oxide materials, which results in an anisotropic etching of silicon by fluorine ions.

4.3 Monolayer Formation of Silica Nanospheres

P-doped silicon (100) wafers were first cleaned in a piranha solution [3:1 concentrated sulfuric acid:hydrogen peroxide (H_2SO_4:30% H_2O_2)] for 30 min and then rinsed repeatedly with deionized water.

These substrates were further cleaned with RCA1, RCA2 solutions and methanol before use in order to promote wetting of the substrate. Then 0.2gr of dry powder of amino functionalized silica nanospheres, (Bangs Laboratories, Inc.), were dispersed in 2mL of methanol and rigorously vortexed for 2 minutes, which resulted in a solution with a density of 0.1gr/cm^3. The vial containing the silica suspension was then placed in a sonic bath for 10 minutes. Viscosity and stability are the two important factors for monolayer formation. The amin additives improve the stability of the nanoparticles. Colloidal solution was spin cast onto silicon substrates to form two-dimensional colloidal crystals. The disperse volume fraction is another important factor for monolayer formation. The diffusion rate must then be precisely controlled; achieved by optimizing the spin parameters. One of the advantages of current spin coating technique is that the thickness of the resulting colloidal crystals can easily be controlled by adjusting the spin speed and duration. Fig. 4.1 shows the Scanning Electron Microscope (SEM) images of resulting nanosphere crystals obtained at various spin speed conditions. The results demonstrate multilayers, double layers and monolayers of the silica nanosphere crystals obtained at 500, 2000, 4000 rpm spin speed, each lasting for 30s.

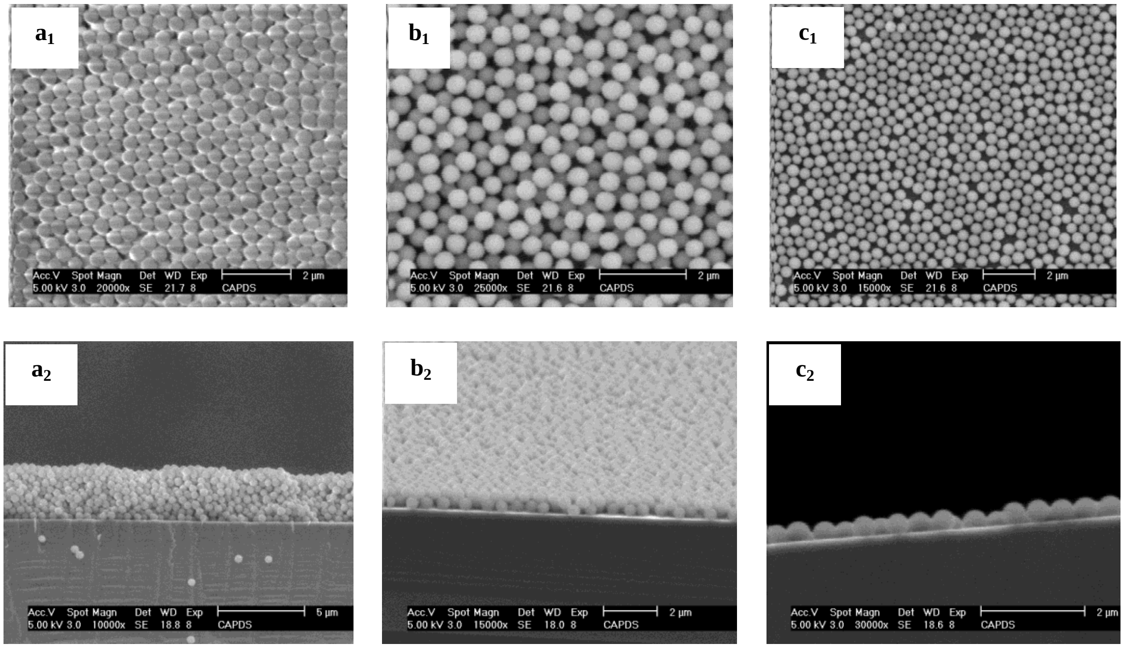

Figure 4.1 SEM image (top view-top & cross section-bottom) of colloidal crystals prepared at a) 500 rpm, b) 2000rpm and c) 4000 rpm, all for 30s using a solution with density of 0.1gr/cm^3

It was observed that the concentration of the solid is the most important parameter in monolayer formation. Fig. 4.2 is the SEM image of a monolayer crystal prepared by spin coating at 1000 rpm for 30 min, using a solution with a density of 0.05gr/cm^3. The long-range ordering of silica nanospheres is clearly evident from the SEM image.

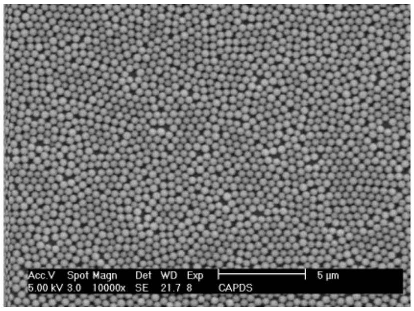

Figure 4.2 SEM image of a monolayer of colloidal crystals spin-coated at 1000rpm for 30s from a solution with density of 0.05gr/cm^3

As mentioned above, by adjusting the spin parameters, single layer, large area and close-packed structures were obtained. Fig. 4.3 shows low magnification and magnified SEM micrographs of the single layer structures of the colloidal crystals, coated from aqueous solution, with a colloidal diameter of 500nm and with optimized viscosity formed on 4 cm^2 silicon wafers. It should be emphasized that this method can be applied for large area applications.

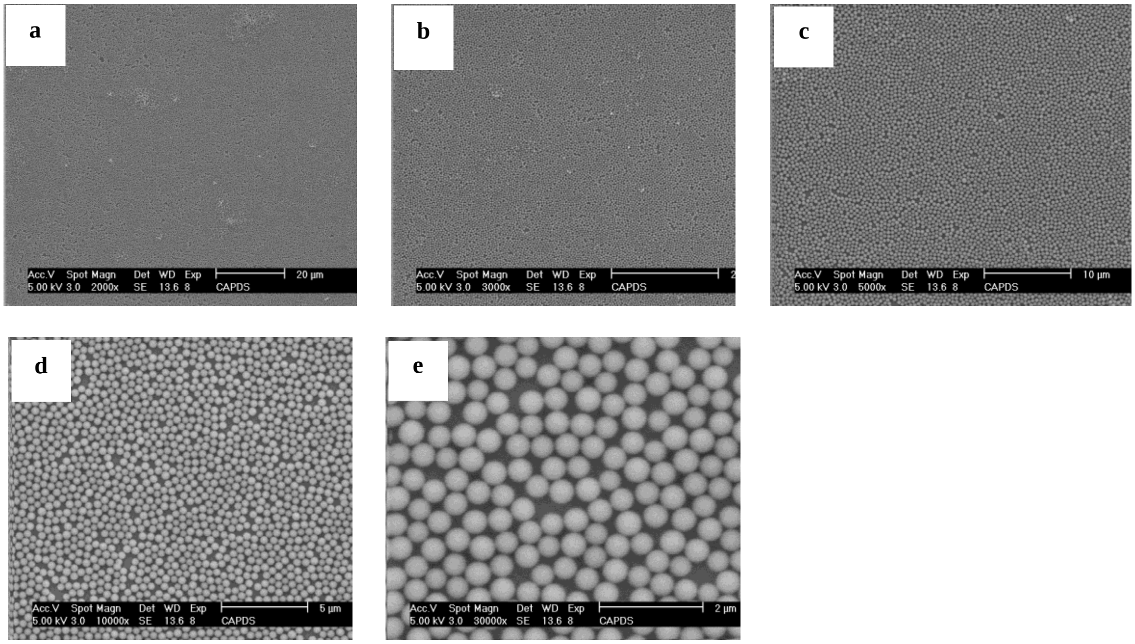

Figure 4.3 a, b, c) SEM images of large area monolayer of silica nanoparticles d, e) Magnified images of silica nanoparticles

4.4 Fabrication of SiNW Array Using a Plasma Etching Process

Using the colloidal crystals functioning as masks, RIE processes were developed to form arrays of NWs on Si substrates. Using a proper reactive ion etching condition, the etching was selective to silicon. By decreasing the etching rate of silica from that of silicon, either nanowires or nanocones were obtained. To fabricate silicon NW arrays, substrates with a monolayer of silica were placed in a 13.56 MHz Trion reactive ion etcher. Various reacting mixtures were introduced. The shape and depth of the NWs were controlled by changing the RIE process conditions. The etch selectivity between the silica masks and silicon was achieved using O_2:SF_6 plasma that is highly oxidizing. In order to study the effect of gas flow rates on array formation in the etching process, a mixture of O_2:SF_6 with a flow rate of 20:5 (sccm), at a total pressure of 10 mTorr and self-bias voltage of 50v was used. Structures and dimensions of the NW arrays were studied by SEM. It was observed that a high ratio of O_2:SF_6 results in good anisotropy. However, NWs appear after an etching cycle of 700s, which is an indication of a fairly low etching rate (Fig. 4.4.a). NWs were realized by further etching. Fig 4.4.b shows 600nm pillars obtained after a 1600s etching cycle. The ratio of $O_{2:}SF_6$ is important for selective etching of silicon. Increasing the O_2 is a trade-off between anisotropy and silica nanosphere etching.

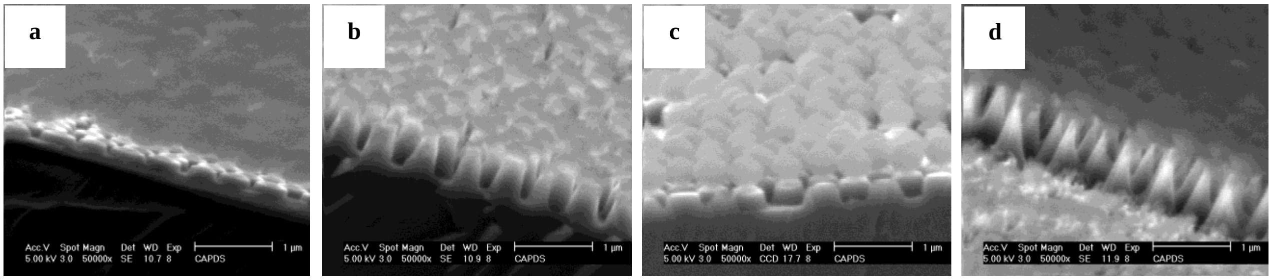

Figure 4.4 NW arrays formed at O_2:SF_6 plasma with flow rate of 20:5 (sccm) for a) 700s and b) 1600s, NW etched at O_2:SF_6 with floe rate of 10:5 (sccm) for c) 200s and d) 1000s respectively.

In the next etching process, a mixture of O_2:SF_6 with flow rate of 10:5 (sccm) using the same plasma parameters, was introduced. The etch rate increased with respect to the previous process. NWs start to appear after 200s of etching by using a lower ratio of O_2/SF_6 (see Fig. 4.4.c). The effect of an etching cycle on array formation can also be observed in Fig. 4.4.d. As the etching time increases from 200s to 1000s the structure turns to a conic-like structure due to the fact that the silica particles etch over time fail

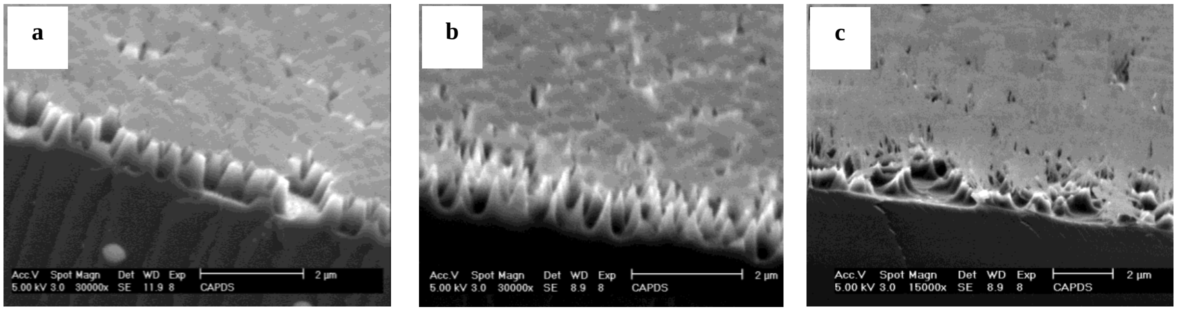

Figure 4.5 NW arrays formed at O_2:SF_6 plasma with the gas flow rate of 10:5 (sccm) at total pressure of 10mTorr under self-bias voltage of a) 50V, b) 100V and c) 200V

to effectively mask the silicon. The effect of self-bias voltage on the array formation was also examined. Increase in self-bias voltage results in etching of the oxides or silicon fluoride oxide compounds (SiO_xF_y) deposited on the sidewalls during the etching cycle. Increased ion bombardment leads to isotropic etching and formation of nanocone structures. Fig. 4.5.a,b compares two structures after 400s of etching at O_2:SF_6 plasma with the gas flow rate of 10:5 (sccm) at a total pressure of 10mTorr under a self-bias voltage of 50V and 100V respectively. A self-bias voltage of 200V high etching rate results in undesired structures.

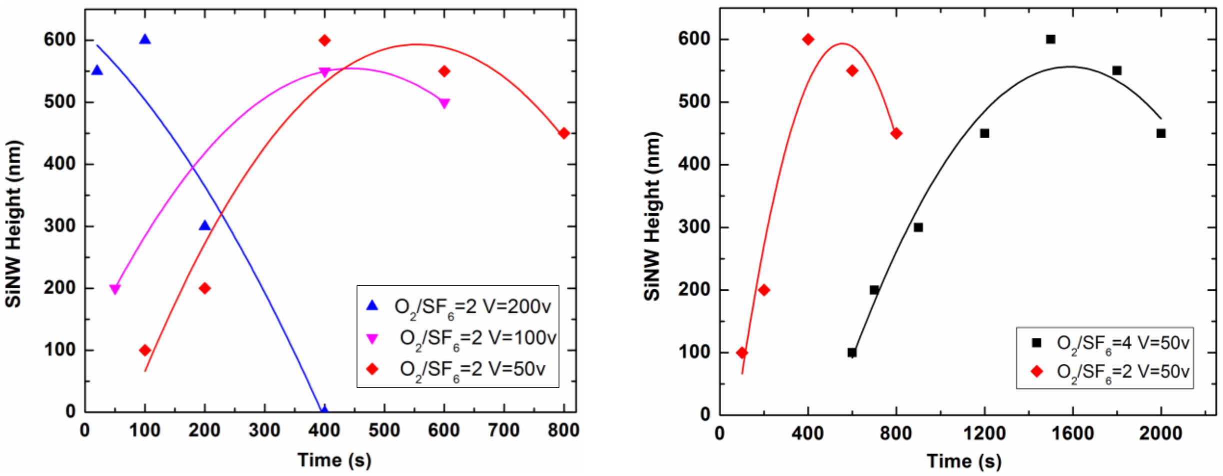

(a)

(b)

Figure 4.6 Effects of the a) self-bias voltages and b) O_2/SF_6 flux ratio on SiNW height

The effects of gas flow rates and self-bias voltage on array formation was summarized in the plot shown in Fig 4.6. High aspect ratio NW arrays with a low risk of silica etching rate can be formed at an optimum O_2/SF_6 flux ratio, self-bias voltage, plasma pressure and etching time. At a constant O_2/SF_6 flux ratio, the NW structures form quickly when higher self-bias voltages are being used, at a risk of etching of the passivation layer deposited on the sidewalls during the etching process which leads to formation of nanocones in a short etching cycle (see Fig. 4.6.a). At a constant self-bias voltage, the NW structures were arranged quickly by using lower O_2/SF_6 flux ratios (see Fig. 4.6.b).

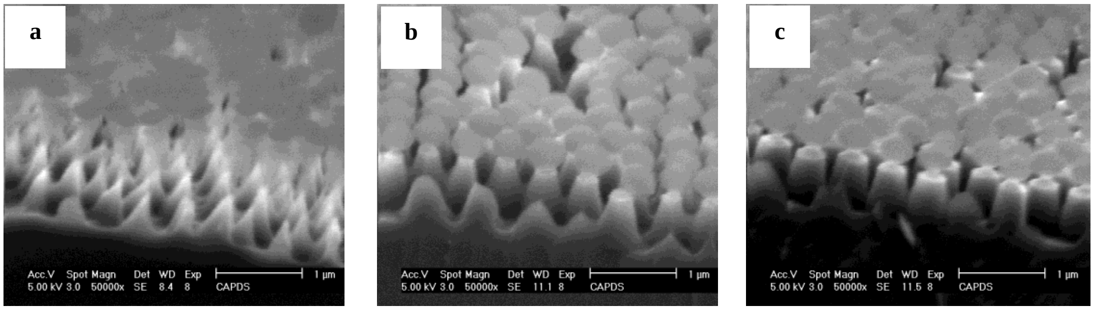

Figure 4.7 NWs formed at O_2:SF_6 plasma with the gas flow rate of 10:5 (sccm) at self-bias voltage of 50V at total pressure of a) 20 mTorr, b) 10 mTorr and c) 5 mTorr

To examine the effect of plasma pressure on the shape of the NWs, a mixture of O_2:SF_6 with the flow rate of 10:5 (sccm) and the self-bias voltage of 50V was used, at a total pressure of 20mTorr. As demonstrated in Fig. 4.7.a, the etching capability is high at this plasma condition and leads to nanocone structures. Tapered Si NW arrays were obtained by decreasing the pressure to 10mTorr (see Fig. 4.7.b). As shown in Fig 4.7.c, wires with vertical sidewalls are the result of etching at a pressure of 5mTorr. Effect of plasma pressure on the shape of the arrays has been demonstrated in Fig. 4.8. It was observed that at a fixed self-bias voltage and O_2/SF_6 flux ratio, NW arrays with vertical sidewalls were obtained at lower pressures.

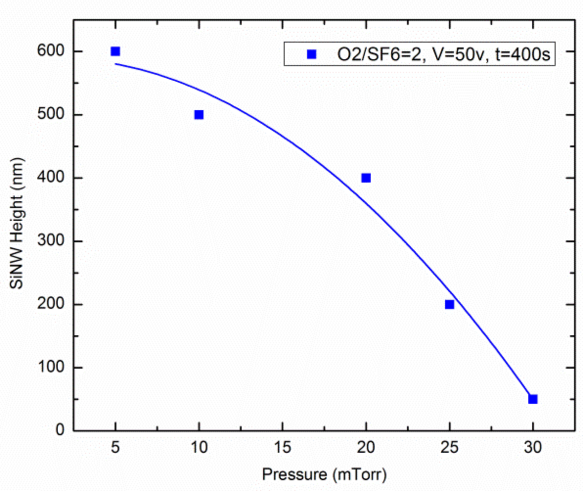

Figure 4.8 Effect of plasma pressure on the height of the SiNWs

The SEM images in Fig. 4.9 show structures, resulting from those shown in Fig. 4.7, after dissolving silica nanoparticles in a 2% hydrofluoric acid aqueous solution. Wires were also cleaned in a 50% hydrochloric acid aqueous solution in order to remove RIE damages from the sidewalls. The preservation of the ordering and the interparticle distance of the templating silica monolayer are apparent for the resulting NW arrays. Shallow dimples are formed on the top surfaces of the wires due to the shrinkage of the silica nanoparticles during prolonged etching. This makes the silica particles small protecting the silicon underneath from being etched. The silicon NW arrays were dark, and no angle-dependent diffraction was observed as the periodicity of the NW arrays is much smaller than the wavelength of visible light. The reflectance properties of the fabricated array structure and the process flow for radial p-n junction array cell fabrication will be dicussed in Chapter 5.

4.5 Conclusions

A simplified method using nanosphere lithography and a top-down approach for NW array formation was presented. A spin coating condition was developed to form ordered arrays of amino-functionalized silica nanospheres on silicon substrate to use as a template for Si etching. The effect of plasma parameters, on

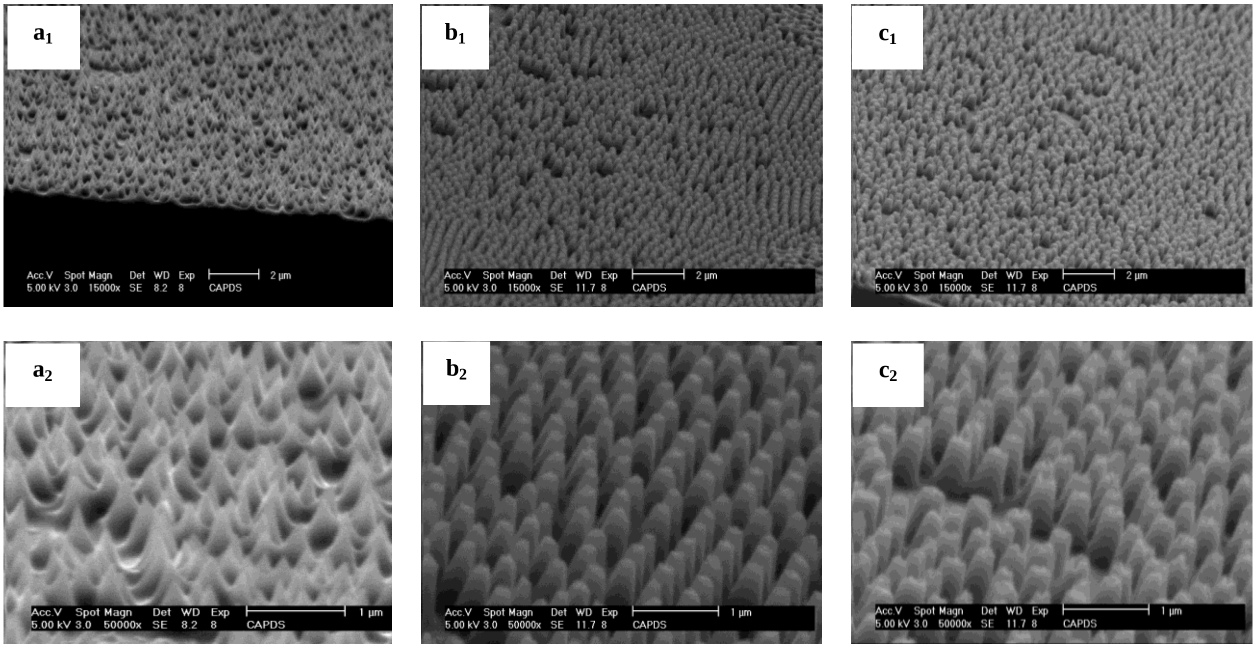

Figure 4.9 SEM and zoomed-in images of (a_1, a_2) conic, (b_1, b_2) tapered and (c_1, c_2) vertical arrays of NWs after nanosphere removal

the shape and the size of the wire arrays, was discussed. SiNW arrays, with vertical sidewalls, were obtained in a plasma etching process with O_2:SF_6 gas mixture with ratio of 2:1, low self-bias voltage of 50V and low pressure of 5mTorr. This method enables large-scale production of periodic nanowires that can be utilized for SiNW-based solar cell fabrication.

Chapter 5

Radial p-n Junction SiNW Solar Cells: Modelling and Fabrication

This chapter demonstrates the feasibility of the fabrication of radial junction silicon solar cells using Si nanowire (SiNW) arrays formed by Reactive Ion Etching (RIE) on Si substrate. Two approaches for fabrication of PV devices with radial p-n junction were used. In the first approach rectifying p-n junctions were obtained by combining maskless RIE etching and thin film deposition for junction formation. In the second approach the NW array cells were fabricated using microsphere lithography, etching and a diffused emitter. Models have been developed in COMSOL multiphysics CAD simulation software for a single core-shell wire with specified geometries in the text for each of the architectures.

For simulation, a core-shell nanowire with a radial p-n junction, p silicon core and hydrogenated amorphous silicon (n^+ *a-Si:H*) shell were studied. These assumptions are made based on the materials used for fabrication of the first architecture. Dark IV characteristics, distribution of the space charge density and electric field in the SiNW core as well as normal electric field distribution in the shell region at reverse bias were analyzed for the first architecture. The simulation results confirm that at shell doping concentrations[2] of $N_D > 10^{17}$ cm^{-3}, the wire is fully depleted with the highest space charge density at doping levels $N_D=10^{20}$ cm^{-3}. At $N_D=10^{20}$ cm$^{-3,}$ the wire offers better rectifying behavior due to the maximized electric field in the depletion region that results in the faster separation of generated electron-hole pairs. We also observed that at dopant concentration[3] of $N_A=10^{15}$ cm^{-3} and $N_D=10^{20}$ cm^{-3}, respectively for the p and n regions, no difference in electric field was observed under the dark measurement condition for the core-shell single wire either embedded in the aluminum doped zinc oxide (AZO) layer or having contact with AZO from the top.

The experimental results reveal that the emitter is not a perfect crystal. Optical characteristics of the AZO anti-reflection coating layer (ARC) were also studied. Furthermore, dependency of the cell performance characteristics to the wire length and shell/TCO thicknesses was examined. The poor performance of the SiNW array cells can be attributed to the poor transparency and conductivity of the shell and top contact layers and further optimizations is required.

To study the second architecture with a core-shell structure by simulation, the core and shell are assumed to be crystalline, due to the technique used for fabrication. Variation of electric potential

---

[2] N_D n region dopant concentration

[3] N_A p region dopant concentration

distribution along the wire at different bias voltages was studied. Depletion region depth variation at different bias voltages, different doping levels of the p-type core region and different doping levels of the n-type shell regions were also examined. The simulation results demonstrated that, by tuning the doping parameters in the p and n regions of the p-n junction, somehow the structure will be designed to have quasi-neutral region in the wire; or a fully depleted wire will be made to benefit from the high electric field across the radial p-n junction.

The fabricated NW array cell structures show relatively high current density (J_{sc}), which is attributed to enhancement of light trapping in NW arrays. The low open circuit voltage (V_{oc}) of the cell is due to the increase in junction area and the resulted high surface recombination rate. An AZO layer was used as passivation and top electrode contact. The poor fill factor of the device can be associated with significant series resistance at the junction which can be reduced using a highly conductive transparent oxide (TCO) layer.

5.1 Modelling and Analysis of Radial p-n Junction Solar Cells

5.1.1 Architecture 1: Radial Junction Cell with Crystalline Core and Amorphous Shell

A single SiNW with radial p-n junction was simulated with a model, developed in the COMSOL 3.5a multiphysics program, in order to study the electric potential distribution along the core-shell NW at different bias voltages. Distribution of space charge density and electric field in the nanowire core, at reverse bias for different levels of doping in the shell region, were inspected in order to better understand when the wire becomes fully depleted. The dark IV characteristics of the device were also examined. This work also investigates the effect of conformal and non-conformal patterns of contact with n-region.

Nanowire Geometry

The software is capable of solving semiconductor drift/diffusion carrier transports differential equations in 3D cylindrical polar coordinates. The structure is defined as a silicon cylindrical NW stand on a Si substrate with radius of 50nm and height of 1µm. The interior core of the NW is considered to be p-type. A 50nm thick layer of n^+ *a*-Si:H forms the exterior shell of the NW. The two and three dimensional core-shell nanowire's geometry appears in Fig. 5.1.

The large dynamic range, of the carrier concentrations, and the geometry make the numerical simulation of the semiconductor equations a difficult task; and especially, the entire range changes in the vicinity of the junction. Therefore the mesh is selected quite carefully; otherwise the solution process might not converge or could give inaccurate results. So, the mesh is made denser around the junction and at the cathode and anode (see Fig. 5.2). A suitable solver is also chosen to obtain additional accuracy.

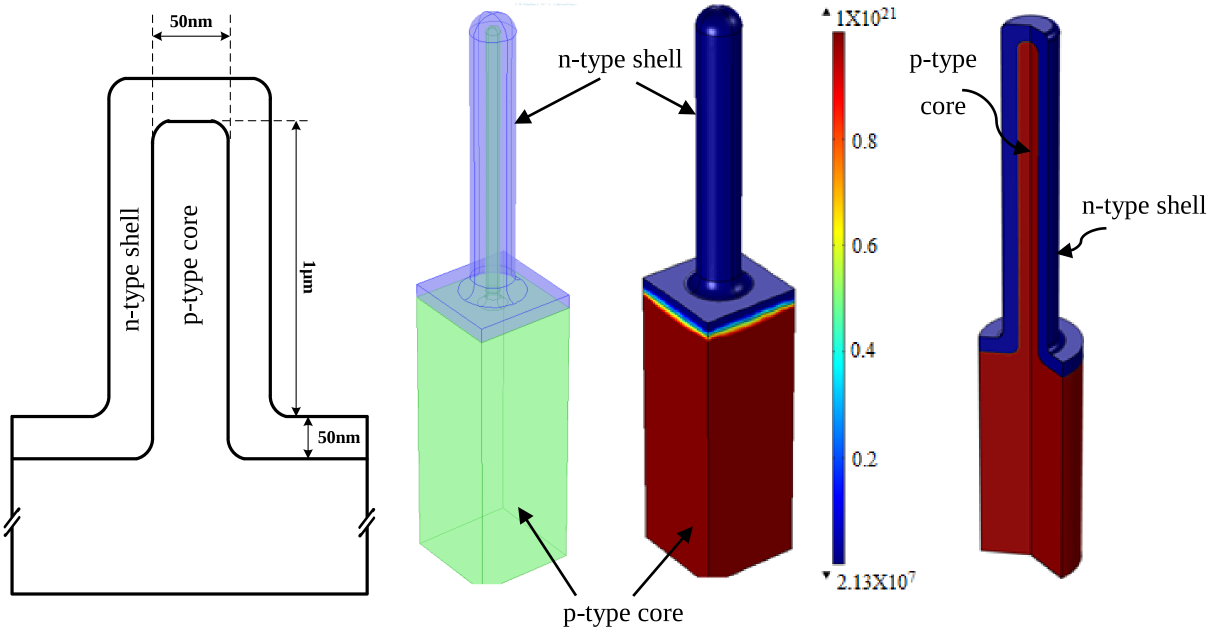

(a) (b) (c) (d)

Figure 5.1 a) 2D cross section view of a core-shell NW, b and c) 3D geometrical structure of a single core-shell wire stands on a silicon substrate, c) 3D cross section view of a core-shell wire

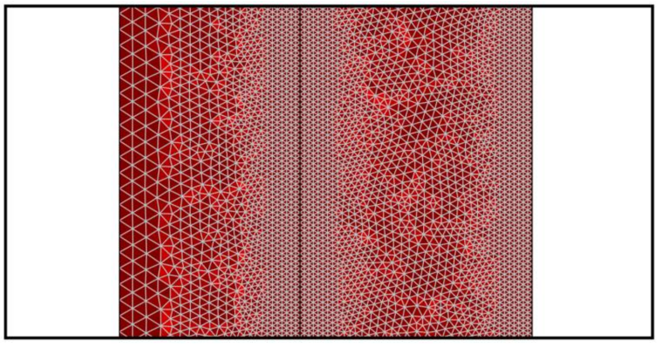

Figure 5.2 Dense mesh at the junction and the cathode/anode

Material Properties

The key material properties used in the model are summarized in table 5.1. The material properties are set according to the thickness of each layer. Mobilities, diffusivities, and carrier lifetime often depend on parameters such as doping, temperature, and recombination centres. Therefore, the proper adjustment was done based on the condition. The mobility or other parameters were changed according to the dopant concentration. The electron mobility is higher than the hole mobility but since in the shell region the dopant concentration is much higher than the core region, it causes very low mobility in the shell region. Doping concentration profile is considered to be constant with distance from the surface, due to the fabrication method used, therefore the junction is assumed to be abrupt. To compute an accurate value of

1.602×10^{-19} [C]	Elementary charge
300 [K]	Room temperature
1.38E-23 [J/K]	Boltzmann constant
11.8	Relative permittivity of a-Si
1.56e10 [cm^{-3}]	Intrinsic concentration of a-Si
1 [$cm^2/(V.s)$]	Electron mobility of a-Si
1 [$cm^2/(V.s)$]	Hole mobility of a-Si
$(K.T/q)\times\mu_n$	Electron diffusivity
$(K.T/q)\times\mu_p$	Hole diffusivity
0.1 [µs]	Electron lifetime
0.1 [µs]	Hole lifetime
1×10^{15} [cm^{-3}]	Acceptor Concentration
1×10^{20} [cm^{-3}]	Donor Concentration

Table 5. 1 Key material properties used in the model.

the current, weak constraints are used for the contact boundary conditions. In order to do that, Lagrange multipliers are introduced on the anode and cathode contacts. Trap density is assumed to be the same throughout the material. The depletion approximation is assumed to be valid. Recombination is assumed to be purely due to Shockley-Read-Hall (SRH) recombination; other recombination processes such as Auger recombination were ignored. Variation of the electric potential distribution along the core-shell nanowire at bias voltages of V_b=-1V, V_b=0V and V_b=1V is shown in Fig. 5.3, where the carrier concentration in the NW is assumed to be 10^{15}cm^{-3} and 10^{20}cm-^{3} in the p and n region respectively.

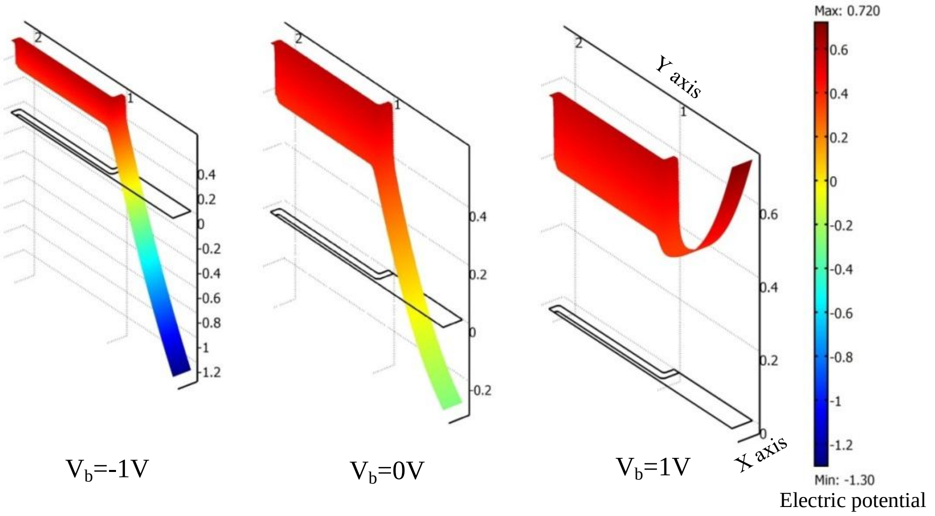

V_b=-1V V_b=0V V_b=1V

Figure 5.3 Electric potential distribution along the core-shell nanowire with N_A=10^{15} cm^{-3} and N_D=10^{20} cm^{-3} at different bias voltages: V_b=-1V (left), V_b=0V (middle), V_b=1V (right)

Dark IV Characteristics

The dark IV characteristics for two wires with N_A=10^{15} cm^{-3} and n region dopant concentration of 10^{18} cm^{-3} and 10^{20} cm^{-3} are plotted in Fig. 5.4. The results show better rectifying behavior for the wire having a shell with higher dopant concentration.

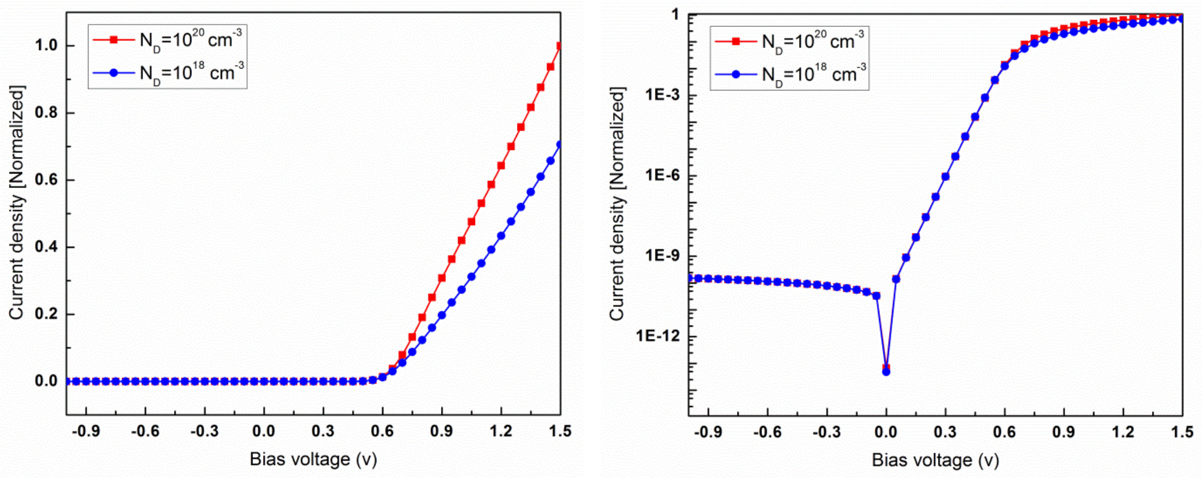

Figure 5.4 Dark I-V of core-shell wires for doping of N_D=10^{20} cm^{-3} and 10^{18} cm^{-3}, N_A=10^{15} cm^{-3}

Distribution of Space Charge Density in the Nanowire Core

The space charge density, in logarithmic scale across the core radial axis at V_{bias}= -1V and N_A=10^{15} cm^{-3} for two levels of doping of the n-region, N_D=10^{18} cm^{-3} and N_D=10^{20} cm^{-3}, is shown in Fig. 5.5.a. The results exhibit that the higher the n-region dopant concentration, the higher the space charges density, hence the higher the level of depletion in the wire. The results also show that the wire is fully depleted at n-region concentration higher than10^{17} cm^{-3} (see Fig. 5.5b).

Distribution of Electric Field in the Nanowire Core

Variation of electric field in logarithmic scale in the nanowire core (at the centre of the wire length), for a shell region doping level of N_D=10^{20} cm^{-3} and N_D=10^{18} cm^{-3} is shown in Fig. 5.6.a. The results indicate that at a constant bias voltage and doping level of p-region of -1V and 10^{15} cm^{-3} respectively, a higher n region doping level results in a higher magnitude of electric field in the depletion region, that leads to faster separation/collection of generated electron-hole pairs (see Fig. 5.6.b).

Normal Electric Field Distribution in Shell Region

Fig. 5.7 presents the normal electric field distribution in the shell region at reverse bias voltage for core-shell SiNW cells embedded in TCO; and for the one having contact with TCO from the top. The results indicate that at a doping level of N_D=10^{20} cm^{-3} and N_A=10^{15} cm^{-3}, for n and p region respectively, no

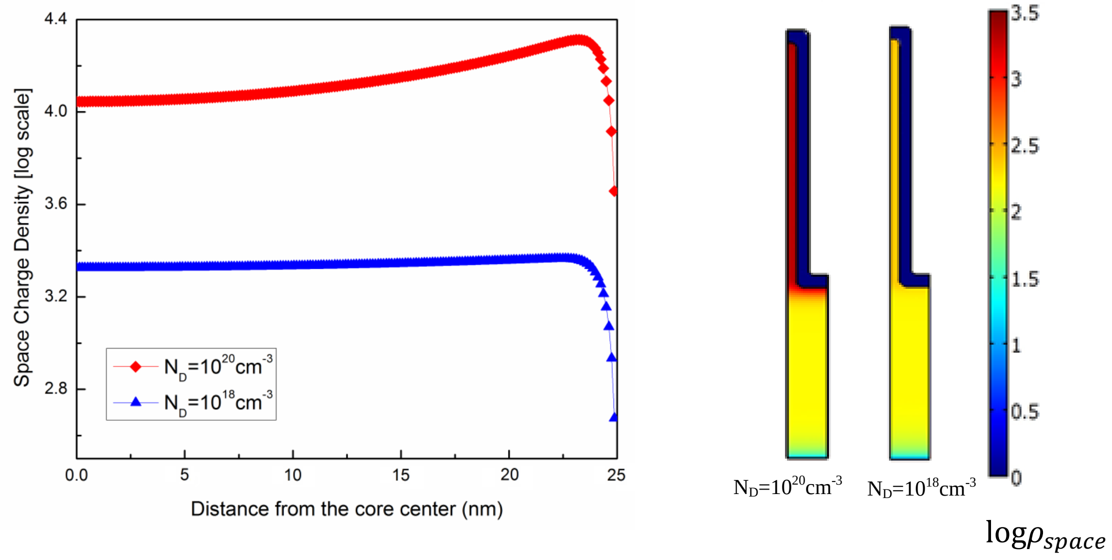

(a) (b)

Figure 5.5 a) Variation of space charge density across the core radial axis at V_{bias}= -1v and $N_A=10^{15}$ cm^{-3} for two levels of doping in shell region; $N_D=10^{20}$ cm^{-3}, $N_D=10^{18}$ cm^{-3}, b) fully depleted wires at $N_D=10^{20}$ cm^{-3}, $N_D=10^{18}$ cm^{-3}.

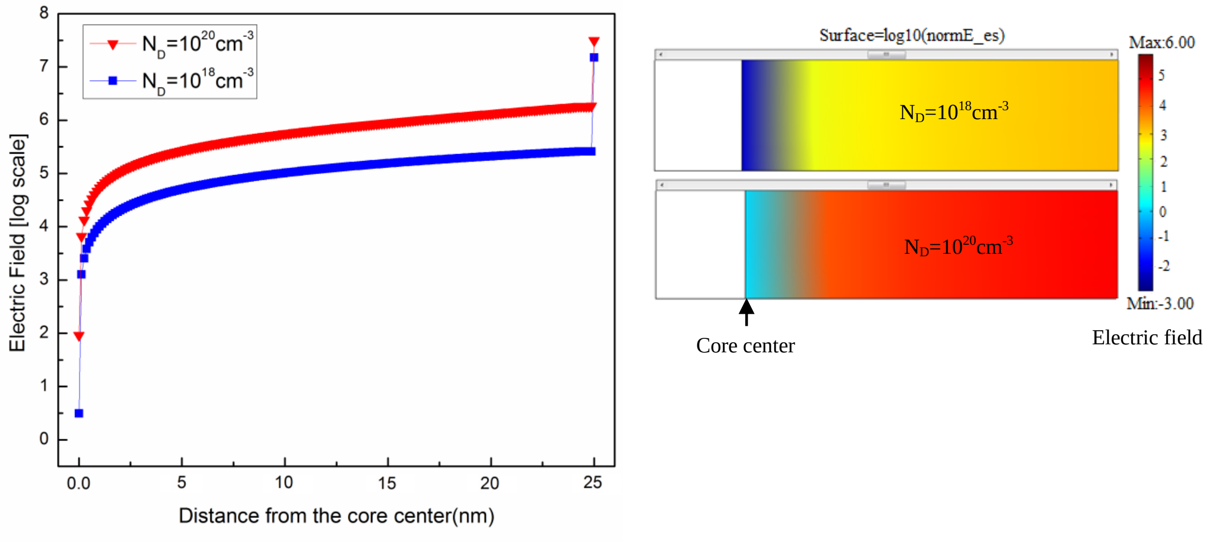

(a) (b)

Figure 5.6 a) Variation of electric field in the nanowire core at V_{bias}= -1v and $N_A=10^{15}$ cm^{-3} for different level of doping in shell region; $N_D=10^{20}$ cm^{-3}, $N_D=10^{18}$ cm^{-3}, b) Electric Field across the core radial axis for doping of $N_D=10^{20}$ cm^{-3} and 10^{18} cm^{-3}

difference is observed in the electric field distribution across the shell region for the core-shell structures with conformal and non-conformal contacts under dark measurement condition.

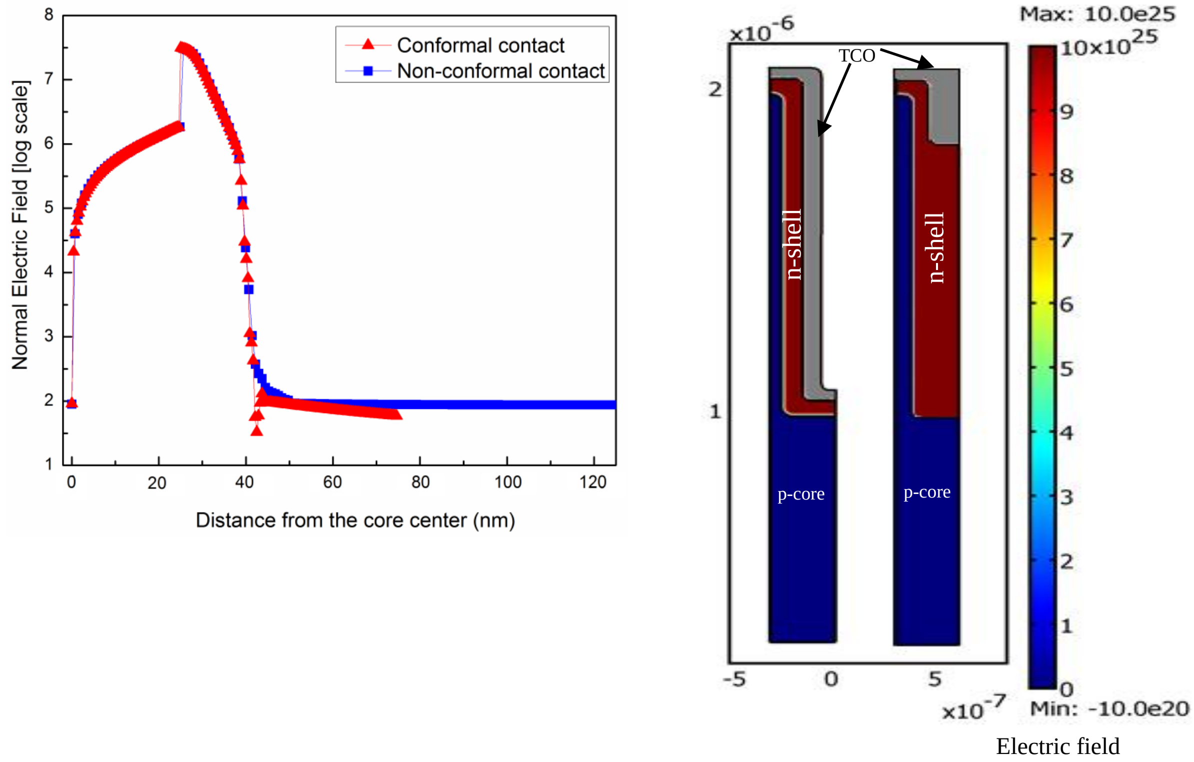

(a) (b)

Figure 5.7 a) Normal electric field distribution in shell region at V_{bias}= -1v, for doping of $N_D=10^{20}$cm^{-3} and 10^{18} cm^{-3}, $N_A=10^{15}$ cm^{-3} for the core-shell structures with conformal and non-conformal contacts, b) no difference in the electric field distribution for the core-shell wires embedded in TCO or having contact with the TCO from top in dark

If the problem associated with the NW could be solved with a thicker amorphous shell, better collection efficiency through the conformal contacts might be achieved, because there is more of a chance for the carriers to become recombined when travelling in a thicker amorphous layer.

5.1.2 Architecture 2: Radial p-n Junction Solar Cell with Diffused Emitter

A single SiNW was simulated with the COMSOL program; in order to verify the electric potential distribution along the NW, examine the depletion region depth variation at different bias voltages, as well as the depletion region depth variation at different doping levels of n and p regions. The conditions in which the wires become fully depleted were studied.

Nanowire Geometry

The structure is defined as a cylindrical single silicon NW stand on a Si substrate with radius of 300nm and height of 700nm. The interior "core" of the NW is considered as being p-type. An n^+ emitter is formed by phosphorous diffusion from an infinite dopant source thereby forming the exterior shell of the NW. The 2D and 3D core-shell nanowire's geometry appear in Fig. 5.8.

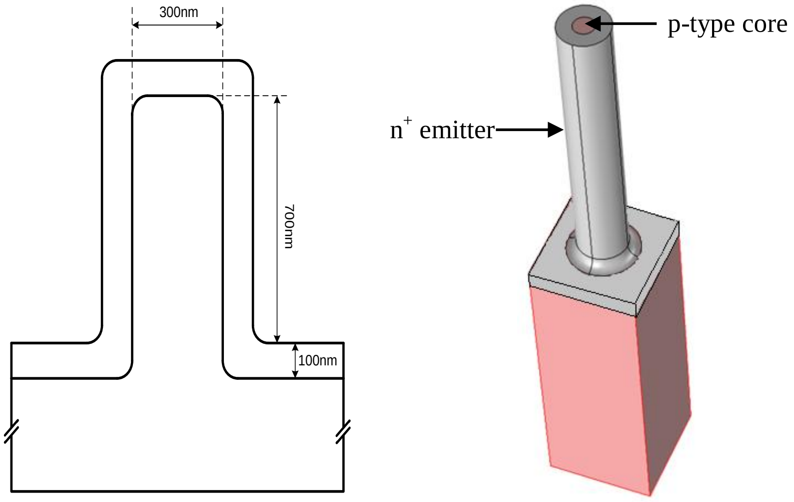

(a) (b)

Figure 5.8 a) 2D and b) 3D cross section view of the core-shell NW structure

Variation of Electric Potential Distribution along the Nanowire

All the assumptions include a constant trap density in the entire material. Depletion approximation and SHR recombination made in previous modelling are also valid in this model. The only difference here is the junction, which is not abrupt. Since diffusion was used for fabricating the junction, the doping profile was considered to change with distance from the surface. The crystalline silicon properties were used for both the core and emitter. Variation of the electric potential distribution along the nanowire at bias voltages of V_b=-1V, V_b=0V and V_b=1V is shown in Fig. 5.9; where the carrier concentration in the NW was assumed to be 10^{15} cm^{-3} and 10^{20} cm^{-3} in the p and n region respectively.

Depletion Region Depth Variation at Different Bias Voltages

Based on simulation results, at a constant doping level of 10^{15} cm^{-3} and 10^{20} cm^{-3} for p and n regions respectively. The depletion region depth was varied by changing the bias voltage. The depletion region thickness increases as the applied voltage decreases. The wire is fully depleted at a bias voltage equal to 0.6v (see Fig. 5.10).

Depletion Region Depth Variation with Different Doping Level of p-type Core Region

The depletion region depth variation with different doping levels of p-type core region was also examined. At a constant bias voltage and doping level of n region fixed at 0.6V and 10^{20} cm^{-3}

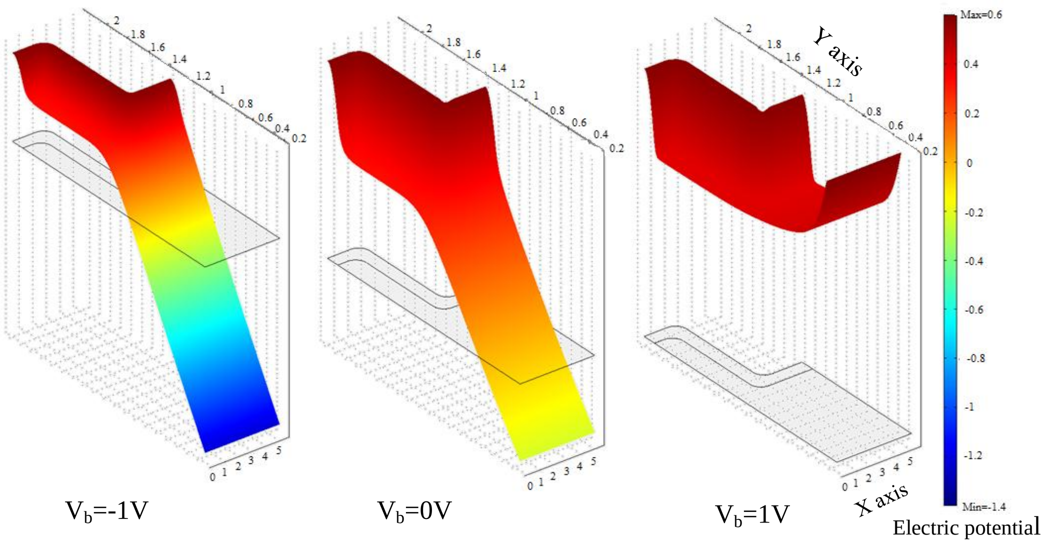

V_b=-1V V_b=0V V_b=1V

Figure 5.9 Variation of electric potential distribution along the nanowire with $N_A=10^{15}$ cm^{-3} and $N_D=10^{20}$ cm^{-3} at different bias voltages: V_b=-1V (left), V_b=0V (middle), V_b=1V (right)

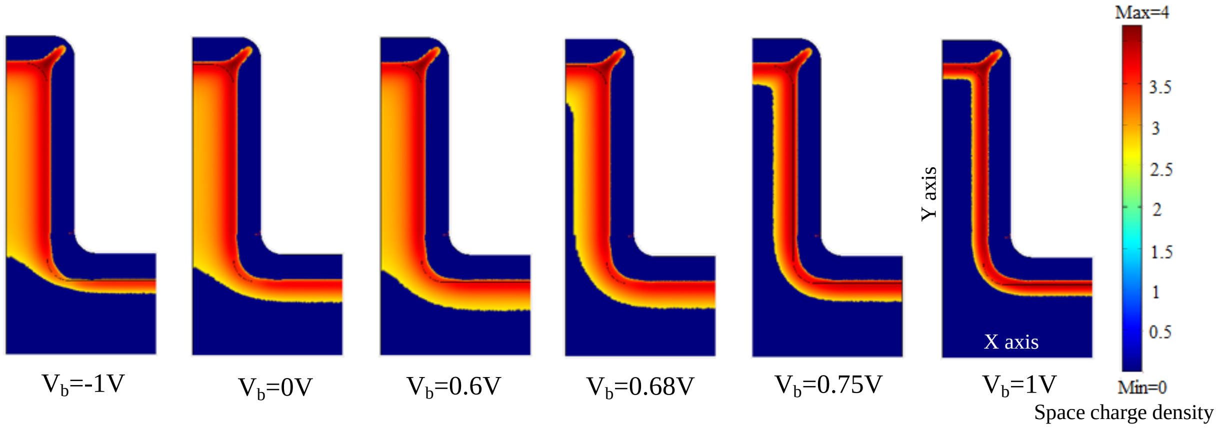

V_b=-1V V_b=0V V_b=0.6V V_b=0.68V V_b=0.75V V_b=1V

Figure 5.10 Depletion region depth variation at different bias voltages

respectively, the simulation results demonstrate that the NW becomes fully depleted by reducing the doping level of the core p-region as shown in Fig. 5.11. The wire is fully depleted at N_A equal to 10^{15}cm^{-3}.

Depletion Region Depth Variation with Different Doping Level of n-type Shell Region

The depletion region depth variation with different doping levels of n-type shell region was also inspected. As illustrated in Fig. 5.12, at a constant bias voltage and doping level of p region, fixed at 0.6 V and 10^{15} cm^{-3} respectively, the NW becomes fully depleted by increasing the doping level of the shell n type region. The wire is fully depleted at N_D equal to 10^{20} cm^{-3}.

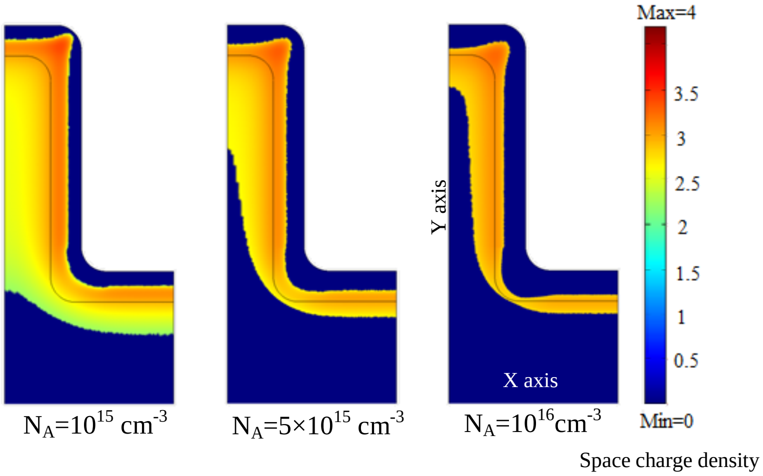

Figure 5.11 Depletion region depth variation with different doping levels of p-type core region at constant bias voltage (V_b=0.6V) and doping level of n-region (10^{20} cm^{-3}): $N_A=10^{15}$ cm^{-3} (left), $N_A= 5\times10^{15}$ cm^{-3} (middle), $N_A= 10^{16}$ cm^{-3} (right)

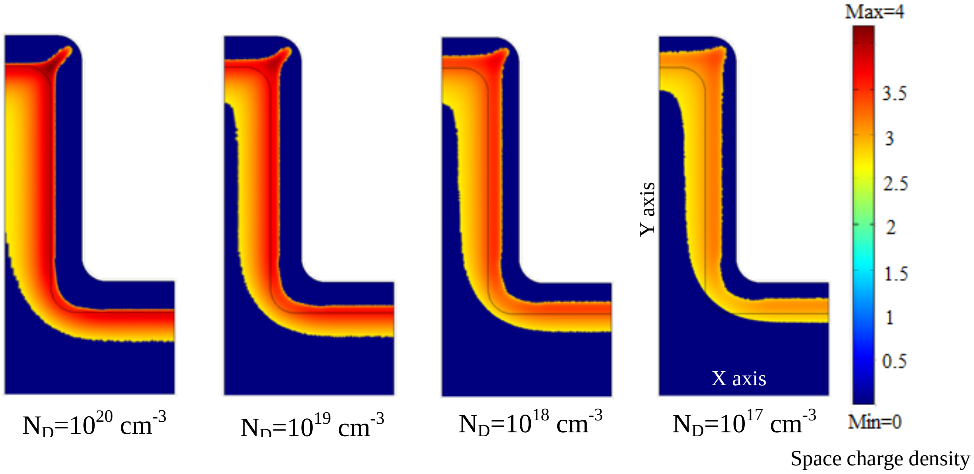

Figure 5.12 Depletion region depth variation with different doping levels of n-type shell region at constant self-bias voltage (V_b=0.6v) and doping level of p region (10^{15} cm^{-3}): $N_D=10^{20}$ cm^{-3}, $N_D=10^{19}$ cm^{-3}, $N_D=10^{18}$ cm^{-3}, $N_D=10^{17}$ cm^{-3}, left to right respectively

By controlling the doping level in both the n and p regions, the depletion region depth can be tuned to benefit from the high electric field of fully depleted wires, particularly for the wires with low trap densities in the depletion region. This means that the efficiency of a solar cell, with a radial p-n junction cell, can remain high despite a high quasi-neutral region trap density at the quasi neutral recombination regime; where the recombination in quasi neutral region is dominant. However, at depletion region recombination regime, having a fully depleted NW with low quality materials results in a significant drop in V_{OC}. NW radius should also be optimized such that it becomes approximately equal to the minority carrier diffusion length.

5.2 Demonstration of Experimental Feasibility: Architecture 1

5.2.1 Fabrication Methodology: from NW Formation to Device Fabrication

The radial junction solar cells fabricated in this study used p-type (1-2 Ωcm, $2X10^{16}$ cm^{-3}, <100>) Si wafers as the starting substrate. The wafers were wet cleaned and placed in the RIE chamber. The device studied consisted of uniform arrays of up-right Si NWs formed on silicon substrate by the maskless RIE technique, as described in Chapter 3. The carbon polymer formed on the surface of the wafer, as the etching process started; and the pattern was transferred to the silicon by reactive ion etching. The Si wires were formed by etching at 800v self-bias voltage and a CF_4 pressure of 10 mTorr at a flow rate of 25sccm. Fig. 5.13.a,b, exhibits SEM and TEM micrographs of the fabricated wires, respectively. Under these conditions, by controlling the time of the etching, up to 2 µm long vertically-oriented Si wire arrays can be formed, with an average wire diameter of 50nm, pitch of 200nm and good pattern integrity across the area of a 3inch wafer.

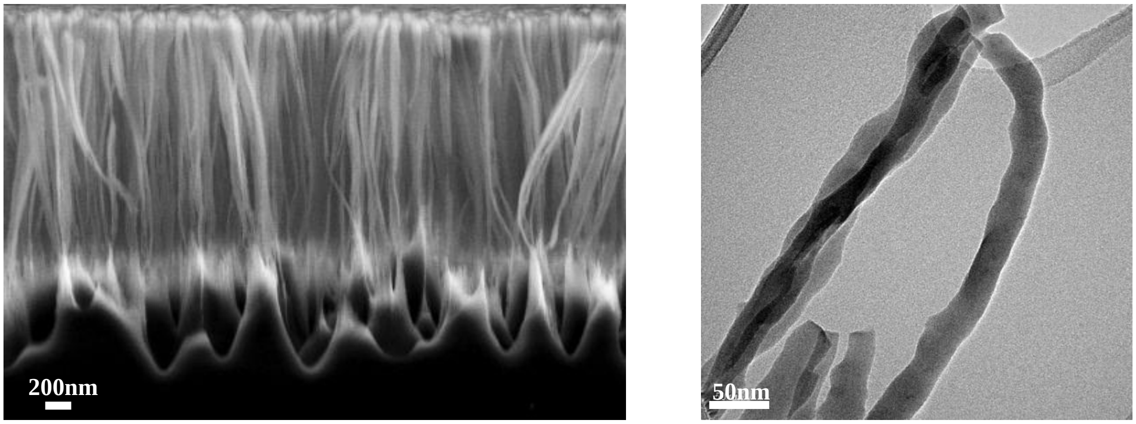

(a) (b)

Figure 5.13 . a) SEM image of the arrays of RIE etched Si wires and b) TEM image of the single wires

For the fabrication of the solar cell, it was essential to effectively remove RIE residue from the tips and sidewalls of the Si wires. The in-situ EDX data, in Fig. 5.14.a, demonstrates that carbonated compounds $(C\text{-}F)_n$ and silicon oxides were the residue components of the RIE process. The Si wire array samples were initially cleaned using a standard RCA process; and then etched with buffered oxide (BHF) and hydrochloric acid (HCL), for removal of the RIE residue. As shown in Fig. 5.14.b, although no residue was detected within EDX data this procedure damaged the wires. The broken wires are believed to be due to the fragile Si wires dipped in polar solutions. A gentle dry etching in SF_6:O_2 plasma was used, as discussed in Chapter 3. The EDX results confirm carbonated compounds etched away, to some degree, from the sidewalls and tips of the nanowires with this process; while the shape of the wires has been maintained (see Fig. 5.14.c). The XPS results previously presented, in Chapter 3, also describe the effect of cleaning processes on NW RIE damage removal.

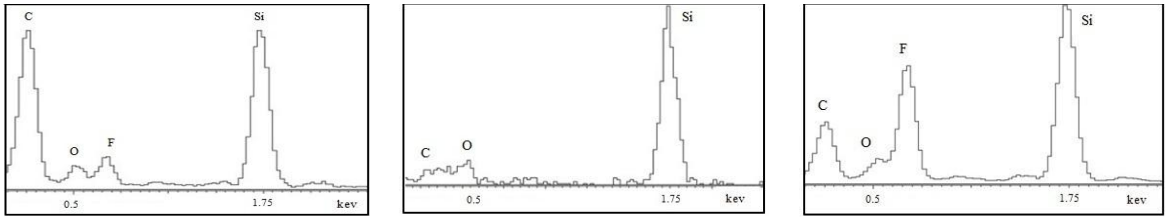

(a) (b) (c)

Figure 5.14 EDX spectrums: (a) as etched wires (b) wires after wet cleaning (c) wires after dry cleaning

The single crystalline nature of the nanowires is confirmed by HRTEM (see Fig. 5.15). HRTEM images and the diffraction patterns (insets), in Fig. 5.15.a and Fig. 5.15.b, are provided on the single wires before and after cleaning respectively. These results indicate that the RIE resulted amorphous layer, formed on the sidewall, is removed from the wires by cleaning (see Fig. 5.15.b). More single dots appeared on the diffraction pattern of the cleaned wire (the inset of Fig. 5.15.b) in comparison to the diffraction pattern of the as etched wire (the inset of Fig. 5.15.a). The extensive transmission electron microscopy studies done, showed that these NWs are single crystal, with different facets on the surface. Fig. 5.15.c demonstrates the zone axis areas where the facets cross. Fig. 5.15.d shows a wire after the cleaning step; and notably, abrupt atomic interfaces with the polycrystalline nature of the surface layer can be observed from the micrograph shown. Intensity variation is a result of the cross cutting of different crystalline planes and thickness variation across the nanostructure due to the circular nature of the wire. Sharp dots with rings on the diffraction pattern are also indications of the polycrystalline nature of the outer surface of the wires which were gently cleaned in a dry process (see the inset of Fig. 5.15.d).

5.2.2 Conformal Deposition of the Shell Layer on the Wires

Core-shell radial p-n junction was fabricated by conformal deposition of the PECVD n^+ *a*-Si:H layer on the fabricated p-SiNWs array. The plasma process conditions developed for growth of the quasi-crystalline n^+ *a*-Si:H layer on the crystalline silicon substrate were used to serve as the n^+ emitter layer [183]. The SiNWs were subjected to 10w plasma with a pressure of 400mTorr and the gas mixture of saline:phosphine:hydrogen (SiH_4:PH_3:H_2) gasses, at the flow rate of 20:8:250 (sccm) at 350 °C. In this experiment, only the Si wires and the area in between the wires were exposed to the phosphine gas. The back of the wafer was placed on the electrode and protected.

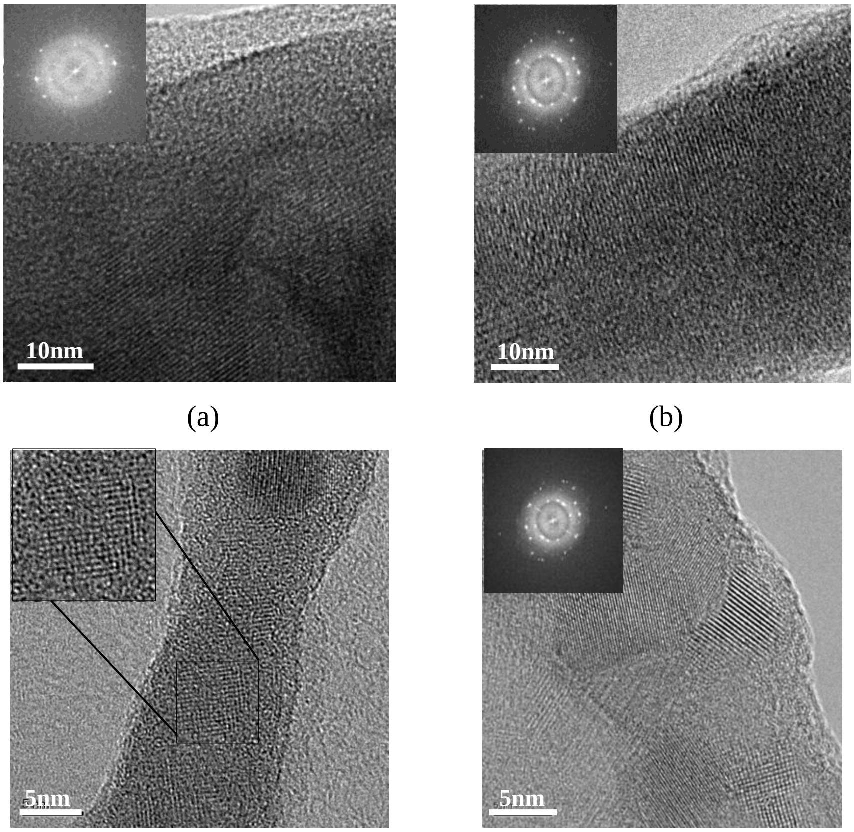

(a) (b)

(c) (d)

Figure 5.15 HRTEM image of a single NW a) before cleaning, b) after cleaning: Insets are diffraction patterns, c) NWs with zone axis areas on surface, d) cross cutting of different crystalline plane across the nanowire: Inset is diffraction pattern

Fig. 5.16.a shows the TEM image of the conformal n^+ *a*-Si:H film deposited on wire arrays. The TEM magnified image, shown in Fig. 5.16.b, exhibits a p-type NW core of 50 nm, coated with a 50nm n^+ *a*-Si:H shell, making the overall diameter about 100nm. The core and the shell part of the wire are hardly distinguishable from the contrast shown in this micrograph. Higher contrast for the crystalline core is expected. This effect can be attributed to the interaction of the electron beam with different crystalline planes present on the surface of the wire as well as the circular nature of the wire. The HRTEM images, as seen in Fig. 5.16.c-e, show the structure of the deposited film on the sidewalls of the wires, the conic-shape base of the wires and the space between the wires (pitches), respectively. The HRTEM image, in Fig. 5.16.c, indicates that the n^+ shell on the sidewalls is mainly amorphous. From a previous study, it was found that on the planar substrates formation of the quasi-crystalline layer, on crystalline substrate by

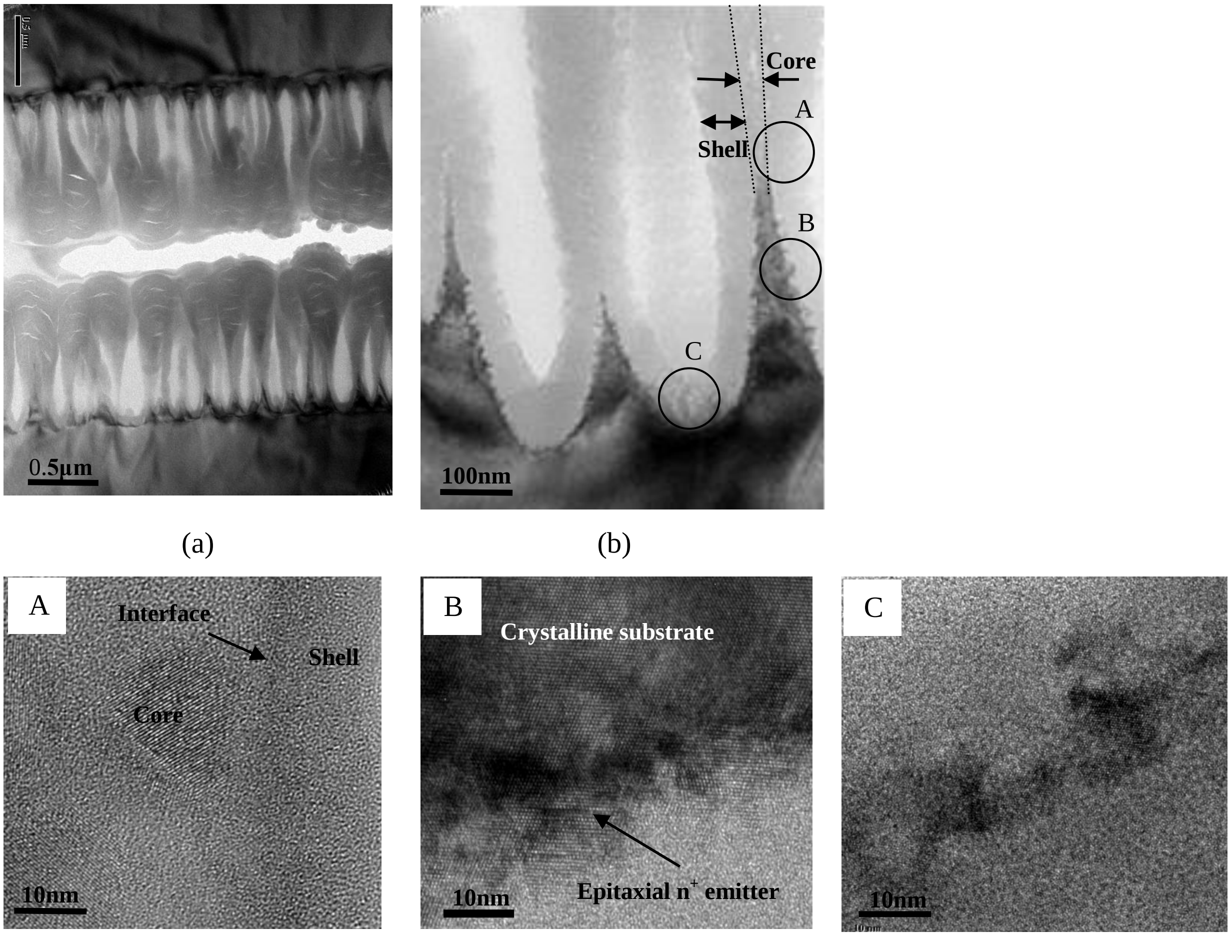

(a) (b)

(c) (d) (e)

Figure 5.16 a,b) TEM images of conformal n$^+$ a-Si:H film deposited on wire arrays. Structure of the deposited film on (c) wire's sidewall, (d) conic-shape base of the wire, (e) space between the wires

PECVD, has directional dependence [184]. Since the NWs have a circular nature with varying crystal orientations, the PECVD deposition on the cylindrical NWs, using the same conditions developed for the planar substrate, results in a loss of crystallinity on the deposited n$^+$ *a*-Si:H layer. The TRTEM image, in Fig. 5.16.d, clearly shows the crystalline conic part of the NWs, the interface and a 10nm quasi crystalline phase of the n$^+$ shell grown over the conic part of the NWs, with less crystal orientation variation. However, this crystalline phase turns to amorphous, as thickness increases, principally due to the plasma damage on the initial NW surface. The loss of the core crystal structure in some sites adds to loss in crystallinity over the large thickness. Fig. 5.16.e shows that the crystal structures continued through the n$^+$ *a*-Si:H layer in some sites, close to the planar substrate, producing a perfect core crystal structures layer, as appears in high contrast in this image.

Conformal deposition of the *n*$^+$*a*-Si:H layer with PECVD is a low temperature means for creating a p-n junction to the SiNWs array. The PECVD process also involves a compromise between ensuring conformality and reasonable quality of the n$^+$ film. To form the radial p-n junctions, two sets of core-shell NW structures, with different shell thicknesses, were fabricated. For the first set, the plasma was introduced to the wire arrays for 13 minutes and resulted in a 50nm conformal shell layer (see Fig. 5.17.a, b). For the second set, the plasma was introduced to the wires for 26min, double the time of the former process, which resulted in a thicker (about 100 nm) shell layer (see Fig. 5.17.c, d).

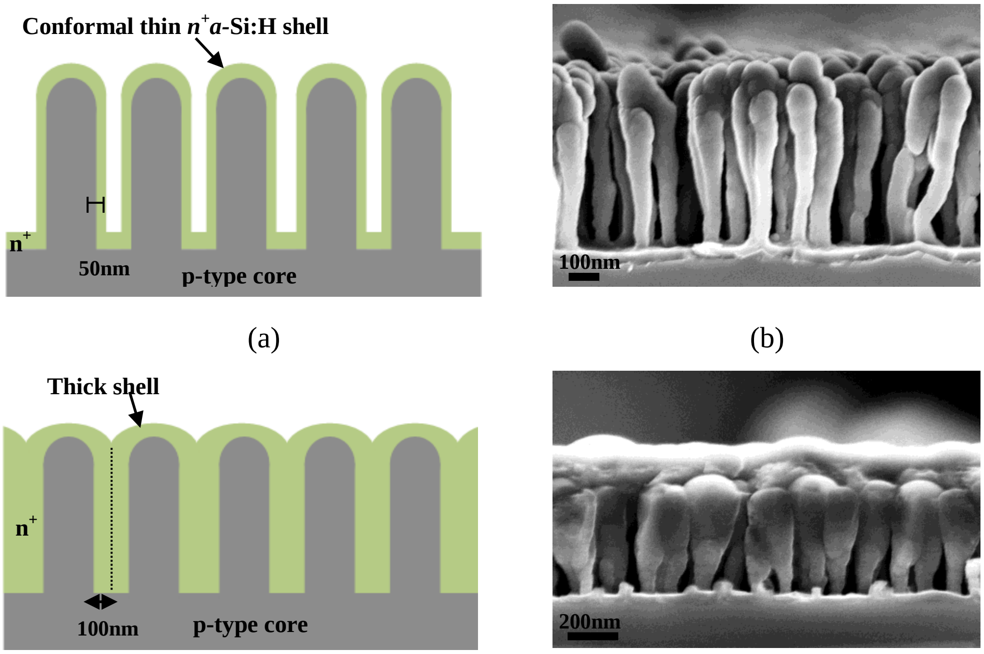

(a) (b)

(c) (d)

Figure 5.17 Conformal a) thin (50nm) b) thick (100nm) n^+ *a*-Si:H shell layer

The resulting NW includes a p-type core and a phosphorous-doped shell. The doping profile of control samples, prepared by growth of the n$^+$ *a*-Si:H layer on planar crystalline silicon substrate under the same plasma condition as used for the NWs, was prepared with the Spreading Resistance Profiling (SRP) technique. The doping concentrations were 10^{20} cm^{-3} for phosphorous-doped shell layer and $3X10^{15}$cm^{-3} for p-type substrate. The sheet resistance of the layer was measured, 60 Ω/□, using this technique (see Fig. 5.18). According to the TEM results, the layer is not crystalline for the NWs as it is for the planar sample, so the electronic properties will be different. In order to provide the doping profile of the NW p-n junction with more precision, other techniques have been proposed by other authors. Understanding the mobility, dopant concentration and dopant distribution will be critical for the fabrication of high performance devices based on nanowires [184- 186]. Determination of the radial dopant profile of individual silicon nanowire field-effect transistors using the capacitance–voltage (CV) technique was recently reported by Garnett et al. [146]. This technique has also been used to determine the mobility of nanowires [187- 190]. The Energy Dispersive X-ray Spectroscopy (EDS) and Electron Energy-Loss

Spectroscopy (EELS*)* are other well-known methods, as suggested by Kempa et al. [12] for the same purpose. These techniques can be applied to the samples and will be considered for future study.

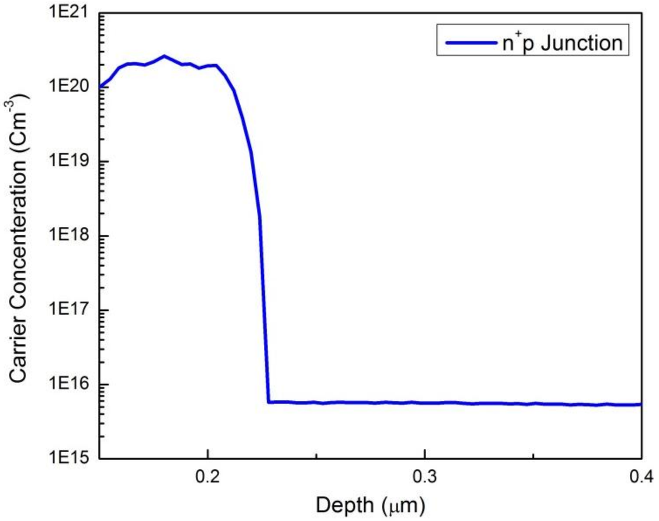

Figure 5.18 Doping profile of a planar p type crystalline substrate with a grown quasi-crystalline n$^+$ layer

5.2.3 Contact Formation

Following the shell formation, an AZO layer was sputtered in RF mode on the n-type region to passivate and planarize the wire structure and use as top contacts. The electrical and optical properties of the sputtered AZO film were optimized, following Minami et al. [191,192]. From the experimental and reported results it was found that the AZO films with low resistivity could be achieved in the low plasma pressure regime (P_{dep} <5 mTorr). Moreover, low ohmic AZO films were achieved without intentionally heating the substrates (T_s <100ºC). Also, it was found that the higher the temperature, the higher the transparency is and the lower the electrical conductivity.

The AZO layer used for the current device was deposited from 4inch ceramic ZnO:Al_2O_3 (2 wt.%) targets, in an RF sputtering chamber of a WLOS cluster sputtering system, with the base pressure of 1 X 10^{-6} mTorr at 100ºC, in a plasma power of 50w, plasma pressure of 2mTorr, substrate to target distance of 10cm, with argon as carrier gas with the flow rate of 10sccm. The deposition rate measured 5nm/min, using the same condition for forming the layer on control samples on silicon and glass substrates. The resulting non-planar SiNW cell structures are presented in the schematics and SEM images shown in Fig. 5.19. After an 80min deposition, under this plasma condition, the wires with a thin n$^+$ shell layer were coated with a conformal AZO layer and planarized (Fig. 5.19.a-c). The core and shell regions can be distinguished in the SEM image in Fig. 5.19.c. A 400nm AZO layer was also deposited on top of the wires with a thick n$^+$ shell layer (see Fig. 5.19.d-f). The top contact formation was completed by sputtering 1μm aluminum (Al) through a shadow mask which enabled low barrier contact to the AZO layer due to the high work function of Al. For the back contact, 1μm of Al was sputtered on the back side of the p-type substrate.

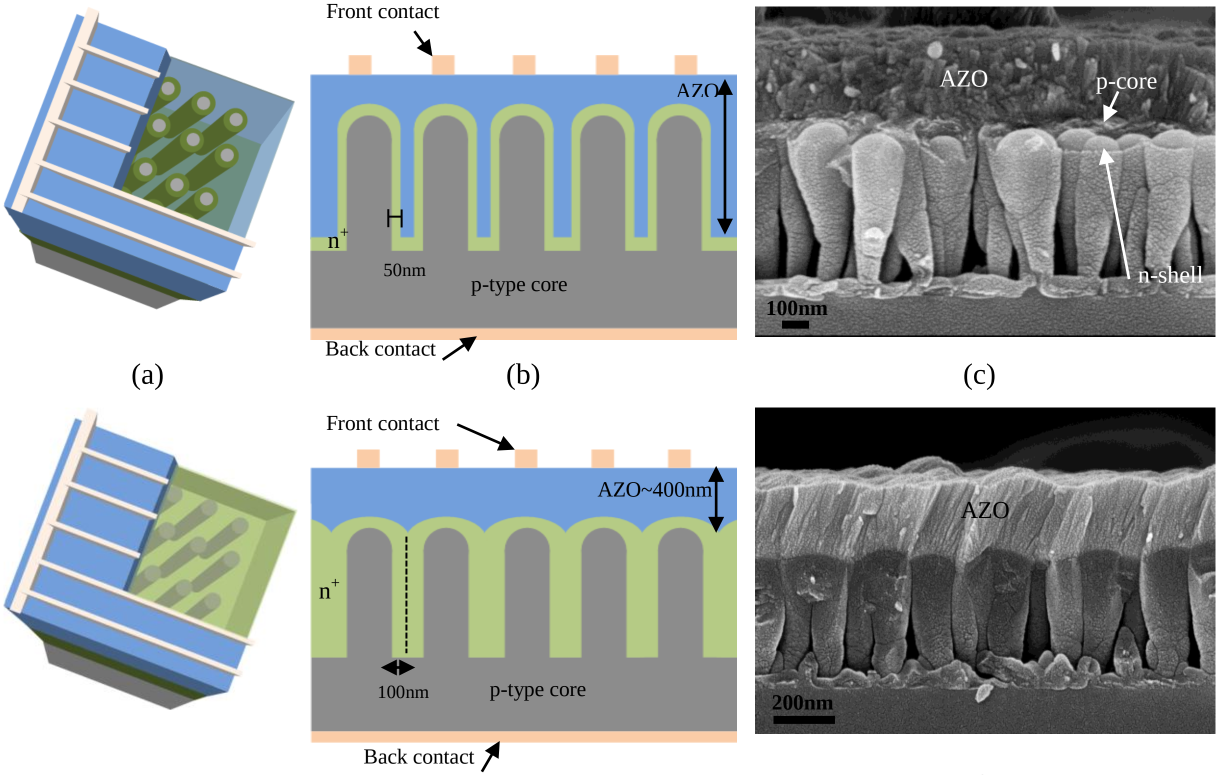

(a) (b) (c)

(d) (e) (f)

Figure 5.19 a)3D, b)2D schematics and c) SEM of the fabricated core-shell SiNW array cell with thin n$^+$ shell layer planarized with AZO, d)3D, e)2D schematics and f) SEM image of wires with thick n$^+$ shell layer and an AZO layer deposited on top

In situ, EDX analysis was performed on different parts of the resulting cell structure, to be sure of the composition of each layer. The result, in Fig. 5.20.a, exhibits that zinc (Zn), Al, oxygen (O) and carbon (C) were detected for the layer that deposited on the top which is the indication of the AZO layer. Al is observable from the EDX of AZO layer. Si is the main component of the shell layer. The existence of tiny percentages of zinc and oxygen is an indication of conformal coverage of the AZO over the shell layer (see Fig 5.20.b). Si is the only component detected in the core, which was expected (see Fig. 5.20.c).

5.2.4 Optical Characteristics of the Fabricated Cell

Optical reflectance and transmittance of the layers were recorded using a Lambda 1050 UV/VIS double beam spectrometer with an integrating sphere, as shown in Fig. 5.21. Reflectivity of about 20% from arrays of 1μm long nanowires, covered with a 50nm n$^+$ layer and subsequently planarized with the AZO

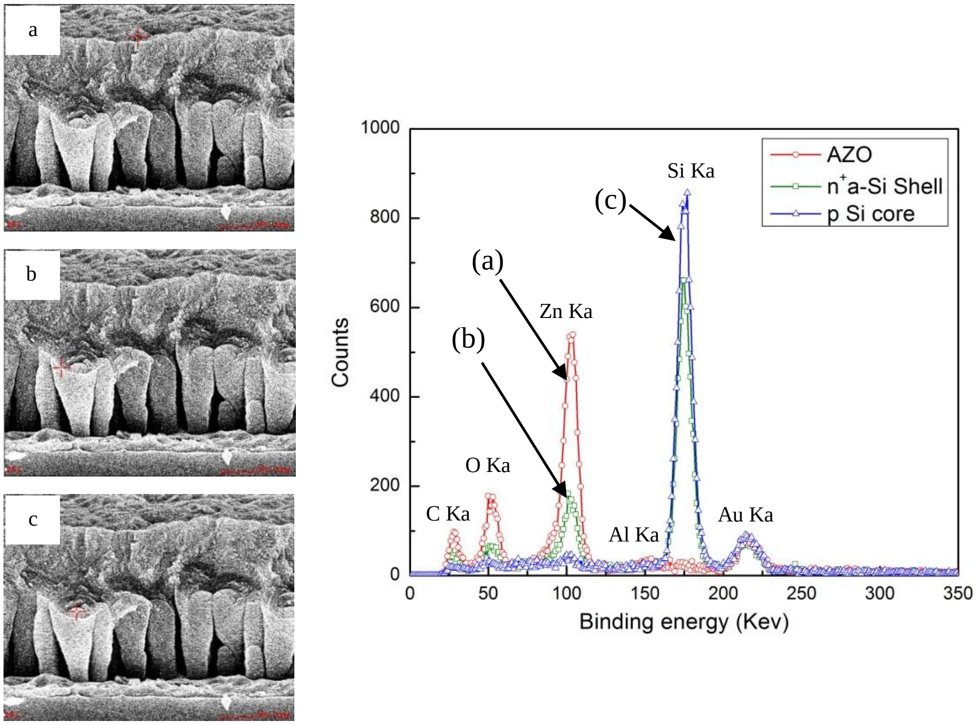

Figure 5.20 EDX analysis on the a) top, b) shell, c) core parts of the fabricated non-planar cell structure

film, was observed. The total thickness of the AZO layer has been estimated as ~400nm (see Fig. 5.19.d). The reflection spectra of the complete cell structure show interference patterns (maxima/minima), because the light passes through different layers, particularly the AZO layer, which is relatively thick. This observation suggests that nanowire array cells potentially reduce the light reflectance. However, the quality and thickness of each layer play a major role in the final reflectance results.

For solar cell applications an AZO transparency of ~83% is needed for visible light. The layer is only 65% transparent in this range for the 50nm n^+ *a*-Si:H/400nm AZO bilayer; and 45% transparent for the 100nm n^+ *a*-Si:H/400nm AZO bilayer. It is even poorer in the blue range of the spectrum. The layer for solar cell applications needs to be optimized. The resistivity, of a 400nm AZO control sample, measured 12 Ω/□.

5.2.5 Dependence of Photocurrent on Shell Thickness

To further examine the effect of geometric configuration of the nanowires on the overall conversion efficiency, devices with thin (50nm) and thick (100nm) n^+ *a*-Si:H shell layers, controlled by the deposition time of the PECVD n^+ *a*-Si:H layer, were fabricated and carefully characterized while maintaining the same overall p core length of 500nm (see Fig. 5.19). The external quantum efficacies

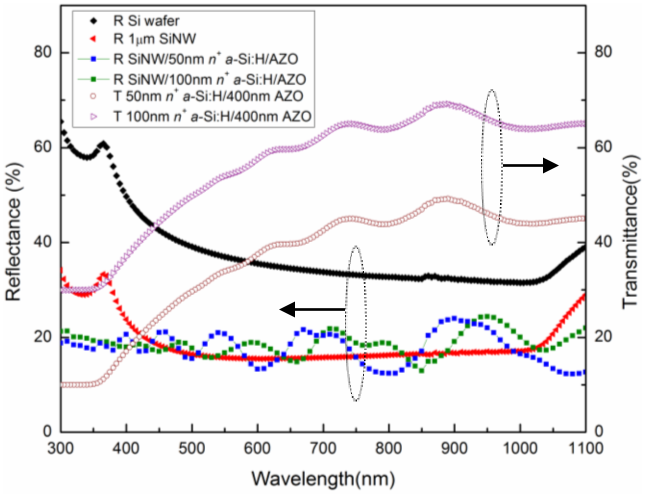

Figure 5.21 Reflectance/transmittance of the 1μm nanowires covered with thin (50nm)/thick (100nm) n^+ shell layer and subsequently planarized with AZO film (In the inset R and T are corresponded to reflectance and transmittance, respectively.)

(EQE) of the cells were measured with a solar cell spectral response measurement system from PV measurement Inc. The power of the reflected light was subtracted from the result of EQE measurements; and the internal quantum efficiency (IQE) of the fabricated cell structures was obtained.

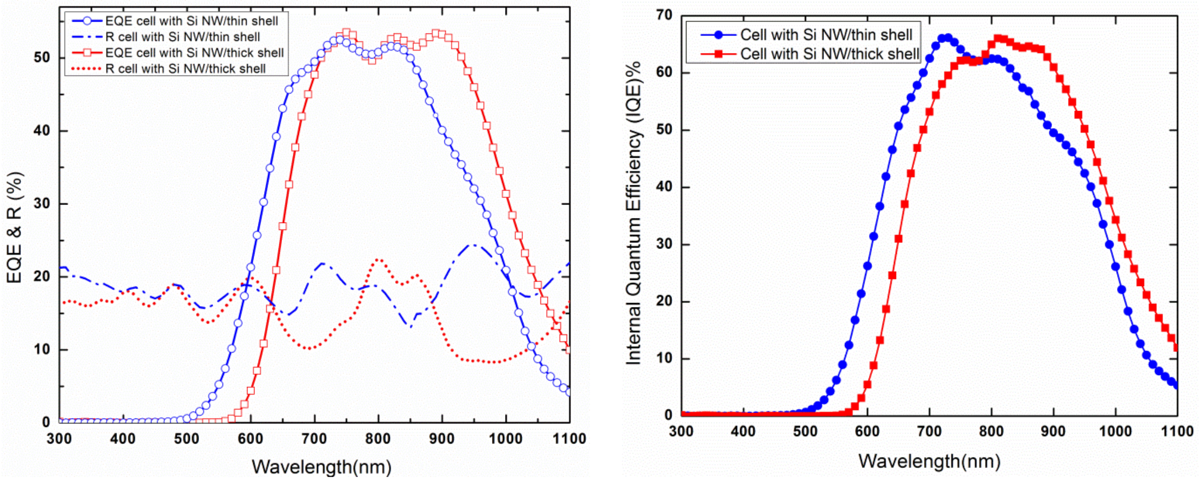

(a) (b)

Figure 5.22 a) EQE and reflectance, b) IQE of the non-planar cell structures with 500nm long p core with thin (50nm) and thick (100nm) *n^+ a*-Si:H shell

The *n^+ a*-Si:H/AZO bilayer shows poor transparency in the shorter wavelength range of the spectrum (see Fig. 5.21), which results in a major cell performance loss (see Fig. 5.22.a,b), because light is shone from the top during measurement. The IQE results also demonstrate that the photocurrent increases, in the 500-600nm range, for the cell with thin shell layer (see Fig. 5.22.b). It can be attributed to the better transparency of the 50nm n^+ *a*-Si:H/AZO bilayer, in this range of the spectrum, with respect to the 100nm n^+ *a*-Si:H/AZO bilayer. The transparency of the shell/AZO bilayer needs to be optimized.

5.2.6 Dependence of the Photocurrent on the Wire Length

Two devices with two different nanowire lengths of 500nm and 1µm, controlled by the etching time of the crystalline silicon substrate, were fabricated and carefully characterized while maintaining the same overall n-shell thickness (~100nm) and doping level. The EQE and reflectance results obtained from the fabricated cells are shown in Fig. 5.23.a. The IQE results exhibit a slight increase in photocurrent as the wire length increases (see Fig. 5.23.b). The photons are absorbed in the axial direction of the wire and as the length of the wire increases the photocurrent increases in the device.

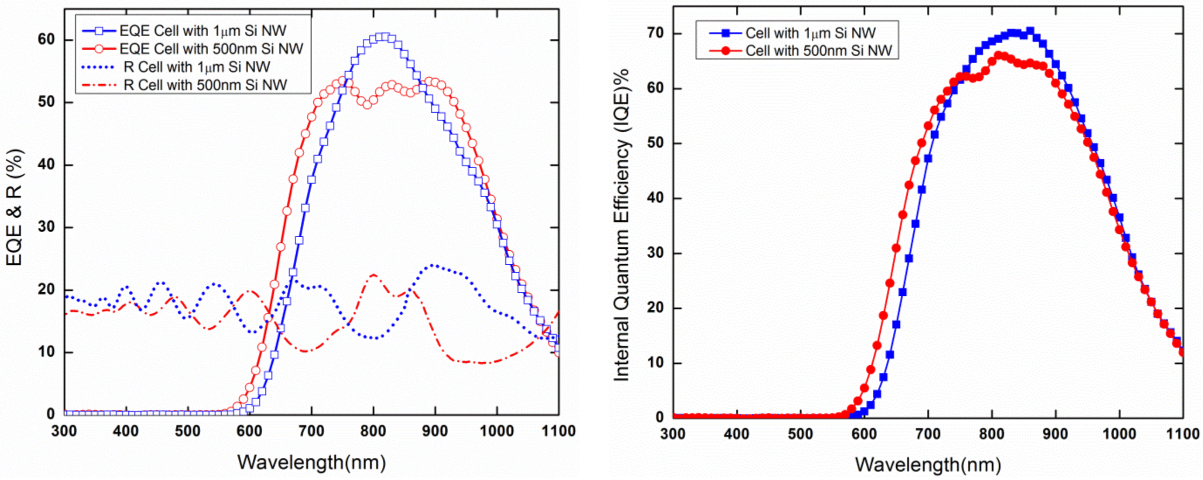

(a) (b)

Figure 5.23 a) EQE and reflectance, b) IQE of the non-planar cell structures with two different nanowire lengths of 500nm and 1µm with the same shell thickness of 100nm and doping level

5.2.7 Dark I-V Characteristics of the Cell

The dark I-V, measured with a semiconductor parameter analyzer (Agilent 4155C), exhibits asymmetric characteristics, that resemble the rectifying behavior of a p-n junction. The effect of post cleaning on the I-V characteristics of the p-n junction Si wire arrays is shown in Fig. 5.24. The device fabricated on a 1µm long wire array, as described above, without the etch step is less rectifying with respect to the devices fabricated on the cleaned wires (see Fig. 5.24.a). Fig. 5.24.b and the inset exhibit reverse saturation currents of $I_o=1.6X10^{-5}$ A, where the current is plotted on a logarithmic scale. This can be due to the residual RIE contamination on the wire tips and sidewalls, which leads to leakage across the junction. After a gentle dry cleaning process to further clean the wire surfaces, the reverse saturation current was measured $I_o=1.9X10^{-5}$ A. The high saturation currents arise partly from the remaining contamination that exists on the surface and partly from the shunt leakage due to edge effects in the device[193].

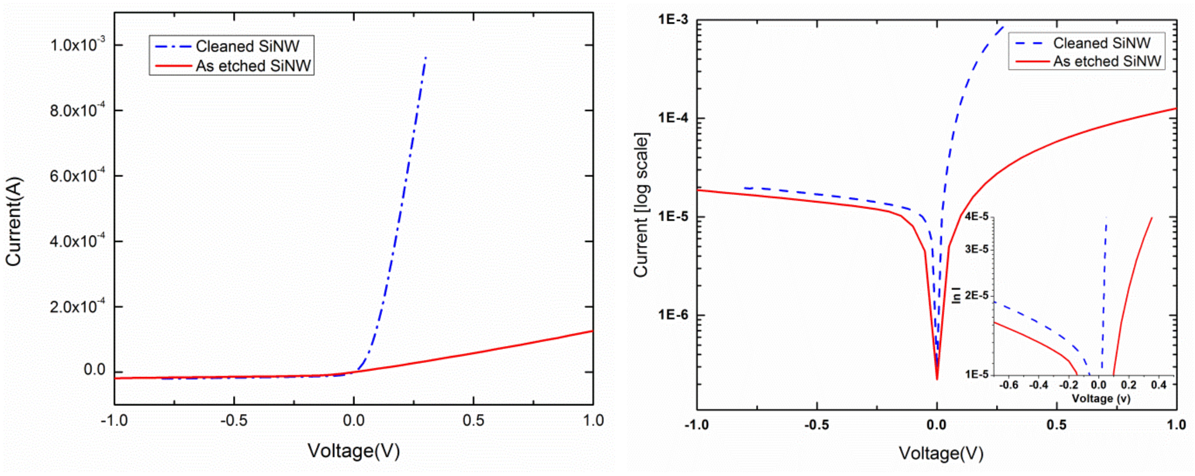

(a) (b)

Figure 5.24 a) Dark I-V, b) Dark I-V in log scale for two SiNW devices fabricated from as etched SiNWs (solid line) and SiNWs cleaned in a dry etch process (dashed line)

5.2.8 Illuminated I-V Characteristics of the Cell

The illuminated IV performance of the cells with an active surface area of 4 cm^2 was characterized using a solar simulator 1000 from the Optical Radiation Corp. Under AM1.5G illumination, I-V characteristics were recorded at room temperature. Positive voltage is defined here, to the case where the top Al contact is at a negative potential with respect to the back contact, which for this particular p–n device configuration, is the forward bias condition.

Table 5.2 demonstrates the illuminated I-V characteristics of 3 cells fabricated as follows; sample 1: thick (100nm) coated junction Si wire array solar cell fabricated with a 50nm diameter by 1µm long Si wires, with a pitch of 200nm. Sample 2: thick coated junction Si wire array solar cell fabricated with a 50nm diameter by 500nm long Si wires, with a pitch of 200nm. Sample 3: thin (50nm) coated junction Si wire array solar cell fabricated with a 50nm diameter by 500nm long Si wires with a pitch of 200nm; all under 100mWcm^{-2} AM 1.5G illumination intensities.

The low V_{oc} values of these wire array cells can be attributed to the relatively high saturation current density and the low shunt resistance when compared to the planar Si cells. In addition to the low shunt resistance due to localized shorting, interface defects and edge affects, which can likely be improved through surface passivation, the cells had a relatively high series resistance which is clear from the I-V curves (see Fig. 5.25 and Fig. 5.26). This can be determined from a linear fit of the illuminated I-V near V_{oc}, which together account for the low FF of these cells [194]. The high series resistance arises from the

Samples	SiNW Array Cell Diameter=50nm	I_{sc} (mA)	J_{sc} (mA/cm^2)	V_{oc} (V)	R_{series} (ohms)	R_{Shunt} (ohms)	Area (cm^2)	Irradiance (mW/cm^2)	FF %	Efficiency η (%)
#1	1µm long-thick n^+ *a*-Si:H (100nm)	26.33	6.58	0.250	0.125	9.8	4	100	25.2	0.47
# 2	500nm long- thick n^+ *a*-Si:H (100nm)	17.51	4.37	0.375	0.033	7.6	4	100	24.6	0.13
# 3	500nm long- thin n^+ *a*-Si:H (50nm)	25.47	6.36	0.312	0.083	11	4	100	21.3	0.55

Table 5. 2 Illuminated I-V characteristics of the fabricated cells

high resistivity of the Si wire core, shell and the top contact material and/or geometry. Further improvements can be achieved through the use of intentional doping and the introduction of a low resistance conformal transparent conductive oxide as a top contact layer. The J_{sc} of these initial Si wire array devices is lower than that reported for the Si wire array solar cells [195], likely due to a combination of the high series resistance, high trap densities in interfaces and not optimized thickness of the light-trapping elements. Nevertheless, the results demonstrate an important step in the development of radial junction solar cell devices fabricated using Si wire arrays fabricated with self-masked RIE.

5.2.9 Dependence of the Illuminated I-V Characteristics on the Shell Thickness

The illuminated I-V characteristics of the device with the 500nm long core-shell wire embedded in AZO with conformal thin shell layer indicates better performance than the device with thick shell (see Fig. 5.25.a,b). The I_{sc} increases from 17.51mA to 25.47mA with a decrease in the shell thickness. It can be attributed to better collection through the thin amorphous layer surrounded with a conductive layer. The core-shell Si arrays which are in contact with AZO from the top shows lower collection efficiency due to the loss of recombined carriers travelling in a thicker amorphous layer to be collected in the top electrode contact. The increased absorption in the thicker n^+ *a*-Si:H layer also plays a role in reducing the efficiency in this device architecture. Optimal film thicknesses are needed in order to have high efficiency devices. The junction area is almost the same for both structures, so the V_{oc} is reported 0.375V and 0.312V for the wires with thick and thin shells respectively, which are relatively close values as expected.

5.2.10 Dependence of the Illuminated I-V Characteristics on Wire Length

The I-V characteristics of the fabricated array cells were examined for two devices, with wires being 50nm in diameter, covered with a 100nm n+ shell and lengths of 500nm and 1µm (see Fig. 5.26.a,b). As shown in Fig. 5.26.b, I_{sc} exhibits a near-linear dependency on the wire length, as the photocurrent is

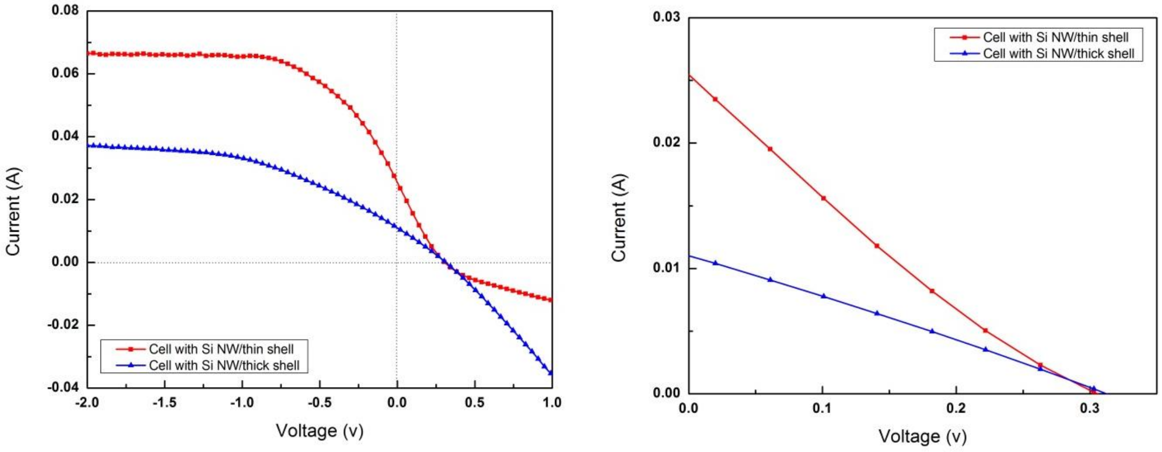

(a) (b)

Figure 5.25 a) Illuminated I-V characteristics of the fabricated array cells for two devices, with wires being 50nm in diameter, with the height of 500 nm covered with 50nm and 100nm n^+ *a*-Si:H shell b) zoom-in view of (a)

proportional to the photon absorption along the wire, considering a constant minority carrier lifetime. The I_{sc} increases from 17.5 mA to 26.33mA with an increase of wire length. The junction area also increases, leading to better electron-hole pair separation-collection. On the other hand, V_{oc} decreases from 0.375V to 0.251V with an increase of wire length, due to more surface trap density and surface recombination.

5.3 Demonstration of Experimental Feasibility: Architecture 2

5.3.1 Schematic Showing Different Steps from NW Formation to the Device Fabrication

Fig. 3.28 demonstrates the schematic diagrams of the steps of the fabrication process involved for formation of the nanowire array solar cell. Fig. 5.27.a demonstrates the formation of a monolayer of silica nanosphere on silicon substrate. Fig. 3.27.b and Fig. 5.27.b.c show an RIE etched SiNW before and after nanosphere removal, respectively. The fabrication method was discussed in Chapter 4. Formation of

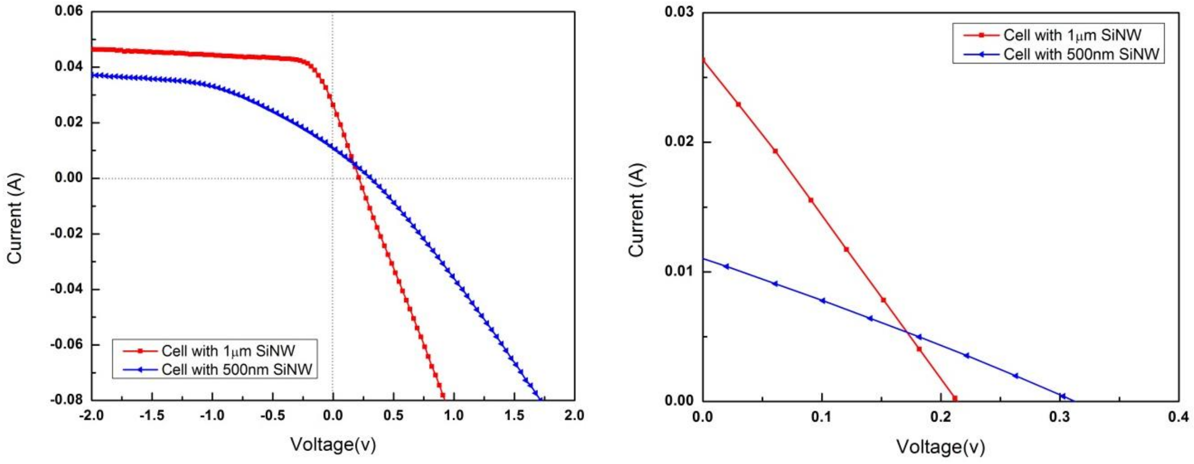

(a) (b)

Figure 5.26 a) Illuminated I-V characteristics of the fabricated array cells for two devices, with wires being 50nm in diameter, covered with a 100nm n$^+$ *a*-Si:H shell and lengths of 500nm and 1μm b) zoom-in view of (a)

emitter on the SiNW is shown in Fig. 5.27.d. Nanowires with emitter after planarization with a TCO layer are presented in Fig. 5.27.e; and Fig. 5.27.f shows the complete device after formation of top and bottom electrode contacts.

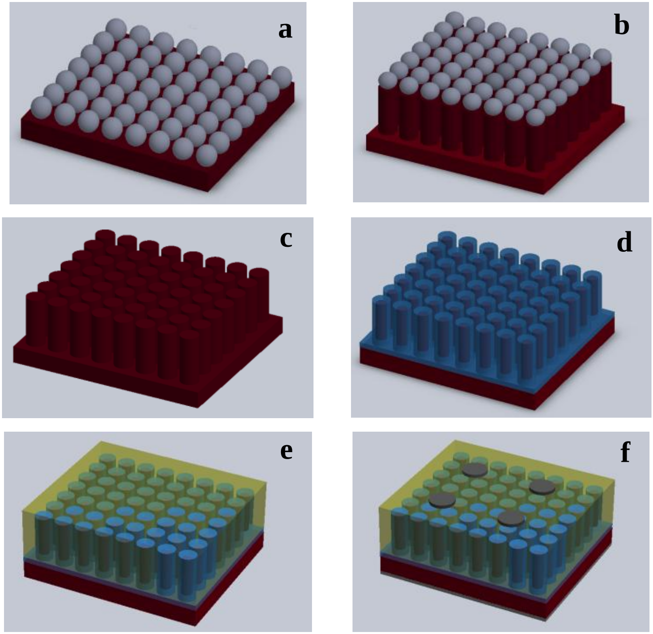

Figure 5.27 Schematic diagram of the nanowire array cell: a) monolayer of silica nanosphere on silicon substrate, SiNW b) before and c) after nanosphere removal, d) SiNW with n$^+$ emitter, e) planarized wires with a TCO layer, f) device after formation of top and bottom electrode contacts

5.3.2 Emitter Formation by Diffusion

A non-planar solar cell structure was fabricated with formation of an emitter layer, on 700nm (height) by 300nm (width) nanowire arrays, by diffusing phosphorous from an SOD source (Filmtronics Inc.). The phosphorus dopant was spin cast on nanowires at 750 rpm for 30s and then diffused into the wires by RTP at about 900ºC for 60s. Low ramps were used in order to maintain the shape of the wires during the annealing process. The SOD was finally removed in a 2% hydrofluoric acid aqueous solution. The SEM image in Fig. 5.28.a shows NWs coated with a layer of SOD. In the top view and cross section images shown in Fig. 5.28.b and Fig. 5.28.c respectively, NWs with an n^+ emitter layer and vertical sidewalls, after diffusion and cleaning cycles, are evident. At this stage the doping level in the NWs was not measured precisely through the use of sophisticated methods, as discussed in section 5.3.2. The method used is described by Garnett et al. [15] and Gunawan et al. [196]. The doping level is estimated by diffusion on planar control samples, with doping density of $2X10^{20}$ cm^3 and sheet resistance of 100Ω/□, measured using spreading resistance profiling (SRP) analysis. The phosphorus dopant concentration in the etched nanowires should be unchanged from that of the starting Si wafer, which was about 1×10^{16} cm^{-3} according to the wafer resistivity of 1-2 Ω·cm. As the emitter doping level is higher, the depletion region is expected to mainly be located in the crystalline NW core (see Fig. 5.28.d). These results were used for the simulation as well. As mentioned earlier, this research is ongoing to benefit from the reported techniques, in order to make a precise measurement on dopant profile and active dopant concentrations in the NWs.

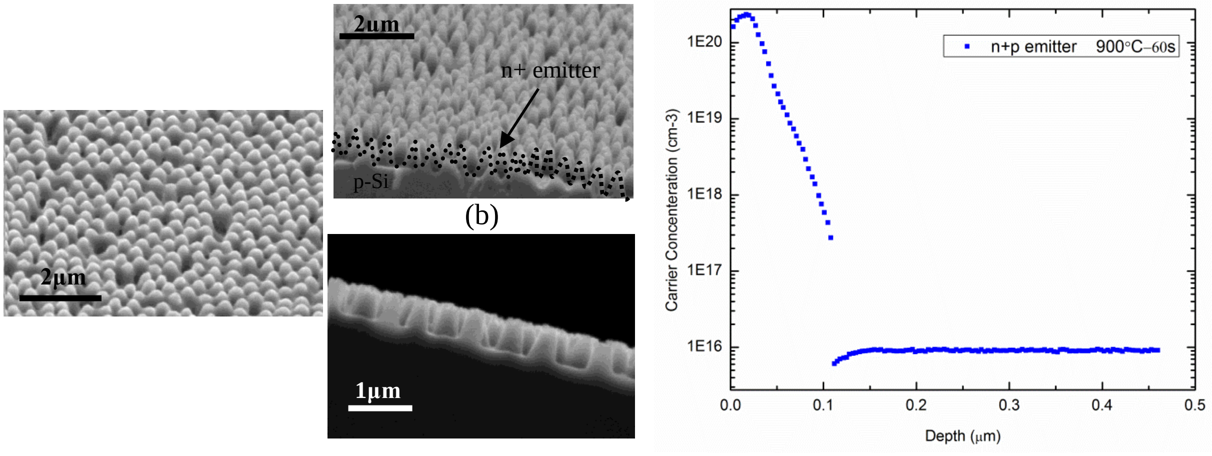

(a) (c) (d)

Figure 5.28 a) NW coated with SOD, b) NW with a n^+ emitter, c) cross section view of NWs after emitter formation, d) dopant profile of a doped planar silicon wafer prepared at the same diffusion process as the wire arrays

5.3.3 Contact Formation

Two NW array cells were prepared by filling the spaces between the nanowires with an n-type emitter layer with sputtered AZO, as well as zinc oxide (ZnO) layers. TCO layers surrounded the nanowires to serve as a passivation layer as well as top contact. Covering the SiNW with the TCO layer also allowed probing without breaking any nanowires. The AZO layer was deposited in an Intelvac RF magnetron sputtered system and the ZnO layer with the AC sputtering mode of the same system. Fig. 5.29.a shows NW with n^+ emitter covered with a conformal layer of AZO; and Fig. 5.29.b shows wires planarized with the AZO layer. The AZO and ZnO deposited films exhibit sheet resistance of 80 Ω/□ and 1KΩ/□ respectively, which were measured by the non-contacting resistivity (NCR) technique. The Al top contact electrode was also sputtered through a shadow mask over the TCO layers.

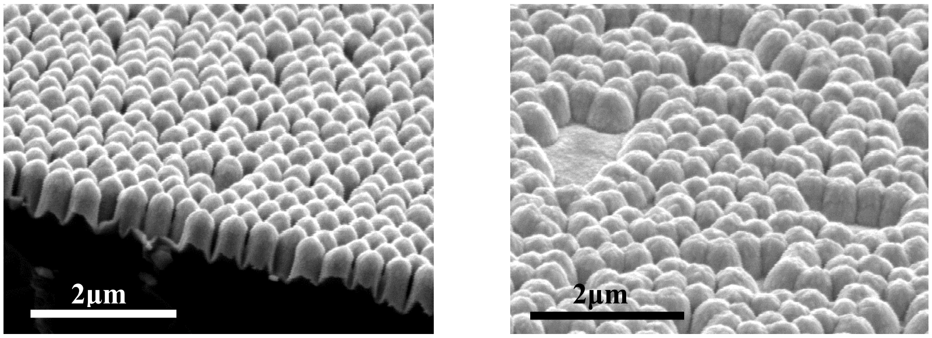

(a) (b)

Figure 5.29 NW with n^+ emitter a) covered with a conformal layer of AZO and b) planarized with an AZO layer

5.3.4 Optical Confinement

SiNWs were planarized with 300nm of AZO and ZnO layers. The reflectance of the layers was measured. The same thicknesses of the layers were also deposited on quartz substrates for transmittance measurements. The AZO layer, was sputter deposited at the RF plasma power of 200w, with the pressure of 100mTorr and Argon flow rate of 50sccm at room temperature. After 60 minutes deposition, a 300nm thick layer was obtained. The deposited film shows the average transparency of 50% in the visible-near infra-red range of the spectrum. The transparency improved 10% by using 300 nm of ZnO layer. AC mode was used to deposit this layer, using argon/oxygen plasma with the flow rate of 55sccm and 2sccm respectively, plasma pressure of 100mTorr and RF power of 400w at room temperature. After 60s, 300nm thick ZnO film was obtained with the average transparency of about 60% in the same spectrum range (see Fig. 5.30). The transparency is poorer in the short wavelength range for both materials.

Integrated sphere reflection was measured in the 300-1100nm range at normal incidence. The specular reflection from a silicon wafer and the NW arrays are also shown in Fig. 5.30. The normal incidence reflection is greatly reduced from >30% for a silicon wafer to <5% for the NW arrays. The sub-wavelength array structure of NWs exhibited excellent broadband antireflective properties, principally due to refractive index matching, showing that the fabricated NW arrays have tunable electro-optic properties that can be beneficially engineered for improved efficiency in PV devices.

This figure also demonstrates that the reflectance of the layer increases from 7% to 14% after the SiNW planarized with ZnO and AZO layers, respectively. The experimental results have shown that oxygen flux, argon pressure, substrate temperature and plasma power are the main factors that affect the electrical-optical properties (transmittance, resistivity) of the TCO films [197]. For these films to be more transparent the layer has to be annealed in a vacuum or the deposition needs to take place at a higher temperature, around 300ºC, at a risk of getting lower conductivity of the film. This research is ongoing in order to find the optimal deposition parameters for the AZO film with lower reflectance and higher transparency, while attaining high conductivity as well.

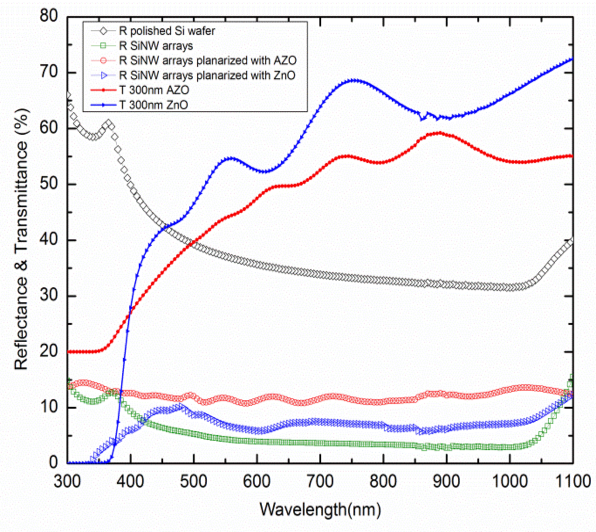

Figure 5.30 Total reflectance and transmittance spectra of SiNW array and the SiNW array planarized with AZO and ZnO layers (In the inset R and T are corresponded to reflectance and transmittance, respectively.)

5.3.5 Device Performance Characteristics

Spectral Response of the fabricated Cells

The spectral response of both devices employing the NW arrays coated with AZO and ZnO layers are demonstrated in Fig. 5.31. EQE measurement was performed on the fabricated devices to investigate the contribution of the wires to the photocurrent of the device. The device having the more transparent TCO layer, with lower reflectivity, showed a higher EQE response (see Fig. 5.31.a). The EQE increased from 30%, for the device with an AZO layer, to 35% for the device with a ZnO layer. However, the low EQE of the devices is most likely related to loss of light energy by absorption/reflection in the relatively thick TCO films. IQE results exclude reflection losses in the TCO layers, demonstrating higher photocurrent for the cell with the AZO layer in respect to the cell with the ZnO layer (see Fig. 5.31.b).

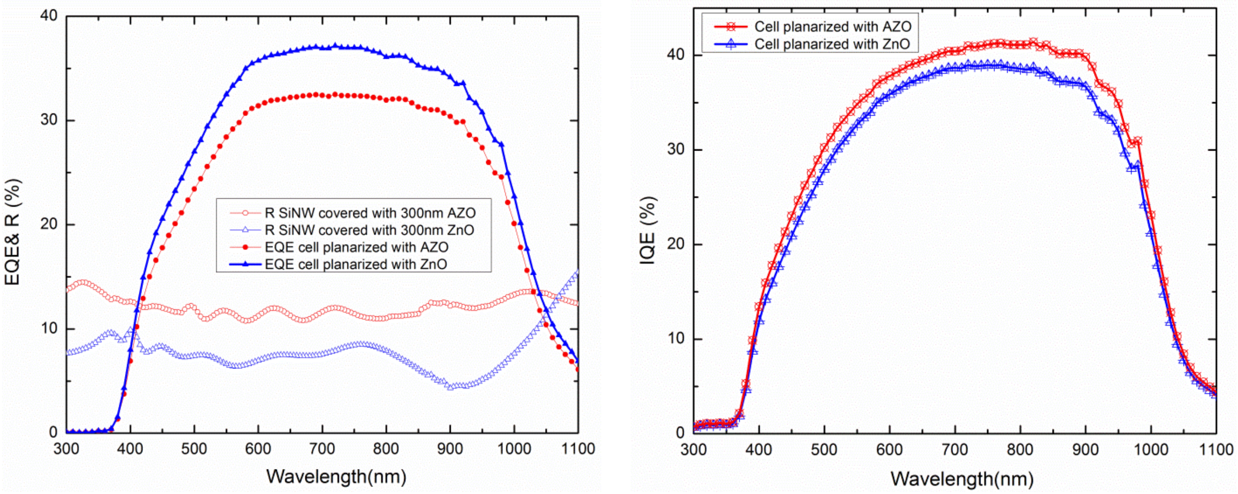

(a) (b)

Figure 5.31 a) EQE, reflectance and b) IQE spectra of the fabricated nanowire array solar cells

I-V Characteristics of the fabricated Cells

Table 5.3 demonstrates the electrical characteristics of the SiNW array solar cells under AM1.5G illumination. The solar cell area is 4 square centimeters (cm^2). The illuminated IV characteristics are also shown in Fig. 5.32. For the cell with 700nm long NWs and planarized with 300nm AZO, the V_{oc} and I_{sc} values of 0.289v and 30.78 mA give an overall efficiency of 0.57%. Nanowires coated with a 300nm ZnO layer show I_{sc} and V_{oc} values of 3.89 mA and 0.259V, with overall efficiency of 0.14%. The results illustrate that the I_{sc} dramatically decreases for the cell covered with ZnO.

SiNW array cell	V_{oc} (V)	I_{sc} (mA)	J_{sc} (mA/cm^2)	FF (%)	η (%)	Area (cm^2)	I (mw/cm^2)
300nm AZO	0.289	30.78	7.70	25.5	0.57	4	100
300nm ZnO	0.259	3.89	1.98	27.5	0.14	4	100

Table 5. 3 Electrical characteristics of the SiNW array solar cell under AM 1.5 G illumination; solar cell area is 4 cm^2

By using a more conductive TCO layer with these cells, improved collection efficiency was observed. As described earlier, the high absorption/reflectance of the incident photons, in the cell planarized with AZO layers, causes the cell to not be as efficient as expected. AZO layer optimization will be continued in the future.

The nanowire geometry enhances the light trapping, but also increases the junction area which leads to surface recombination. From the illuminated I-V results, shown in Fig. 5.32, it is apparent that the NW array cell with the 300nm AZO layer has high short circuit current (I_{sc}=30.78mA), low open circuit voltage (V_{oc}=0.289V) and poor fill factor (FF=25.5%). The low V_{oc} is due to the surface recombination. The poor fill factor is also associated with significant series resistance. The series resistance can be reduced using an optimized layer of conducting AZO. The silicon nanowire array cell efficiency can be improved this way. Moreover, the local shunt resistance or shorting at junction could also be another reason limiting the effectiveness of the radial p-n junction geometry. The dark IV characteristic, in the inset of Fig. 5.32, illustrates the rectifying behaviour of the fabricated device.

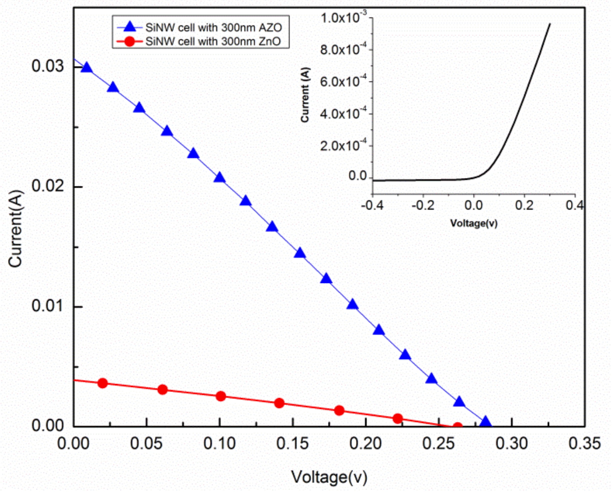

Figure 5.32 Solar cell illuminated I-V characteristic: inset is the dark IV of the device

5.4 Conclusions

Cost effective approaches for fabrication of ordered arrays of single crystalline SiNWs were examined. In the first approach, the PV device was fabricated on wires formed with maskless RIE. Thin and thick conformal layers of n^+ *a*-Si:H were deposited over the NWs by PECVD deposition. The core-shell Si NW array cells were planarized with sputtered AZO layer. Al contacts were sputter deposited on top of the structures, as well as the back side of the silicon substrate. The experimental and theoretical results provided important insights into the impact of the geometrical structure of the SiNW arrays on the cell performance. A single SiNW with radial p-n junction was simulated with a model developed in the COMSOL 3.5a multiphysics program. The electric potential distribution along the core-shell NW at different bias voltages, distribution of space charge density and electric field in the nanowire core at reverse bias for different levels of doping in the shell region were studied, in order to better understand when the wire becomes fully depleted. The dark IV characteristics of the device and the effect of conformal and non-conformal patterns of contacts were also examined. The experimental dark IV results showed a diode behavior of the fabricated SiNW cell, yet the role of surface traps in the transport and recombination mechanisms of the studied devices must be emphasized. Cleaning was found to significantly improve the diode characteristics of Si wire array solar cells fabricated by RIE. A gentle dry cleaning process removed residues coated on the sidewalls resulting in a better rectifying behavior of the device.

In the second approach, nanosphere lithography and a top-down approach were utilized for NW formation. This method will enable large-scale production of periodic nanowires, with desirable size and spacing, which can be utilized for NW array solar cell fabrication. The simulation results demonstrated that, by tuning the doping parameters and equally the wire geometry, somehow the structure can be designed to either have quasi-neutral region in the wire or a fully depleted wire will be made. The experimental results confirmed the enhancement of light trapping in NW array structures which led to an increase in current density and as a result enhanced carrier collection efficiency. However, the junction area increased the surface recombination rate and resulted in low open circuit voltage of the device. The poor fill factor of the device was also associated with significant series resistance of the TCO layer. The series resistance can be reduced using an optimized layer of conducting AZO. This way the silicon nanowire array cell efficiency can be improved.

These approaches have potential for implementing SiNW array solar cells on silicon substrates with enhanced carrier collection efficiency, arising from the geometric configuration of the radial p-n junction. The conversion efficiency, of the SiNW array solar cells reported here, is low and further improvements are needed to meet the high-performance application requirements. It is speculated that the efficiency can readily be enhanced in the future through further device and materials optimization; for instance, by using top contacts with higher optical transparency and lower parasitic resistance. Specifically, the top contacts resulted in a ~50% efficiency loss owing to their low transparency level, which can readily be improved in the future.

Chapter 6

Base Technology Development for Crystalline Silicon Solar Cells

Crystalline silicon solar cells were fabricated replacing all conventional furnace processes with two low thermal budget rapid thermal process steps. The simple spin coating technique provided clean diffusion sources that resulted in shallow junctions with a high degree of uniformity. In order to reduce surface recombination and reflection losses, PECVD silicon nitride layers with optimum thicknesses were deposited on the cells to provide efficient passivation and anti-reflection coating. The texture patterns were also provided on the surfaces using an alkaline-based random texturing process to further reduce the reflection losses. Sputtered metal films were deposited on the devices to form the electrical contacts.

The profile and sheet resistance of the fabricated junctions were determined by performing a spreading resistance profile (SRP). Current-voltage (IV), external quantum efficiency (EQE) and reflectance spectroscopic measurements were performed to characterize the fabricated cells. The developed technology will serve as the base technology baseline for further development of advanced devices, through the integration of the nanostructured materials, as described in previous chapters; and will be further discussed in Chapter 7 and Chapter 8.

6.1 Solar Cell Structure and Process Sequences

Solar cells were fabricated on 3-in diameter, 350-400μm thick p-type and n-type, 1-2 Ωcm resistivity Czochralski (CZ) wafers. Fig. 6.1.a and Fig. 6.1.b show the corresponding fabrication process steps and the schematic structure of the fabricated cell, respectively. After cleaning, in order to fabricate the n^+pp^+ cell, a commercially available boron dopant spin-on source was deposited on the back side of the p-type samples. The samples were annealed in RTP for the formation of BSF in the first high temperature step. After removing the borosilicate glass, a phosphorous dopant spin-on source was deposited on the front side and the second high temperature process was carried out for the formation of an emitter. In another experiment, the emitter and BSF were co-diffused in a high temperature process. A characteristic feature of the temperature profile used for diffusion of dopants is shown in Fig. 6.1.c. After removing the phosphosilicate glass, the cell was covered with a 75nm PECVD SiN_x film for reducing reflection and passivating the surface. The front contact was realized using photolithography and Al sputtering; while the rear contact consists of 2 μm of sputtered Al. Finally, the contact was annealed at 350 °C for 30 min in hydrogen: helium plasma. The same process sequence used to fabricate p^+nn^+ cells.

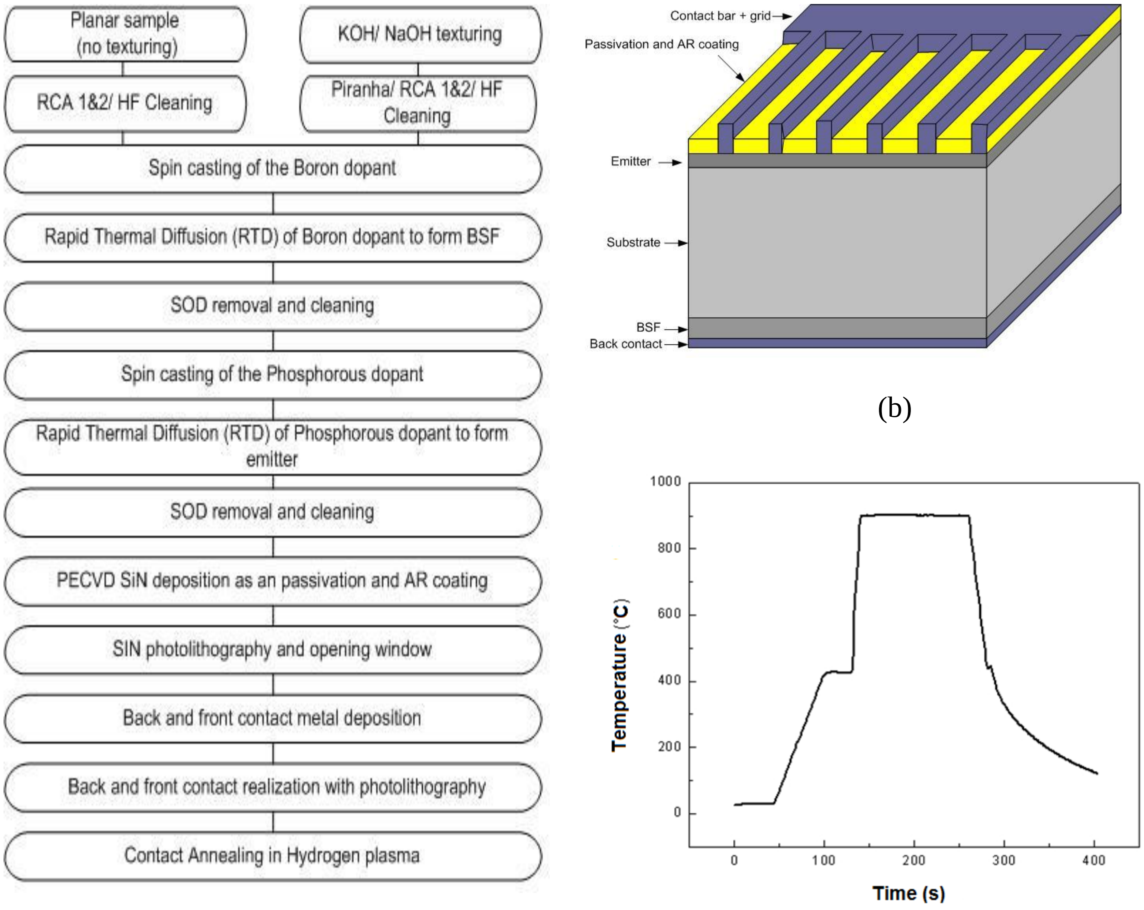

(b)

(a) (c)

Figure 6.1 a) Processing sequence for the silicon solar cells, b) schematic design of a planar silicon solar cell, c) an RTP profile used for junction formation

6.2 Junction Characteristics

In order to characterize the fabricated junctions, the active carrier concentration profiles and the sheet resistance of the doped layer were obtained by the Spreading Resistance Profile (SRP) analysis. The annealing temperature of 900°C and 1050 °C for durations of 60 and 180s were used to provide shallow or deep junctions on the silicon wafer. The effects of annealing temperature and time on the profiles of the n^+p and p^+n junctions were compared as shown in Fig. 6.2.a,b and Fig. 6.2.c,d.

The active carrier concentrations were increased with temperature and became saturated at high temperatures. This behavior can be attributed to an increase in the solubility of dopants into silicon when the diffusion temperature is increased as the Si-Si bonds break due to the photonic effect during heating

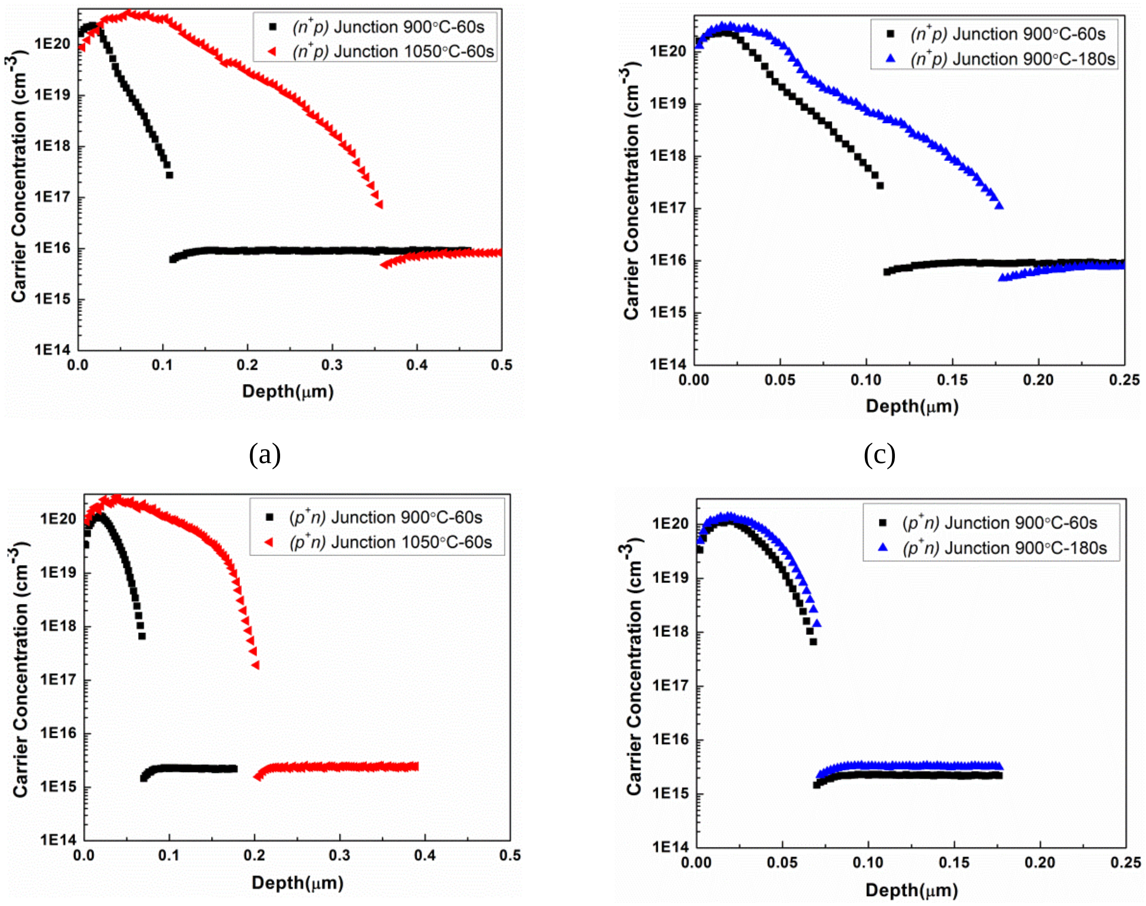

(a) (c)

(b) (d)

Figure 6.2 SRP profiles showing the effect of annealing temperature on the profile of a) *n^+p* and b) *p^+n* junctions effect of annealing time on the profile of c) *n^+p* and d) *p^+n* junctions.

by the lamps[198]. A maximum surface concentration of about 2 x 10^{20} cm^{-3} after 900 °C processing was obtained. In contrast, much lower surface concentrations can be obtained at lower temperatures (less than 850ºC). The junction depths were increased when the temperature was increased. At the processing temperature of 900 °C, the n^+p and p^+n junction depths are 0.12 µm and 0.07 µm, respectively. At 1050 °C, the junction depths were measured to be 0.35 µm and 0.2 µm, respectively. Several RTD experiments were performed by varying the RTP temperatures and cycles in order to optimize the process. Table 6.1 shows the SRP results for the junction profile depth and sheet resistance of the n^+p and p^+n junctions as a function of RTD conditions, with the same initial composition of deposited phosphosilicate or borosilicate, respectively.

6.2.1 Back Surface Field via High-Low Junctions

To obtain high efficiency solar cells, both bulk and surface recombination must be low. Various surface passivation methods have been investigated for the front surface. A back surface field (BSF) provides a

RTP condition	n^+p junction depth (μm)	Sheet resistance (Ω/□) (n^+ emitter)	p^+n junction depth(μm)	sheet resistance (Ω/□) (p^+ emitter)
900°C-60s	0.12	110	0.07	320
900°C-180s	0.155	60	0.08	200
1050°C-60s	0.35	20	0.2	54

Table 6. 1Variation of SRP measured junction depths and sheet resistances with RTP conditions

built-in electric field at the back surface of the device, hence reduces back surface recombination. The recombination rate at the surface is related to excess concentration of minority carriers at the surface. The BSF created by the high-low junction (p^+p) prevents the minority carriers from reaching the rear surface and thus increases their chance of being collected by the p-n junction.

6.3 Surface Texturing of Silicon Wafer

In order to enhance the light trapping in the cells a cost and time efficient surface texturing method, using diluted inorganic alkaline-solutions, was utilized. It is a random texturing method without any masking patterns. The hydrogen bubbles evolving during the etching reaction [199] stick to the silicon surface and their masking effect results in a lateral etching action of the solution, which is essential for the pyramid formation process. The diameter of the bubbles, their density and the rate of the etching reaction define the geometry of the textured silicon surface [200].

p-type and n-type 3x3 inch^2, <100> oriented c-Si wafers were randomly textured in aqueous solutions, consisting of potassium hydroxide (KOH) and isopropyl alcohol (IPA) (see Fig. 6.3.a), as well as solutions consisting of sodium hydroxide (NaOH) and IPA (see Fig. 6.3.b). Homogeneous surfaces, which are fully covered with random pyramids of small size, are the result of these methods of texturing.

Figure 6.3 shows a textured silicon surface with 100% pyramid density. The solution consists of 1 wt% KOH (or NaOH) and 7 vol% IPA, at 70°C. The increase of solution concentration results in an enhanced etch rate. A strong dependence of the etch rate on the IPA concentration was observed. The wafer shown in Fig. 6.4.a was textured in a solution consisting of a high and low percentage of KOH and IPA, respectively; while the wafer shown in Fig. 6.4..b was textured in a solution consisting of a low and a high percentage of KOH and IPA, respectively. The former process results in the formation of large pyramids with a base length of up to 15 μm with nonhomogeneous surface coverage. In the second process the surface is completely covered with pyramids with a base length up to 5 μm.

A high density of starting points leads to a high density of pyramids of small size and thus to a more homogeneous surface. IPA acts as the initiator of the pyramid growth process by leading to a

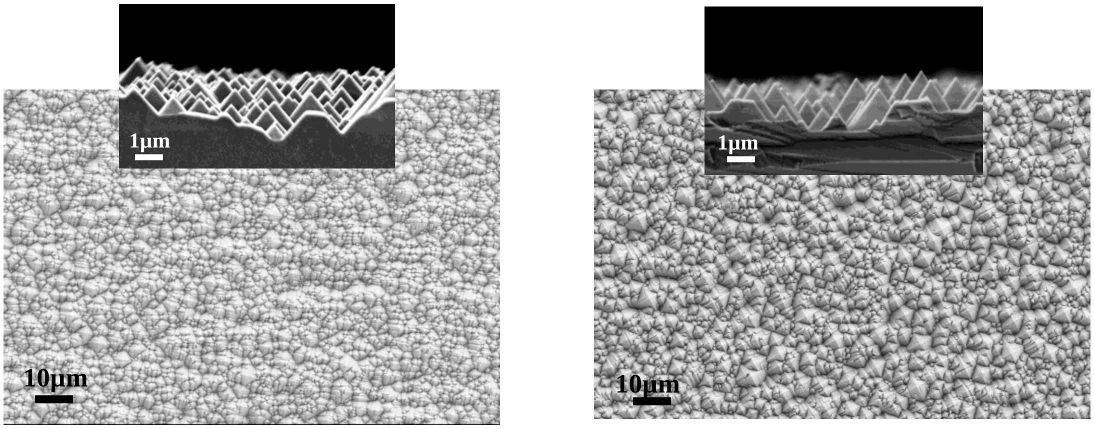

(a) (b)

Figure 6.3 Textured silicon surface with 100% pyramid density using a) KOH solution, b) NaOH solution: insets are the cross section views

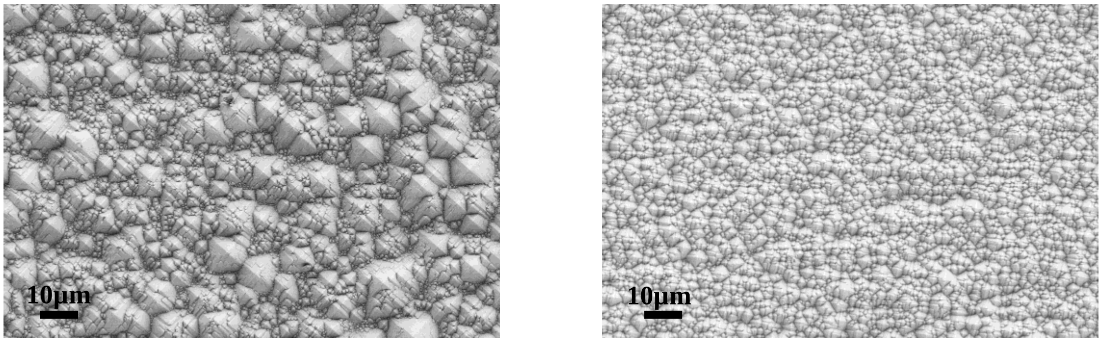

(a) (b)

Figure 6.4 SEM microphotograph of a textured surface after 40 min in a solution a) consisting of *5* wt% KOH and 3 vol% IPA, b) 1 wt% KOH and 7 vol% IPA, at 80°C

micromasking of the surface [88]. The etch rates vary from 0.2 µm/min for low KOH and high IPA concentrations; to 0.9 µm/min for high KOH and low IPA concentrations. The temperature also has a strong effect on the etching rate. The etching rate, in the same solution, varies from 0.35 µm/min, at 70°C,to 0.85 µm/min, at 90°C. Best results were obtained by using low concentrations of KOH (1%) and high concentrations of IPA (7%), at temperatures between 65°C and 80°C. Effective removal of the alkaline ions was performed in a piranha cleaning solution. The optical images of fabricated planar and textured cells are shown in Fig. 6.5.

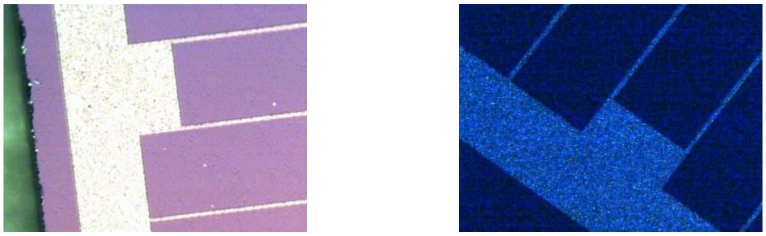
(a) (b)

Figure 6.5 Optical images of the fabricated (a) planar and (b) textured c-Si solar cells

6.4 I-V Characteristics of the Fabricated Devices

For cell characteristic measurements, cells of area 1cm^2 were cut from the 3 inch wafer. Dark and illuminated I-V measurement, spectral response and spectroscopic reflectance measurements were performed to electrically and optically characterize the fabricated devices.

6.4.1 Dark I-V Characteristic Parameters of the Fabricated Cells

In order to measure the dark IV of the fabricated cells, after forming junctions on both sides of the sample, 2µm aluminum was sputtered on the front and back surfaces. The front surface was patterned with a mask with a 10µm^2 feature size, designed for diode characteristic measurements. In order to isolate the diodes, the sample was then placed in an RIE chamber and etched in a SF_6:O_2 plasma with the flow rate of 20 and 3 sccm, respectively, at a self-bias voltage of 40V and pressure of 50 mTorr. The etch rate of this plasma condition is 0.5 µm/s. The diodes were completely isolated after 600s of etching. Finally, the sidewalls were covered with SiN_x. The dark I-V characteristics for a p-type cell with n^+ emitter (n^+pp^+) and an n-type cell with p^+ emitter (p^+nn^+) are shown in Fig. 6.6.a and Fig. 6.6.b respectively.

From the measured dark I-V curve of the n-type cell (see Fig 6.6.b), the saturation current (I_{01}) of 1.0018e^{-11} was obtained. As shown in Figure 6.6 the I-V curve cannot be fitted using the two diodes' equivalent circuit. The I_{02} is very small as compared to I_{01}. This is the reason that the n_2 vanishes and n_1 was calculated equal to 1.405 (I_0=1.0018e^{-11}, n_1=1.405). One reason for the low V_{oc} of the cell can be due to the depletion region recombination current, I_{02}, but as this parameter wasn't obtained from the dark I-V measurement, the low V_{oc} can be attributed to the other loss sources, thereby reducing the V_{oc}.

6.4.2 Illuminated I-V Characteristic of the Fabricated Cells

The illuminated IV performance of the p and n type cells with junction depth of 0.3um and an active surface area of 1 cm^2 were characterized using a solar simulator 1000 from the Optical Radiation Corp, under AM1.5G illuminations. The results are presented in Fig. 6.7. The illuminated I-V parameters of the fabricated cells are summarized in Table 6.2.

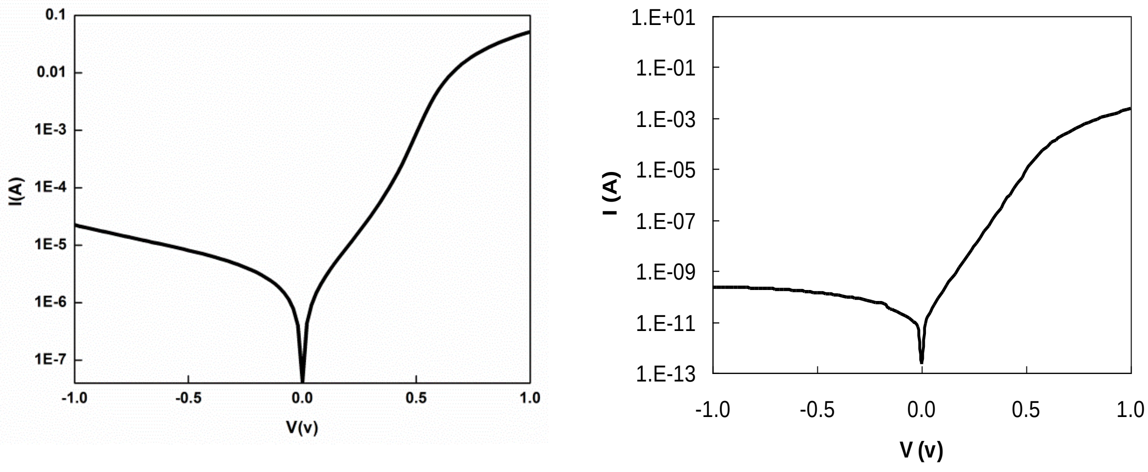

(a) (b)

Figure 6.6 Dark I-V characteristics of the fabricated a) p-type cell with n^+ emitter (n^+pp^+ cell) and b) n-type cell with p^+ emitter (p^+nn^+ cell)

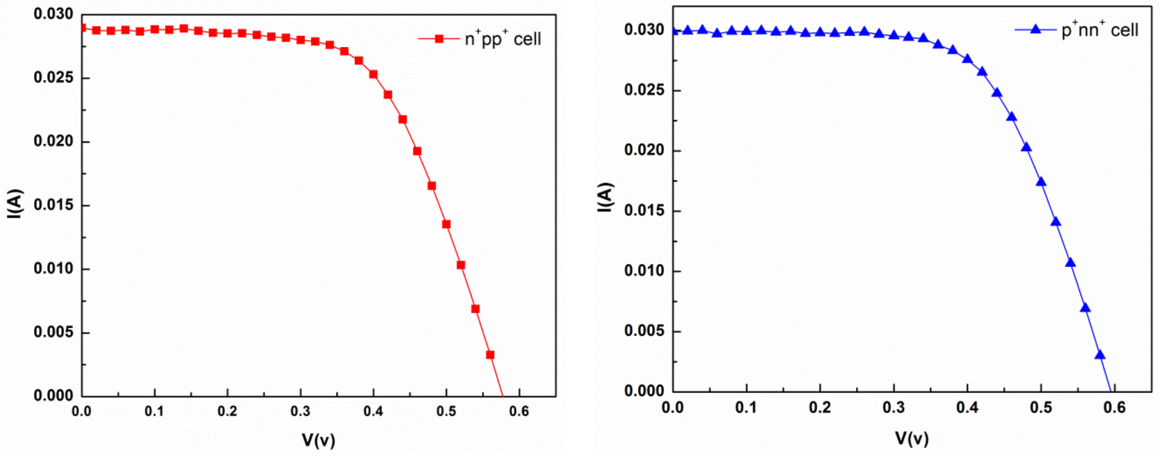

(a) (b)

Figure 6.7 Illuminated I-V characteristics of a) p-type cell with n^+ emitter (n^+pp^+ cell) and b) n-type cell with p^+ emitter (p^+nn^+ cell)

Solar cell	I_{sc} (mA)	J_{sc} (mA)	V_{oc} (mV)	FF (%)	P_{max} (mW)	R_{shunt} (Ohms)	η (%)	Area (cm^2)	Irradiation (mW/cm^2)
n^+pp^+	29	29	580	60	10.12	2.6E+2	10.12	1	100
p^+nn^+	30	30	600	62	11.14	5.8E+2	11.14	1	100

Table 6. 2 Illuminated *I–V* parameters of the n^+pp^+ and p^+nn^+ cells

The planar $n^{+}pp^{+}$ cell has a V_{oc} of 580 mV and an I_{sc} of 29 mA/cm^2. For the $p^{+}nn^{+}$ cell, the V_{oc} is 600 mV and the I_{sc} is 30 mA/cm^2. Phosphorus as an emitter and boron as a back surface field were applied to fabricate $n^{+}pp^{+}$ solar cells. RTP-BSF $n^{+}pp^{+}$ cells with spin-on dopants have a low V_{oc} of less than 600 mV. One reason for the low V_{oc} can be due to a degradation of the carrier diffusion length after high temperatue process on the boron dopant source. It is assumed that impurities or contamination from boron-dopants diffuse into the bulk of silicon materials in high thermal processes. Also, the effective lifetime of the p-type wafer is lower than the n-type which is another reason for obtaining lower V_{oc} for the $n^{+}pp^{+}$ cell.

In addition, the V_{oc} strongly depends on the surface recombination. It can be concluded that the surface passivation quality might not be the same for these cells. Hydrogen in the nitride layers is generally bonded to silicon (Si-H) or nitrogen (N-H). When PECVD deposited SiN_x is annealed at temperatures above 400°C, the N-H bonds break first, the density of Si-H bonds increases and the Si-H bonds break. Released H_2, due to the bond break, can also passivate silicon dangling bonds at the interface between silicon and the silicon nitride [201]. The contacts were also annealed at 350 °C for 30 min in 900 mTorr Hydrogen: Helium (300:500 sccm) plasma to reduce the contact series resistance due to the poor adhesion of the Al to the n^{+} highly doped surfaces (see Figure 6.8.a).

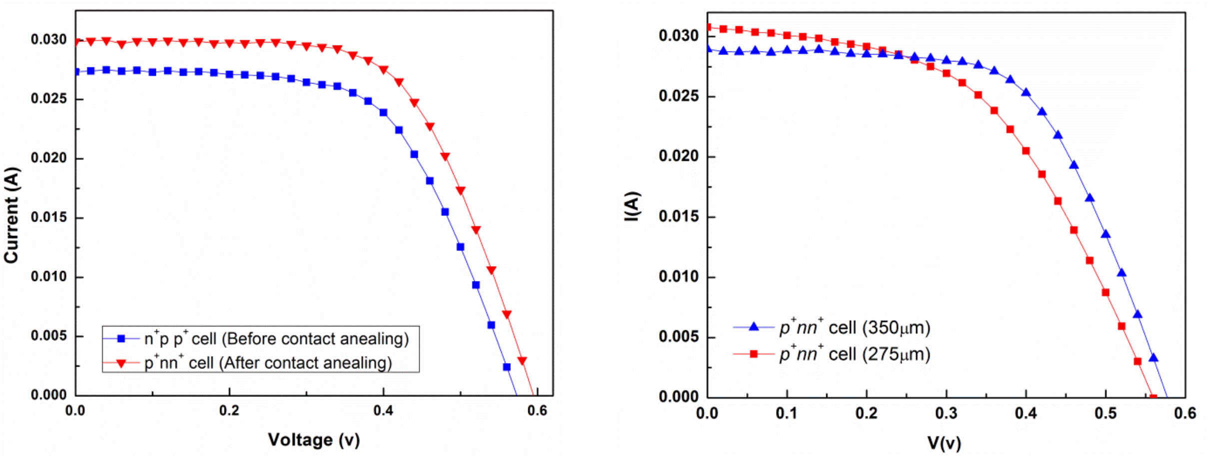

(a) (b)

Figure 6.8 a) Effect of the contact annealing on IV characteristics of the cell, b) effect of BSF on the IV characteristics of thin and thick cells

In order to improve the BSF effect, the wafers were thinned down in a silicon etchant solution containing HNO_3: HF: CH_3COOH (4:1:1). The cell was then fabricated on the thin substrate. The IV characteristics of the 275 µm cell were compared to the cell fabricated on a 350 µm thick substrate (see Fig. 6.8.b). The results demonstrate an increase in the short circuit current for the cell fabricated in thinner substrate.

Accurate I_{sc} values were obtained by a spectral response measurement system from PV Measurements Inc., under standard AM1.5. These measurements were performed on five samples with specifications as listed in Table 6.3. The n^+pp^+ cell with shallow junction has an I_{sc} of 32.56 and the p^+nn^+ thin cells with shallow junction have an I_{sc} of 34.43, which are the best results obtained for the fabricated planar cells.

Planar Cells	I_{sc} measured under AM. 1.5 G(mA/cm^2)
350µm p^+nn^+ cell with deep emitter=0.4 µm	31.20
350µm p^+nn^+ cell with shallow emitter=0.07 µm	34.35
220µm p^+nn^+ cell with shallow emitter=0.07 µm	34.43
350µm n^+pp^+ cell with deep emitter=0.2 µm	32.14
350µm n^+pp^+ cell with shallow emitter=0.1 µm	32.56

Table 6. 3 I_{sc} of the fabricated cell measured under AM1.5 G

Short Circuit Current Losses

The reasons for short circuit current losses can be due to the reflection losses, light absorption in the layer, broad metal grids; and recombination in the bulk and at surfaces. Low-weighted reflectance (< 7%) can be obtained by textured cells and passivation, with a material with an appropriate refractive index and low extinction coefficient, to transfer light to the cell with minimum absorption. Reflection from the metallic fingers results in current loss as well. A good design of contact mask with minimum coverage of the front surface can decrease the non-optical reflection. To reduce the recombination in bulk, Float Zone (FZ) wafers with high bulk lifetime can also be substituted with CZ wafers, which are a preferable substrate for high temperature processes. Finally, to reduce the recombination in front and rear surfaces, the junction formation process needs to be optimized to obtain best values for active dopant concentration and junction depth.

Open Circuit Voltage Losses

Recombination is the fundamental process which determines the V_{oc}. Both Bulk lifetime and the surface recombination velocity are important parameters in this regard. The loss in V_{oc} is strongly associated with the passivation quality on the front and rear side in solar cells. In addition, the short circuit current and recombination in the depletion region have strong effects on the open circuit voltage. The higher the short circuit is, the higher the open circuit voltage. Low recombination in the depletion region enhances the V_{oc} as well.

6.5 Spectral Response of the Fabricated Cells

The external quantum efficiency (EQE) of fabricated n^+pp^+ and p^+nn^+ cells are demonstrated in Fig. 6. 9.a. The results indicate that both cells have a reduced EQE in the short-λ (<400 nm) and in the long-λ (>950 nm) range of the spectrum, which can be attributed to the increased reflection in these ranges (see Fig 6.9.b). The mismatch between the band gap of the silicon and the incident light is the main reason for these losses. Solutions to overcome this problem were proposed in Chapter 2. Optimizing of an AR coating layer through development of new material and graded index structures is demanded. The high EQE response of the cells in short wavelength (400-500 nm) confirms the formation of shallow junctions, which results in absorption of the blue photons within the bulk silicon. The EQE response of the cells in the wavelength between 400 and 800 nm is high due to the low reflection in this spectrum range. The p^+nn^+ cell showed a higher response at intermediate wavelengths as compared to the n^+pp^+ cell, which can be attributed to the higher bulk lifetime of the n-type silicon wafer that was used in this study. The high surface recombination velocity and low bulk lifetime resulted in a decrease in the EQE response in the near infrared range. On the other hand, in the long wavelengths (>950nm) the response of the cells was decreased drastically. This is associated with both the bulk lifetime and degradation of rear surface passivation. The boron-dopants that were used to form the BSF in p-type wafers severely degraded the bulk lifetime of the material. It is likely that the contamination from dopants is diffused in the bulk during the high temperature diffusion process.

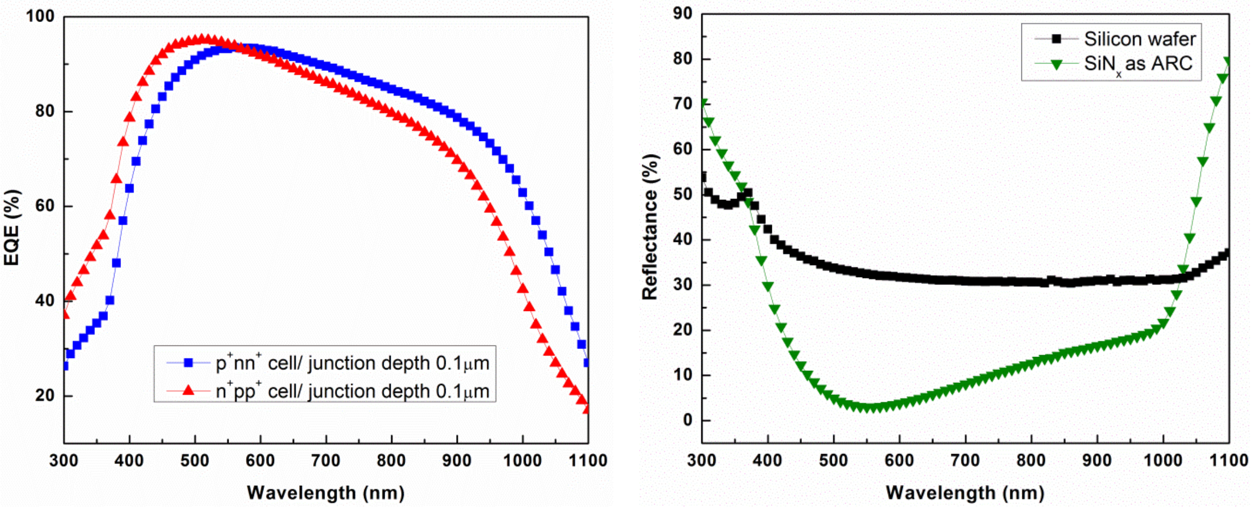

Figure 6.9 External quantum efficiency (EQE) of n^+pp^+ and p^+nn^+ solar cells

6.5.1 Effect of BSF on the Cell Response

Figure 6.10.a demonstrates the cell response for two p^+nn^+ cells fabricated on 350 µm silicon with shallow (=0.07 µm) and deep (=0.4 µm) junctions. The results show that the response of the cell with

shallow junction is higher in the short-λ range than with respect to the cell with deep junction. In another experiment a cell was fabricated on the 220 µm thick substrate. A 350 µm commercially available n-type wafer was thinned down in a silicon etchant solution containing HNO3/HF/CH_3COOH (4:1:1). The response of the cells with shallow emitters fabricated on the thick and thin substrates were studied (see Fig. 6.10.a). The increase of the EQE response of the thin cell in the near infrared region is due to an efficient BSF. To make a clear conclusion regarding BSF, IQE and reflectance results are required. In the thick cells, the minority carriers recombine in the bulk even before they can diffuse and reach the rear surface. The job of the BSF is to push back the minority carriers tending to reach the rear surface and recombine. Therefore if only a few carriers can reach the rear surface (in the case of thick wafer), having BSF or not will not have a big effect on the response of the cell. On the other hand, in thin wafers, there are more chances that the minority carriers can reach the rear surface and recombine. This needs to be avoided. Therefore, the importance of the BSF is higher here. One should also consider the back internal reflection of infra-red photons by the aluminum film.

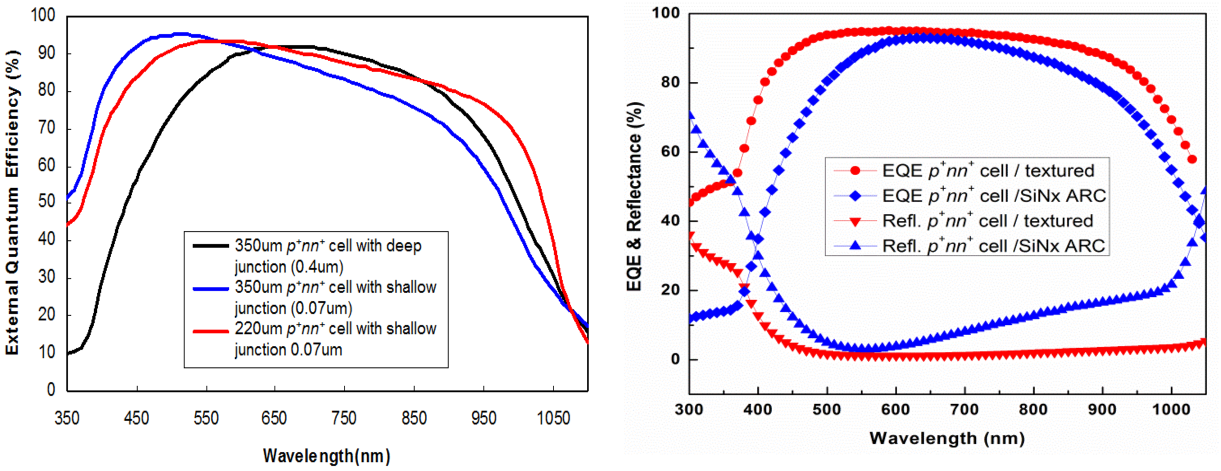

(a) (b)

Figure 6.10 a) External quantum efficiency (EQE) of p^+nn^+ cells with shallow and deep emitter junctions formed on the thin and thick substrate and 220µm substrate, b) EQE and reflectance of p^+nn^{++}cell with and without textured surface.

Higher efficiencies can be achieved with textured surfaces because of more efficient light trapping in the cell. Reflection is strongly reduced by the texturing process leading to improved external quantum efficiency (see Fig. 6.10.b). Texturing also results in an increase in the short circuit current density (J_{sc}). Due to the enlarged surface recombination no gain, in the open circuit voltage, generates in the absence of a good surface passivation layer.

6.6 Conclusions

Planar and textured crystalline solar cells were fabricated and characterized. The junctions were formed utilizing the spin-on-dopant sources and RTP. Low sheet resistances (80-100 Ω/□) and high active carrier concentrations (> 1 x 10^{20} cm^{-3}) are obtainable with the developed technology. The diode characteristics of the cells were demonstrated with dark I-V through measurement and modelling. The cells fabricated on the n-type wafers exhibit better illumination I-V responses with respect to the ones fabricated on the p-type substrate; which is mainly due to the higher bulk lifetime of the n-type substrates. The spectral performance of the cell is improved, after texturing, as a result of reduction in the reflectance in a wide range of the spectrum. These cells can be used as a benchmark for research on the luminescence down-shifting layers, as will be discussed in Chapter 7.

Chapter 7

Quantum Dot Layer for Luminescence Down-Shifting

In this chapter, practical and potentially low-cost methods are explored in order to improve the performance of solar cells using spectral down shifting. Luminescent down shifting ((LDS) layers containing cadmium selenide/zinc sulfide(CdSeZnS) quantum dots (QDs) with emission wavelength (λ) of 610 nm and luminescent quantum efficiency (LQE) of 30% as wavelength-shifting materials were embedded in transparent materials including oxide and spin on glass (SOG) and stacked on top of crystalline silicon (c-Si) solar cells. By means of absorption and re-emission, QDs shift the wavelength of the incident photons from the wavelengths where the spectral response (SR) of the solar cell is low to the wavelengths where the spectral response is high. Internal reflection of the re-emitted photons in the transparent host material ensures collection of the re-emitted light in the underlying solar cells which causes the photo voltaic device exhibits a better response.

Attempts on formation of the LDS layer, deployment of the layer on the c-Si cell and preliminary cell performance results on experimental verification of the spectral down-shifting of the incident photons in the LDS layer were reviewed. Results of the cell stacked with an LDS layer were compared with a control cell, which is defined as a cell with a non-luminescent layer of oxide/SOG, with the same thickness as used for the LDS layer. It was experimentally shown that the spectral response of the c-Si solar cell with an LDS layer is increased, with respect to the cell with a layer of QDs deposited on top. This is in contrast to the higher reflectance/absorbance of the LDS layer in comparison to the QD layer in ultraviolet-near infra-red (UV-NIR) ranges of the spectrum. This verifies the beneficial impact of LDS layers on c-Si cell. . No beneficial effect on the overall efficiency was observed for the cell with the LDS layer, as compared to the control cell. This is mainly due to the reflection/absorption losses in the LDS layer as a result of isotropic emission from the QDs which alters the light path.

Since LDS is a passive approach, it eliminates any interference with the active material of a PV device which is financially and technically favorable. Hence, the method does not add any complication to the production of the existing device. The factors that limit the LDS method from being perfectly beneficial include a high spectral response of the cells at short wavelength (λ), absorption in the host material, low quantum yield (QY) of QDs, a small portion of blue photons in the terrestrial spectrum, air mass 1.5 Global (AM1.5G), that normally uses SR measurements and finally isotropic re-emission of the emitted photons. Exploiting highly luminescent species, highly transparent host materials, alternate cell design structures, as well as using blue-weighted spectra needs to be considered to gain from the LDS method.

The suitability of the available materials for further progress on developments in this area is discussed. Finally, possible future research in the field of the LDS method, are highlighted.

7.1 Down Shifting to Enhance the Performance of c-Si Solar Cells

The impact of any new concept upon wafer-based silicon devices is of particular interest for the PV world, since about 90% of the global PV module production is involved [202]. A typical λ-dependent response of a solar cell can be described by external quantum efficiency (EQE), defined as the ratio of the number of electron-hole pairs generated to the number of photons incident on the front surface of the cell. Representative EQEs for a typical c-Si solar cell is shown in Fig. 7.1.

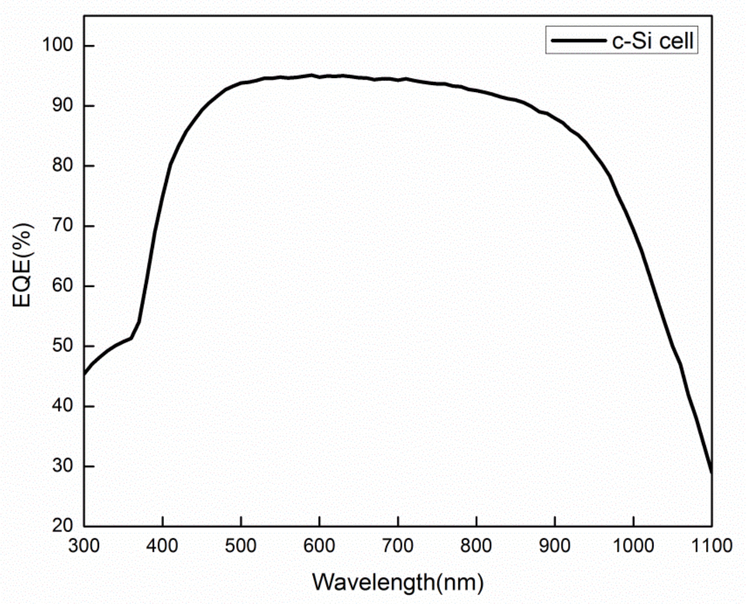

Figure 7.1 EQE of a c-Si solar cell

These cells exhibit EQE higher than 90% for most of the visible (VIS) part of the spectrum. Poor EQE is exhibited by the c-Si at λ<500nm, where interaction with higher energy photons occurs. Inefficient operation of the device in the UV regions of the spectrum is partly due to higher reflection and absorption by the anti-reflective coating (ARC), which are optimized for longer λ, and also increased emitter recombination due to its heavy doping. In order to better utilize the short-λ part of the solar spectrum adjustments in the design and technical processes of a device it is necessary to benefit from better electrical properties. However, these steps are complicated and expensive to exploit. Alternatively, implementation of an LDS layer on top of the cell can be most relevant. This layer is optically coupled to the cell with no interference with the active material of a PV device.

Wafer-based Si devices using the LDS method have been investigated by many research groups. A variety of materials and configuration of device layers have been investigated, in both theoretical and experimental approaches, causing a large disparity of results.

Some authors obtained very impressive values, of 30%-40%, due to many assumptions they made in their modelling and simulation including: high LQE of luminescent species, isotropic profile of emission spectra, zero re-absorption losses, minimum transmission losses, ideal properties of the host material, and ideal interfaces [107,203]. However, other approaches have led to more moderate results with up to 10% performance improvements [204]. Many authors utilized the cell without ARC and have reported an impressive improvement in cell performance due to the addition of the LDS layer. However, the large part of this improvement is because of the reduction in front surface reflection, due to the anti-reflection properties of the host materials when applied to the bare cell [23, 86,92 ,205, 206]. Only a few authors address the fact that a small portion of the performance improvement can be attributed to the LDS [95]. In all of these cases, by applying the LDS, a 0.5-3% improvement in overall efficiency has been reported. A small gain is predicted through re-optimization of the ARC for the new spectrum. Wafer-based Si devices are expected to benefit slightly from application of the LDS method as well. For the results to be more comparative and informative a device with an LDS layer was compared with a control cell coated with a non-luminescent layer of the same material, as well as a cell coated with a layer of QD. Nevertheless, there is potential to re-optimize the LDS layer to the red-shifted spectrum that is incident upon the cell.

The importance of the device dimensions should also be highlighted where it has been proven that the edge losses play quite a significant role in the improvement. A 1cm^2 cell was used; although this parameter was not considered in these experiments. Another important parameter, that needs to be noted, is that the authors have not measured cell performance in a uniform manner. Different solar spectra have been used by various authors for the EQE measurements. This is another reason for the discrepancy of the reported results. For all the measurements, AM1.5G was used.

The importance of selecting the luminescent material appropriate for the host material shouldn’t be neglected. The QY of the luminescent species should be maintained after inclusion in the host material. QDs and oxide/glass were used as luminescent and host material respectively. It is shown that the QY of QDs was maintained in the oxide/glass layers.

Finally, for any method with a prospect of commercialization, specifically for Si wafer-based PV devices, the efficiency improvement should be achieved at low cost and with minimal further complication in the manufacturing process. These are two key points that have been considered in the design and fabrication process of the LDS layer. Glass, an existing material, is utilized as the host material for the luminescent species, which can be applied on top of the Si PV device as passivation, ARC and encapsulation. Deployment of the LDS layer, containing CdSe/ZnS QDs in transparent oxide/glass medium, on a c-Si cell for spectral down-shifting of the incident photons is discussed in the following sections.

7.2 CdSe QDs: Structural and Optical Characteristics

In an approach using QDs as luminescent materials for PV, octadecylamine (ODA), stabilized CdSe quantum dots of various sizes with LQE of about 20% were purchased from a commercial manufacturer. Fig. 7.2.a shows a cuvette cell containing monodispersed colloidal QDs in liquid solvent. Fig. 7.2.b shows transmission electron microscopy (TEM) images of a diluted ensemble of CdSe quantum dots dropped and dried on TEM carbon coated copper grids and measured in a JEOL 2010F system. The image demonstrates that the quantum dots are separated from each other and no agglomeration is observed. The inset on top of this figure exhibits a high resolution transmission electron microscopy (HRTEM) image of the lattice structure and size of the QDs. The image reveals that the nanocrystals with an absorption peak at 610nm have a diameter of about 5nm. The Wurtzite crystalline orientation of CdSe QDs is evident in the Fast Fourier transform (FFT) image (see the bottom inset).

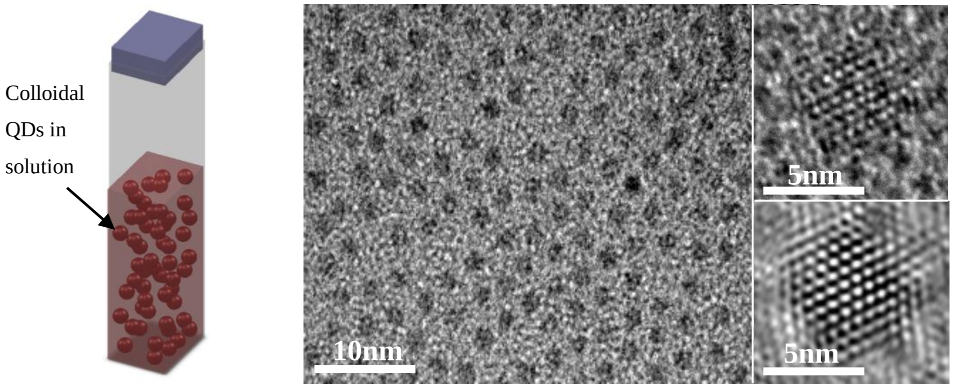

(a) (b)

Figure 7.2 a) Monodispersed colloidal QDs in liquid form, b) TEM images of the diluted ensemble of the CdSe QDs. The top inset is the HRTEM image of single CdSe QDs, the bottom inset is the FFT image of the QD.

QDs are nanometer-sized semiconductor crystals. Their emission wavelength can be tuned by their size [7]. Fig. 7.3.a shows schematic band diagram of CdSe QDs with diameters of 2.2nm, 3nm and 5nm overcoated with organic ligands, which result in emitted wavelengths of 470nm (blue), 540nm (green) and 610nm (red), respectively. As the size of QDs increases their band gap decreases, which results in a reduction in energy of the emitted photons.

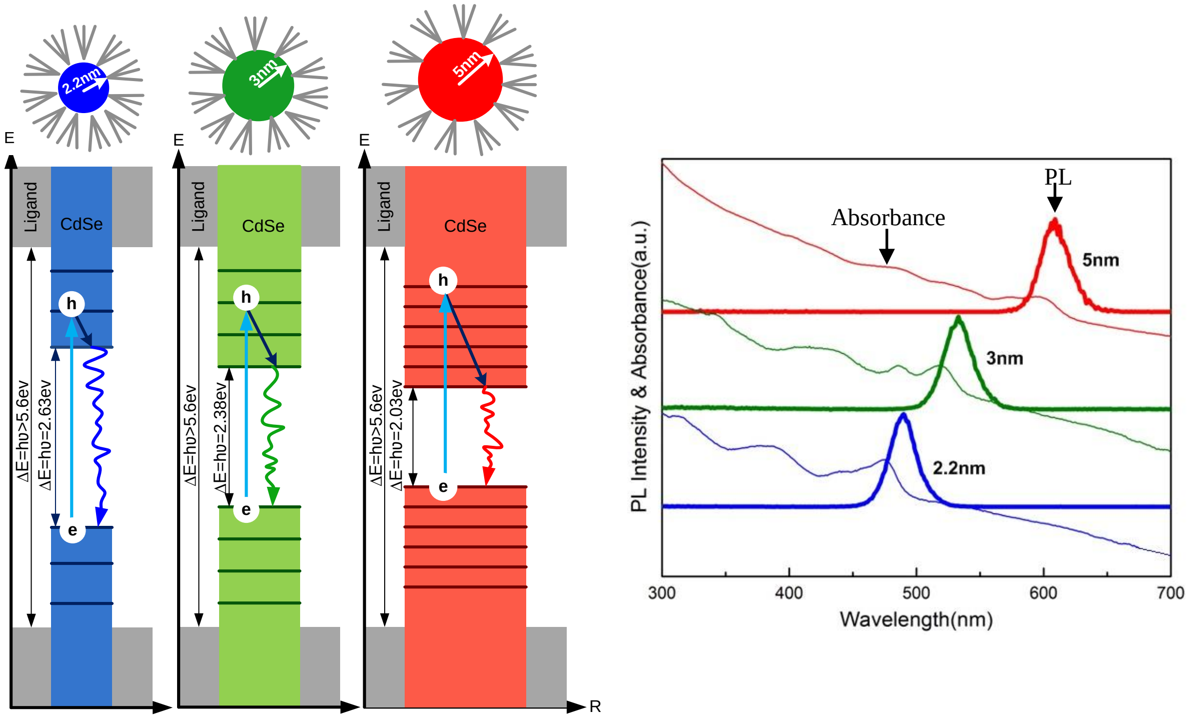

(a) (b)

Figure 7.3 a) Schematic band diagram of 3 sizes CdSe QDs overcoated with organic ligands, b) absorption/emission spectra of 3 sizes QDs CdSe QDs, capped with ODA dispersed in solution

Absorption and photoluminescence (PL) measurements were performed in a Lambda 1050 PerkinElmer UV-VIS spectrophotometer and a PL system from Edinburgh Instruments, respectively. This was done to obtain absorption-emission spectra of the CdSe quantum dots dispersed in solution. The cuvette cells with the equal quantum dot concentration were used for this experiment. Fig. 7.3.b shows that CdSe quantum dots, with a diameter of 2.2nm to 5nm, emit in a wide range from 470-610nm under 400nm excitation. Depending on the size of the quantum dots, the absorption and PL peaks appear in different wavelengths. Smaller sizes of QDs have a blue shifted spectrum in respect to the larger size nanocrystals.

These spectrums show that CdSe quantum dots are appropriate candidates to use as down-shifting luminescent materials for silicon solar cells; assuming that the device has optimum spectral response in the visible/red range of the spectrum. QDs have broad absorption bands that result in absorption of the entire light wavelength smaller than the absorption maximum. Introducing appropriate sizes of QDs in the LDS layer resulted in absorption of photons with λ<500nm where the response of the cell was low; and red shifted them to longer λ in the visible/red range where the SR of the cell is high. High brightness, stability, broad absorption band and high quantum efficiency are the advantages of QDs with respect to other luminescent material [33], which makes them potential candidates for use in down-shifting layers.

7.3 Core/Shell CdSe/ZnS QDs

7.3.1 Structural Characteristics in Liquid Form

Fig. 7.4 exhibits the TEM microstructure of the core/shell CdSe/ZnS QDs from commercial sources dispersed in toluene and stabilized by ODA ligands. The samples were prepared by dropping the diluted solution onto a carbon coated copper grid and air-drying them for a couple of minutes. No obvious aggregation can be observed in the images appearing in the bottom inset. The average particle size is 5nm. The lattice structure of the QDs in the zone axis is clear in the HRTEM image which indicates their Wurtzite crystalline structures (see inset on the top). The unclear interface between the CdSe core and ZnS shell can be due to the epitaxial growth of the shell. According to the manufacturer, the thickness of the shells is supposed to be <10nm; thinner than the coating of the TEM grids which is about 15nm. This could be another reason why the shell layer is not appearing in the image.

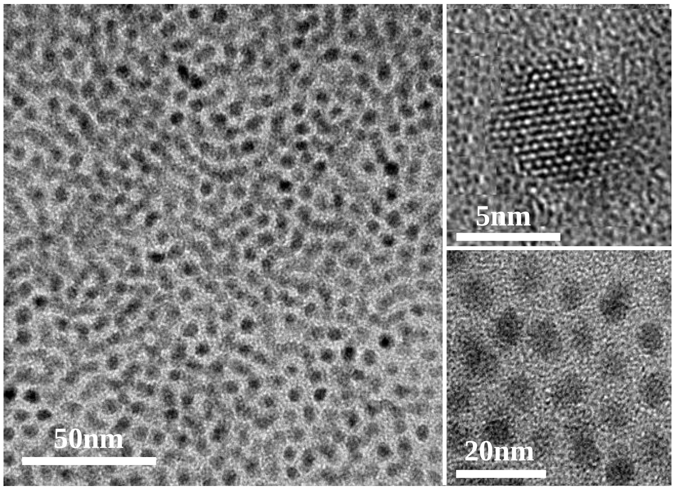

Figure 7.4 TEM micrograph of core/shell CdSe/ZnS QDs. The inset on the bottom right is the magnified TEM image of the QDs dispersed on the carbon copper grid. The inset above it is the HRTEM image of single QDs.

7.3.2 Layer Formation and Optical Characterization

CdSe/ZnS quantum dots were spin cast for layer formation from the material in toluene colloidal solution stabilized by ODA ligands. Spin coating conditions were controlled for the diluted and concentrated ensemble of CdSe/ZnS quantum dots to obtain thin films containing CdSe/ZnS with specific thickness and uniformity. Fig. 7.5.a shows schematics of a uniform QD layer deposited on a rigid substrate. A dedicated glove-boxed experimental setup was used to ensure a safe environment for processing and to have a controlled ambient for the film formation.

For the deployment of QDs in the LDS layer, QDs of centre emission wavelength of 610nm were used. Thus, they would absorb both blue as well as green incident light. The assumption was that the solar cell had an optimum spectral response in the red; hence at this wavelength the strongest effects were expected. The absorption and emission spectra for the QD layer deposited on a quartz substrate are shown in Fig 7.5.b. These spectra have been normalized with respect to the absorption and emission maximum occurring at 600 and 610nm, respectively. The particle diameter is 5nm according to the HRTEM image shown in the previous section. The diameter can also be determined from the relation between absorption maximum and particle diameter as reported in literature [206].

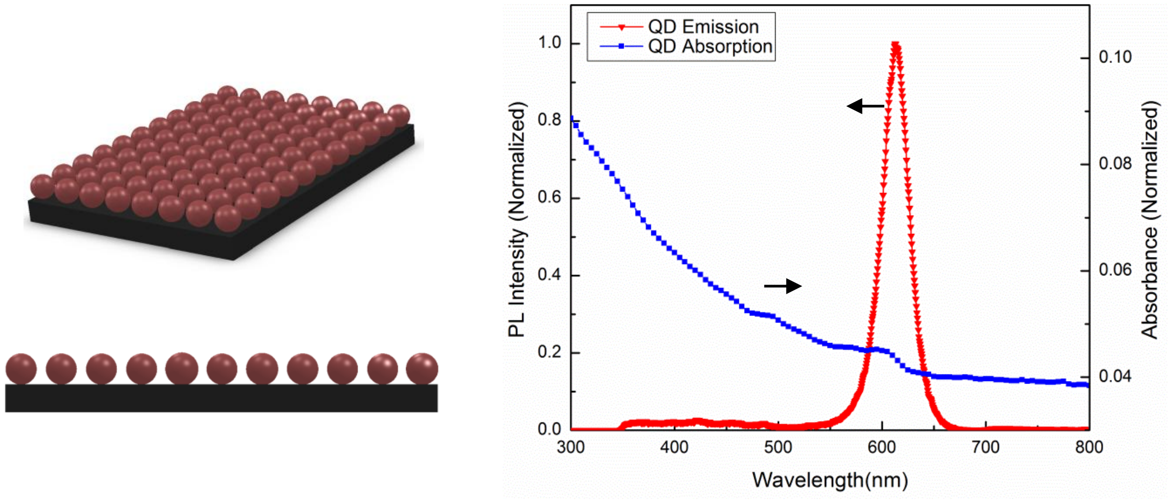

(a) (b)

Figure 7.5 a) Schematics of a uniform QD layer formed on a substrate, b) absorption/emission spectra of 5nm core/shell CdSe/ZnS QD layer

The excitation and emission scans were performed on the QD layer in order to find the excitation and emission maximum of the sample. The graph in Fig. 7.6 indicates that for the 5nm QDs the emission peak is at 610nm. The emission maximum intensity is achieved when the sample excites at 400nm (excitation maximum). These measurements were performed in an integrating sphere. The absolute value of the quantum efficiency of the QDs was measured at about η=30%.

The emission map of the CdSe/ZnS QDs is presented in Fig. 7.7. Looking at the graph in Fig. 7.7.a, it is clear that the highest emission intensity is related to the excitation at 400nm, which is the excitation maximum wavelength. The inset in this graph shows that the emission intensity is almost zero at the excitations in the 200nm-250nm range. It is still very low, at the excitation wavelengths in the range of

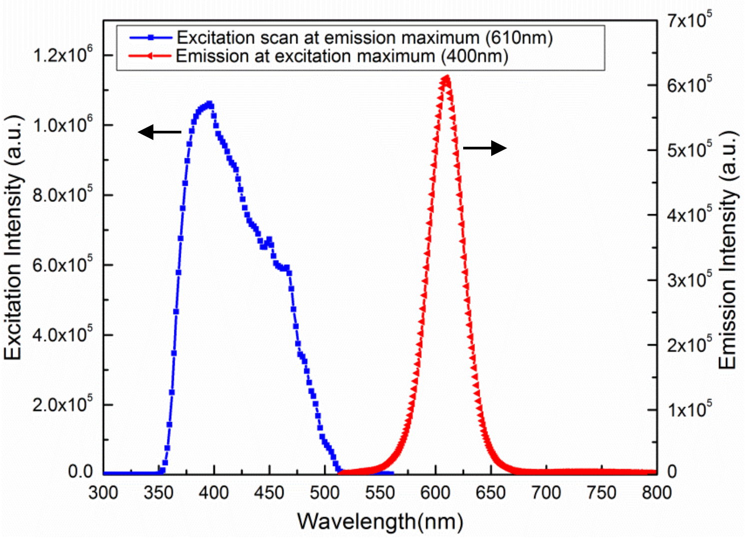

Figure 7.6 Blue line: excitation scan for CdSe/ZnS QDs at emission maximum (610nm); red line: emission scan at excitation maximum (400nm)

300-350nm, when compared to the excitation at 400-500nm. The emission map shown in Fig. 7.7.b depicts the excitation wavelengths at which the emission spectrum has been recorded. The map has been recorded in a 3-D image for more clarification. This image clearly shows that the emission peak is the highest when the QDs excite at 400nm. The emission intensity decreases at the excitation wavelength close to this wavelength. Also, there is no emission at the excitation wavelength, very much lower (<300nm) or very much higher (>600nm) than the excitation maximum (400nm).

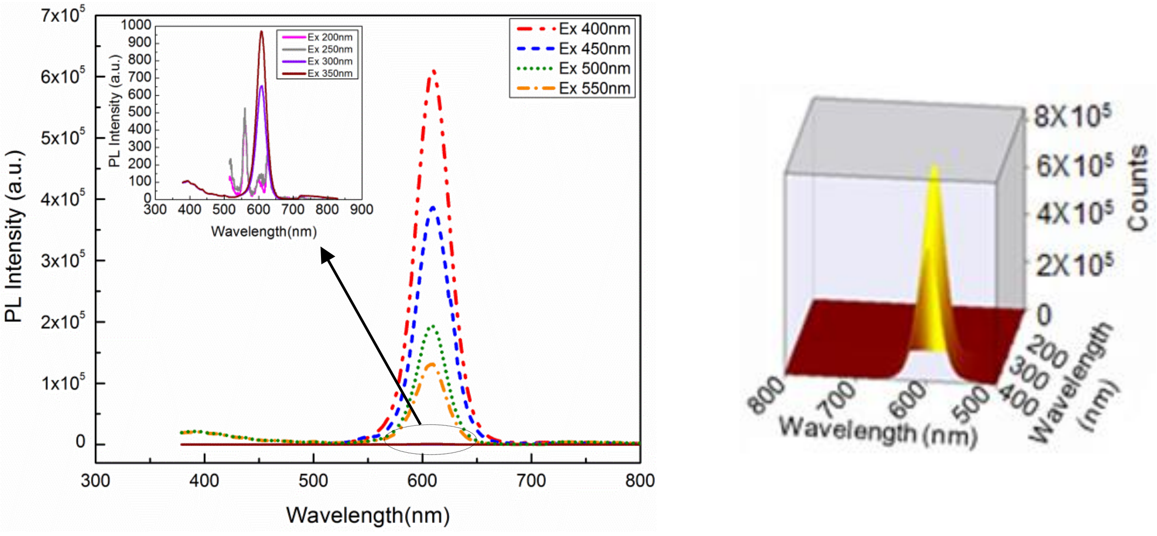

(a) (b)

Figure 7.7 a) Emission map at different excitation wavelengths for CdSe/ZnS QDs. The inset shows the weak peaks corresponding to the excitation wavelength lower than 400nm, b) 3-D excitation-emission map.

7.3.3 Core (CdSe) QDs vs. Core/Shell (CdSe/ZnS) QDs Photoluminescence Response

The absorption and emission spectra of CdSe/ZnS QDs and CdSe QDs, both deposited at equal concentration on a quartz substrate, are compared in Fig. 7.8.a. CdSe and CdSe/ZnS QDs exhibit a transition in the visible range with an excitonic absorption at 590nm and 600nm respectively. Core-shell CdSe/ZnS QDs exhibit stronger and narrower excitonic luminescence as compared to CdSe QDs under 350nm excitation, due to surface passivation. The apparent stokes shift is related to the influence of the shell part (ZnS), at a QD surface, on the electronic structure of nanocrystals. Adding a layer also affects the refractive index of the whole structure. Fig. 7.8.b compares exciton decays in CdSe (core) and CdSe/ZnS (core/shell) QDs; while Fig. 7.8.c compares the exciton decays in QDs with different sizes.

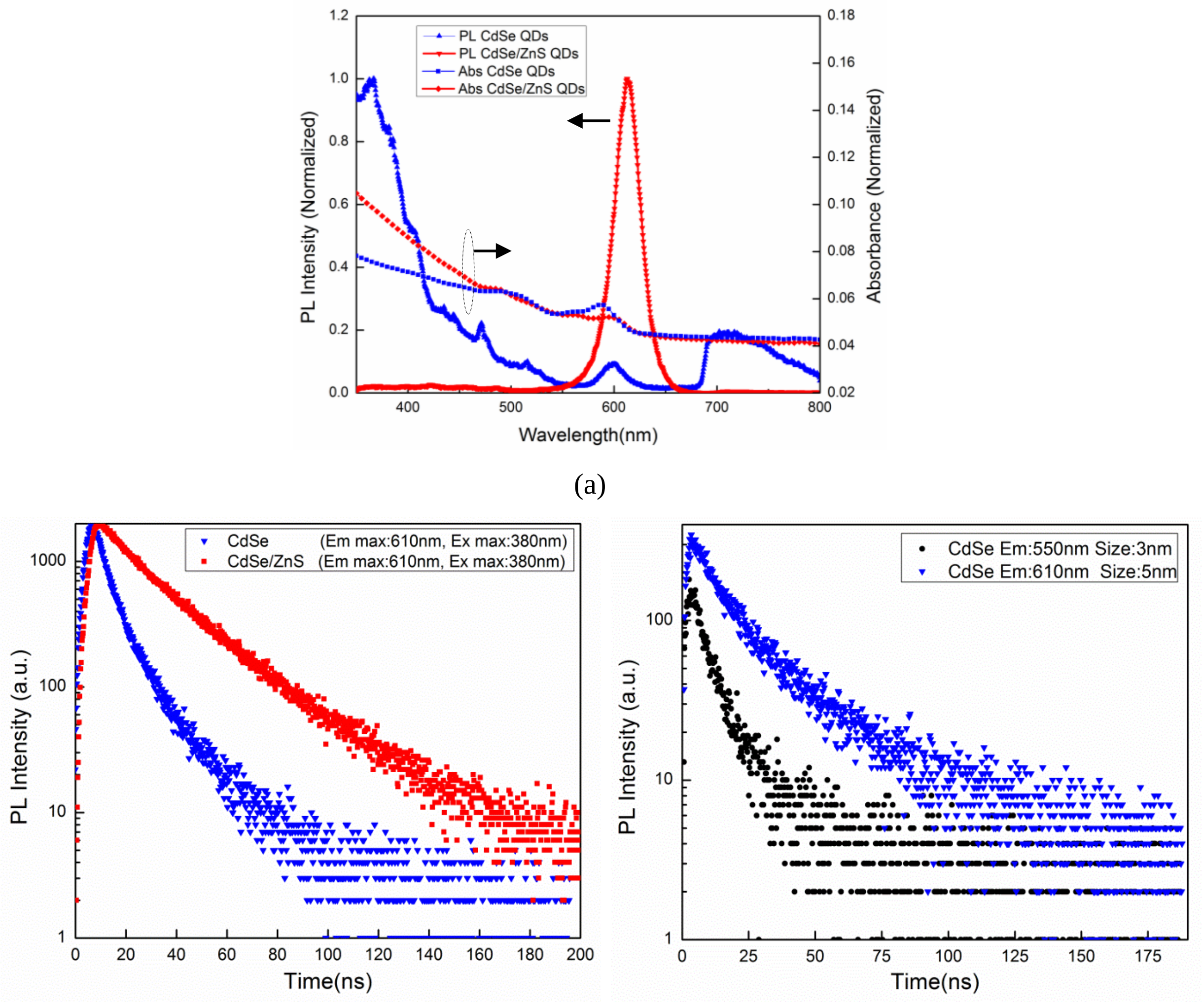

(a)

(b) (c)

Figure 7.8 a) Absorption and PL spectra of a layer of CdSe/ZnS and CdSe QDs; The emission spectrum was recorded using excitation at 350 nm, b) exciton decays in CdSe (core) and CdSe/ZnS (core/shell) QDs, c) exciton decays in CdSe QDs with different sizes

All the decays are measured at room temperature (300k). The results indicate faster decay for core QDs in respect to core/shell QDs. Rapid decays were also observed for the smaller size QDs. The high decay rate is normally due to nonradiative transitions.

7.3.4 Physics of Photoluminescence in Passivated and Non-passivated QDs

The small shift, in the absorption/emission spectra of QDs to the red (lower energies) after overcoating them with ZnS shell, can be due to partial leakage of the exciton into the ZnS matrix. It has been observed that this red shift is more pronounced in smaller dots where the leakage of the exciton into the ZnS shell would have a more dramatic effect on the confinement energies of the charge carriers. This effect is schematically shown in Fig. 7.9.

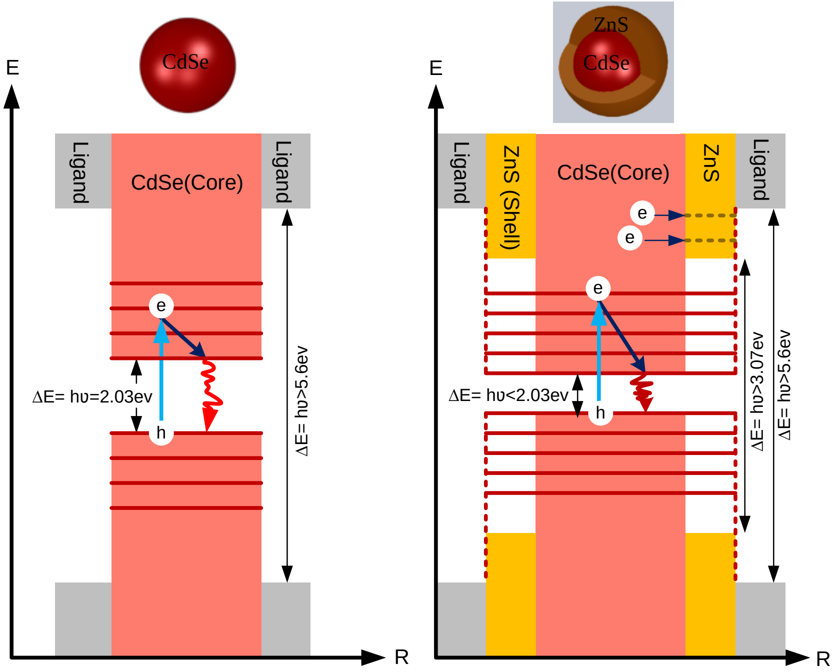

Figure 7.9 Schematic illustration of the red shift in the absorption/emission spectra of CdSe/ZnS with respect to CdSe

The high surface to volume ratio of the organically capped QDs, with no additional coating layers, results in the PL being dominated by broad deep trap emissions due to the incomplete surface passivation. The passivation of QDs with ZnS suppresses deep trap emission by passivating most of the vacancies on the crystalline surface, resulting in the dramatic increase in the PL yield dominated by band edge recombination (See Fig 7.10).

In Fig 7.10 a schematic illustration of the different decay paths in core/shell QDs is also presented. As mentioned earlier, rapid decay is normally due to nonradiative transitions. Nonradiative transitions increase for the QDs with higher surface states. At a temperature above 2K the exciton lifetime of QDs depends on QD size and surface. Surface defects are more prevalent in core QDs with respect to the core/shell QDs hence the decay rate is higher in non-passivated QDs. Stabilization of surface trap states, lengthening their average lifetime, could occur by a light-activated rearrangement of surfactant molecules. This would increase the probability of thermalization back to the lowest emitting exciton states thus enhancing QD PL. ZnS shell also stabilized the surface. Thus, intense PL could be seen in core/shell structures with respect to the core structures. In core/shell QDs, the interface states also cause non-radiative transitions.

A lower PL for the smaller size QDs is in agreement with the expectation of the electron-hole exchange interaction for decreasing QD sizes. At T>20K, in smaller size QDs, the surface becomes more important and lead to non-radiative transition and lower the PL. Core/shell structures were used, as they were found to be more efficient to use as luminescent shifting materials in the LDS layers.

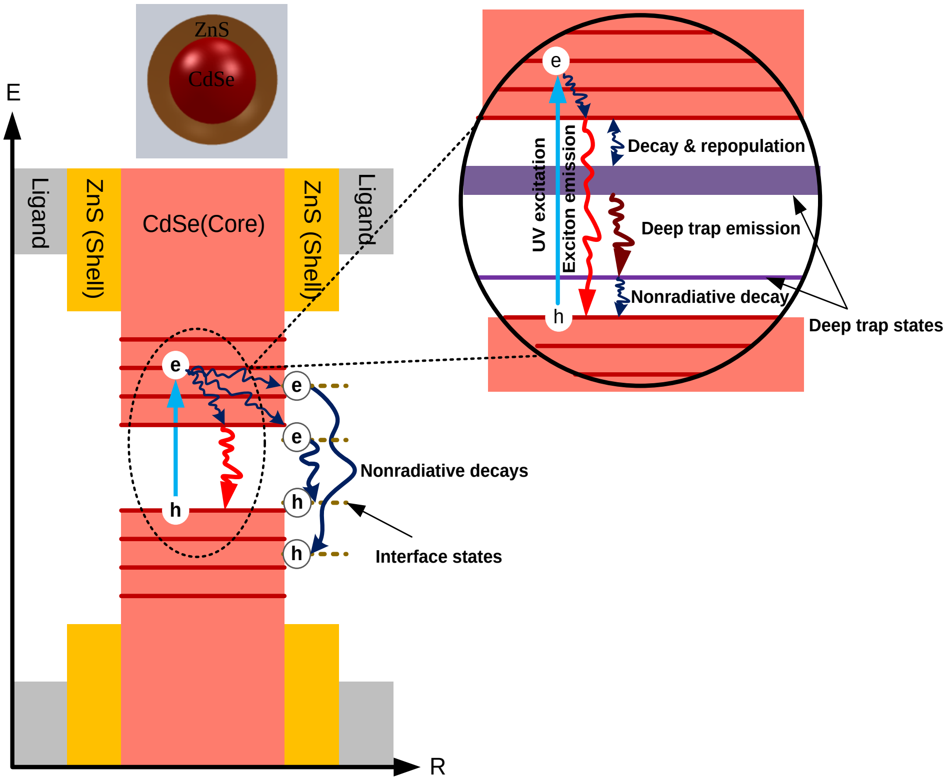

Figure 7.10 Schematic illustration of the different decay paths in core/shell QD structure

7.4 Methodology for LDS Layer Design and Fabrication

7.4.1 Device Configurations

The device configurations that were studied are depicted in Fig. 7.11. In the first architecture, QDs were spin cast on a thin transparent layer deposited on top of the c-Si solar cell to isolate the luminescent material from the cell. The schematic in Fig. 7.11.a illustrates the steps involved when the QD layer is added on top of the cell. In the second architecture, the QDs are fully buried in the transparent layer, by deposition of the second layer of the host material onto the QDs, to form the LDS layer on top of the cell. The schematic in Fig. 7.11.b illustrates the steps involved in the deployment of the LDS layer on top of the cells. Thickness of the QD layer can be varied by spin coating conditions and QD concentration. As the QD concentration increases, the modified photon flux density increases [96]. Optimum values for QD concentration are required in order to provide a large number of emitted photons. It should be noted here that highly concentrated QD layers would not be as efficient as expected, due to the re-absorption of the emitted photons by the QDs, where there is an overlap for the absorption and emission spectra. This will lower the number of emitted photons that enter the solar cell. At an optimum QD concentration unabsorbed blue and green light also enters the solar cell. The thickness and transparency of the oxide

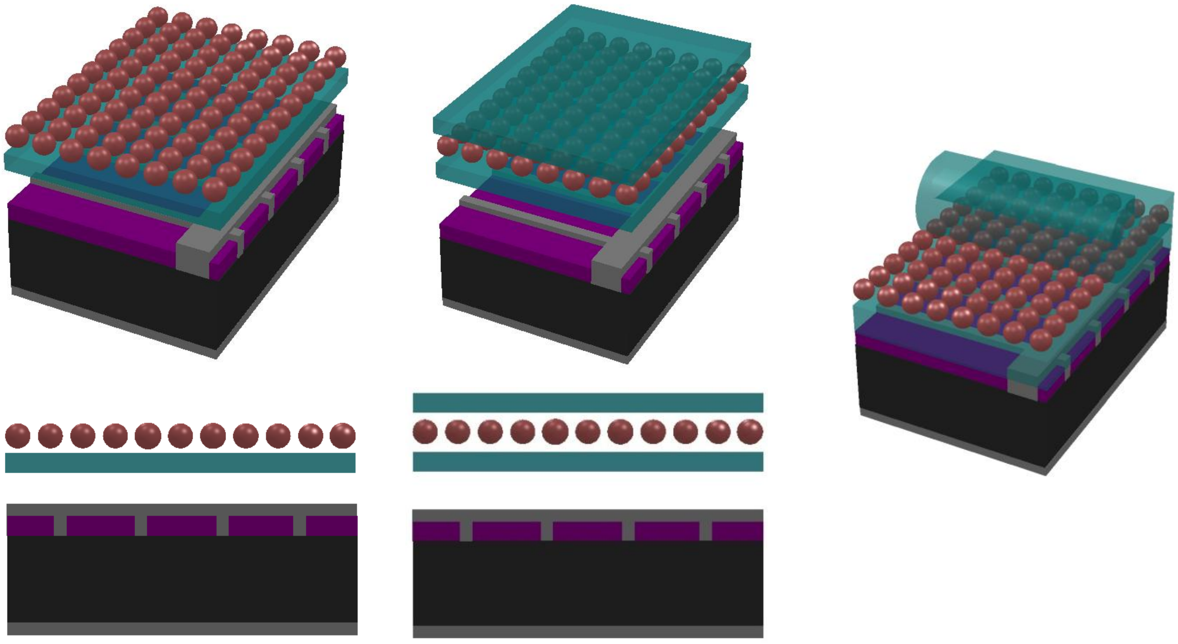
(a) (b) (c)

Figure 7.11 3-D and cross section schematics illustrating steps involved in deployment of the a) QD and b) LDS layers on top of the cells, c) schematic of the cell with an LDS layer

layer also play key roles. Nevertheless, a relative increase of nearly 10% is realizable by applying the LDS. The schematic in Fig. 7.11.c demonstrates a cell with an LDS layer deployed on top.

A simplified diagram of the optical processes, involved in an LDS layer applied on top of a cell, are presented in Fig. 7.12. Light having wavelength within the absorption band of the luminescent species will be absorbed and re-emitted at a longer λ. The emphasis of these diagrams is on the path of down-shifted photons. By having a cap layer with refractive index larger than the air, a large proportion of the luminesent down-shifted photons are transmitted to the underlying cell, either directly or following internal reflection. A small proportion of the down-shifted photons scatters to the top escape cone. A part of the emitted photons enters the cell via reabsorption and re-emission by another luminescent species.

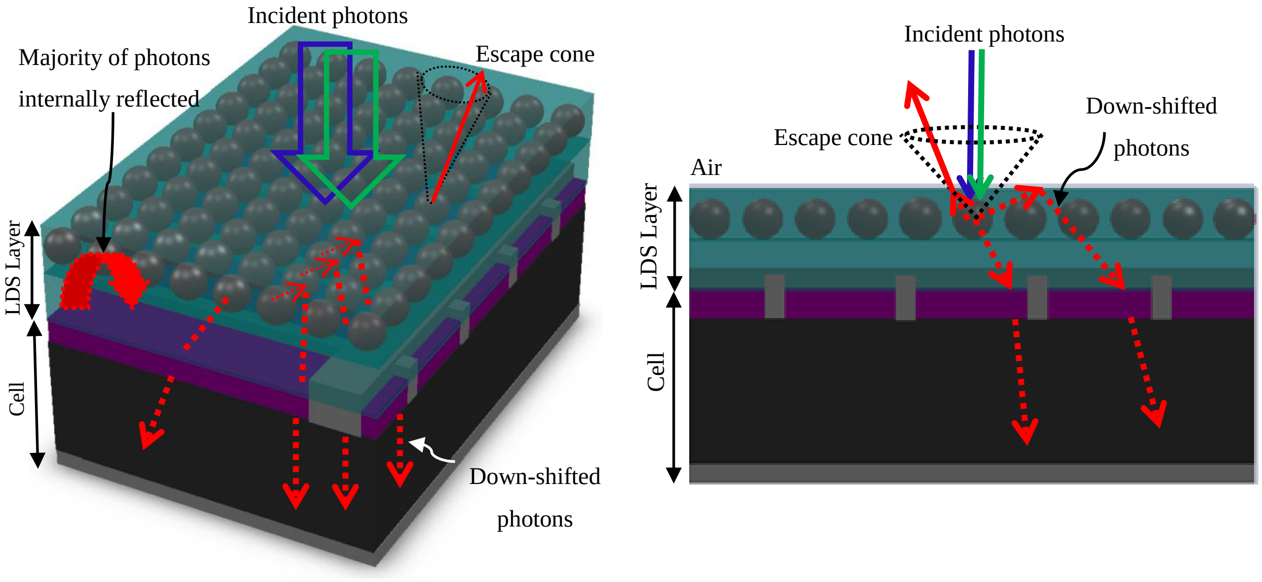

(a) (b)

Figure 7.12 Diagrams of a cell with an LDS layer on top. Both blue and green lights are absorbed by the QD and re-emitted in the red; a majority of them are expected to subsequently absorb in the solar cell via internal reflection in the medium

The emphasis of the diagrams exhibited in Fig. 7.13 is on the path of down-shifted photons for the configuration, with no capping layer. Only a small proportion of the luminesent down-shifted photons are transmitted to the underlying cell. A large proportion of the down-shifted photons will scatter to the top escape cone. Note that in both cases a portion of the luminescence will be emitted through the side of the LDS layer. Only a slight part of the light, that is not absorbed by the luminescent species, will be transmitted to the cell.

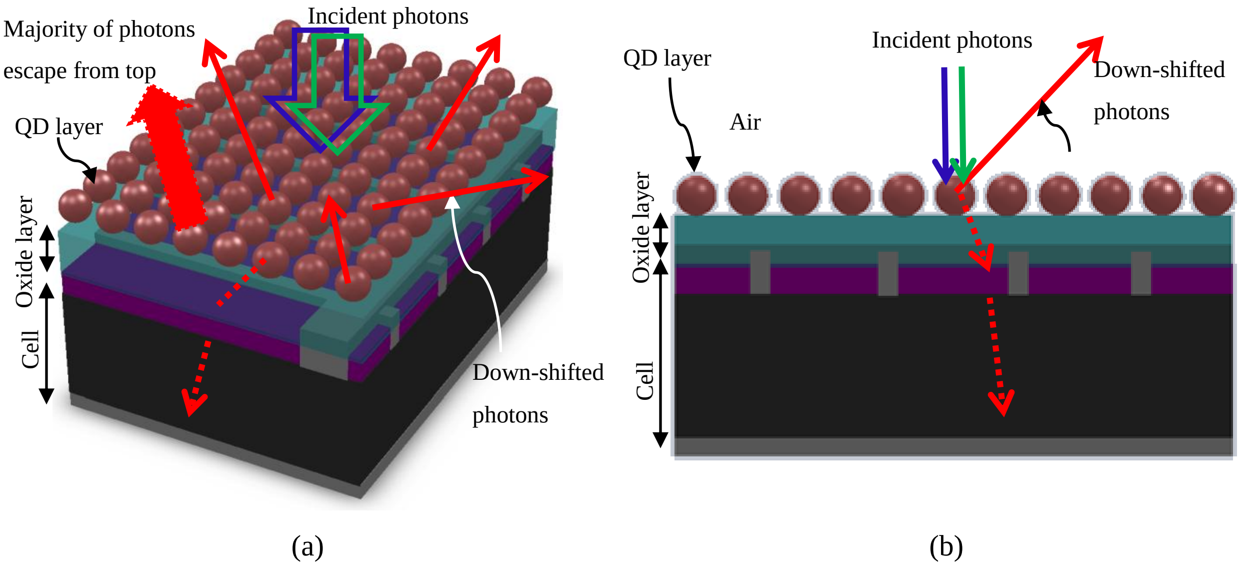

Figure 7.13 Diagrams showing a cell with a QD layer deposited on top with no capping layer. Both blue and green lights are absorbed by the QD and re-emitted in the red, majority of them escape from the top escape cone.

7.4.2 Formation, Structural and Optical Characteristics of the LDS Layers

Architecture 1. CdSe/ZnS QDs Embedded in Oxide Layers

A transparent layer consisting of ordered arrays of core/shell CdSe/ZnS QDs embedded in thin oxide layers were prepared by embedment of the films of QDs in an oxide layer to use as spectral down-shifter. The oxide layer was deposited by an electron beam (e-beam). The formation of well-ordered arrays of QDs is revealed by TEM, PL measurement and fluorescence imaging. High transparency and intense PL peaks are the main characteristics of the arrays of QDs introduced into the oxide layer. The EQE results show that near-optimum QDs and oxide thicknesses increase the quantum yield while decreasing the reflection of the layer in the UV-NIR range respectively. The scattering of the emitted photons to the top escape cone of the cell reduces the effectiveness of the layer.

Formation and Structural Characteristics

The QDs were embedded in an oxide medium using a combined e-beam layer deposition of SiO_2 and spin cast of QD films. After RCA cleaning of the substrate and also dipping the silicon substrates in 2% hydrofluoric acid (HF), samples were loaded in the chamber of an Intlvac e-beam system. At a base pressure of $1.6X10^{-6}$ mTorr and substrate temperature of 150ºC, a thin layer of oxide was deposited on the wafers from silicon dioxide pellets at a rate of 12A°/s.

A monolayer of QD formed on the deposited oxide layer by dropping 2μL of CdSe/ZnS QD from a 5mgmL^{-1} solution and rotating for 30s at 2500rpm. The samples were then loaded in the e-beam system and another layer of SiO_2 was deposited onto the QDs to completely bury them in oxide and form a capping layer. The TEM images in Fig. 7.14 a_1, b_1 show a layer of QDs deposited on the oxide layer before and after full embedment in oxide respectively. In the latter structure the QD layer was deployed between two thin layers of oxide with a thickness of about 5nm. Fig. 7.14.a_2, b_2 are the magnified images of the same structures, revealing the formation of the quantum dot arrays. The HRTEM images in Fig. 7.14.a_3, b_3 clearly indicate the crystalline structure of the QDs, as well as the periodic spacing between the dots for these structures. Also the e-beam process helps fill the narrow gaps between QDs.

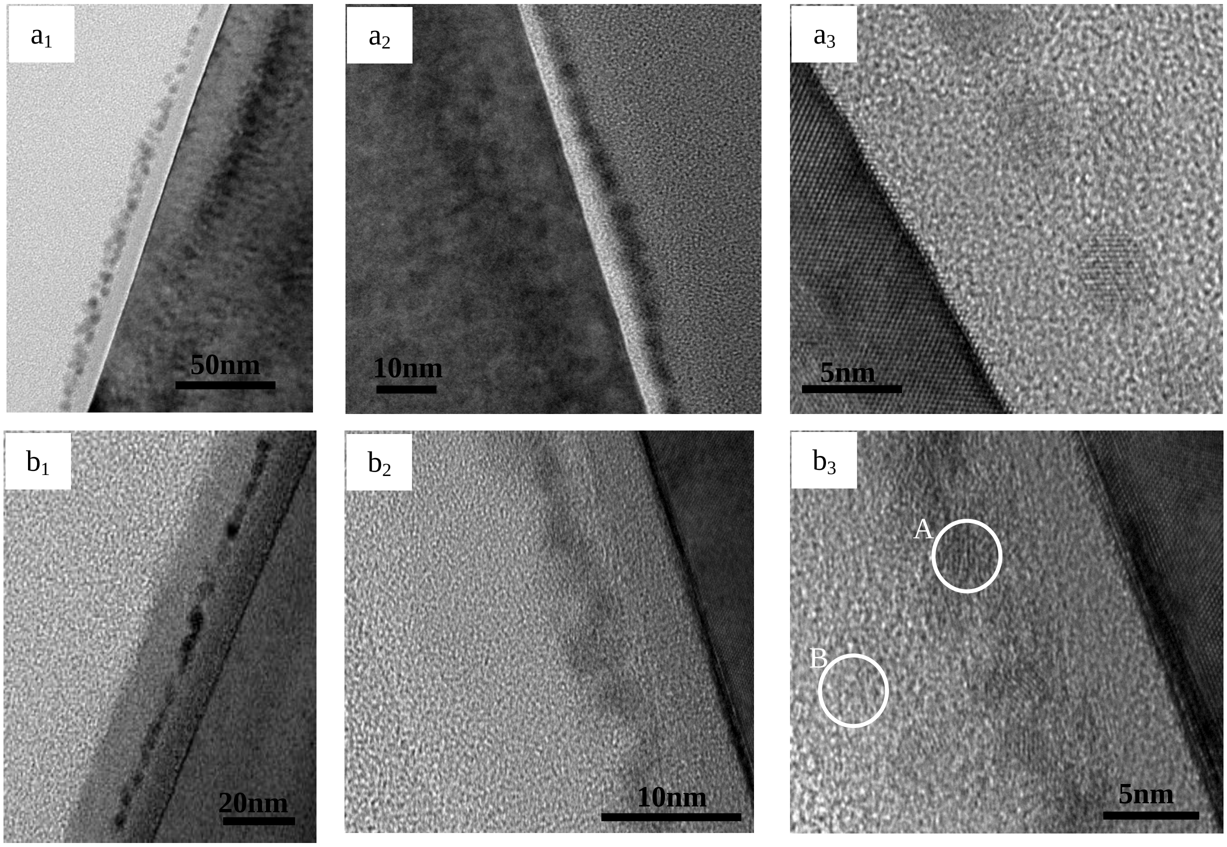

Figure 7.14 TEM and HRTEM micrograph of the ordered arrays of QDs, deposited on an oxide layer with no cap layer (Group a); TEM and HRTEM micrograph of the QDs after deposition of the cap layer and complete embeddment in oxide (Group b)

In Fig. 7.15.A,B, the composition of QDs inside the oxide medium (Fig. 7.14.b_3-A) and the oxide layer (Fig. 7.14.b_3-B) is shown using an in situ energy dispersive X-ray (EDX) analysis. From the EDX data the main components of the oxide/QDs/oxide structure are oxygen, sulfur, cadmium, selenium, zinc and silicon.

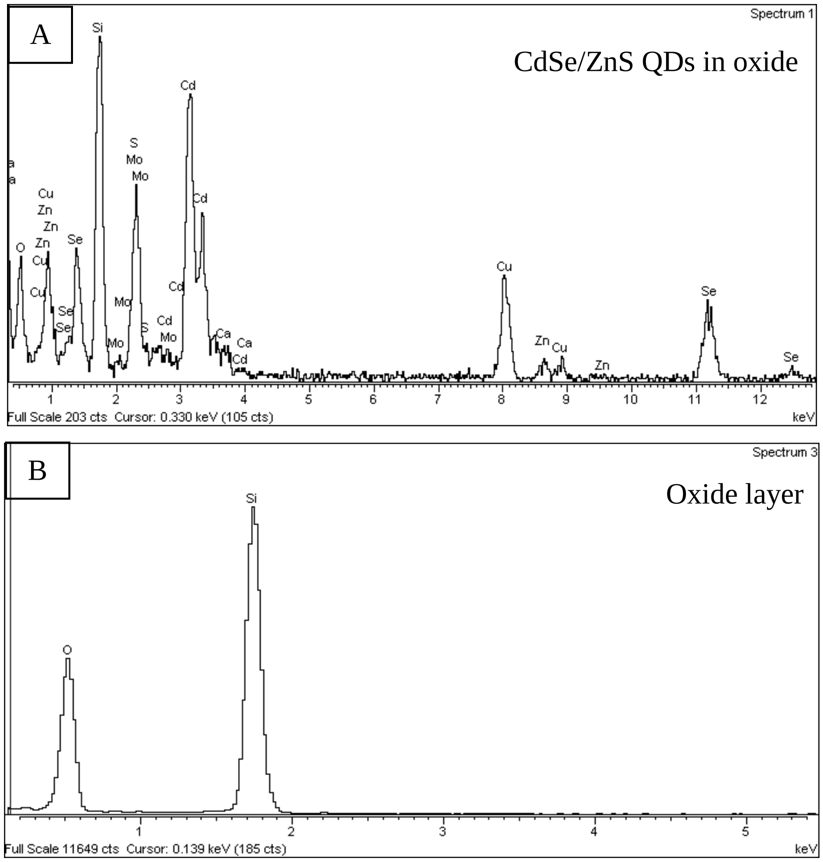

Figure 7.15 EDX of A) CdSe/ZnS QDs embedded in oxide medium, B) oxide layer

Optical Characteristics

It needs to be noted that the QY of QDs decreases after inclusion in some mediums. One key factor in choosing the medium is that the QY of the luminescent species should be maintained after inclusion in the host material. In Fig. 7.16, the absorption/emission spectra of the QDs are compared before and after embedment in an oxide matrix. No significant scattering was detected in the absorption spectra; and the oxide layer was transparent. The PL spectra of the QDs remained unchanged after incorporation into the oxide layer. The narrow peak at 610nm in PL spectra revealed the uniform dispersion of QDs in the oxide matrix. The intense PL peak showed a fairly high QY of the medium. The results showed that the optical properties of the QDs were preserved in oxide.

The fluorescence images of the QD layers, before and after embedment in oxide, are shown in Fig. 7.17 group-a and group-b, respectively. These images are also the indication of the formation of uniform layers of QDs with relatively high QY. The CCD camera is capable of capturing the black and white images as shown in Fig. 7.17.a_1, a_2 and Fig. 7.17.b_1, b_2. The color was applied to the images by the Image-Pro 6.1 software. Red tint, close to the real fluorescence color of the sample (see Fig. 7.17 a_3, b_3), was selected.

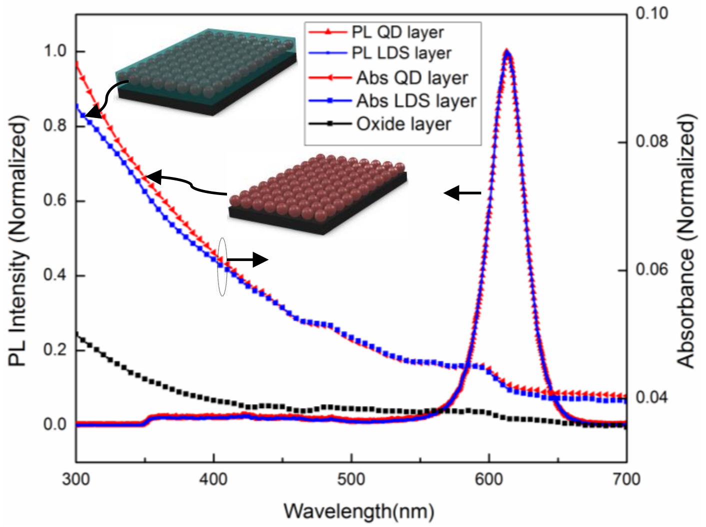

Figure 7.16 Absorbance and PL of the LDS and QD layer

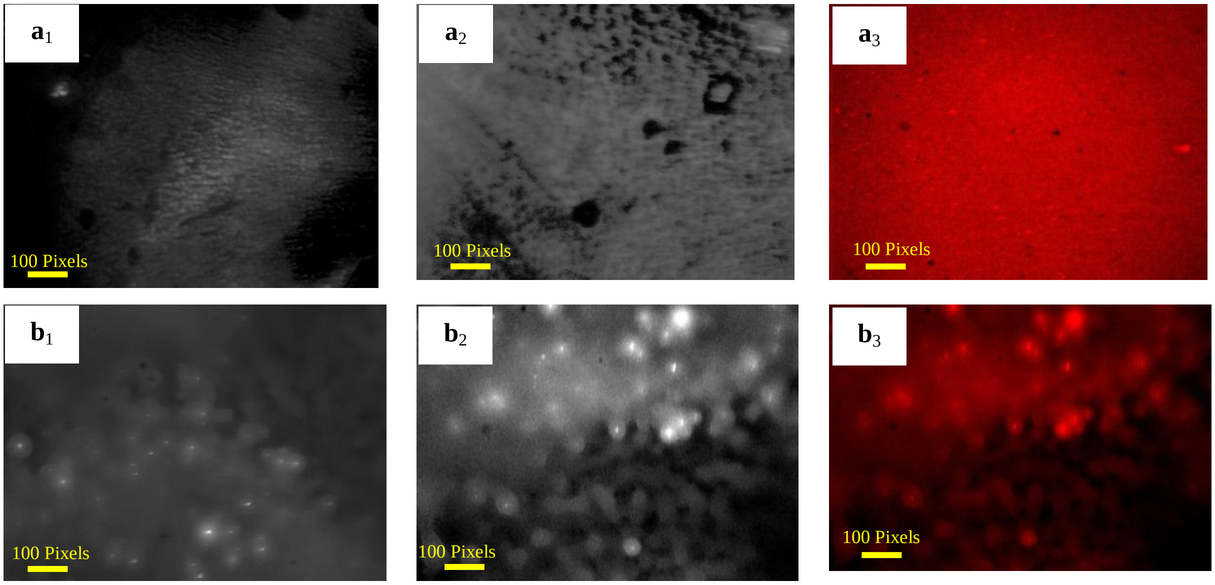

Figure 7.17 Flourescence images of the QD layer before (group-a) and after (group-b) embedding in oxide

Cell Characteristics after Deployment of the LDS Layer: Proof of Down-shifting

The QD and LDS layers were deployed on top of the c-Si cells and the performance of these cells was compared with a control cell. As a result of the luminescent process, a proportion of the incoming photons were shifted to longer wavelengths, before they reached the photoconductive layers of the cell, which then responded better to the altered spectrum. Hence, more electron–hole pairs can be created per incident photon and a higher short circuit current (I_{sc}) can be generated and the EQE will be increased. The open-circuit voltage (V_{oc}) and fill factor (FF) will not change significantly, since there is no change in the electronic properties of the semiconducting material. Thus, an increase in conversion efficiency is expected as a result of the increased current generation.

An n^+pp^+ c-Si cell was used; fabricated in the laboratory as described in Chapter 6, in a 1cm^2 area, with a thickness of 300μm, shallow diffused emitter of 100 **Ω/□** and with no preliminary passivation. The aim of applying QDs as wavelength shifters is only sensible when an appreciable difference exists in spectral response, between the QD centre emission wavelength and the lower wavelengths. The initial SR of the fabricated c-Si is low at short-λ, hence some beneficial effects may be achieved upon the LDS application.

Fig. 7.18.a, b, represents the experimental verification of the LDS method. In order to have a uniform comparison, the EQE and reflectance three types of cells are compared: a cell with a non-luminescent layer of oxide; a cell with a coating of QD layer isolated from the cell by an oxide layer and a cell with a DSL layer. Normalized emission and absorption spectra of CdSe/ZnS QDs, along with the spectral irradiation of the 900W Xe lamp, which was used as the excitation source for PL measurement, are illustrated in Fig. 7.18c. The spectra show that the lamp is intense in the range of 300-650nm with the highest intensity at 480nm. Light having λ within the absorption band of the QDs (300nm-600nm) will be absorbed and re-emitted at longer λ (~610nm).

The graphs, in Fig. 7.18.a-c, visually represent how the LDS process shifts parts of the spectrum to a region of higher cell EQE. The c-Si cell exhibits a decreasing EQE for λ<600 nm (see Fig. 7.18.a, b). CdSe/ZnS QDs that absorb in the region with λ<600nm and emits at λ>600nm are shifting part of the incident irradiation (see Fig. 7.18.b,c), from wavelengths where the cell is performing poorly (EQE of 0–15%), to longer ones where the cell is performing better (EQE of ~65% with no antireflection coating).

The spectral distribution of the photon flux for different solar spectra [207] is also plotted in Fig. 7.18.d. This is in order to consider the process in terms of available blue/green photons for LDS. Note that more gains can be made when more photons are available to be shifted. It has been shown that blue weighted spectrums such as an air mass zero (AM0) spectrum exhibit a 50% greater improvement in comparison to AM 1.5G [208]. The diffuse solar irradiation (AM 1.5diff) results in three times higher relative improvement in comparison to AM1.5G and four times in comparison to direct solar spectrum (AM 1.5D) [96].

As shown in Fig. 7.18.b, the spectral response of the cell, with a coating of a QD layer, is lower than the cell with no luminescent layer; which seems to be related to the amount of absorption. This absorbance is quantified through Lambert Beer’s law.

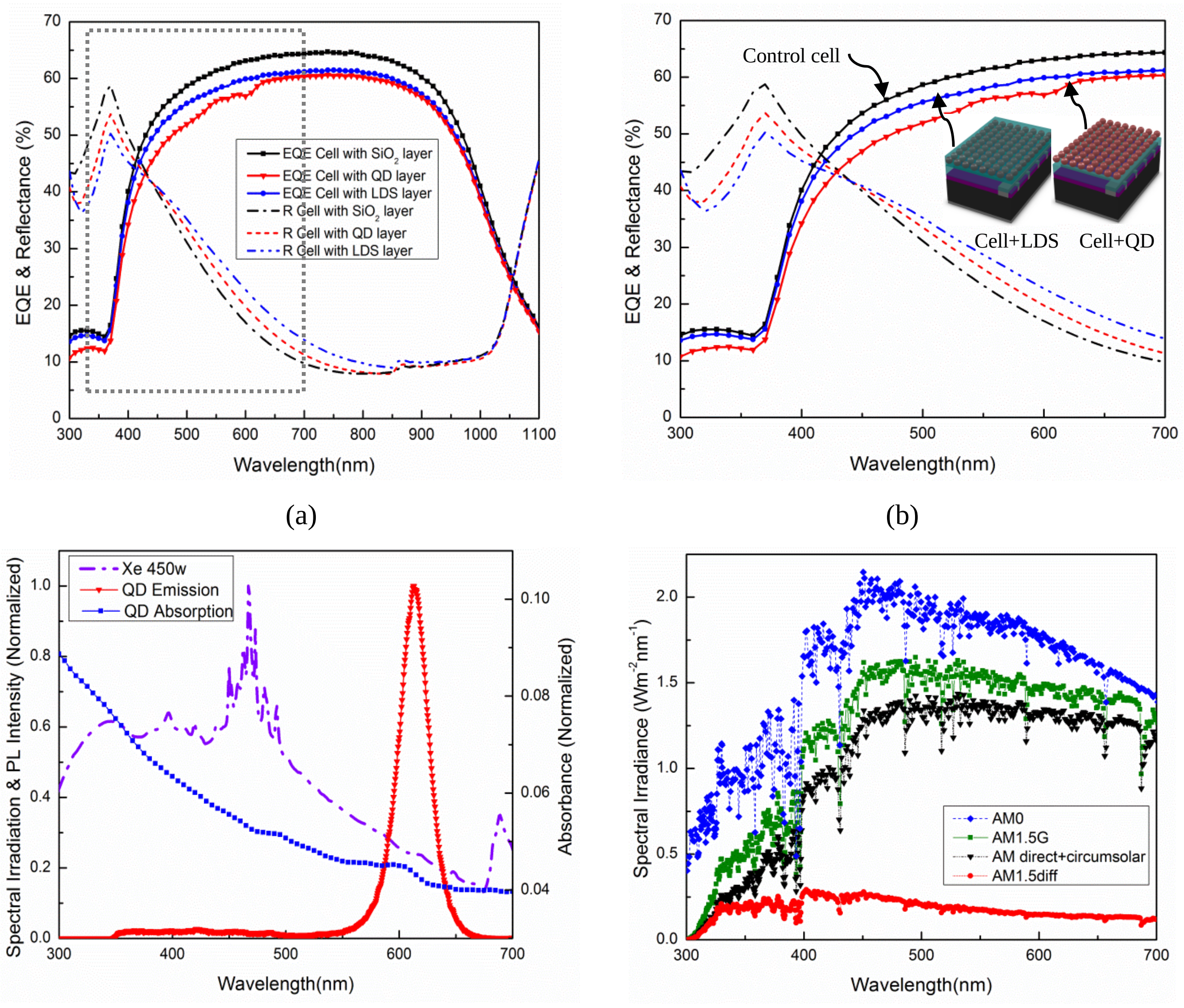

(a) (b)

(c) (d)

Figure 7.18 a) EQE and reflectance of cells with a non-luminescent layer of oxide (black), an LDS layer (blue) and a layer of QD (red) deployed on top, b) zoom-in view of (a) in the 300-700nm range, c) absorption/emission of the QDs embedded in the oxide medium. The spectral irradiation of the Xe lamp is also shown, d) solar spectra

$$A = log_{10}\frac{I}{I_0} = \varepsilon(\lambda)Lc \qquad (7.1)$$

In equation (1) A is the absorption which is defined as the logarithmic relative decrease of intensity where I_0 and I are the intensities before and after the light passes through the QDs. The absorption is also called optical density (OD), so if OD=1, this states that only 10% of the light passes (i.e. 90% is absorbed). The wavelength dependent coefficient ε (λ) is called molar absorptivity and is given in units of $M^{-1}cm^{-1}$. L is the optical path length, which is the thickness of the sheet (cm) and c is the QD concentration (g cm^{-3}). If the product of concentration and thickness is too large there is too much absorption, which lowers the beneficial effects. The short circuit current and accordingly the spectral intensity decrease.

It is obvious in Fig. 7.18.b, that the inverse absorption spectrum is reflected in the SR curve. This normally happens for the samples that have greater thickness and higher concentration. Also, assuming that the emission is isotropic, for a layer of QDs with no capping, the majority of the light will be emitted out of the cell through the top escape cone or through the side of the LDS layer. Only a fraction of the luminescence photons are emitted to the cell directly. In addition, the isotropic profile of luminescence will result in an altered distribution, of the incident angle of photons to the interface, between the QD layer and cell. Reflection is dependent on the angle of incidence and increases with an increasing angle [209] causing increased reflection losses (See the reflection spectra in Fig. 7.18b). Moreover, the absorption of the incident photons in the oxide layer prior to the cell can also cause the reduction in the spectral response.

However, the spectral response of the cell with LDS layer is improved in respect to the cell having a coating of a QD layer on top. At 300nm$<\lambda<$450nm, the EQE increases in the DSL layer as the reflectance decreases in this layer with respect to the QD layer. However, a fraction of this improvement can be attributed to the down-shifting effect. The improvement in the Internal Quantum Efficiency (IQE) of the cell with DSL layer in the range of 380-450nm, as shown in Fig. 7.19, verifies that the effect is more pronounced in this range where the emission intensity is the highest. The low photon flux of the AM 1.5G spectrum in the range of 300-450nm reduces the beneficial effects of the LDS layer (see Fig. 7.18.d).

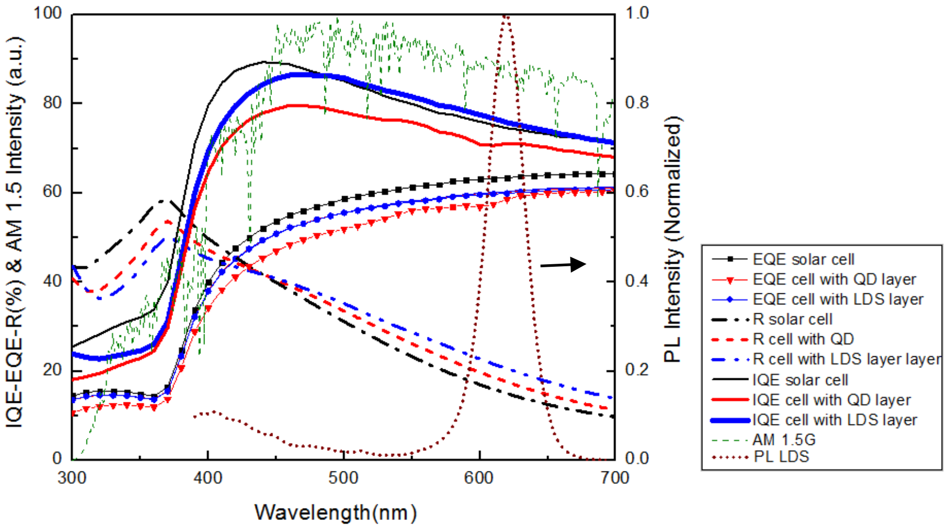

Figure 7.19 EQE and reflectance of: cell with a non-luminescent layer of oxide (solid-black); cell with a coating of QD layer (solid-red) and cell with DSL layer (solid-blue). IQE of a cell with a non-luminescent layer of oxide (dash dot); cell with a coating of QD layer (short dots) and cell with DSL layer (short dash dot); AM1.5G spectra (solid-green) and PL band of QD (dash dot dot)

Fig. 7.18.b and Fig. 7.19 clearly depict that the EQE of the cell with LDS layer is improved in the range of 450nm-620nm, where the reflectance of this cell is higher at this wavelength in comparison to the cell coated with an uncapped QD layer. This is attributed to down-shifting. Here it has been experimentally verified that in an LDS layer, containing QDs buried in an oxide matrix, with a refractive index larger than air and lower than the Si, the majority of the luminescent photons are emitted to the cell, either directly, or following internal reflection at air/ LDS interface. In contrast, for the QD layer with no capping layer the majority of the emitted photons escape from the top escape cone or the edges and don't contribute to the photocurrent and only a few enter the cell. Fig 7.20 is a visual representation of the LDS method. The SR curves for wavelengths above 600 nm are essentially unchanged, which is to be expected. The predicted beneficial effect for the UV/visible response is corroborated. The high reflection loss in the LDS layer can be attributed to the isotropic profile of emission and unoptimized layer thickness to be a good ARC.

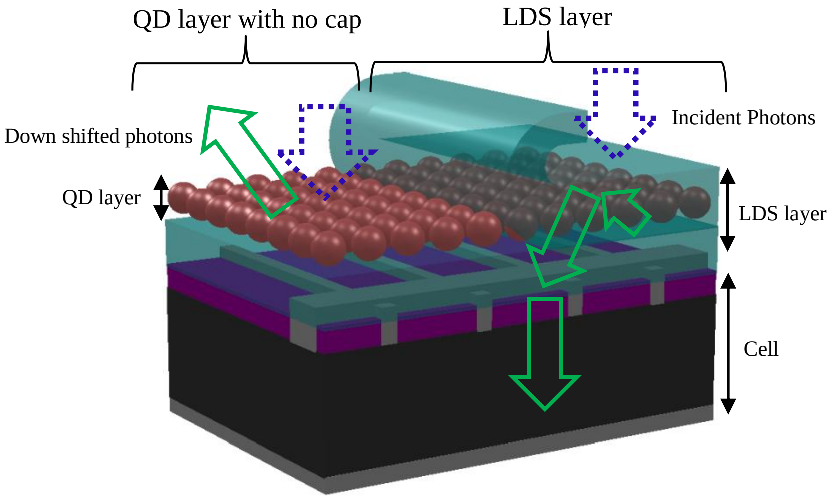

Figure 7.20 Summarized paths of the down-shifted photons in the LDS layer and QDs with no capping layer

Another key parameter influence the effectiveness of the layer in this range (450-620nm) is the flux of the photons. Looking at the AM 1.5G, the flux of the photons is highest in this range. So, this means that as there are more photons in this range of the spectrum, there is a higher chance that these photons will be absorbed within the QDs. Hence the concept is easier to prove in this range and the down-shifting effect is more pronounced here. The overall spectral response, of the cell with the LDS layer, is lower than the cell coated with a non-luminescent layer of oxide. This transparency/ reflection loss in the LDS layer, scattering of the emitted photons towards the top escape cone and the low LQE of the QDs, are considered as the main factors that imply the lack of gain in general.

At present, the inconsistency between predicted and observed effects cannot be adequately explained. Further research in the synthesis of QDs with high quantum efficiency and further optimization through the design of the LDS layer and host material clearly is necessary. Differences between theory and experiments that originate from the design can be overcome by considerations in the designing stage to somehow eliminate the re-absorption effect in the layer. Also, the quantum efficiency of the QDs used in the experiments is much lower than what has been assumed in theory. Only when the QD quantum efficiency equals unity and when in addition all emitted photons enter the solar cell, a pronounced increase in spectral response and correspondingly in short circuit current will be observed. A part of these considerations will be addressed in Chapter 8. In addition the cell performance measurements require being performed under blue-weighted spectra.

Architecture 2. Sequentially deposited QDs/oxide layers

In order to benefit from the LDS, adjustment in the design structure of the layer is required. Unoptimized concentration of QDs in the layer results in transparency/ reflectance loss, as shown in a previous section; along with a re-absorption effect which is not desirable. By increasing the spacing of the QDs, it is expected that the odds of the re-absorption of the emitted photons in the layer are lowered, while a uniform and transparent layer will be produced. The reflection loss can also be reduced. Due to the fact that the concentration of the QDs would be very low in a single layer, multiple depositions are required. Deposition of the QD layers, one on top of the other, provides an effective layer in terms of PL, also the reflectance remains low to an optimum thickness. It was observed that when the thickness of the QD layer exceeded a specific thickness the reflectance dramatically increased. Also, very thick layers destroy the transparency of the DSL layer, which will limit the effectiveness of the layer to a large degree.

Device Configuration

To provide a layer with low reflectance and re-absorption, while having a highly transparent layer with intense PL, a sequential deposition of QD and oxide layers is proposed, as shown in the schematics in Fig. 7.21; with the optimum deposition cycle, which results in the formation of a red shifting layer with intense PL and optimized ARC properties. Schematics, in Fig. 7.21.a, show the stack layers of 1 size of QDs embedded in an oxide layer. Schematics, in Fig. 7.21.b, show the stack layers of different sizes of QDs with large band gap nanocrystals deposited on the top and gradually decreasing band gaps to the bottom layer. This results in an optically well-designed LDS layer with graded index properties, where the small size QDs have a lower refractive index and a modified absorption profile of the layer.

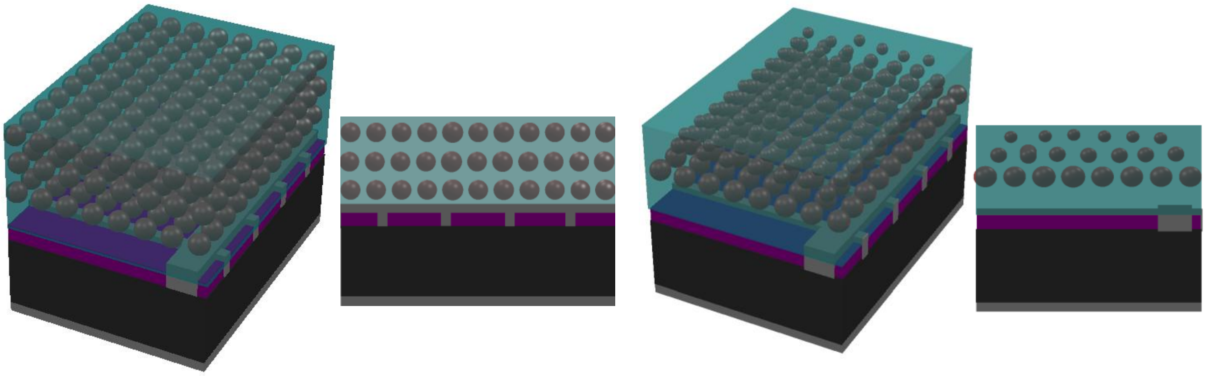

(a) (b)

Figure 7.21 Sequential deposition of QDs/oxide layers from a) 1 size QDs, b) different sizes QDs

Formation and Structural Characteristics

QDs were spin coated at a high spin speed (~3500 rpm) as the aim was to deposit one single layer of QDs with acceptable spacing between the QDs. According to the TEM image, shown in Fig. 7.22.a, the deposited QDs layer depicts a uniform continuous layer. For these sets of samples, 2KA°of oxide layer was deposited at each deposition cycle to isolate the QD layers from the cell and from each other. According to the HRTEM micrographs, shown in Fig. 7.22.b, the thickness of the oxide layer is about 5nm. Layers of QDs and oxide were deposited sequentially to form the LDS layer. In one set of samples all the QD layers were deposited from a solution containing 5nm QDs with emission peak at 610nm. Alternatively, in the second set the QDs layers were deposited from 3 sizes of QDs with the emission peak at 520nm, 590nm and 610nm, starting the first layer with bigger QDs and ending by deposition of the smaller sized one. The TEM micrographs, in Fig. 7.22.c, d, show the formation of the LDS layers containing 3 sizes of QDs, after the second and third consecutive depositions of QDs and oxide layers, respectively. The second and third layers containing smaller size QDs do not appear very clearly in the micrograph, likely due to the resolution limit of the TEM machine.

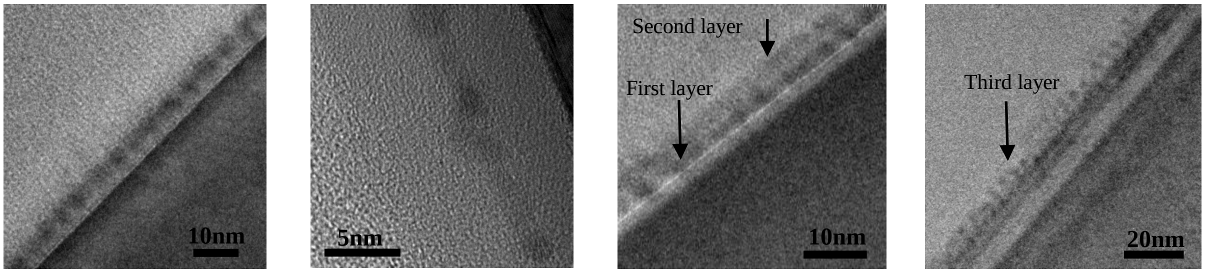

(a) (b) (c) (d)

Figure 7.22 TEM micrographs showing formation of the LDS layer containing three sizes QDs after a, b) first, c) second and d) third deposition cycles

Optical Characteristics

Absorption and PL spectra of the LDS layers are shown in Fig. 7.23. The layer, containing 1 size QDs, shows the absorption and emission peak at 600nm and 610nm, respectively (see Fig. 7.23.a, b). In the layer prepared by sequential deposition of three sizes of QDs, the absorption spectrum does not show the exact absorption peak of each size of the QDs, but the emission peaks appearing in the PL spectrum are the combinations of the emission from all sizes of QDs (see Fig. 7.23.b). PL of the two bigger sizes of QDs, with the emission peak at 590nm and 610 nm, were fitted in this spectrum for clarification. The resulting peak covers the spectrum range of 480nm-670nm (VIS/NIR), as shown with a Gaussian curve fitted to this spectrum (see Fig. 7.23.b).

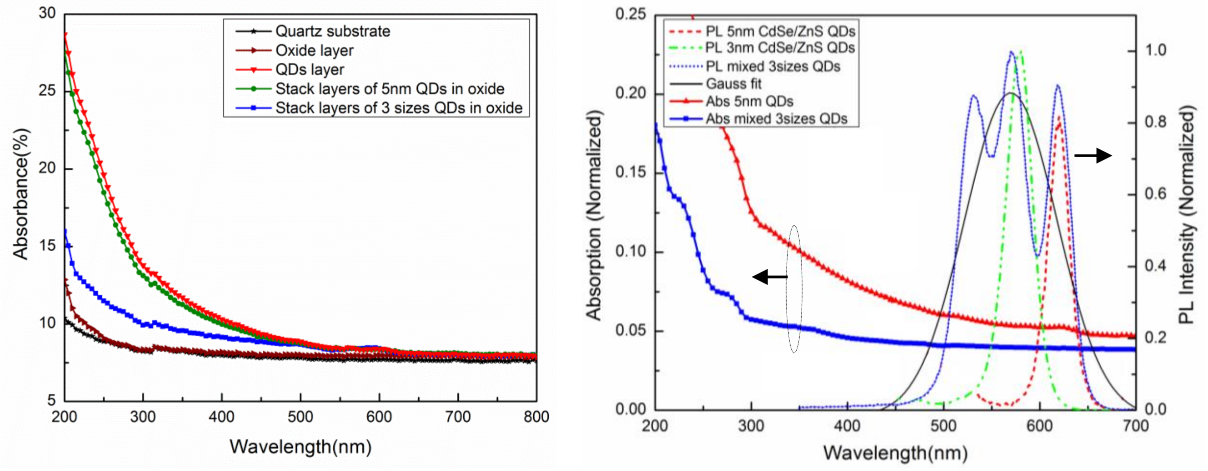

(a) (b)

Figure 7.23 a) Absorption, b) emission spectra of the stack layers of QDs

Cell Characteristics after Deployment of the LDS Layer: Proof of Down-shifting

The improvement in the EQE of the cells, after applying the LDS layers, can partly be attributed to the lower reflectance of these layers (See Fig. 7.24.a). The IQE results show a part of the improvement in the cell response, for the cell with the LDS layers is due to the down-shifting (see Fig. 7.24.b). The results show that the improvement is more pronounced for the LDS layer containing 3 sizes QDs. This is proof of the success of this design. The thickness of the layer and consequently the concentration of the QDs need to be optimized by adding more layers to obtain a good down-shifting ARC layer.

Architecture 3. Composite Solution of CdSe/ZnS QDs/SOG

In another approach CdSe/ZnS QDs were dispersed in a SOG solution to examine the possible LDS property of the layer. The schematic of the new cell structures, created by applying the LDS containing

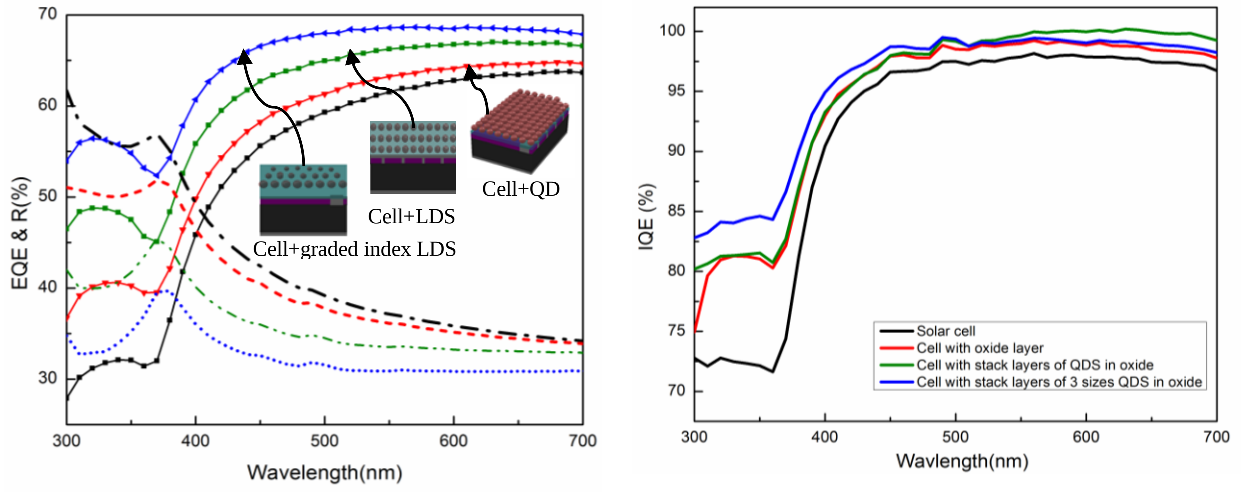

(a) (b)

Figure 7.24 a) EQE and reflectance, b) IQE of the cells with no passivation layer (black), a QD layer (red), an LDS layer containing stack layers of 1 size QDs (green) and an LDS layer containing stack layers of 3 sizes QDs (blue) deployed on top

QD/SOG composite layer, is exhibited in Fig. 7.25.

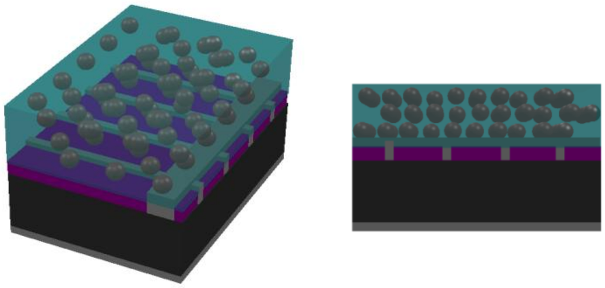

Figure 7.25 Schematic of the new cell structure created by applying the LDS layer containing QD/SOG composite layer

Formation, Structural and Optical Characteristics

In order to optimize the layer, various QD and QD/SOG solutions were coated on top of the quartz/silicon substrates by means of spin casting and were dried at 150ºC under nitrogen. For formation of the QD layers, two samples were prepared by spin casting of 1.5µL CdSe/ZnS QDs, from solution with concentration of 5mgmL^{-1}, onto the substrate in a single spin cycle, at the spin speeds of 500rpm and 200rpm for 30s. Also , a sample was prepared by triple deposition cycles of 1.5µL CdSe/ZnS QDs solution at 500rpm for 30s (sample#1).

For the QD/glass layer preparation, in the first set of the experiment, the SOG solution was diluted by adding 4ml of isopropanol alcohol (IPA) to 1mL of SOG solution, resulting in a diluted SOG solution with the total volume of 5mL. Further, 1.5µL and 3 µL of QDs were added separately into 5mL of the prepared SOG solution. A quantity of 1.5µL of the resulting former solutions was used for the film formation of sample#2. The same amount of the latter solution was used for formation of sample#3, using triple cycles of spin casting onto the substrate at 500rpm for 30s.

In the second set of the experiment for formation of the QD/glass layer, 1.5µL of QDs was added into the 0.5mL of the previously described diluted SOG solution. 1.5µL of the resulting solutions was used for the film formation of sample#4 by triple cycles of spin casting onto the substrate at 500rpm for 30s.

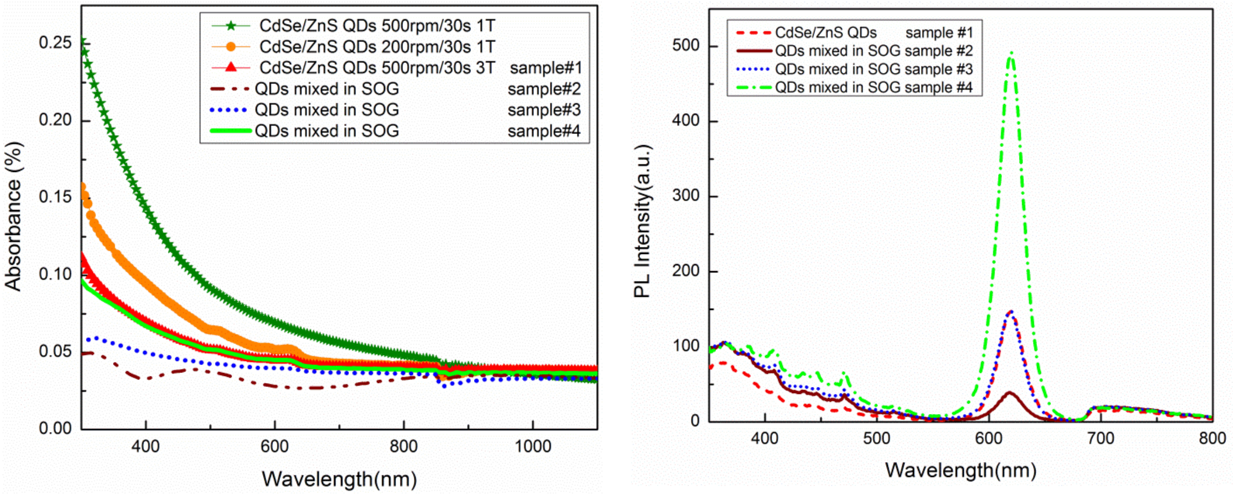

(a) (b)

Figure 7.26 a) Absorption spectra and b) Photoluminescence spectra of CdSe/ZnS and CdSe/ZnS QDs dispersed in SOG

Fig. 7.26.a indicates that for the QD layers, the absorption peaks appear for the layers prepared at lower spin speeds. The optimization of the film is also accomplished by multiple depositions from the solutions onto already dried films. For the QD/SOG layers, those layers with QDs, which were diffused in a smaller volume of SOG, seemed to be more efficient.

One major thing required to be considered is that the quantum efficiency of QDs needs to be retained after dispersion in SOG. The absorption peak of sample #2 is not clear, which can be either attributed to the relatively thick SOG layer surrounding the QDs that causes scattering in the layer or the concentration of the QDs which could be low. By increasing the QD concentration (sample #3) the absorption spectra became more acceptable with a fairly clear absorption peak. The appearance of the absorption peak in sample#4 is due to the lower scattering in the thinner SOG layer. No photoluminescence quenching from QDs dispersed in SOG was observed (see Fig. 7.26.b). The highest QY was attained for samples #1 & 4.

TEM results of the composite QD/SOG layer were obtained from QD solution and after layer formation. The sample for TEM of the QD/SOG solution was prepared by droping and drying on the carbon grid (see Fig. 7.27.a). Fig. 7.27.b is the magnified image of site A, shown in Fig. 7.27.a. There are some sites in the layer, shown as B in this image, with higher contrast. Fig. 7.27.c is the HRTEM image of the B sites representing the agglomeration of QDs in small areas. However, Fig. 7.27.d is the HRTEM image of site C which is representative of most of the layer. This micrograph illustrates that the composite layer is uniform. The rings in the Fast Fourier Transform (FFT) image, of Fig. 7.27.d, indicate the incorporation of the crystals inside the amorphous layer (see the Fig. 7.27.d-inset).

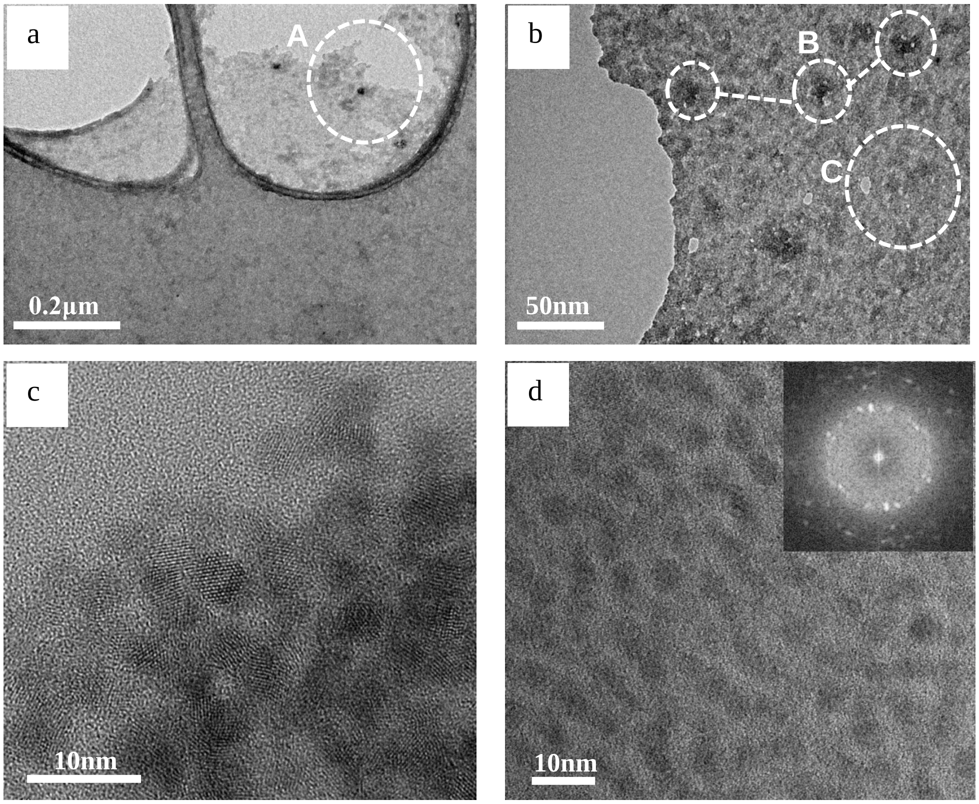

Figure 7.27 a) TEM image of the QD/SOG composite layer prepared by drop and dry from the prepared solution on the carbon grid, b) magnified image of site A shown in (a), c) HRTEM image of site B representing agglomeration of QDs in small areas, d) HRTEM image of site C representing that most of the composite layer is fairly uniform. Inset is the diffraction pattern of (d) indicating the incorporation of the crystals inside an amorphous layer

The conditions developed for sample#1 (containing QD layer) and Sample#4 (containing layer of QD/SOG composite material) to examine the LDS method were used. Fig. 7.28.a shows the HRTEM result of the QD/SOG composite after film formation. The image shows a sample consisting of 3 layers of QD/SOG, which was prepared by three deposition cycles from the QD/glass solution onto the already dried films. The thickness of each layer is about 30nm according to the TEM results. Absorption/emission spectra presented in Fig7.28.b illustrate that the optical properties of the QDs are preserved after incorporation in SOG and the host material (SOG) is transparent to a good extent.

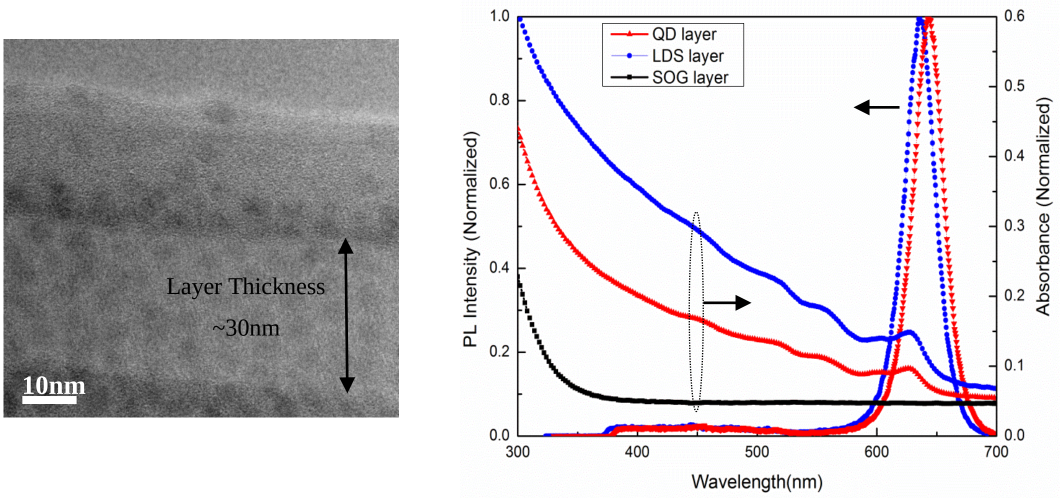

(a) (b)

Figure 7.28 HRTEM image of a sample consists of 3 layers of QD/SOG, b) absorption/emission spectra of the SOG, QDs layer and QD/SOG composite LDS layer

Cell Characteristics after Deployment of LDS Layer: Proof of Down-shifting

The layers were applied individually on top of the c-Si cell. The EQE and reflectance of the cell structures with QD layer and LDS layer, compared with the EQE and reflectance of a cell with a SOG layer having the same thickness as used in the LDS layer but with no luminescent materials (see Fig. 7.29).

To explain the results, a closer look is needed, in the blue to VIS/NIR part of the spectrum, in order to study the EQE results in detail. By looking at the absorption/emission spectra of the QDs, it is clear that if there is any down-shifting effect in the layer, it would appear in these ranges (see Fig. 7.28.b). Fig. 7.29 illustrates that at $\lambda<450$nm (blue range), the reflectance of the cell with QD layer, is lower than the cell with no luminescent layer (control cell). However, the EQE of this cell is lower than the reference cell that is attributed to the absorption in the QD layer in the blue range of the spectrum and to the scattering of a large amount of the down-shifted photons to the top escape cone.

At 400nm$<\lambda<$750nm, the reflectance of the cell with QD layer is higher than the control cell. As discussed earlier, this is due to reflection loss, which happens due to the isotropic emission from the QDs that alternate the emitted photons path. The EQE of this cell is much lower than the control cell at the VIS/NIR range of the spectrum which is partly due to the reflection loss. It can also be due to the

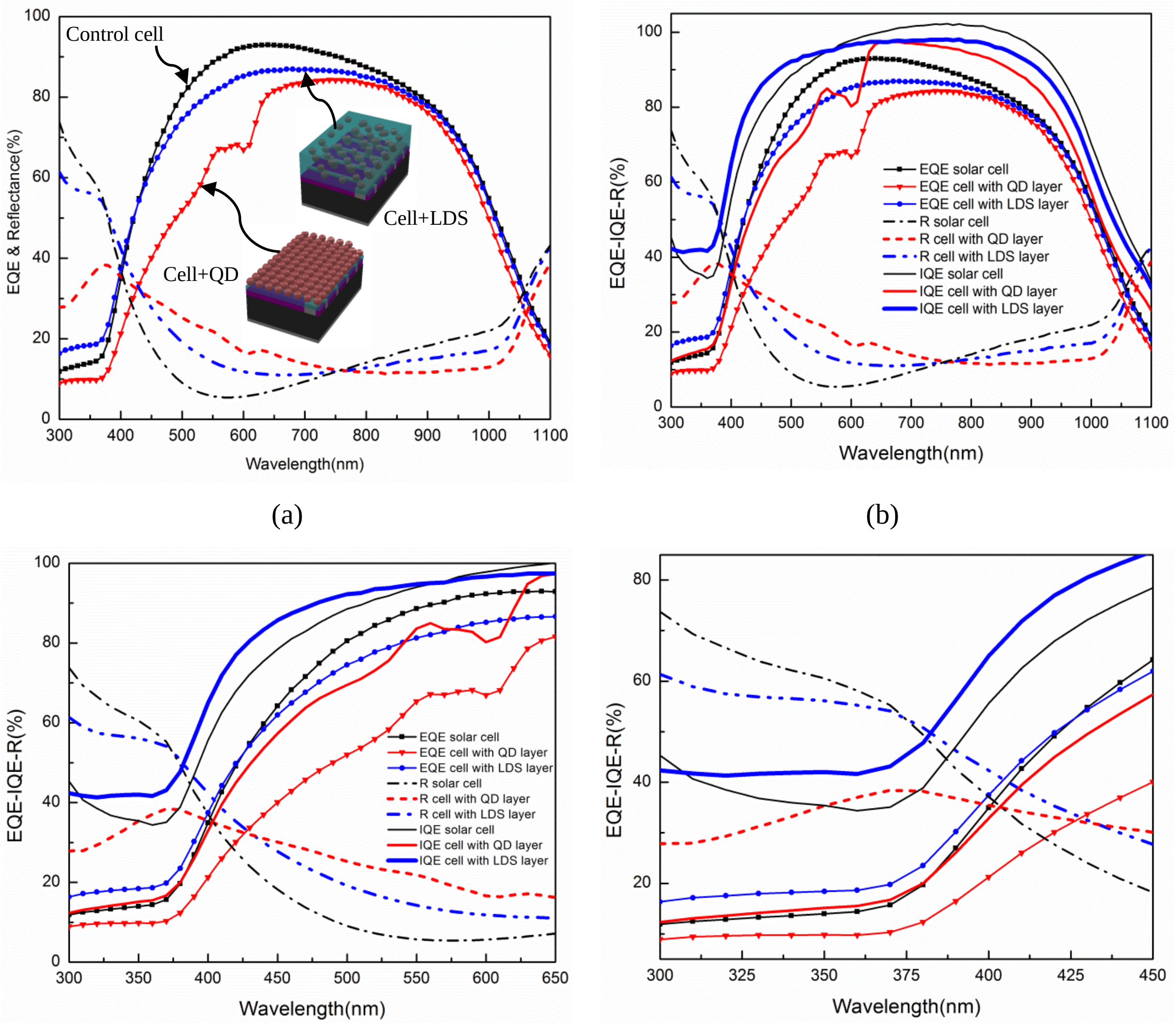

(a)

(b)

(c)

(d)

Figure 7.29 a) EQE and reflectance of the cells with a SOG layer, a QD layer and an LDS layer, b) IQE of these cells emphasized in this graph, c) zoom in view of graph (b), d) zoom in view of graph (c)

absorption in the QD layer or can also be attributed to the scattering of the down-shifted photons towards the top escape cone or the edges, instead of transmitting to the underlying cell. Another part of the loss in both cases can also be due to the low LQE of the QDs.

On the other hand, by applying the LDS layer consisting of the QD/SOG composite on top of the cell, the EQE of this cell structure with LDS was improved with respect to the cell with a QD layer in the whole spectrum range. The short circuit current also increased from 27.33 mA for the cell with QD layer to 30.95mA for the cell with LDS.

At λ<425nm (UV range), although the reflectance of the cell with LDS layer is higher, the EQE of the cell is improved for the cell with LDS, with respect to the cell with QD layer. This can be attributed to the down-shifted photons transmitted to the underlying cell. At 425nm<λ<750nm (VIS/NIR range), the reflectance of the cell with the LDS layer is lower than the cell with the QD layer, hence, this can result in a higher EQE of the cell with LDS. However, the improvement in SR is much larger, which can only be due to the low reflectance. One can conclude that a part of the improvement is because of the lower reflectance, while another part could be attributed to the down-shifting photons that transmitted more efficiently to the underlying cell.

To compare the EQE results for the cell with the LDS layer and the cell with no-luminescent material, three spectrum ranges are looked at; at λ<375nm, the improvement in SR for the cell with LDS could be due to its lower reflectance. However, from the IQE results shown in Fig. 7.29.b-d where Fig. 7.29.d is a zoomed in image of Fig. 7.29.b, c, in the 300nm<λ<450nm range, a part of the improvement can be attributed to the down-shifting effect. This conclusion is due to the fact that the IQE for the cell with the LDS layer is higher than the cell with a layer of QDs in this range, although the reflectance of the former cell is lower. Also, at 375nm<λ<425nm, the improvement in EQE could be due to the down-shifting effect and to the fact that the reflectance of the cell with LDS layer is increased with respect to the cell with no luminescent material (see Fig. 7.29.d). At 425nm<λ<600nm the reflectance of the cell with LDS increased with respect to the control cell due to the isotropic profile of the emitted photons, that in turn causes the drop in the EQE. Even though the down-shifting effect might exist, the high reflectance of the cell with LDS masks the effect. This drop can also be partly due to the absorption in the SOG, which can be overcome by optimizing the thickness of the layer.

Because of the points mentioned above, no overall performance improvement can be reported, as the increase in EQE at short= λ is cancelled out by a lowering of EQE at longer λ. The calculated short circuit current for the control cell and cell with LDS layer were 32.41mA and 30.95mA respectively. Again, the low QY of the commercially available luminescent species, absorption in the SOG, scattered down-shifted light to the top escape cone suggest the small beneficial effect of down-shifting.

Architecture 4. Closely Packed QD Layer Encapsulated with a SOG Layer

In another approach, in order to examine the LDS method, transparent layers consisting of close- packed core/shell QD films capped with an SOG layer to use as spectral down-shifter were prepared. The schematic of the new cell structures are shown in Fig. 7.30.

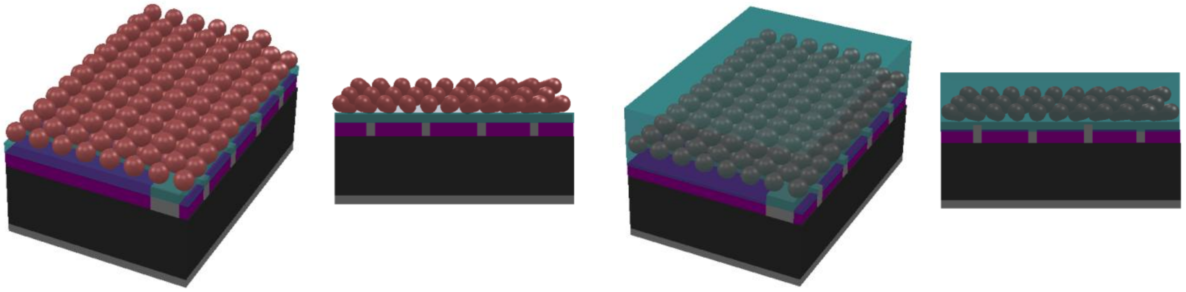
(a) (b)

Figure 7.30 Schematic of the cell structure by applying the a) closely packed QDs layer, b) LDS layer containing closely packed QDs layer in SOG.

Formation and structural characteristics

TEM micrographs in Fig. 7.31.a,c respectively, reveal ordered arrays of QDs with considerable spacing of about 0.2μm in SOG after deposition of a thin layer of SOG on the pre-formed layer of QD, both spin cast at 1000 rpm for 30s from 1.5μL of their relevant solutions (SOG and QD solution, respectively) on the silicon substrate. The inset in Fig. 7.31.c is the indication of presence of nanocrystals in amorphous medium. Subsequent annealing at 200°C applied after each deposition in order to evaporate the solvents and dry the films. Also the organic ligands of the QDs can partially remove during this annealing step.

The areas with bright contrast in Fig. 7.31.b can be attributed to the drops of SOG that does not uniformly cover the QDs and dissolve clusters of QDs at specific sites. That can be happened due to the unoptimized spin coating conditions, high viscosity of the SOG solution or the remained solvents in either SOG or QD layer or both. As apparent in these images, using the fast spin coating condition for formation of QD layer results in very low concentration of the QDs embedded in the layer which led to low QY. The SOG from the Filmtronics P20 solution, with no further processing, was also used. The high viscosity of this solution results in a thick glass layer of about 0.4μm which is not desirable for this application.

Low reflection, high transparency and intense PL peaks are the main characteristics of the arrays of QDs introduced into the oxide layer to utilize as LDS layer. An attempt was made to optimize the LDS layer by using a lower spin speed (500rpm) for the layer formations particularly for the QD layer in order to provide a highly luminescent layer. The SOG solution was also diluted, in order to obtain thin transparent film in which the QDs are embedded. The TEM micrograph and the magnified image in Fig. 7.32.a,b respectively, illustrate the formation of the closely packed QDs embedded in glass layer. The HRTEM image in Fig. 7.32.c shows the crystalline structure of the QDs which uniformly formed on a very thin glass layer. Here it needs to be noted that in order to apply this layer on the cell, the QD layer should be isolated from the active part of the cell. Hence, a layer of SOG was deposited prior to the

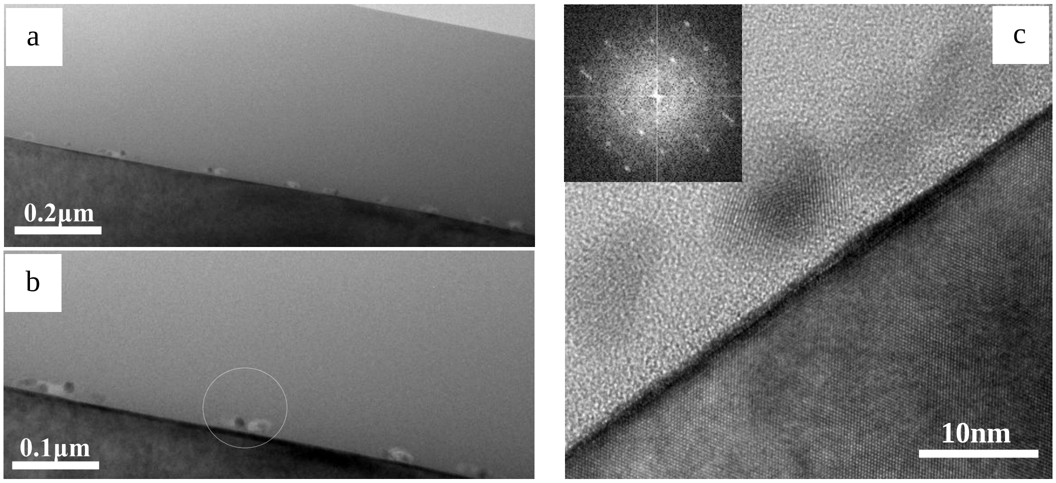

Figure 7.31 a,b)TEM and c) HRTEM images of the QDs embedded in glass both spin cast from the solution of QDs and SOG at 1000rpm for 30s. The layers dried at 200°C.

deposition of QD layer on top of the cell. This thin layer is clear in the HREM image. Due to the inherent property of the spin coating method, the top SOG layer does not have an exact thickness through the entire surface (See Fig. 7.32.a). However the average thickness of the layer depicted as thin as 60nm which is acceptable for the layer to show good ARC properties. The rings in the FFT image are the indication of crystalline structure in amorphous medium (see the inset of Fig. 7.32.c).

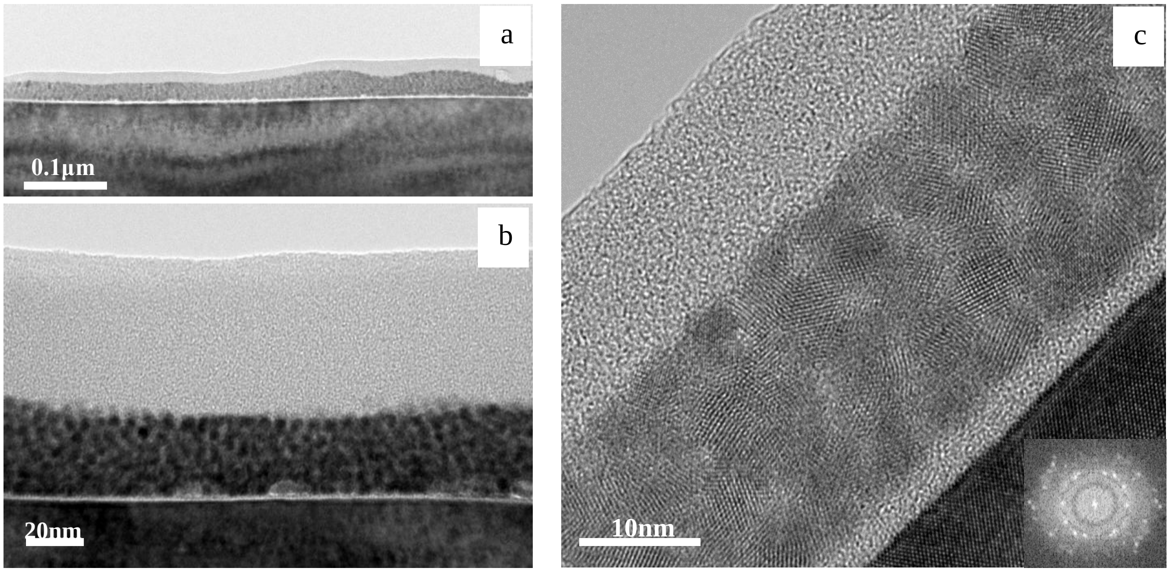

Figure 7.32 a) TEM, b) magnified TEM micrographs illustrating the formation of closely packed QDs embedded in glass layer. c) HRTEM image showing the crystalline structure of the QDs which uniformly deposited on a very thin glass layer used for isolation of the LDS layer from the cell. The inset is the FFT image of the (c).

Optical characteristics

The Fourier Transform Infrared (FTIR) spectroscopy of the QD and LDS layers were performed in a FIIR system from Bruker Optics and the results are presented in Fig. 7.33.a,b respectively. The OH vibration peak at 3430 cm^{-1} comes from the water. Water adsorbs on the surface of quantum dots because of their high surface-to-volume ratio. QDs are stabilized in ODA ligands and the appeared peak at 1500 cm^{-1} is in agreement with the literature [210]. This peak is appeared for both structures illustrating that the ligands were not completely removed in the layer after annealing the layer at 200°C. The band at around 1090 cm^{-1} in Fig. 7.33.b can be assigned as a Si-O stretching implying that the QDs are incorporated in a glass matrix. Host material and the size of the QDs affect the vibrational states of quantum dots that should be considered in order to optimize the optical behavior of the layer. The large surface-to-volume ratio of quantum dots strongly affects the optical properties mainly due to the interactions between quantum dots and surrounding materials which results in a red shift of Raman spectra. Mismatch of the thermal expansion between nanocrystals and their host material and the surface tension are inherent properties of the quantum dots in glass matrices and increase with decreasing of the size of nanocrystals [211].

Phonon modes of QDs in a glass matix were investigated by Raman spectroscopy. The phonon energies are observed to be dependent on the host matrix as well as quantum dot size. The Raman spectra were recorded with 90° scattering configuration at 300k in a Renishaw system. The 514nm line of Ar$^+$ laser was used as an excitation source. A monochromator with grating was employed. The observed Raman spectra of QDs and QDs/SOG layers at 300K are shown in Fig. 7.33.c and Fig. 7.33.d respectively. The Raman peak at 210 cm^{-1} is identified as the phonon mode of CdSe/ZnS structure [212]. This figure demonstrates no considerable shift for the QDs dispersed in glass matrix.

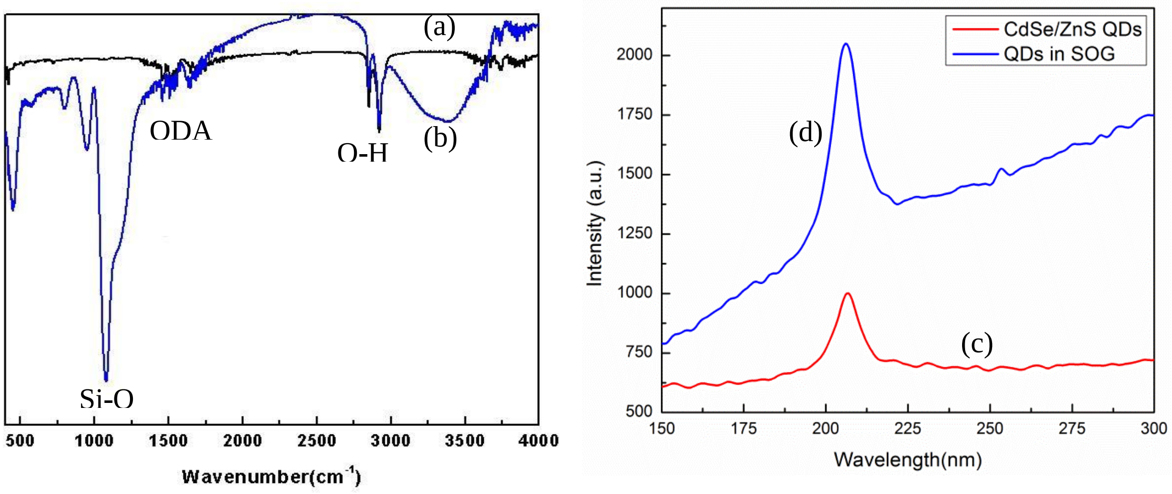

Figure 7.33 FTIR spectra of a) CdSe/ZnS QDs, b) QDs embedded in glass matrix. Raman spectra at T=300K for c) CdSe/ZnS QDs and d) QDs/SOG layers.

The absorption and emission spectra of the QDs were maintained after embedment in the glass layer. These results shown in Fig. 7.34 reveal that the spin cast QDs layer introduced in a glass layer is capable to convert the incident high energy photons to lower energy photons that can be more efficiently absorb within the underneath c-Si solar cells. The PL spectrum reveals that emitted photons were not quenched in the layer of QDs capped with SOG. The emission spectra of the LDS layer shows a small blue shift with respect to the QD layer which could be attributed to the changes in refractive index of the medium consist of QDs and glass. Surface oxidation could be another explanation of this observation. The maxima and minima patterns appeared in the absorption spectrum of the QD/SOG layer are the result of interferences of light going through the stacked planar layers. The thickness of the glass layer should be also optimized for the minimum absorption of the photons.

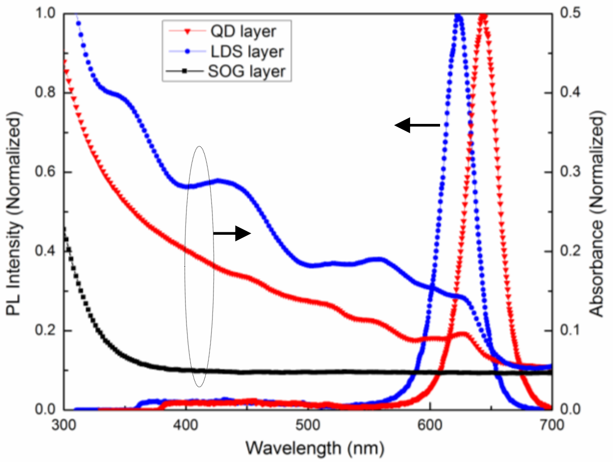

Figure 7.34 Absorption/emission spectra of the SOG, QDs and LDS layers.

Cell Characteristics after Deployment of the LDS Layer: Proof of Down-shifting

The close-packed QDs layer, capped with SOG for the LDS layer, was utilized. The layer was applied on top of the c-Si cell to examine the down-shifting effect on the performance of the device. In Fig. 7.35.a, the EQE and reflectance of the cell structures with QD layer and LDS layer compared with the EQE and reflectance of a cell with the same thickness of SOG layer as used in the LDS layer, but with no luminescent materials. The IQE of these cells is emphasized in Fig. 7.35.b. The zoomed in view, in Fig. 7.35.c, is that of the graph shown in Fig. 7.35.b. The zoomed in view, in Fig. 7.35.d, is that of the graph shown in Fig. 7.35.c, for clarification. The average reflectance of 15% was measured for both the QD and LDS layers, which is an improvement with respect to the reflectance of the bare silicon (~30%). However the layers need to be optimized for ARC. The interference patterns appearing in the reflectance spectrum of the LDS layer is due to the interference of the light passing through the SOG and QD layer. The inverse of the reflectance spectrum is reflected in the EQE of the cell with an LDS layer. The inverse absorption spectrum of the QD layer is also reflected in the EQE of the cells with a QD layer.

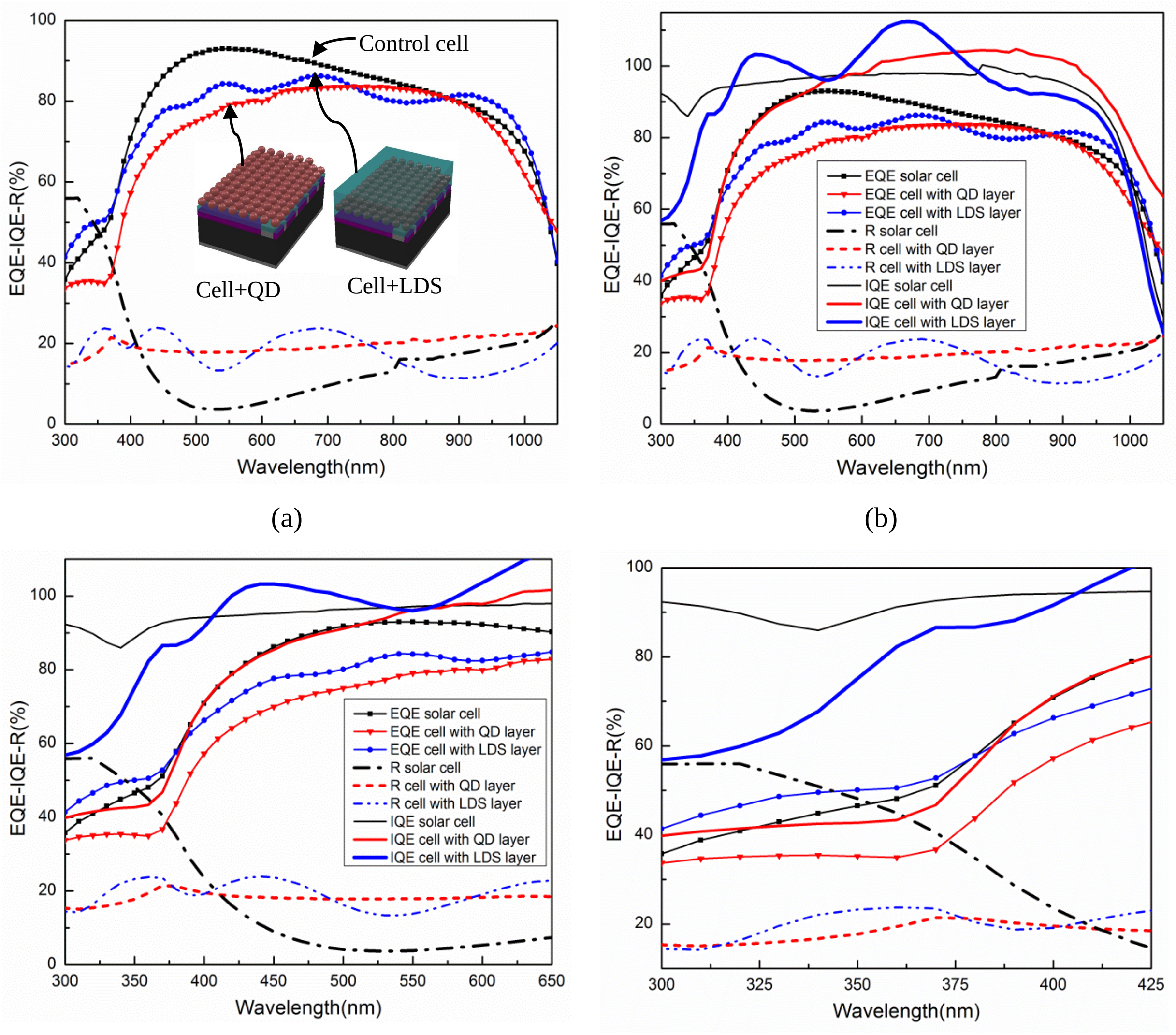

(a) (b)

(c) (d)

Figure 7.35 a) EQE and reflectance of the cells with SOG layer, QD layer and LDS layer, b) IQE of these cells emphasized in this graph, c) zoomed in view of graph (b), d) zoomed in view of graph (c)

First the QD layer and the cell with no luminescent material were compared. At λ<410nm the reflectance of the cell with QD is lower than the standard cell. However, the EQE is lower as the result of the high absorption of photons with the energy in this range by the QDs; and the scattering of a large part of the down-shifted photons to the front escape cone or the edges (see Fig. 7.35.a or Fig 7.35.c). At 410nm<λ<1050nm the reflectance of the cell with a QD layer is larger than the cell with a non-luminescent glass layer deposited on top of the cell as ARC. The reflectance loss is due to the isotropic emission from the QDs which alternate the light path. The EQE of the cell with QD layer is lower than the reference cell, as a result of reflection loss in the QD layer, absorption loss and scattering of the emitted photons instead of transmitting to the underlying cell. The absorption loss can be better proven by looking at the IQE of these cells as shown in Fig. 7.35.b or Fig. 7.35.c. At 410nm<λ<600nm the reflectance of the cell with a layer of QD is higher with respect to the control cell. The IQE of this cell is lower, attributed to either the absorption of the incoming light by the QDs or the re-absorption of the emitted light by the other QDs in the layer. At the wavelength longer than 600nm, where the effect of absorption with the QD layer doesn't exist, the IQE of the cells corresponds to their reflectance behaviors.

Comparing the EQE of the cells with the QD layer and LDS layer in Fig. 7.35.a, one can see that the average reflectance of the LDS layer is close to the reflectance of the QD layer, All the while, the EQE of the LDS layer is improved in the whole range of the spectrum with respect to the QD layer. Looking at the absorption spectra (see Fig. 7.34), one can see that the absorbance of the LDS layer is also higher than the QD layer. It can be concluded that the improvement in the SR of the LDS layer is due to the transmission of the down-shifted photons to the underlying cell. The IQE of these cells also supports this idea (see Fig. 7.35.b or Fig. 7.35.c). The IQE of the cell with an LDS layer is higher with respect to the cell with a QD layer, in the range of the spectrum where the QDs are effective (300nm<λ<610nm).

However, the deployment of the LDS has not improved the overall cell performance. At λ<410 the EQE of the cell with LDS layer is higher than the control cell (see Fig. 7.35.d). This improvement is due mainly to the lower reflectance in the LDS layer. The IQE results also show no improvement in the layer related to down-shifting. The results are just paralleled to the reflectance spectra. At 425nm<λ<800nm, the reflectance of the cell with LDS is higher than the standard cell, hence the EQE of the cell with LDS drops (see Fig. 7.35.b). The IQE of the cells is also paralleled to their reflectance behaviors. The parasitic absorption in the SOG layer also limits the effectiveness of the layer.

Moreover, the flux of blue photons in the solar spectrum used for the EQE measurements plays a major role for the LDS effect to be more pronounced. Optimum concentration of QDs with high quantum yield, near-optimum SOG thickness, and low absorption/reflection from the LDS layer in the UV-NIR range of the layer, is desirable. Very high QD concentration causes scattering that tends to reduce the effectiveness of the layer.

7.4.3 Advantages and Disadvantages of Each Method

In the approach using ordered QD in oxide, the space between the QDs can successfully be filled using an e-beam technique. This will lead to reduction in scattering/reflection and establishment of a homogeneous layer to avoid light interference. There is also better control on the oxide thickness. The QD/SOG composite layer also provides a homogenous layer. In close-packed QD layers capped with SOG, two separate layers cause the interference of the light. In all approaches a graded index structure of layers, with descending refractive index values along the direction of the incident light, to absorb a broader portion of the solar spectrum more efficiently with lower reflectance, was used. However, the thickness of the QD and host layers needs to be optimized in each design.

7.5 New Design Structure to Fully Overcome the Problems

7.5.1 Graded Index Structure

Absorption is sensitive to size, refractive index of capping ligand, solvent in which the quantum dot dispersed and the medium in which they embedded [213]. In order to minimize the reflection loss and to maintain the transmittance required for solar cell applications, a graded index structure can be optimized for embedment of QDs. Stack layers of QDs with engineered band gaps and stack layers of QDs with decreasing band gap, can be introduced in an appropriate graded index oxide structure for layer embedment optimization, in order to efficiently vary the optical parameters of the composite materials in a wide range. In addition, the spacing and the size of the QDs are the main parameters that affect the refractive index of the superlattice layers. Future study can include determination of the refractive index of the QD superlattice layers using different designs, by changing the spacing and the size of the QDs.

7.5.2 Self-Assembled QD Layer

Transparent oxide layers with desirable thicknesses can be realized by means of vacuum techniques but it is necessary to have dedicated systems for such experiments. This is due to the inherent properties of the QDs which does not allow for clean processes. A desired QD layer for the LDS would be well-ordered arrays which cannot easily be obtained by the spin coating technique. A self-assembled QD layer results in well-ordered arrays of QDs. A well-known method for formation of such a layer is the Langmuir-Blodgett (LB) self-assembling technique [140] which appears to have its own technical difficulties.

Self-assembled QD arrays can also be fabricated utilizing core/shell/shell structures. The core and the first shell form the typical QDs. The second shell should be a transparent layer such as oxide. Any metallic nanoparticles such as gold (Au) can be other options for the second shell if they are transparent in the UV/NIR range, at a specific thickness grown by this technique. At the same time, gold might help to benefit from the plasmonic effect. Future work is involved in synthesizing the core/shell/shell structures that is addressed in Chapter 8. The LDS design that is proposed in the next chapter is utilizing the $CdSe/ZnS/SiO_2$ structure for the purpose of establishment of well-ordered arrays of QDs with the desired spacing. This can be achieved by optimizing the outer shell thickness.

7.5.3 Surface Plasmonic Effect

Metal nanoparticles (e.g. silver (Ag), Au) of particular shape, size and density produce surface plasmon resonance (SPR) that enhance the lateral scattering of the incident light and increase the chance of absorption of a given wavelength in a medium. SPR happens when the size of the nanoparticles is much smaller than the photon wavelength. This technique has been widely used to enhance absorption in thin film solar cells [127,128]. The LDS method can also benefit from SPR through implementation of appropriate particles, with appropriate size and spacing on top of the LDS layer, to produce resonance in the VIS-NIR range. This technique would increase the chance of directing the re-emitted photons to the underlying cell, as the photons are scattered toward the cell by these particles, instead of escaping from the top (see Fig. 7.36). Incident photons are collected by metal nanoparticles with their large extinction coefficient, so the incident photons radiate to the LDS layer in multiple angles; hence the optical path increases in the layer which provides more chance for the photons to be absorbed by QDs. This concept will also be briefly addressed in the next chapter.

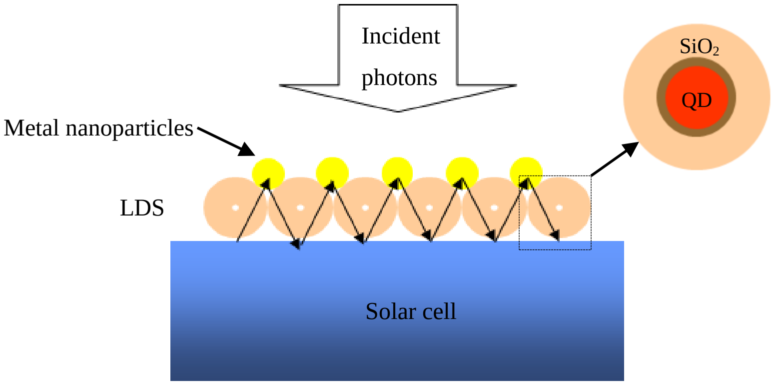

Figure 7.36 Plasmon enhanced LDS effect in CdSe/ZnS doped material

This principal is studied particularly for absorption of long wavelength photons (>700nm). Here, the challenge is finding a material with plasmon resonance in the UV-NIR range where more blue photons need to be captured by QDs; and more emitted photons need to be directed towards the cell underneath. It has been shown that gold nanoparticles result in a considerable increase in the PL of the CdSe/ZnS QD layers, which would be beneficial for the LDS method. It is also an indication that gold can be a good candidate for the UV-NIR range. Future work is involved in finding appropriate metallic nanoparticles with resonance properties in the UV-NIR range and developing a method to implement these particles onto the cell.

7.6 Conclusions

A new generation of PV cells was developed in which a luminescent down shifting layer was deposited on top surface of a c-Si cell to improve the poor spectral response of the cell in short wavelength light. The LDS layer is a planar layer consists of quantum dots as wavelength-shifting materials embedded in an oxide layer transparent medium. The quantum dots shift the wavelengths where the spectral response is low to the wavelengths where the spectral response is high.

Spin-cast formation of layers of core/shell CdSe/ZnS QDs was presented. By controlling spin coating conditions and using optimum concentration of QDs, uniform QD-containing thin films with specific thicknesses and concentrations were obtained. Four LDS architectures consist of QDs in oxide and SOG matrices were deployed distinctly on front surface of the PV device to examine the down shifting potential of each design. The fabricated devices employ QDs embedded in oxide layers, sequentially deposited QD arrays/oxide layers, composite layer of QDs/SOG, and closely packed QDs layer covered with a SOG layer. TEM and HRTEM were used for the structural characterization of the layers and the results revealed formation of uniform layers. Optical characteristics of these layers were investigated via photoluminescence, fluorescence imaging and UV-Vis spectroscopic measurements. Relatively low reflection, high transparency and intense PL peaks of these layers verified the down shifting ability of the QDs embedded in oxide/glass layers.

Preliminary results on experimental verification for the spectral down shifting of the incident photons via LDS layer were also discussed. The effects of LDS on the spectral response of c-Si solar cells was examined for two cases; i) QDs spin casted on top of a c-Si solar cell, ii) LDS layer implement on top of the c-cell.) In order to quantify and compare LDS results, all results compared to a control sample, which consists of the same host material but without the luminescent materials being present. This avoids false attribution of LDS gains to what are, in fact, simply a reduction in reflectance losses. Also for consistency the evaluation of LDS layers for all the samples were conducted under the established AM1.5G spectrum.

It was experimentally verified that QDs with a center emission wavelength of 610 nm included in an oxide layer are capable of improving the spectral response of the cell with respect to the cell with QD layer. However no overall performance increase can be reported due to the losses associated with low quantum efficiency of the commercially available luminescent species, isotropic emission, absorption in the non-optimized oxide/glass layer, and scattering of the emitted photons towards the top scape cone instead of transmitting to the underlying cell. In the case of LDS layers containing QDs in SOG, the increase in EQE at short λ is cancelled out by a lowering of EQE at longer λ where the reflectance and absorption is higher implying the lack of the effectiveness of the layer.

In order to see the full effect of down shifting, the layer needs to be optimized by striving for near-unity quantum efficiencies and maximum light trapping properties. Stack layers of QDs with engineered band gaps can be introduced in an appropriate graded index oxide structures in order to efficiently vary the optical parameters of the composite materials in a wide range. Moreover, the choice of the illuminating spectrum has a significant effect upon the obtained results. When measured under blue-weighted spectra, the improvements realized by LDS are generally higher than under terrestrial solar spectra.

QDs are attractive due to their tunable absorption and emission bands, continued research is required to improve their LQE and lower their fabrication cost. Oxide and SOG are practical choices to use as host materials due to their good optical properties, easy processing method, and low cost. Yet several challenges in the design of the layer still need to be addressed in order to realize the full potential of the LDS method on a c-Si cell. An appropriate design for the LDS layer can be self-assembled QD structures with relatively high LQE embedded in large thin sheets of transparent material. This will minimize the optical losses in the LDS layer. In the next chapter a synthesis method for the formation of silica coated QD and how this structure would benefit the LDS structure will be discussed.

Chapter 8

Synthesis of Silica Coated QDs for Spectral Engineering

As discussed in previous chapter, the luminescence properties of QDs are sensitive to surface interaction. The degree of surface passivation is a crucial parameter in determining the QDs' luminescent quantum efficiency. In this chapter experimental work in the synthesis of silica coated QDs is discussed. Depth optical characterization on the fabricated structures will be addressed in detail. Although a tremendous amount of chemistry is involved in the synthesis method, improving knowledge and experimental skill, to produce QDs with high quantum efficiency and performing fundamental studies on them after preparation, is very critical. It provides flexibility to produce the QDs with optimized structure, quantum efficiency, surface bonds and ligands, as well as optical and electrical properties that are looked for in spectral engineering through LDS.

Hydrophobically ligated CdSe/ZnS QDs were incorporated in transparent matrices by formation of CdSe/ZnS/SiO_2 core/shell/shell structures using a microemulsion synthesis method. The optical properties of the QDs over-coated with a chemically grown oxide layer were studied. Intense luminescence properties of the QD/silica nanoparticles (NPs) were observed using steady state photoluminescence measurements. Confocal microscopy demonstrates the fluorescence of the single core/shell/shell nanoparticles. The results obtained, along with the SEM and TEM images, provide information on the geometry of the QDs. The excitonic emissions of nanoparticles were also studied using a liquid nitrogen cryostat in the 77K - 300K range. The temperature dependent PL spectra of the film demonstrate the temperature-dependent band gap shrinkage of the QDs. Decay lifetime experimental data was fitted to exponential decay function and distribution tail fitting analysis was also performed. Excitonic lifetime constants in the nanosecond range were obtained. Temperature dependent excitonic decay of QD/silica nanoparticles demonstrates that the quantum yield (QY) of the QDs at room temperature is limited by two main non-radiative processes; namely, the carrier trapping at the interface of QD/silica and the exciton-phonon coupling. The temperature, illumination, QD size, ligand and passivation were observed to affect the decay time. These studies give insight to exploit the QD/silica films for photon down-shifting and multiple exciton generation for application in photovoltaics.

8.1 Microemolsion Method for the Growth of CdSe/ZnS/SiO_2 Nanoparticles

The CdSe/ZnS/SiO_2 nanoparticles were grown by an oil-in-water microemulsion approach with cyclohexane as the oil phase and poly (ethylene glycol) nonylphenyl ether (NP-9) as the surfactant [214].

This method yields high-quality CdSe/ZnS coated with SiO_2 and presents high PL quantum yields at room temperature.

The preparation consisted of incorporating 10 mL of cyclohexane, 1.3 mL of NP-9, 400 μL of hydrophobically ligated CdSe/ZnS QDs stock solutions (TOPO and ODA ligated QDs) in chloroform, and 80 μL of tetraethyl orthosilicate (TEOS) 99.999%, in a flask under vigorous stirring. Thirty minutes after the microemulsion system was formed, 150 μL of ammonia aqueous solution (33 wt %) was introduced to initiate the polymerization process. The silica growth was completed after 24 h of stirring. After adding acetone, the solution was centrifuged to isolate the nanoparticles from the microemulsion. The resultant precipitate, of CdSe/ZnS/SiO_2 composite particles, was washed in sequence with 1-butanol, 1-propanol, ethanol and water. Finally, highly luminescent aqueous dispersions of the composite particles were obtained by dispersing the precipitate in methanol.

The structure, size and morphology of the resulting nanoparticles were determined by TEM and SEM microscopy. For the TEM studies, samples were prepared by adding drops of prepared solutions on carbon coated copper grids. PL spectra were acquired on an Edinburgh Instrument Fluorescence Spectrometer, upon excitation at 380 nm, with a 450 W Xenon lamp used as the excitation source. The emitted light was then either directly led to a double monochromator through a bandpass filter and detected by a PMT detector, for spectroscopic measurements, or collimated into an optical fiber cable, leading to a CCD camera, for fluorescence imaging. UV-visible absorption spectra were recorded on a Perkin-Elmer Lambda 1050 UV/Vis spectrophotometer. The decay curves were obtained by a time correlated single-photon counting (TCSPC) method with nanosecond flash lamp excitation. The sample was mounted in a cryostat (Optistat Oxford Instruments) allowing for measurements down to 77 K. The raw decay data were iteratively deconvoluted from the instrument response function (IRF) and fitted to decay functions using FAST software, which allowed more than 4 decay constants to be obtained. The fit quality was assessed by $\chi^2 < 1.3$.

8.2 Structure and Morphology of the QD/Silica Nanoparticles

From the experimental results and reported results in literature [215], it has been found that reaction conditions such as time, temperature, concentration of reactants, ligands and speed of stirring have a profound influence on the size, monodispersity, multiplicity of QDs per silica particle and overall quality of the resulting QD/silica particles. Monodisperse silica spheres were grown in the size range of 40-70 nm by this method, using the controlled hydrolysis of TEOS within reverse micelles [216].

It was found that the concentration of QDs influences the multiplicity of QDs per silica. A 400 μL QD stock solution with concentration of 0.2, 0.8 and 1mg/ml was used. With 0.2mg/mL concentrated QDs the dispersity was acceptable, but many silica particles without QDs appeared (see Fig. 8.1.a). Particles with multiple QDs inside resulted due to the 1mg/mL concentrated QDs. TEM results show that, at this concentration even when multiple QDs were silica coated, they were found mostly in the middle of the silica particles. Therefore, the QDs seem to act as nuclei for the silica growth (see Fig. 8.1.b). With optimal conditions, using 0.8mg/mL concentrated QDs, only one QD was found in the centre of a silica particle as displayed in Fig. 8.1.c.

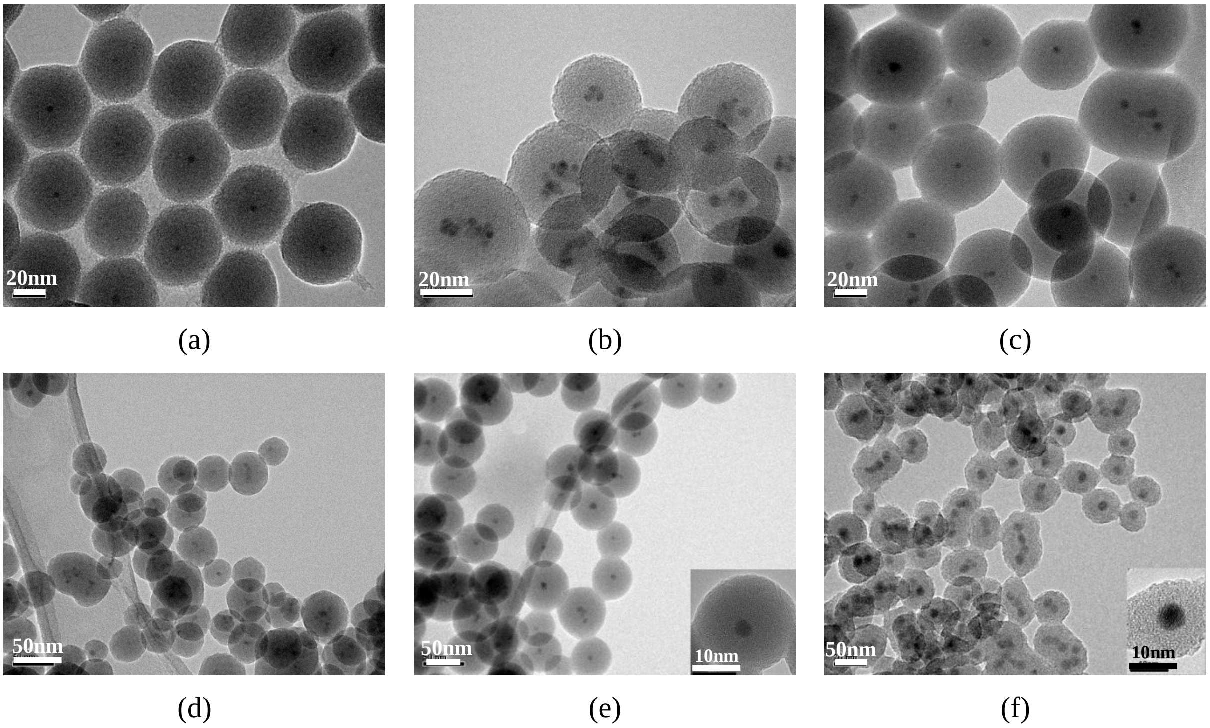

Figure 8.1 TEM micrograph of core/shell/shell structured CdSe/ZnS/silica particles prepared at a) low (0.2mg/mL), b) high (1mg/mL) and c) optimum concentration (0.8mg/mL) of the QDs, (d) CdSe/ZnS/silica particles prepared with a mixed 3.5nm & 6.5nms QDs, e) CdSe/ZnS/silica particles prepared with TOPO-stabilized QDs and f) ODA-stabilized QDs: Insets in e) and f) are high resolution images showing the crystalline structure of the core

In another process 3.5nm and 6.5nm QDs were mixed and added to the solution. From the TEM in Fig. 8.1.d it is observed that the size of the resulting particle is correlated to the QD seed. To study the influence of the hydrophobic nature of the capping layer in more detail, CdSe/ZnS QDs with different ligand for incorporation in silica were also used. Fig. 8.1.e and Fig. 8.1.f show the results after silica growth for TOPO and ODA coated CdSe/ZnS QDs, respectively. The QDs with ODA ligands were incorporated in more polydisperse silica spheres with a larger spread in the number of QDs per silica particle. Insets in Fig. 8.1.e and Fig. 8.1.f are high resolution images showing the crystalline structure of the core.

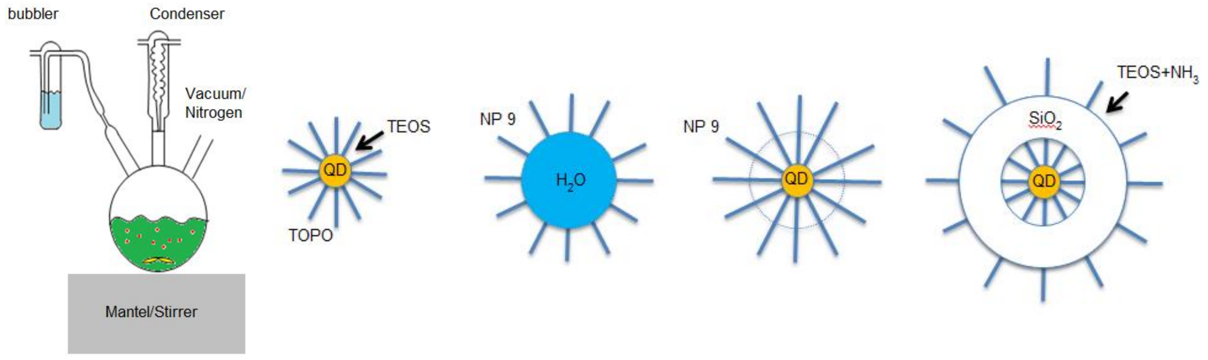

(a) (b) (c) (d) (e)

Figure 8.2 a) Synthesis flask, b-e) growth mechanism for the QD/Silica NP

The synthesis flask used for QD/Silica NP formation is shown in Fig. 8.2.a. A possible growth mechanism for the QD/Silica NP can be suggested as phase transfer without ligand exchange. QDs with hydrophobic ligands can be easily transferred to water by means of tensides (Fig. 8.2.a, b). In this mechanism, the surfactant (NP-9) could form an inverse bilayer around the TOPO or ODA-ligated QDs (Fig. 8.2.d). On addition of the ammonia catalyst, the silica could grow between the tenside layers (Fig. 8.2.e). This hypothetical mechanism is supported by the observation of QD multiplicity on increasing amount of QDs and slow silica growth rate. The third argument for this mechanism is the fact that the QDs are mostly found exactly in the centre of the silica nanoparticles.

8.3 PL Spectra and Fluorescence Response

Films of silica nanoparticles, with embedded CdSe/ZnS QDs, were prepared by drop casting. Structure, photoluminescence and fluorescence images of the layers were investigated. Since the shell growth affects the peak energy of the absorption bands, the absorption spectra in Fig. 8.3.a indicate a successful growth of the silica shell on hydrophobically ligated CdSe/ZnS QDs. PL spectra of nanoparticles, before and after silica encapsulation, show strong photoluminescence in QDs with different sizes, while the silica shell causes a slight red shift of the photoluminescence maximum (see Fig. 8.3.b). Measurement using confocal microscopy of the film demonstrates fluorescence of the core/shell/shell nanoparticles (see Fig. 8.3.c,d). The fluorescence yield of QD-doped silica nanoparticles is not very high due to the low QD content per silica sphere.

8.3.1 Temperature-Dependent PL of the QD/Silica Nanoparticles

The PL spectra of the film containing QD/Silica nanoparticles as a function of the temperature are shown in Fig. 8.4.a. As the sample temperature is increased, the PL intensity decreases, the emission energy redshifts, and the spectra become broader. The temperature dependence of the main PL peak energy,

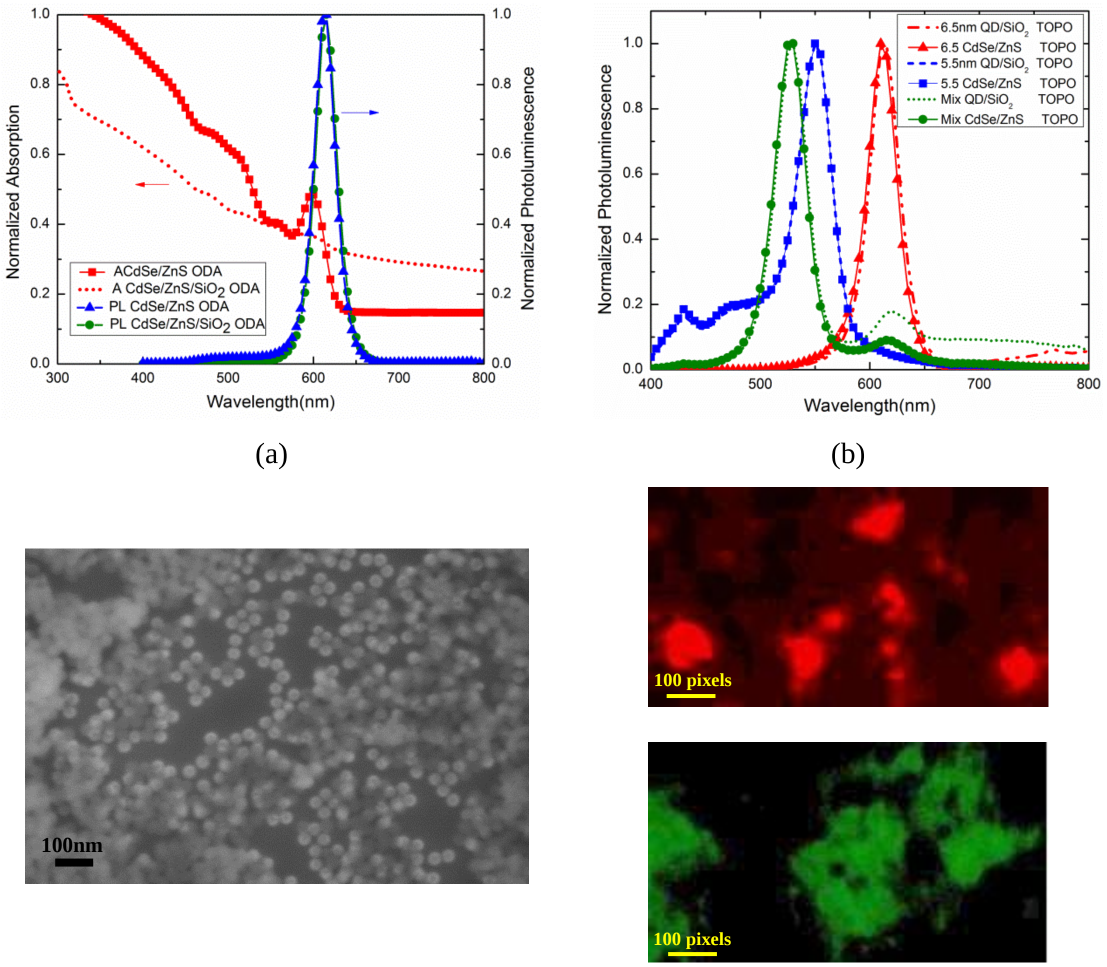

(a) (b)

(c) (d)

Figure 8.3 a) Normalized absorption and PL spectra of ODA-stabilized CdSe/ZnS and QD/SiO$_2$ nanoparticles, b) PL correlated to QD and QD/silica nanoparticles with different sizes; mix QD=3.5nm, 6.5nm (black lines), QDs=5.5nm (blue lines) and QDs=6.5nm (red lines), c) SEM image of a film of QD/silica nanoparticles, d) fluorescence image at excitation wavelength of 380 nm for 6.5nm (top) and 5.5nm (bottom) QD/silica nanoparticles

which represents the energy gap of the average size dots, is reported in Fig. 8.4.b. The QD energy gap shows a redshift of about 60 meV as the temperature increases from 77 K to 300 K.

The experimental data were fitted to the relation shown in equation (8.1), which describes the temperature dependence of PL peak energy in QDs [217].

$$E_g(T) = E_{g0} - \frac{\alpha T^2}{(T+\beta)} \qquad (8.1)$$

Where E_{g0} is the energy gap at 0K, α is the temperature coefficient, and the value of β is close to the Debye temperature of the material. The best fit curve, with α=0.89meV/K and β=960K, reproduces the

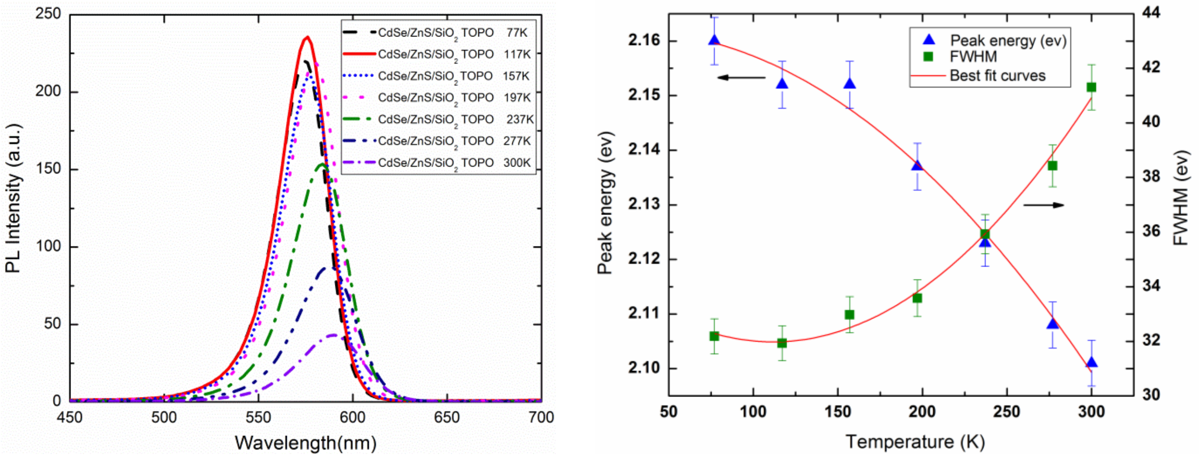

(a) (b)

Figure 8.4 a) PL spectra as a function of the temperature (all measured at 380nm excitation), b) PL peak energy (blue triangles) and FWHM (green squares) as a function of the temperature. The red lines are the best-fit curves as discussed in the text.

experimental data. These values are close to the values in the literature for bulk CdSe [218], demonstrating that the energy shift is due to the temperature-dependent band gap shrinkage of the QD. The full width, at half maximum (FWHM) Γ of the PL peak (see Fig. 8.4.b), increases with the sample temperature. The experimental data were fitted to equation (8.2) which describes the temperature dependence of the excitonic peak broadening in QDs [219]:

$$\Gamma(T) = \Gamma_{inh} + \sigma T + \Gamma_{LO}(e^{\frac{E_{LO}}{K_B T}} - 1)^{-1} \qquad (8.2)$$

Where Γ_{inh} is the inhomogeneous broadening and the last two terms represent the homogeneous broadening due to exciton-phonon interactions. σ is the exciton–acoustic phonon coupling coefficient, Γ_{LO} represents the exciton longitudinal-optical (LO) phonon coupling coefficient, E_{LO} is the LO-phonon energy and K_B is the Boltzmann constant. The best fit parameters are in agreement with the experimental data for $\Gamma_{inh=}$29 meV, σ=9.5 μeV/K, Γ_{LO}=17meV and E_{LO}=29.5meV. The extracted value of σ ~ 9.5μeV/K is about the same as the values reported for bulk CdSe, which is around 8 meV/K [220]. This indicates that the acoustic phonon coupling between the QDs and SiO_2 matrix is negligible as opposed to that of the QDs and organic matrix [221]. The scattering of the optical phonons, with the best fit value of Γ_{LO}=29.5 meV, is considerably reduced with respect to the bulk value [222]. The homogenous broadening can mainly be attributed to the presence of surface defects or trap states [223].

8.3.2 Temperature-Dependent Excitonic Decay of QD/Silica Nanoparticles

In order to analyze the role of nonradiative processes on the relaxation dynamics of core/shell/shell nanoparticles, the temperature dependent PL relaxation using the TCSPC method was studied. The raw decay data was deconvoluted from the instrument response function (IRF) and then fitted to multi-exponential decay function, using an algorithm implemented in FAST software. The results from the exponential tail fitting analysis show that the decay rate increases at higher temperatures, as demonstrated in Fig. 8.5.

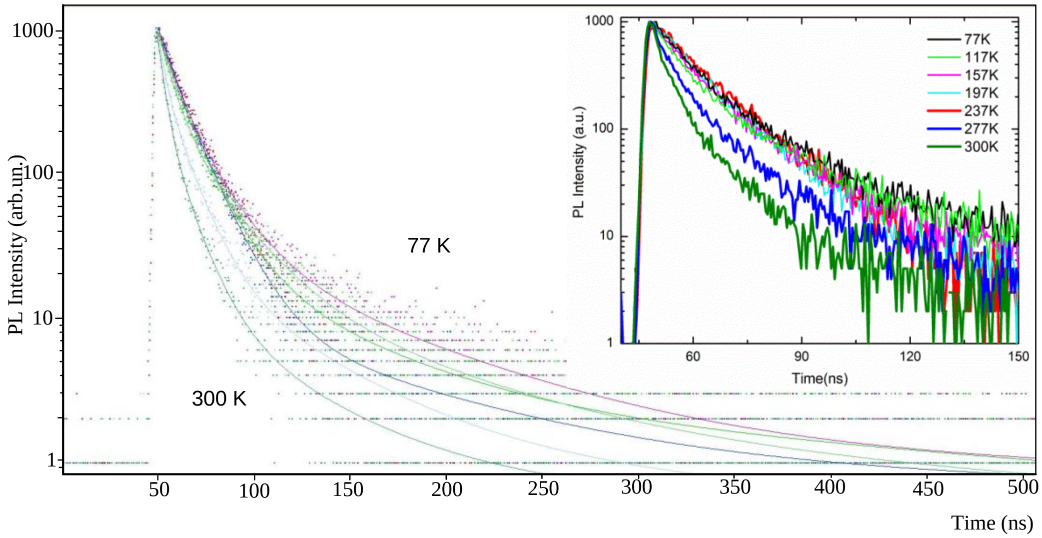

Figure 8.5 Relaxation dynamics as a function of the sample temperature. The solid lines are the best-fit curves.

Distribution analysis was also performed to better study the TCSPC data. The lifetime histograms, in Fig. 8.6.a-g, demonstrate that the average lifetime decreases at higher temperatures. Due to the limited instrument response, it was only possible to study the slow relaxation process. Four slow relaxation components with time constant in the ns range were clearly determined, from both the exponential and tail fitting analyses, at each temperature. The determined values of decay components acquired from the distribution analysis are shown in Table 8.1.

Decay component (ns)	T=77K	T=117K	T=157K	T=197K	T=237K	T=277K	T=300K
τ_1	0.50	0.50	0.50	0.50	-	0.50	0.50
τ_2	9.35	6.64	6.65	6.80	5.96	3.30	3.15
τ_3	42.21	13.98	14.65	18.02	21.36	11.24	-
τ_4	327.6	81.06	56.18	74.96	73.06	-	-
χ^2	0.93	1.14	1.29	1.27	1.27	0.89	0.8

Table 8. 1 Decay components acquired from the distribution analysis.

The fit quality was assured by criteria $\chi^2<1.3$. The relaxation components point to the existence of a number of discrete relaxation pathways, each with an individual associated lifetime. The second component of the decay time (2-pair decay τ_2), as extracted from a distribution fit analysis of the experimental results of the decay dynamics as a function of temperature, is shown in Fig. 8.6.h. The PL decay time is decreasing rapidly as the temperature increases from 77K to 117K, and then a slow decrease is observed in the range 117-237 K and finally another rapid decrease in the range 237-300K is apparent. This behaviour suggests the presence of two temperature-dependent nonradiative processes in the system. The first nonradiative process in the range 77K-150K and the last one in the range 237-300K, which limits the nanoparticle quantum efficiency at room temperature, can be attributed to the thermal escape from the dot assisted by the scattering with LO phonons [224]. In addition, another thermally activated process in the range 117-237K can be due to carrier trapping in surface states, probably at the dot/silica interface (quenching regime) [225]. The surface defects trapping is expected to be more marked in core nanocrystals, which are characterized by a higher surface defects density than core/shell or core/shell/shell nanocrystals.

8.3.3 Effect of Illumination Period on the PL Intensity and Decay Time of the QD/Silica Nanoparticles

As mentioned earlier, intense luminescence properties of the QD/silica nanoparticles were observed, as shown in Fig. 8.7.a The ensemble was illuminated for different periods of time and as a result significant improvement in the QD/silica PL was observed for the samples illuminated for longer periods of time (see Fig. 8.7.b). All 8 periods of illumination resulted in a steady shift to the blue, revealing a slight blue shift of the exciton absorption and confirming a slight reduction in average dot sizes. Fig. 8.7.c shows the PL intensity slightly increased for both the core CdSe QDs and core/shell CdSe/ZnS QDs after 25min of illumination. Significant PL enhancement corresponds to the core/shell/shell CdSe/ZnS/SiO_2 sample. The PL enhancement was able to be explained, as a result of dark dots photon induced fluorescence [226]. The blinking effect [227, 228] might in some way be inhibited to reduce the amount of “off” time; or the illumination could cause a chemical change in the luminescent dots that would result in higher fluorescence efficiency during the “on” periods [229].

Fig. 8.7.d shows the PL decay lifetime and Fig. 8.7.e, f demonstrates the lifetime histograms, with the decay time constant components obtained from the distribution analysis of QD/silica NPs before and after the 25min illumination. The slow decay rate (slow emission rate) and relative increase in average PL decay lifetimes, for the NPs illuminated for the longer periods of time, is likely due to the photo induced chemical change in luminescent dots that caused the PL efficiency to increase. The previously dark dots

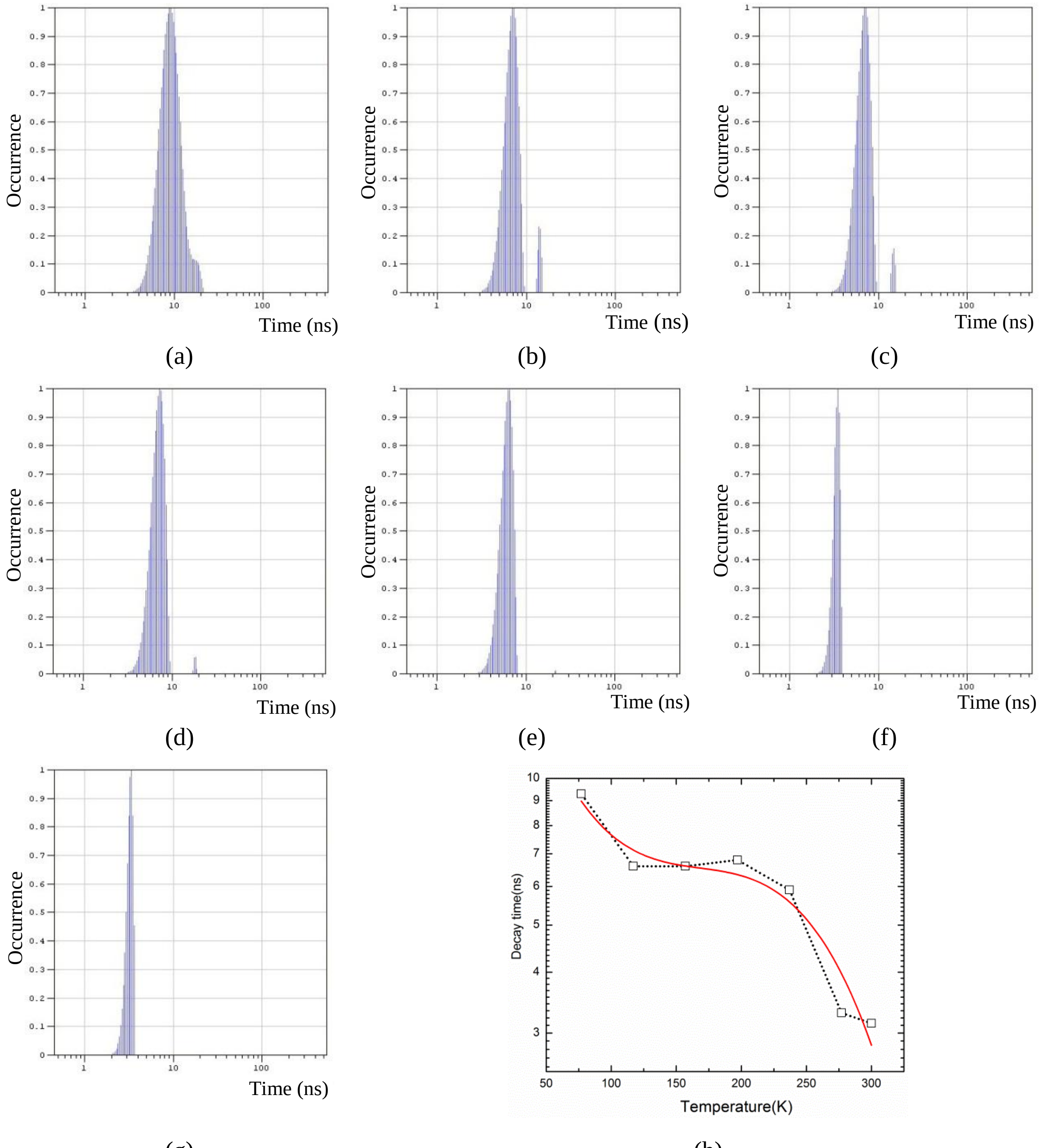

(a) (b) (c)

(d) (e) (f)

(g) (h)

Figure 8.6 Lifetime histograms obtained from distribution analysis at a) 77K, b) 117K, c) 157K, d) 197K, e) 237K, f) 277K, g) 300K, h) PL decay as a function of temperature

have a longer PL lifetime than the already present luminescent dots. Moreover, the transient on or off dots should not cause a change in the decay lifetime by increasing the on period [230].

8.3.4 Effect of QD Size on Excitonic Decay of CdSe/ZnS/SiO$_2$ Nanoparticles

Size dependence of the energy relaxation in CdSe/ZnS QDs and silica coated QD NPs was investigated.

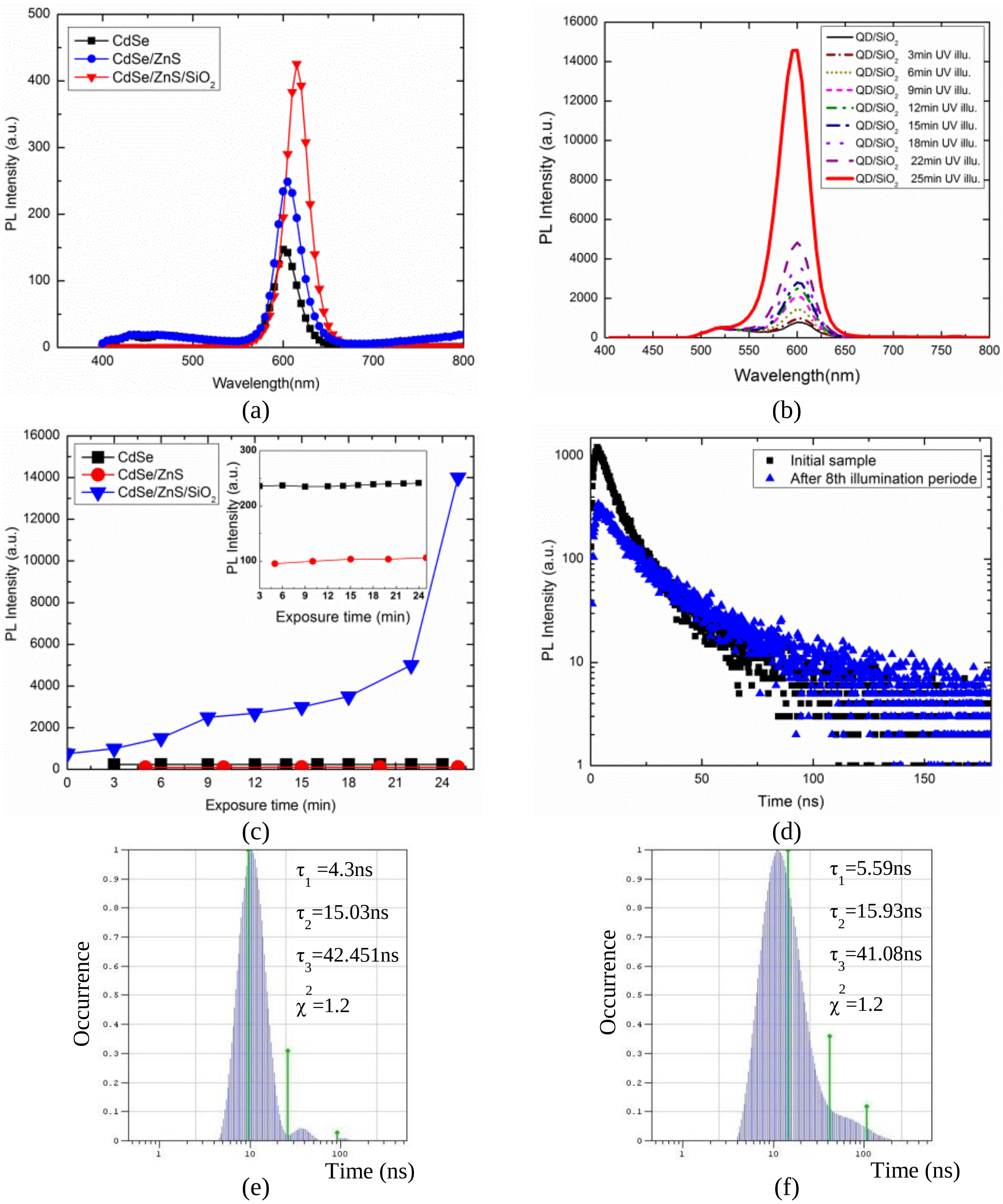

(a) (b) (c) (d) (e) (f)

Figure 8.7 a) Luminescence properties of the core, core/shell and core/shell/shell (QD/silica) nanoparticles, b) QD/Silica ensemble with higher fluorescence efficiency during the "on" periods, c) PL intensity after periods of illumination for core, core/shell QDs (inset) and core/shell/shell NPs, d) Fluorescence decay kinetics of QD/Silica NPs, taken before and after the 25min illumination period. Lifetime histograms obtained from distribution analysis for QD/Silica quantum dots, e) before and f) after the 25min illumination period

The slow relaxation component with a time constant of several nanosecond shows particle size dependence. This lifetime can be contributed by thermal mixing of bright and dark excitons [230]. Lifetime is modelled with a three-level scheme by the Boltzmann distribution of excitons, between these two levels. The total decay rate can be written as [231]:

$$\Gamma = \frac{\Gamma_d + \Gamma_b e^{-\Delta E/k_B T}}{1+e^{-\Delta E/k_B T}} \qquad (8.3)$$

Where Γ_d and Γ_b are decay rates of bright and dark states. Reduction in the QD size increases the confinement energies and the e-h wave function overlapping, thereby enhancing the e-h exchange interaction, resulting in an increase of the energy gap. According to equation (8.3), at constant values of Γ_d and Γ_b , the QD decay rate $\Gamma(\tau^{-1})$ decreases with decreasing QD size, therefore decay lifetime increases. This is not in agreement with the experimental observations. The lifetime constants decrease with decreasing particle size.

In Fig. 8.8.a, b, the decay dynamics for CdSe/ZnS QDs and QD/Silica NPs of different sizes were compared. The time constants were obtained by the distribution tail fitting for all nanoparticle sizes, as shown in Fig. 8.8.c-f. The time constants, measured for CdSe/ZnS QDs decay, followed the same size dependence as that of the QD/Silica sample. For instance, for the silica coated sample the τ_2 time constant decreased from 15.035ns to 14.239 ns, when the dot radius was reduced from 6.5nm to 5.5 nm, indicating a decrease in decay time. This would be attributed to the pronounced surface transformation of smaller size QDs during the growth process. Although no ligand exchange for the proposed mechanism was expected, some unknown chemical effects caused the silica coated QDs to experience nonradiative energy transfers. This effect is more profound for the particles with smaller core size. In addition, it is suggested that the enhancement in the decay rate in smaller particles is caused by an effective increase in carrier concentrations resulting from the increased spatial confinement [232].

8.3.5 Effect of QD Ligand on Excitonic Decay of QD/Silica Nanoparticles

The decay dynamic of the hydrophobically ligated QD/silica nanoparticles (see Fig. 8.9.a) and the time constant obtained from the distribution analysis (see Fig. 8.9.b, c) show low decay rate and accordingly improvement in slow relaxation components for ODA ligated QD seeds. From the results it is predicted that the surface transition during silica growth is more for TOPO-stabilized QDs in respect to the ODA-stabilized QDs.

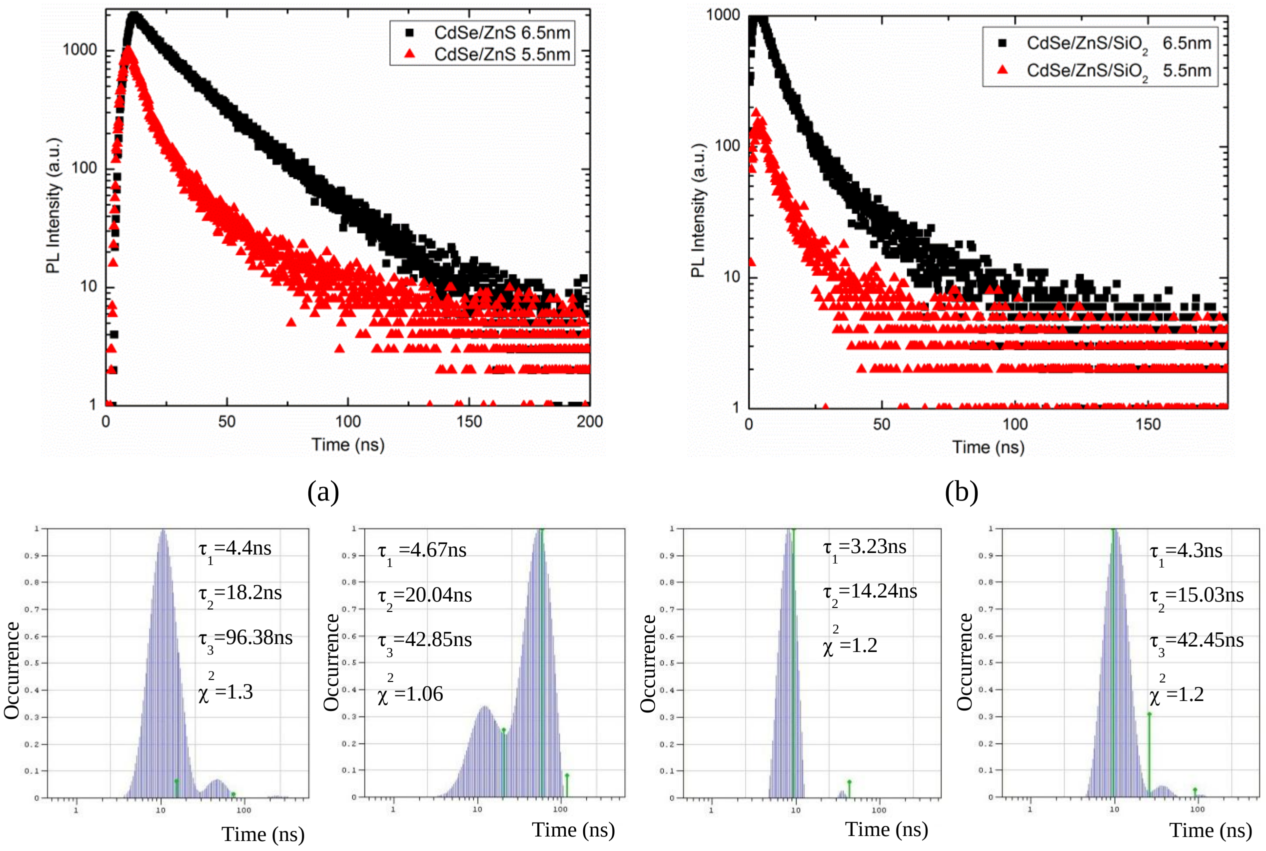

(a) (b)

(c) (d) (e) (f)

Figure 8.8 Size-dependent energy relaxation in a) CdSe/ZnS QDs NP, b) Cdse/ZnS/SiO$_2$ NPs Lifetime histogram and time constants obtained by the distribution tail fitting for c) 5.5nm, d) 6.5nm CdSe/ZnS QDs and silica coated QD NPs with e) 5.5nm, f) 6.5nm seed size

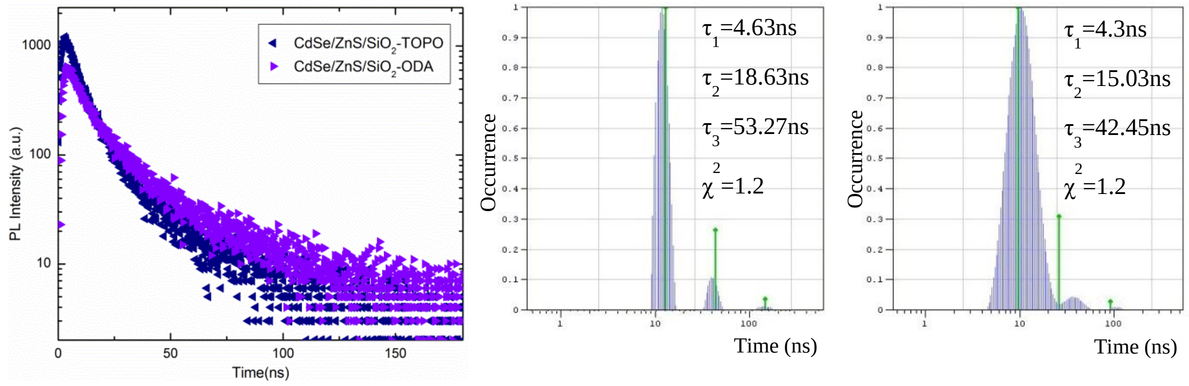

(a) (b) (c)

Figure 8.9 Excitonic decay of hydrophobically ligated QD/Silica nanoparticles; Lifetime histogram and time constants obtained by the distribution tail fitting for b) ODA and c) TOPO ligated QD/silica NPs

8.3.6 Effect of QD Passivation on Excitonic Decay of QD/Silica Nanoparticles

Excitonic decays of core, core/shell QDs and core/shell/shell NPs with CdSe core diameter of 6.5nm were also investigated. As mentioned, surface or interface effect plays an important role in determining the optical properties and carrier dynamics in semiconductor QDs. CdSe QDs surface states, trapping sites at the Cdse/ZnS QDs interface (between the core and the shell), dangling bonds and add atoms at the surface of the QD/silica NP are generally localized in the band gap of the semiconductor and may act as nonradiative traps for the photogenerated carriers resulting observed energy relaxation in Fig. 8.10. Results were obtained for both ODA (see Fig. 8.10.a) and TOPO (see Fig. 8.10.b) ligated QD seeds. Lifetime histogram and time constants were also obtained by the distribution tail fitting for ODA ligated CdSe QDs, CdSe/ZnS QDs,CdSe/ZnS/SiO$_2$ NPs (see Fig. 8.10.c-e) and for TOPO ligated CdSe/ZnS QDs and CdSe/ZnS/SiO$_2$ NPs (see Fig. 8.10.f, g). The decay time increases as the CdSe QDs is passivated by a ZnS layer. The reason for the decrease in the lifetime of the QD/silica NPs could be explained by the transformation of QD surface in the oxide growth step.

8.4 Plasmon Enhanced Luminescence Combined with 3D-Structure of Down-shifting Layer

In order to use colloidal quantum dots, for a new generation of photovoltaic devices, thin films of QDs have to be realized [233]. As discussed in previous chapter, close-packed nanocrystal (NC) superlattices ordered over a large area, produce a media with great potential for deployment as luminescence down-shifter (LDS) layers on the solar cells, for efficiency enhancement. The larger the nanocrystals are, the easier to form self-assembled layers.

The growth of the oxide layer on the CdSe/ZnS QDs can be beneficial for LDS layers with enhanced PL intensities and increased size of the resulting particle, as well as the optically transparent oxide medium in which QDs are embedded. Monolayers (see Fig. 8.11.a) or multilayers (see Fig. 8.11.b) of silica coated QDs can be coated on the solar cell to form the LDS layer containing well-ordered arrays of QDs embedded in a transparent medium. The thickness of the oxide layer can be tuned to provide superlattices with desired photonic crystal properties.

The LDS layer can also benefit from the surface plasmon resonance (SPR) through employment of metal nanoparticles on top of the layer. As discussed in Chapter 7, metal nanoparticles of particular shape, size and density with large extinction cross sections in the UV-NIR range can be used to enhance the light absorption in this layer through enhanced scattering. This structure boosts the absorption of blue photons by QDs, which results in enhanced PL. It also provides more chance for the emitted photons to be directed towards the cell and be absorbed.

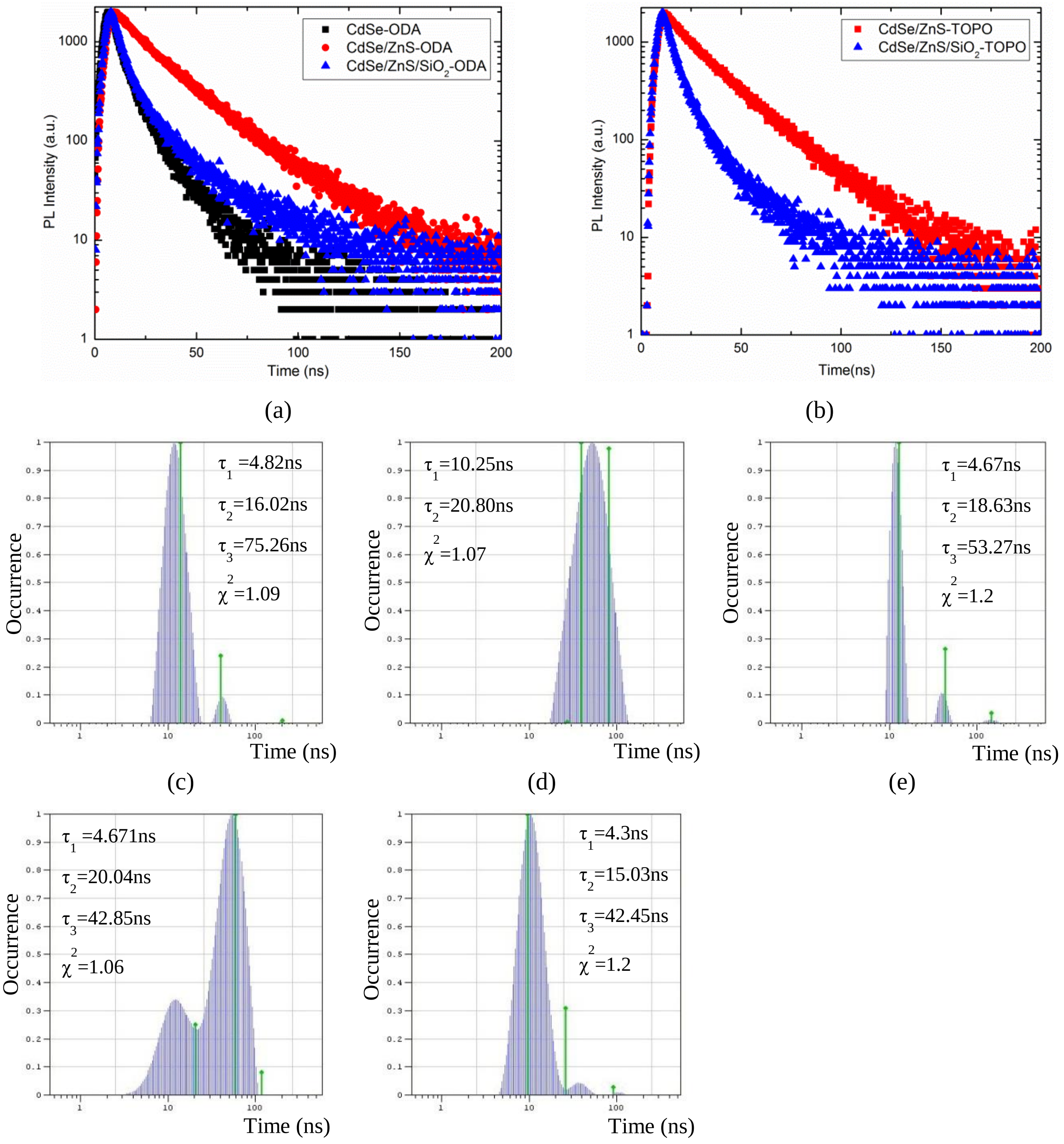

(a) (b)

(c) (d) (e)

(f) (g)

Figure 8.10 Excitonic decay of a) ODA, b) TOPO ligated QDs with different passivations; Lifetime histogram and time constants obtained by the distribution tail fitting for ODA ligated, c) CdSe QDs, d) CdSe/ZnS QDs, e) CdSe/ZnS/SiO$_2$ NPs and for TOPO ligated f) CdSe/ZnS QDs and g) CdSe/ZnS/SiO$_2$ NPs

Future work would involve fabrication of plasmon enhanced luminescence combined with a 3D-structure of down-shifting layer (see Fig. 8.11.b). In order to provide a close-packed self-assembled layer of QD/SiO_2 , the surface of the oxide layer needs to be functionalized. Finding a material with plasmon resonance in the UV-NIR range and optimizing the optical properties of the PR layer would be the next steps. The periodic structure of the metal nanoparticles can easily be formed on top of the QD/SiO_2 3D-structures by seating into the hexagonal spacing between the closely packed NPs (see Fig. 8.11).

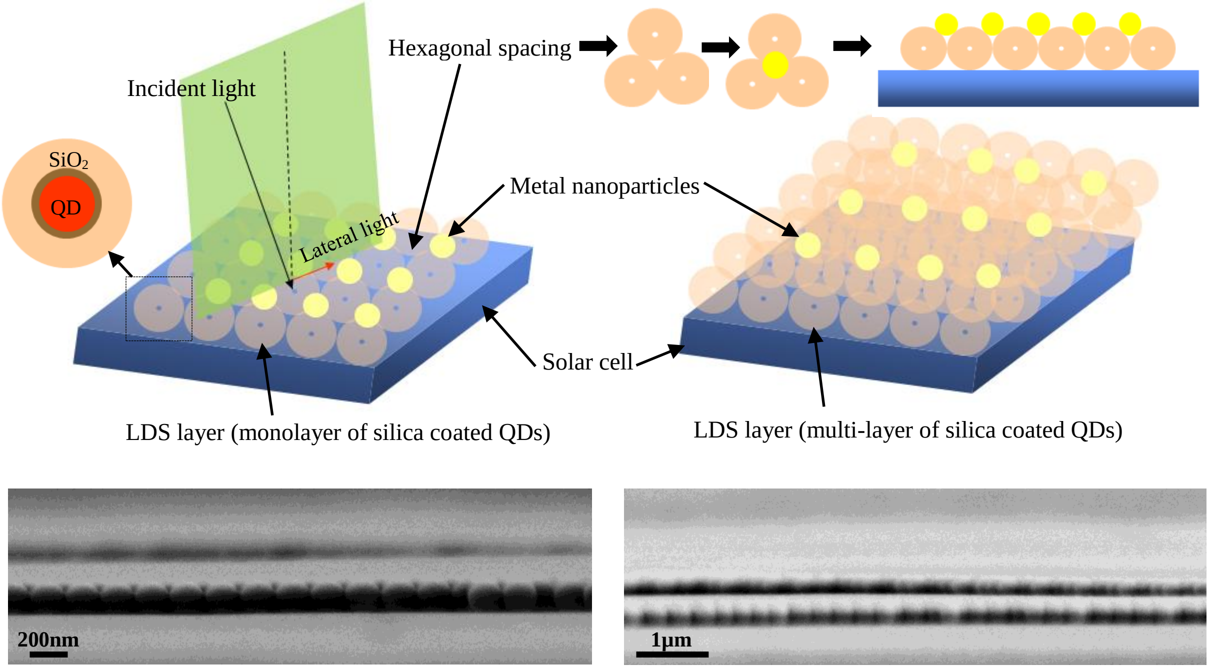

(a)

(b)

Figure 8.11 Schematic (top) and SEM (bottom) of plasmon enhanced luminescence combined with 3D-structure of down-shifting layer containing: a) Monolayer and b) multilayers of silica coated QDs photonic crystals

Similar synthesis processes can be used to coat the silica with thin metal (e.g. Au) layer. A close-packed ordered layer of QD/silica/Au NP can also be utilized as a plasmon enhanced LDS structure (see Fig 8.12). The use of this structure can benefit from enhanced absorption, through the photonic crystal properties of the ordered QDs embedded in transparent matrix and the plasmonic properties of the metallic outer shell, at the same time.

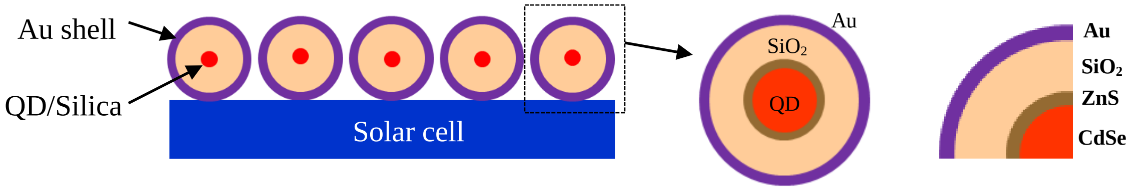

Figure 8.12 Close-packed ordered layer of QD/silica/Au NP as plasmon enhanced LDS structure

8.5 Conclusions

The incorporation of different sizes, of hydrophobically-stabilized CdSe/ZnS core/shell QDs within silica spheres, was investigated using the reverse microemulsion method. The resulting silica particles of 40-70 nm are highly monodisperse and have one QD incorporated exactly in the centre of the sphere. This method gives a high degree of control and indicates that the QDs act as nucleation centres. The resulting QD/silica nanoparticles show intense PL behavior. The temperature dependent PL spectra of the film demonstrate the temperature-dependent band gap shrinkage of the QDs. The relaxation dynamics of the system suggest that the carrier trapping at the QD/silica interface and LO phonons scattering are the main two temperature dependent, nonradiative relaxation processes of the nanoparticles. Temperature, illumination, QD size, ligands and passivation affect the nanoparticle decay dynamics. Close-packed QD/silica NP superlattices, ordered over a large area, produce a medium with a great potential to be deployed as luminescence down-shifting layers on the solar cells for efficiency enhancement.

Chapter 9

Conclusions

In this doctoral study simple and low cost methods were developed for the fabrication of nanowires and quantum dots employed in advanced solar cell architectures such as SiNWs array cells and crystalline silicon cell with a down shifting layer. This work concentrates on two closely related subjects, namely; (i) fabrication and characterization of SiNWs using dry etching processes for SiNWs array cell application and (ii) fabrication and characterization of QDs and luminescence down shifting layers. Here the most significant contributions of this research are summarized.

Achieved random and periodic nanowire arrays using simple processes

- Ordered arrays of upright sub-λ structures of SiN_y and SiNWs were fabricated on silicon substrate by a simple maskless plasma etching process. A simplified method using nanosphere lithography and a top-down approach for NW formation was presented which enables large-scale production of periodic nanowires with desired diameters. The structural, surface and optical properties of the fabricated structures were modeled and characterized. The anti-reflection coating (ARC) properties of SiN_x and SiNWs were confirmed by spectroscopic measurements. The SiN_x nanostructures results in efficient light trapping as compared to silicon due to their low surface recombination velocity (SRV). They can also be used as templates for formation of SiNWs with desired geometry. The results from microwave photoconductivity decay (μ-PCD) and photoluminescence (PL) measurements also show that the optoelectronic properties of SiNWs can be tuned by passivation, embedment in transparent layers, and engineering of the particle dimension. The photon conversion ability of the fabricated structures was verified by PL. the simplicity, repeatability, and scalability of the developed processes have strong potential for use with photovoltaic device architectures. In addition to serving as passive components; to enhance the optical performance of the solar cells, these fabricated SiNWs can be used as active part of new device architectures.

Developed two architectures for radial junction nanowire solar cells

- Simple and cost effective approaches for fabrication of SiNWs array cells were examined. In one approach, a non-planar PV device was fabricated on the wires formed with maskless etching. The junction was formed by the conformal thin film deposition of n^+ *a*-Si:H. Conformal transparent AZO contact layers were then sputter deposited to planarize the arrays and facilitate the formation of the metal fingers. In another approach, combination of nanosphere lithography and top-down approaches were utilized for NW formation. In order to better understand how the geometrical structure of the NWs affects the charge separation, theoretical simulations were performed in COMSOL multiphysics. Space charge density and electric fields across the junction for a single core-shell wire with different doping levels of p and n regions, as well as wire with conformal and non-conformal contacts were investigated. The simulation results demonstrate that by tuning the doping parameters and the wire geometry, it is possible to design the structure with quasi-neutral or fully depleted wire. We will be able to design our structure to either have quasi-neutral region in the wire or making a fully depleted wire. The experimentally obtained results confirm the enhancement in current density due to the enhanced light trapping and carrier collection efficiency owing to optimized device configuration. The poor fill factor of the devices was associated with significant series resistance of the TCO layer and the surface defects. The conversion efficiency of our first-generation SiNWs array solar cells reported here is low and further improvements on the surface and the optical and electrical properties of the TCO layer are needed to satisfy the high-performance application requirements. These studies gives insights to improve the materials and designs in order to benefit more from the implementation of SiNWs array cells by enhanced efficiency at lower cost

Experimentally proved the concepts of luminescent down shifting for crystalline silicon solar cells

- A planar solar cell comprised of a luminescent down shifting layer on top of a c-Si cell were fabricated and characterized. For this purpose, a laboratory scale c-Si solar cell fabricated and fully characterized. Luminescence down-shifting architectures consist of quantum dots in oxide and spin-on-glass matrices were then devised and deployed on the fabricated c-Si cells to examine the down shifting properties of each design. Improvement of the spectral response of the c-Si cell with the LDS layer with respect to the cell with the QD layer was verified. No overall performance enhancement can be reported at this stage due to the losses associated with low quantum efficiency of the commercially available luminescent species, isotropic emission, absorption in the non-optimized oxide or glass layer, and scattering of the emitted photons towards the top scape cone instead of transmitting to the underlying cell. In order to gain the benefit from down shifting, the layer needs to be optimized for near-unity quantum efficiencies and maximum light trapping. Continued research is required to improve the luminescence quantum efficiency of the quantum dots. QDs, oxide and SOG are practical choices to use in LDS layer due to their good optical properties, easy processing method, and low cost.

Synthesized silica coated QDs and demonstrating formation of closely packed layer and enhanced luminescent quantum efficiency

- A synthesis method for the formation of silica coated QD were reported. An appropriate design for the LDS layer is a self-assembled QD structure with relatively high LQE embedded in large thin sheets of transparent material as this will minimize the optical losses in the LDS layer. Signatures of enhanced PL properties show the potential of the method to provide QDs with improved LQE. In addition, the proposed synthesis method can produce NPs with larger dimensions that can be easily formed into close packed layer of QD. QD superlattices in oxide medium with photonic crystal properties produce a media with a great potential to deploy as down shifter layers on the solar cells and enhance the efficiency of the device.
- In this work the possibility of employing the nanowires made with maskless reactive ion etching and wires formed with nanosphere lithography and etching, for the construction of the SiNWs array cells was also explored. Significant progresses were made in the development of SiNW array fabrication processes. The effects of the wire geometry on the device characteristics were simulated. Fabrication of crystalline silicon cell was reported to use as the base device of the advanced architectures incorporating LDS layers. LDS layer containing CdSe/ZnS QDs in oxide and SOG matrices were fabricated for down shifting. QD-double shell structure with an oxide layer grown as the outer shell was proposed, fabricated, and characterized to utilize in down shifting layers. The noticeable properties of the fabricated architectures can be utilized to advance the functionality of the future devices. Nevertheless, several fabrication challenges must be resolved to achieve the full potential of the proposed designs.

Future Work

Despite the extensive research carried out throughout this study, many unexplored and unsolved issues still remain concerning the material properties and the efficiencies of the new devices. A compact summary of such issues and the recommended solutions are summarized here.

- The fabricated SiN_x nanostructures presented in Chapter 3 can be used as templates for etching of the silicon substrate to form Si nanostructures with desirable shape and properties. Gentle plasma cleaning processes can be developed for formation of graded index Si nanostructures with enhanced optical properties. As shown in Fig. 9.1 self-aligned emitter solar cell structure can be also fabricated employing this method. Gain can be obtained from this architecture due to the formation of highly conductive negatively charged nanostructures with small junction area and reduced reflectance.

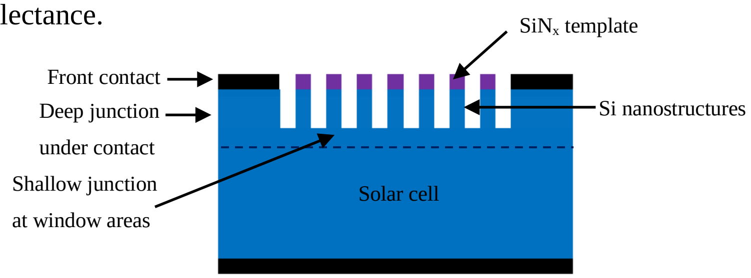

Figure 9.1 Self-aligned selective emitter solar cell structure.

- The optical and electrical properties of the SiNWs fabricated with maskless reactive ion etching presented in chapter 3 are affected by surface defects which resulted in weak PL and increase in SRV. The developed methodology described in Chapter 4 for formation of SiNWs based on nanosphere lithography must be used for fabrication of high aspect ratio wires with controlled structural dimensions. The size of the wires must be in the range of 100-500nm, so the wires are mechanically robust and can survive the damage removal or oxidation processes. High aspect ratio wires with no surface damages can be utilized in the fabrication of SiNWs array cells resulting in higher open circuit voltage and improved performance.
- In Chapter 3, the weak photoluminescence of the SiNWs can be attributed to the non-radiative recombination centers at the surface of the wires. The PL intensity can be improved in the wires with clean sidewalls. In addition, as shown in Fig. 9.2 the size of the wires can also be reduced using multiple oxidations and cleaning steps that leads to enhanced PL results.

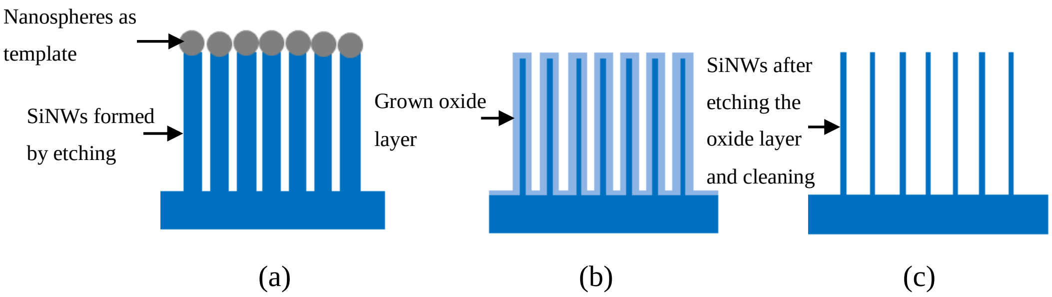

Figure 9.2 SiNWs array formed by microsphere lithography and etching, b) reducing the size of the wires by oxidation, c) wires after oxide etching and cleaning.

- The fabricated SiNWs array cell that was presented in Chapter 5 has a hybrid axial-radial structure as illustrated or shown in Fig 9.3.a. High aspect ratio wires on a thin substrate must be developed to benefit more efficiently from the radial geometry of the junction (see Fig. 9.3.b). Moreover, due to the enhanced carrier separation and collection in a radial p-n junction cell, these structures can be fabricated on low quality material at lower cost.

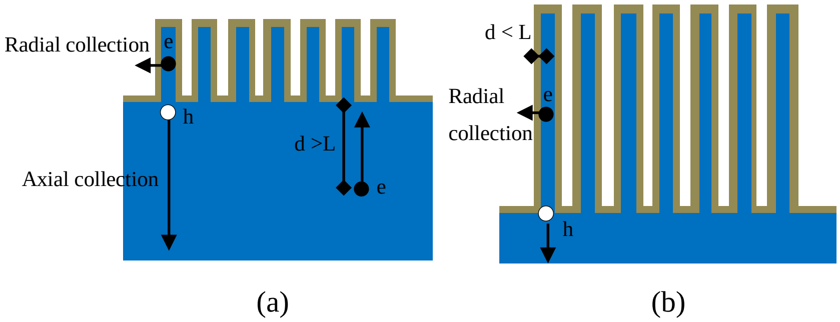

Figure 9.3 a) Hybrid axial-radial SiNWs array cell, b) radial SiNWs array cell (L is the diffusion langth of the minority carrires. D is the distance of the generated carriers from the junction).

- Determination of the radial dopant profile of individual silicon nanowire in a more sophisticated method is necessary. Energy Dispersive X-ray Spectroscopy (EDS) and Electron Energy-Loss *Spectroscopy* (EELS) are methods that can be applied to the samples for future study.
- Stack layers of QDs with engineered band gaps can be introduced in an appropriate graded index structure, in order to enhance the optical parameters of the LDS layer in a wide range (see Fig 9.4.a). Some future studies can be work on the refractive index of the QDs super lattice layers using different designs by changing the spacing and the size of the QDs.
- Fabrication of plasmon-enhanced luminescence combined with 3D-structure of down shifting layer is demanded (see Fig. 9.4.a). CdSe/ZnS/SiO_2 core/shell/shell structures can be employed for

production of well-ordered arrays of QDs with the desired spacing. This can be achieved by optimizing the outer shell thickness. Close-packed ordered layers of QD/silica/Au NP may be employed as plasmon-enhanced LDS structure (see Fig 9.4.b). An efficient LDS layer can be produced due to the improved absorption in the QD photonic crystal layer and the plasmonic properties of the metallic outer shell.

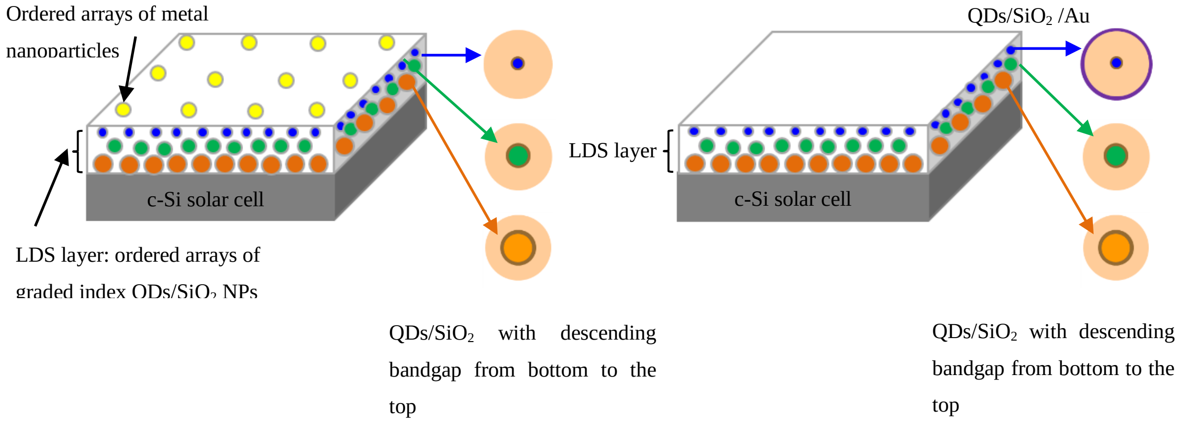

(a) (b)

Figure 9.4 Plasmon-enhanced luminescence combined with 3D-structure of down-shifting layer; a) graded index QD/silica structures with descending band gap from bottom to the top b) the QD/silica/Au NPs were used on the top layer.

- Future research to improve dimensions, surface quality of the wires, optical and electrical properties of the shell, and the contact layers of SiNWs array devices is demanded. Development of QD synthesis methods to produce nanocrystals with high luminescence quantum yield and LDS layers with enhanced optical properties is crucial. As demonstrated in Fig. 9.5 SiNWs and LDS layer can be integrated to form an ultra-high efficiency hybrid device. Integrating quantum dots serve as light harvesting agent for UV photons in the light trapping wires. Using this structure, enhencement in UV response and overal conversion efficiency of the device is expected.

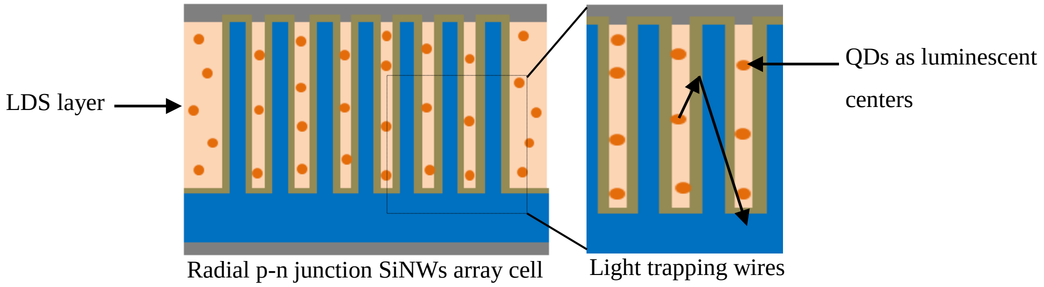

Figure 9.5 Hybrid architecture; LDS layer integrated with radial p-n junction SiNWs array cell.

References

[1] M.A. Green, *Solar Cells: Operating Principles, Technology and System Applications,* Prentice-Hall, Englewood Cliffs, NJ, USA, 1982.

[2] H.J. Hovel, R.T. Hodgson, and J.M. Woodall, “The effect of fluorescent wavelength shifting on solar

[2] H.J. Hovel, R.T. Hodgson, and J.M. Woodall, “The effect of fluorescent wavelength shifting on solar cell spectral response,” *Sol. Energy Mater.*, vol. 2, no. 1, pp. 19-29, Sept.-Nov. 1979.

[3] M.A. Green, K. Emery, Y. Hishikawa, and W. Warta, “Solar cell efficiency tables,” *Prog. Photovolt: Res. Appl.,* vol. 16, no. 1, pp. 6-12, Jan. 2008.

[4] M.A. Green, *Third Generation Photovoltaics.* Springer Verlag, Berlin, Germany, 2003.

[5] M. Bedair, M.F. Lamorte, and J.R. Hauser, “A two-junction cascade solar-cell structure,” *Appl. Phys. Lett.,* vol. 34, no. 1, pp. 38-39, Jan. 1979.

[6] M.Taguchi, K.Kawamoto, S.Tsuge, T.Baba, H.Sakata, M.Morizane, K. Uchihashi, N.Nakamura, S.Kiyama, and O.Oota, “HITTM cells-high-efficiency crystalline Si cells with novel structure,” *Prog. Photovoltaics,* vol. 8, no. 5, pp. 503-513, Nov. 2000.

[7] A. Luque and A. Marti, “Increasing the efficiency of ideal solar cells by photon induced transitions at intermediate levels,” *Phys. Rev. Lett.*, vol. 78, no. 26, pp. 5014-5017, Jun. 1997.

[8] A. J. Nozik, “Multiple exciton generation in semiconductor quantum dots,” *Chemical Physics Letters*, vol. 457, no. 1–3, pp. 3–11, 2008.

[9] Y. Takeda, T. Ito, T. Motohiro, D. Konig, S. Shrestha, and G. Conibeer, “Hot carrier solar cells operating under practical conditions,” *J. Appl. Phys*., vol. 105, no. 7, p. 074905, 2009.

[10] T. Trupke, M.A. Green, and P. Würfel, “Improving solar cell efficiencies by down-conversion of high-energy photons,” *J. Appl. Phys.,* vol. 92, no. 3, pp. 1668-1674, Aug. 2002.

[11] M. A. Green, *Third Generation Photovoltaics,* Sydney: Bridge Printery, 2001.

[12] T. J. Kempa, B. Tian, D. R. Kim, J. Hu, X. Zheng, and C. M. Lieber, “Single and tandem axial *p-i-n* nanowire photovoltaic devices,” *Nano Lett*., vol. 8, no. 10, pp.3456–3460, 2008.

[13] B. M. Kayes, H. A. Atwater, and N. S. Lewis, “Comparison of the device physics principles of planar and radial p-n junction nanorod solar cells,” *J. Appl. Phys*., vol. 97, no. 11, p. 114302, 2005.

[14] L. Hu and G. Chen, “Analysis of optical absorption in silicon nanowire arrays for photovoltaic applications,” *Nano Lett.* vol. 7, no. 11, pp. 3249–3252, 2007.

[15] E. C. Garnett and P. D. Yang, “Silicon nanowire radial p-n junction solar cells,” *J. Am. Chem. Soc.*, vol. 130, no. 29, pp. 9224–9225, 2008.

[16] M. Law, L. E. Greene, J. C. Johnson, R. Saykally, and P. D. Yang, “Nanowire dye-sensitized solar cells,” *Nature Mater.*, vol. 4, pp. 455–459, 2005.

[17] M. D. Kelzenberg, D. B. Turner-Evans, B. M. Kayes, M. A. Filler, M. C. Putnam, N. S. Lewis, and H. A. Atwater, “Photovoltaic measurements in single-nanowire silicon solar cells,” *Nano Lett.,* vol. 8, no. 2, pp. 710–714, 2008.

[18] J. Zhu, Z.Yu, G.F. Burkhard, C. Hsu, S.T. Connor, Y. Xu, Q. Wang, M. McGehee, S. Fan, and Y. Cui,“Optical absorption enhancement in amorphous silicon nanowire and nanocone arrays,” *Nano Lett*., vol. 9, no 1, pp. 279-282, 2008.

[19] G. S. Oehrlein and Y. Kurogi, "Sidewall Surface Chemistry in Directional Etching Processes," *Mater. Sci Eng.*, vol. 24, no. 4, pp. 153–183, 1998.

[20] C. Hsu, S. T. Connor, M. X. Tang, and Y. Cui, "Wafer scale silicon nanopillars and nanocones by langmuir-blodgett assembly and etching," *Appl. Phys. Lett*, vol. 93, no. 13, p. 133109, 2008.

[21] J. A. Czaban, D. A. Thompson, and R. R. LaPierre, "GaAs core-shell nanowires for photovoltaic applications," *Nano Lett*., vol.9, no.1, pp. 148–154, 2009.

[22] B. Tian, T. J. Kempa, and C. M. Lieber, "Silicon nanowire photovoltaics," *Chem. Soc. Rev.*, vol. 38, pp. 16–24, 2009.

[23] T. Maruyama, A. Enomoto, and K. Shirasawa, "Solar cell module colored with fluorescent plate," *Sol. Energy Mater. Sol. Cells,* vol. 64, no. 3, pp. 269-278, Sept. 2000.

[24] B. S. Richards and K.R. McIntosh, "Overcoming the poor short wavelength spectral response of CdS/CdTe photovoltaic modules via luminescence down-shifting: ray-tracing simulations," *Prog. Photovolt. Res. Appl.*, vol. 15, no. 1, pp. 27-34, Jan. 2007.

[25] A. LeDonne, M. Acciarri, S. Binetti, S. Marchionna, D. Narducci, and D. Rotta, "Enhancement of solar energy conversion efficiency by light harvesting of organolanthanide complexes," *Presented at the 23rd EU PVSEC,* Valencia, Spain, Sept. 2008.

[26] W. Viehmann, "Thin-film scintillators for extended ultraviolet (UV) response silicon detectors," in *Proc. Soc. Photo-Opt. Instrum. Eng.*, vol. 196, pp. 90–95, Aug. 1979.

[27] A. Goetzberger and W.Greubel, "Solar energy conversion with fluorescent collectors," *Appl. Phys.*, vol. 14, no. 2, pp. 123-139, Oct. 1977.

[28] B. C. Rowan, L.R. Wilson, B.S. Richards, "Advanced material concepts for luminescent solar concentrators," *IEEE J. Sel. Top. Quantum Electron*., vol. 14, no. 5, pp. 1312–1322, Sept.-Oct. 2008.

[29] A.W. Czanderna and F.J. Pern, "Encapsulation of PV modules using ethylene vinyl acetate copolymer as a pottant: a critical review," *Sol. Energy Mater. Sol. Cells*, vol. 43, no. 2, pp. 101–181, Sept. 1996.

[30] L.R. Wilson and B.S. Richards, "Measurement method for absolute PLQY of fluorescent organic dyes in PMMA for luminescent solar concentrators," *Appl. Opt.*, vol. 48, no. 2, pp. 212–220, Jan. 2009.

[31] B. C. Hong and K. Kawano, "Organic dye-doped thin films for wavelength conversion and their effects on the photovoltaic characteristics of CdS/CdTe solar cells," *Jpn. J. Appl. Phys.,* vol. 43, no. 4a, pp. 1421–1426, Apr. 2004.

[32] S.V. Gaponenko, *Optical Properties of Semiconductor Nanocrystals.* Cambridge University Press, Cambridge, U.K., 1998.

[33] M. Bruchez Jr., M. Moronne, P. Gin, S. Weiss, and A.P. Alivisatos, "Semiconductor nanocrystals as fluorescent biological labels," *Science,* vol. 281, no. 5385, pp. 2013-2016, Sept. 1998.

[34] K. Kawano, K. Arai, H. Yamada, N. Hashimoto, and R. Nakata, "Application of rare- earth complexes for photovoltaic precursors," *Sol. Energy Mater. Sol. Cells,* vol. 48, no. 1–4, pp. 35-41, Nov. 1997.

[35] W. Shockley and H. J. Queisser, "Detailed balance limit of efficiency of p-n junction solar cells," *J. Appl. Phys.,* vol. 32, no. 3, pp. 510–519, 1961.

[36] J. M. Luther, Thesis, Colorado School of Mines, 2007.

[37] K. Tanabe, “A review of ultrahigh efficiency III-V semiconductor compound solar cells: multijunction tandem, lower dimensional, photonic up/down conversion and plasmonic nanometallic structures,” *Energies*, vol. 2, no. 3, pp. 504–530, 2009.

[38] A. J. Nozik, “Quantum dot solar cells,” *Physica E*, vol. 14, no. 1–2, pp. 115–120. 2002.

[39] R. T. Ross and A. J. Nozik, “Efficiency of hot-carrier solar energy converters,” *J. Appl. Phys*., vol. 53, no. 5, pp. 3813–3818, 1982.

[40] A. J. Nozik, “Spectroscopy and hot electron relaxation dynamics in semiconductor quantum wells and quantum dots,” *Annu. Rev. Phys. Chem*., vol. 52, pp. 193–231, 2001.

[41] F. Williams and A. J. Nozik,” Irreversibilities in the mechanism of photoelectrolysis,” *Nature*, vol. 271, pp. 137–139, 1978.

[42] T. Trupke, M. A. Green, and P. Würfel, “Improving solar cell efficiencies by up-conversion of sub-band-gap light,” *J. Appl. Phys*., vol. 92, no. 7, pp. 4117–4122, 2002.

[43] J. E. Granata, J.H. Ermer, P. Hebert, M. Haddad, R.R. King, D.D. Krut, M.S. Gillanders, N.H. Karam, and B.T. Cavicchi, “Advancements in GaInP2/GaAs/Ge solar cells - production status, qualification results and operational benefits,” in *Proc. of the 29th IEEE Photovoltaic Specialist Conference, IEEE*, 2002, pp. 824–827.

[44] R. R. King, D. C. Law, C. M. Fetzer, R. A. Sherif, K. M. Edmondson, S. Kurtz, G. S. Kinsey, H. L. Cotal, D. D. Krut, J. H. Ermer, and N. H. Karam, “Pathways to 40% efficient concentrator photovoltaics,” in *Proc. of 20th European Photovoltaic Solar Energy Conference, Barcelona*, pp. 118-123, 2005.

[45] K. Emery, M. Meusel, R. Beckert, F. Dimroth, A. Bett, and W. Warta, “Procedures for evaluating multijunction concentrators,” in *Proc. of 28th IEEE Photovoltaic Specialists Conference*, 2000, pp. 1126-1130.

[46] A. Marti and G. L. Araujo, “Limiting efficiencies for photovoltaic energy conversion in multigap systems,” Sol. Energy Mater. Sol. Cell, vol. 43, no. 2, pp. 203–222, 1996.

[47] R. R. King, D. C. Law, K. M. Edmondson, C. M. Fetzer, G. S. Kinsey, H. Yoon, R. A. Sherif, and N. H. Karam, “40% efficient metamorphic GaInP/GaInAs/Ge multijunction solar cells,” *Appl. Phys. Lett*., vol. 90, no. 18, p. 183516, 2007.

[48] M. Wolf, R. Brendel, J. H. Werner, and H. J. Queisser, “Solar cell efficiency and carrier multiplication in Si1-xGex alloys,” *J. Appl. Phys.*, vol. 83, no. 8, 4213–4221, 1998.

[49] D. S. Boudreaux, F. Williams, and A. J. Nozik, “Hot carrier injection at semiconductor-electrolyte junctions,” *J. Appl. Phys*., vol. 51, no. 4, pp. 2158–2163, 1980.

[50] A. J. Nozik, “Multiple exciton generation in semiconductor quantum dots,” *Chemical Physics Letters*, vol. 457, no. 1–3, pp. 3–11, 2008.

[51] A. Shabaev, A. L. Efros, and A. J. Nozik, “Multiexciton generation by a single photon in nanocrystals,” *Nano Lett.*, vol. 6, no. 12, pp. 2856–2863, 2006.

[52] R. D. Schaller and V. I. Klimov, “High efficiency carrier multiplication in PbSe nanocrystals: implications for solar energy conversion,” *Phys. Rev. Lett*., vol. 92, no. 18, pp. 186601-4, 2004.

[53] V. N. Ivakhno, “Quantum efficiency of the internal photoelectric effects and impact ionization in Ge,” *Sov. Phys. Solid State*, vol. 14, no. 1, pp. 157–160, 1972.

[54] O. Christensen, “Quantum efficiency of the internal photoelectric effect in silicon and germanium,” *J. Appl. Phys*., vol. 47, no. 2, pp. 689–695, 1976.

[55] J. Bude and K. Hess, “Thresholds of impact ionization in semiconductors,” *J. Appl. Phys*., vol. 72, no. 8, pp. 3554–3561, 1992.

[56] R. D. Schaller, M. Sykora, J. M. Pietryga, and V. I. Klimov, “Seven excitons at a cost of one: redefining the limits for conversion efficiency of photons into charge carriers,” *Nano Lett*., vol. 6, no. 3, pp. 424–429, 2006.

[57] J. M. Luther, M. Law, M. C. Beard, Q. Song, M. O. Reese, R. J. Ellingson, and A. J. Nozik, “Schottky solar cells based on colloidal nanocrystal films,” *Nano Letters,* vol. 8, no. 10, pp. 3488–3492, 2008.

[58] Z. Lin, A. Franceschetti, and M. T. Lusk, “Size dependence of the multiple exciton generation rate in cdse quantum dots,” *ACS Nano,* vol. 5, no. 4, pp. 2503–2511, 2011.

[59] R. D. Schaller and V. I. Klimov, “High efficiency carrier multiplication in PbSe nanocrystals: implications for solar energy conversion,” *Phys. Rev. Lett*., vol. 92, no. 18, pp. 186601-4, 2004.

[60] S. K. Stubbs, S. J. O. Hardman, D. M. Graham, B. F. Spencer, W. R. Flavell, P. Glarvey, O. Masala, N. L. Pickett, and D. J. Binks, “Efficient carrier multiplication in InP nanoparticles,” *Physical Review B,* vol. 81, no. 8, p. 081303, 2010.

[61] J. E. Murphy, M. C. Beard, A. G. Norman, S. P. Ahrenkiel, J. C. Johnson, P. Yu, O. I. Micic, R. J. Ellingson, and A. J. Nozik, “PbTe colloidal nanocrystals: Synthesis, characterization, and multiple exciton generation,” *J. Am. Chem. Soc.*, vol. 128, no. 10, pp. 3241–3247, 2006.

[62] R. D. Schaller, M.A. Petruska, and V. I. Klimov, “Effect of electronic structure on carrier multiplication efficiency: Comparative study of PbSe and CdSe nanocrystals,” *Appl. Phys. Lett*., vol. 87. no. 25, p. 253102, 2005.

[63] R. D. Schaller, J. M. Pietryga, and V. I. Klimov, “Carrier multiplication in InAs nanocrystal quantum dots with an onset defined by the energy conservation limit,” *Nano Lett*., vol. 7, no. 11, pp. 3469–3476, 2007.

[64] M. C. Beard, K. P. Knutsen, P. Yu, J. M. Luther, Q. Song, W. K. Metzger, R. J. Ellingson, and A. J. Nozik, “Multiple exciton generation in colloidal silicon nanocrystals,” *Nano Lett*., vol. 7, no. 8, pp. 2506–2512, 2007.

[65] J. L. Blackburn, R. J. Ellingson, O. I. Mićić, and A. J. Nozik, “Electron relaxation in colloidal InP quantum dots with photogenerated excitons or chemically injected electrons,” *J. Phys. Chem. B*, vol. 107, no. 1, pp. 102–109, 2003.

[66] R. J. Ellingson, M. C. Beard, J. C. Johnson, P. Yu, O. I. Micic, A. J. Nozik, A. Shabaev, and A. L. Efros, “Highly efficient multiple exciton generation in colloidal PbSe and PbS quantum dots,” *Nano Lett*., vol. 5, no. 5, pp. 865–871, 2005.

[67] R. D. Schaller, M. Sykora, J. M. Pietryga, V. I. Klimov, “Seven excitons at a cost of one: Redefining the limits for conversion efficiency of photons into charge carriers,” *Nano Lett.*, *6,* 424–429, 2006.

[68] M. C. Hanna and A. J. Nozik, “Solar conversion efficiency of photovoltaic and photoelectrolysis cells with carrier multiplication absorbers,” *J. Appl. Phys.*, vol. 100, no. 7, p. 074510, 2006.

[69] M. Law, M. C. Beard, S. Choi, J. M. Luther, M. Hanna, and A. J. Nozik, “Determining the internal quantum efficiency of PbSe nanocrystal solar cells with the aid of an optical model,” *Nano Lett*, vol. 8, no. 11, pp. 3904–3910, 2008.

[70] I. Mora-Sero, J. Bisquert, F. Fabregat-Santiago, G. Garcia-Belmonte, G. Zoppi, K. Durose, Y. Proskuryakov, I. Oja, A. Belaidi, T. Dittrich, R. Tena-Zaera, A. Katty, C. Levy-Clement, V. Barrioz

and S. J. C. Irvine,, "Implications of the negative capacitance observed at forward bias in nanocomposite and polycrystalline solar cells," *Nano Lett*., vol. 6, no. 4, pp. 640–650, 2006.

[71] T. Kirchartz and U. Rau, "Modeling charge carrier collection in multiple exciton generating PbSe quantum dots," *Thin Solid Films*, vol. 517, no. 7, pp. 2438–2442, 2009.

[72] G. Conibeer, M. Green, E. Cho, D. König, Y. Cho, T. Fangsuwannarak, G. Scardera, E. Pink, Y. Huang, T. Puzzer, S. Huang, D. Song, C. Flynn, S. Park, X. Hao, and D. Mansfield, "Silicon quantum dot nanostructures for tandem photovoltaic cells," *Thin Solid Films*, vol. 516, no. 20, pp. 6948–6756, 2008.

[73] Y. Takeda, T Ito, T. Motohiro, D. Konig, S. Shrestha, and G. Conibeer, "Hot carrier solar cells operating under practical conditions," *J. Appl. Phys*., vol. 105, no. 7, p. 074905, 2009.

[74] C. W. Jiang, M. A. Green, E. C. Cho, and G. Conibeer, "Resonant tunneling through defects in an insulator: modeling and solar cell applications," *J. Appl. Phys.*, vol. 96, no. 9, pp. 5006–5012, 2004.

[75] D. König, K. Casalenuovo, Y. Takeda, G. Conibeer, J. F. Guillemoles, R. Patterson, L. M. Huang, M. A. Green, "Hot carrier solar cells: Principles, materials and design," *Physica E*, vol. 42, no. 10, pp. 2862–2866, 2010.

[76] M. F. O'Dwyer, R. A. Lewis, C. Zhang, and T. E. Humphrey, "Electronic efficiency in nanostructured thermionic and thermoelectric devices," *Phys. Rev. B*, vol. 72, no. 20, p. 205330, 2005.

[77] Y. Ando, *Encyclopedia of nanoscience and nanotechnology*, vol. 1, H. S. Nalwa, Ed. Valencia, CA: American Scientific Publishers, 2004.

[78] J. Kong, H. T. Soh, A. M. Cassell, C. F. Quate, and H. Dai, "Synthesis of individual single-walled carbon nanotubes on patterned silicon wafers," *Nature*, vol. 395, pp. 878–881, 1998.

[79] K. M. Yu, W. Walukiewicz, J. Wu, W. Shan, J.W. Beeman, M. A. Scarpulla, O. D. Dubon, and P. Becla, "Diluted II-VI oxide semiconductors with multiple band gaps," *Phys. Rev. Lett*., vol. 91, no. 24, p. 246403, 2003.

[80] A. J. Nozik, "Quantum dot solar cells," *Physica E*, vol. 14, no. 1–2, pp. 115–120. 2002.

[81] K. W. J. Barnham, I. Ballard, J.P. Connolly, N.J. Ekins-Daukes, B.G. Kluftinger, J. Nelson, and C. Rohr, "Quantum well solar cells," *Physica E*, vol. 14, no. 1–2, pp. 27–36, 2002.

[82] A. Martí, E. Antolín, C. R. Stanley, C. D. Farmer, N. López, P. Díaz, E. Cánovas, P. G. Linares, and A. Luque, "Production of photocurrent due to intermediate-to-conduction-band transitions: a demonstration of a key operating principle of the intermediate-band solar cell," *Phys. Rev. Lett*., vol. 97, no. 24, p. 247701, 2006.

[83] F. Auzel, "Upconversion and anti-stokes processes with f and d ions in solids," *Chem. Rev.*, vol. 104, no. 1, pp. 139–174, 2004.

[84] D. Chen,Y. Wang, and M. Hong, "Lanthanide nanomaterials with photon management characteristics for photovoltaic application," *J. Nano Energy*, vol. 1, no. 1, pp.73–90, 2012.

[85] J. L. Sommerdijk, A. Bril, and A. W. de Jager, "Luminescence of Pr^{3+}-activated fluorides," *J. Lumin.*, vol. 9, no. 4, pp. 288–296. 1974.

[86] L. H. Slooff, R. Kinderman, A. R. Burgers, N. J. Bakker, J. A. M. van Roosmale, A. Büchtemann, R. Danz, and M. Schleusener, "Efficiency enhancement of solar cells by application of a polymer coating containing a luminescent dye," *J. Sol. Energy-Trans. ASME*, vol. 129, no. 3, pp. 272–276, 2007.

[87] K. Kawano, N. Hashimoto, and R. Nakata, “Effects on solar cell efficiency of fluorescence of rare-earth ions,” *Mater. Sci. Forum,* vol. 239–241, pp. 311–314, 1997.

[88] K. Kawano, K. Arai, H. Yamada, N. Hashimoto, and R. Nakata, “Application of rare- earth complexes for photovoltaic precursors,” *Sol. Energy Mater. Sol. Cells,* vol. 48, no. 1–4, pp. 35–41, 1997.

[89] V. Svrcek, A. Slaoui, and J. C. Muller, “Silicon nanocrystals as light converter for solar cells,” *Thin Solid Films,* vol. 451–452, pp. 384–388, Mar. 2004.

[90] K. Yamada, Y. Wada, and K. Kawano, “Improvement of efficiency of solar cells by application of the rare earth ions doped fluorescent glass,” *J. Kidorui (Rare Earths),* vol. 36, pp. 252–253, 2000.

[91] S. Inoue, T. Jin, K. Machida, and G. Adachi, “Luminescence property and application of rare earth complexes incorporated in ORMOSIL matrices,” *J. Kidorui (Rare Earths),* vol. 30, pp. 190–191, 1997.

[92] T. Maruyama and J. Bandai, “Solar cell module coated with fluorescent coloring agent,” *J. Electrochem. Soc*., vol. 146, no. 12, pp. 4406–4409, Dec. 1999.

[93] B.S. Richards and A. Shalav, “The role of polymers in the luminescence conversion of sunlight for enhanced solar cell performance,” *Synthetic Met*., vol. 154, no. 1–3, pp. 61-64, Sept. 2005.

[94] L.H. Slooff, R. Kinderman, A.R. Burgers, N.J. Bakker, J.A.M. van Roosmalen, A. Buchtemann, R. Danz, and M. Schleusener, “Efficiency enhancement of solar cells by application of a polymer coating containing a luminescent dye,” *J. Sol. Energy-Trans. ASME*, vol. 129, no. 3, pp. 272-276, Aug. 2007.

[95] W.G.J.H.M.v. Sark, A. Meijerink, R. Schropp, J.v. Roosmalen, and E. Lysen, “Modeling improvement of spectral response of solar cells by deployment of spectral converters containing semiconductor nanocrystals,” *Semiconductors+,* vol. 38, no. 8, pp. 962–969, 2004.

[96] F. Galluzzi and E.Scafe´, “Spectrum shifting of sunlight by luminescent sheets: performance evaluation of photovoltaic applications,” *Sol. Energy,* vol. 33, no. 6, pp. 301-307, Jan. 1984.

[97] K.R. McIntosh, G. Lau, J.N. Cotsell, K. Hanton, D.L. Batzner, F. Bettiol, and B.S. Richards, “Increase in external quantum efficiency of encapsulated silicon solar cells from a luminescent down-shifting layer,” *Prog. Photovolt: Res. Appl.*, vol. 17, no. 3, pp. 191-197, May 2009.

[98] A. LeDonne, M. Acciarri, S. Binetti, S. Marchionna, D. Narducci, and D. Rotta, “Enhancement of solar energy conversion efficiency by light harvesting of organolanthanide complexes,” *Presented at the 23rd EU PVSEC,* Valencia, Spain, Sept. 2008.

[99] K. Kawano, N. Hashimoto, and R. Nakata, “Effects on solar cell efficiency of fluorescence of rare-earth ions,” *Mater. Sci. Forum,* vol. 239–241, pp. 311–314, 1997.

[100] K. Kawano, K. Arai, H. Yamada, N. Hashimoto, and R. Nakata, “Application of rare-earth complexes for photovoltaic precursors,” *Sol. Energy Mater. Sol. Cells,* vol. 48, no. 1–4, pp. 35-41. Nov. 1997.

[101] S. Inoue, T. Jin, K. Machida, and G. Adachi, “Luminescence property and application of rare earth complexes incorporated in ORMOSIL matrices,” *Kidorui (Rare Earths),* vol. 30, pp. 190–191, 1997.

[102] K. Machida, H. Li, D. Ueda, S. Inoue, and G. Adachi, “Preparation and application of lanthanide complex incorporated ormosil composite phosphor films,” *J. Lumin.*, vol. 87–89, pp. 1257–1259, 2000.

[103] S. V. Gaponenko, *Optical properties of semiconductor nanocrystals.* Cambridge, U.K: Cambridge University Press, 1998.

[104] G. Seybold, G. Wagenblast, “New perylene and violanthrone dyestuffs for fluorescent collectors,” *Dyes Pigments*, vol. 11, no. 4, pp. 303–317, 1989.

[105] R. E. Sah, G. Baur, and H. Kelker, “Influence of the solvent matrix on the overlapping of the absorption and emission bands of solute fluorescent dyes,” *J. Appl. Phys*., vol. 23, no. 4, pp. 369–372, 1980.

[106] D. Sarti, F. Le Poull, and P. Gravisse, “Transformation of solar radiation by fluorescence: application to the encapsulation of cells,” *Sol. Cells*, vol. 4, no. 1, pp. 25–35, 1981.

[107] C. Strumpel, M. McCann, G. Beaucarne, V. Arkhipov, A. S. laoui, V. Svrcek, C. del Canizo, and I. Tobias, “Modifying the solar spectrum to enhance silicon solar cell efficiency-an overview of available materials,” *Sol. Energy Mater. Sol. Cells*, vol. 91, pp. 238–249, 2007.

[108] K. R. McIntosh and B. S. Richards, “Increased mc-Si module efficiency using fluorescent organic dyes: a ray-tracing study,” in *Conference record of the IEEE 4th World Conference on Photovoltaic Energy Conversion*, vol. 2, pp. 2108–2111, May 2006.

[109] S. Riekeberg, P. P. Altermatt, and R. Brendel, “Decoupling thermalisation from solar cells,” in *Proc. of the 21st EU PVSEC*, Sept. 2006, pp. 294–297.

[110] J. De la Torre, G. Bremond, M. Lemiti, G. Guillot, P. Mur, and N. Buffet, “Using silicon nanostructures for the improvement of silicon solar cells’ efficiency”, *Thin Solid Films*, vol. 511-512, pp. 163–166, 2006.

[111] B. C. Hong and K. Kawano, “PL and PLE studies of KMgF3:Sm crystal and the effect of its wavelength conversion on CdS/CdTe solar cell,” *Sol. Energy Mater. Sol. Cell*, vol. 80, no. 4, pp. 417–432, 2003.

[112] B. González-Díaza, R. Guerrero-Lemusa, P. Haro-Gonzáleza, D. Borchertb, and C. Hernández-Rodrígueza, “Down-conversion properties of luminescent silicon nanostructures formed and passivated in HNO3-based solutions,” *Thin Solid Films*, vol. 511–512, pp. 473, 2006.

[113] W. G. J. H. M. van Sark, C. De Mello Donegá, C. Harkisoen, R. Kinderman, J. van Roosmalen, R. Schropp, E. Lysen, “Improvement of spectral response of solar cells by deployment of spectral converters containing semiconductor nanocrystals,” in *Proc. 19th EPVSEC*, Paris, 2004.

[114] A. Shalav, B. S. Richards, T. Trupke, K. W. Krämer, and H. U. Güdel, “Application of NaYF4:Er^{3+} up-converting phosphors for enhanced near-infrared silicon solar cell response”, *Appl. Phys. Lett.*, vol. 86, no. 1, p. 013505, 2005.

[115] A. Shalav, B. S. Richards, and M. A. Green, “Luminescent layers for enhanced silicon solar cell performance: Up-conversion,” *Sol. Energy Mater. Sol. Cells*, vol. 91, no. 9, pp. 829–842, 2007.

[116] F. Auzel, “Upconversion processes in coupled ion systems,” *J. Lumin*., vol. 45, no. 1–6, pp. 341–345, 1990.

[117] P. Gibart, F. Auzel, J. C. Guillaume, and K. Zahraman, “Below band-gap IR response of substrate-free GaAs solar cells using two-photon up-conversion,” *Jpn. J. Appl. Phys.*, vol. 35, no. 1, pp. 4401–4402, 1996.

[118] S. A. Maier and H. A. Atwater, “Plasmonics: Localization and guiding of electromagnetic energy in metal/dielectric structures,” *J. Appl. Phys.*, vol. 98, no. 1, p. 011101, 2005.

[119] H. A. Atwater, “The promise of plasmonics,” *Sci. Am*., vol. 296, pp. 56–62, 2007.

[120] B. Choi, H. Lee, S. Jin, S. Chun, and S.-H. Kim, "Characterization of the optical properties of silver nanoparticle films," *Nanotechnology*, vol. 18, no. 7, p. 075706, 2007.

[121] J. R. Cole, and N. J. Halas, "Optimized plasmonic nanoparticle distributions for solar spectrum harvesting," *Appl. Phys. Lett.*, vol. 89, no. 15, p. 153120, 2006.

[122] D. Pacifici, H. J. Lezec, H. A. Atwater, "All-optical modulation by plasmonic excitation of CdSe quantum dots," *Nat. Photonics*, vol. 1, pp. 402–406, 2007.

[123] V. E. Ferry, L. A. Sweatlock, D. Pacifici, and H. A. Atwater, "Plasmonic nanostructure design for efficient light coupling into solar cells," *Nano Lett.*, vol. 8, no. 12, pp. 4391–4397, 2008.

[124] S. A. Maier, M. L. Brongersma, and H. A. Atwater, "Electromagnetic energy transport along Yagi arrays," *Mater. Sci. Eng. C*, vol. 19, no. 1–2, pp. 291–294, 2002.

[125] D. M. Schaadt, B. Feng, and E. T. Yu, "Enhanced semiconductor optical absorption via surface plasmon excitation in metal nanoparticles," *Appl. Phys. Lett.*, vol. 86, no. 6, p. 063106, 2005.

[126] O. Stenzel, A. Stendal, K. Voigtsberger, and C. von Borczyskowski, "Enhancement of the photovoltaic conversion efficiency of copper phthalocyanine thin film devices by incorporation of metal clusters," *Solar Energy Materials and Solar Cells*, vol. 37, no. 3–4, pp. 337–348, 1995.

[127] S. Pillai, K. R. Catchpole, T. Trupke, and M. A. Green, "Surface plasmon enhanced silicon solar cells," *J. Appl. Phys.*, vol. 101, no. 9, p. 093105, 2007.

[128] D. Derkacs, S. H. Lim, P. Matheu, W. Mar, and E.T. Yu, "Improved performance of amorphous silicon solar cells via scattering from surface plasmon polaritons in nearby metallic nanoparticles," Appl. Phys. Lett., vol. 89, no. 9, p. 093103, 2006.

[129] K. Tanabe, K. Nakayama, H. A. Atwater, "Plasmon-enhanced absorption and photocurrent in ultrathin GaAs solar cells with metallic nanostructures," in *Proceedings of the 33rd IEEE Photovoltaic Specialists Conference*, San Diego, CA, USA, p. 129, May 2008.

[130] H. R. Stuart and D. G. Hall, "Absorption enhancement in silicon-on-insulator waveguides using metal island films," *Appl. Phys. Lett.*, vol. 69, no. 16, pp. 2327–2329, 1996.

[131] C. Wen, K. Ishikawa, M. Kishima, and K. Yamada, "Effects of silver particles on the photovoltaic properties of dye-sensitized TiO2 thin films," *Sol. Energy Mater. Sol. Cells*, vol. 61, no. 4, pp. 339–351, 2000.

[132] H. Diepers, "Method of manufacturing solar cells, utilizing single-crystal whisker growth," US patent no. 4155781, May 1977.

[133] A. I. Hochbaum and P. Yang, "Semiconductor nanowires for energy conversion," *Chem. Rev.*, vol. 110, no. 1, pp. 527–546, 2010.

[134] V. Schmidt, J. V. Wittemann, and U. Gösele, "Growth, thermodynamics, and electrical properties of silicon nanowires," *Chem. Rev.*, vol. 110, no. 1, pp. 361–388, 2010.

[135] H. J. Fan, P. Werner, and M. Zacharias, "Semiconductor nanowires: from self-organization to patterned growth," *Small*, vol. 2, no. 6, pp. 700–717, 2006.

[136] Z. Fan, H. Razavi, J. Do, A. Moriwaki, O. Ergen, Y. Chueh, P. W. Leu, J. C. Ho, T. Takahashi, L. A. Reichertz, S. Neale, K. Yu, M. Wu, J. W. Ager, and A Javey, "Three-dimensional nanopillar-array photovoltaics on low-cost and flexible substrates," *Nature Mater.*, vol. 8, no. 8, pp. 648–653, 2009.

[137] H. Schmid, M. T. Björk, J. Knoch, H. Riel, and W. Riess, "Patterned epitaxial vapor-liquid-solid growth of silicon nanowires on Si(111) using silane," *J. Appl. Phys.*, vol. 103, no. 2, p. 024304, 2008.

[138] Z. Huang, H. Fang, and J. Zhu, "Fabrication of silicon nanowire arrays with controlled diameter, length, and density," *Adv. Mater.*, vol. 19, no. 5, pp. 744–748, 2007.

[139] Z. Huang, X. Zhang, M. Reiche, L. Liu, T. Shimizu, S. Senz, and W. Lee, "Extended arrays of vertically aligned sub-10 nm diameter [100] Si nanowires by metal-assisted chemical etching," *Nano Lett.*, vol. 8, no. 9, pp. 3046–3051, 2008.

[140] E. C. Garnett and P. Yang, "Light trapping in silicon nanowire solar cells," *Nano Lett.*, vol. 10, no. 3, pp. 1082–1087, 2010.

[141] S. Jeong, L. Hu, H. R. Lee, E. Garnett, J. W. Choi, Y. Cui, "Fast and scalable printing of large area monolayer nanoparticles for nanotexturing applications," *Nano Lett*., vol. 10, no. 8, pp. 2989–2994, 2010.

[142] D. Zschech, D. H. Kim, A. P. Milenin, R. Scholz, R. Hillebrand, C. J. Hawker, T. P. Russell, M. Steinhart, and Ulrich Gösele, "Ordered arrays of <100>-oriented silicon nanorods by CMOS-compatible block copolymer lithography," *Nano Lett*., vol. 7, no. 6, pp. 1516–1520, 2007.

[143] J. C. Ho, R. Yerushalmi, Z. A. Jacobson, Z. Fan, R. L. Alley, and A. Javey, "Controlled nanoscale doping of semiconductors via molecular monolayers," *Nature Mater*., vol. 7, no. 1, pp. 62–67, 2008.

[144] B. Tian, X. Zheng, T. J. Kempa, Y. Fang, N. Yu, G. Yu, J. Huang, and C. M. Lieber, "Coaxial silicon nanowires as solar cells and nanoelectronic power sources," *Nature*, vol. 449, no. 7164, pp. 885–889, 2007.

[145] D. E. Perea, E. R. Hemesath, E. J. Schwalbach, J. L. Lensch-Falk, P. W. Voorhees, and L. J. Lauhon, "Direct measurement of dopant distribution in an individual vapour-liquid-solid nanowire," *Nat. Nanotechnol.*, vol. 4, no. 5, pp. 315–319, 2009.

[146] E. C. Garnett, Y. Tseng, D. R. Khanal, J. Wu, J. Bokor, and P. Yang, "Dopant profiling and surface analysis of silicon nanowires using capacitance-voltage measurements," *Nat. Nanotechnol.*, vol. 4, no. 5, pp. 311–314, 2009.

[147] M. A. Green, *Solar Cells: Operating Principles, Technology and System Applications*. Kensington, NSW, Aust. Univ. New South Wales, 1982.

[148] A. L. Briseno, T. W. Holcombe, A. I. Boukai, E. C. Garnett, S. W. Shelton, J. J. M. Fréchet, and P. Yang, "Oligo- and polythiophene/ZnO hybrid nanowire solar cells," *Nano Lett.*, vol. 10, no. 1, pp. 334–340, 2010.

[149] A. L. Fahrenbruch and R. H. Bube, *Fundamentals of Solar Cells: Photovoltaic Solar Energy Conversion*, New York: Academic, 1983.

[150] J. M. Spurgeon, H. A. Atwater, and N. S. Lewis, "A comparison between the behavior of nanorod array and planar Cd(Se, Te) photoelectrodes," *J. Physical Chemistry C*, vol. 112, no. 15., pp. 6186, 2008.

[151] Z. Fan, D. J. Ruebusch, A. A. Rathore, R. Kapadia, O. Ergen, P. W. Leu, and A. Javey, "Challenges and prospects of nanopillar-based solar cells," *Nano Research*, vol. 2, no. 11, pp. 829, 2009.

[152] J. Zhu, Z. Yu, G. F. Burkhard, C. Hsu, S. T. Connor, Y. Xu, Q. Wang, M. McGehee, S. Fan, and Y. Cui, "Optical absorption enhancement in amorphous silicon nanowire and nanocone arrays," *Nano Lett.*, vol. 9, no. 1, pp. 279–282, 2009.

[153] J. Zhu, C. Hsu, Z. Yu, S. Fan, Y. Cui, “Nanodome solar cells with efficient light management and self-cleaning,” *Nano Lett.*, vol. 10, no. 6, pp. 1979–1984, 2010.

[154] M. A. Green, K. Emery, Y. Hishikawa, and W. Warta, “Solar cell efficiency tables”, in *Prog. Photovolt. Res. Appl.*, vol. 18, pp. 346–352, 2010.

[155] M. D. Kelzenberg, S. W. Boettcher, J. A. Petykiewicz, D. B. Turner-Evans, M. C. Putnam, E. L. Warren, J. M. Spurgeon, R. M. Briggs, N. S. Lewis, and H. A. Atwater, “Enhanced absorption and carrier collection in Si wire arrays for photovoltaic applications,” *Nat. Mater.*, vol. 9, no. 3, pp. 239–244, 2010.

[156] Z. Fan, R. Kapadia, P. W. Leu, X. Zhang, Y. –L. Chueh, K. Takei, K. Yu, A. Jamshidi, A. A. Rathore, D. J. Ruebusch, M. Wu, and A. Javey, “Ordered arrays of dual-diameter nanopillars for maximized optical absorption,” *Nano Lett.*, vol. 10, no. 10, pp. 3823–3827, 2010.

[157] O. L. Muskens, J. G. Rivas, R. E. Algra, E. P. Bakkers, and A. Lagendijk, “Design of light scattering in nanowire materials for photovoltaic applications,” *Nano Lett.*, vol. 8, no. 9, pp. 2638–2642, 2008.

[158] L. Tsakalakos, J. Balch, J. Fronheiser, B. A. Korevaar, O. Sulima, J. Rand, “Silicon nanowire solar cells,” *Appl. Phys. Lett.*, vol. 91, no. 23, p. 233117, 2007.

[159] M. D. Kelzenberg, D. B. Turner-Evans, M. C. Putnam, S. W. Boettcher, R. M. Briggs, J. Yeon Baek, N. S. Lewis, and H. A. Atwater, “High-performance Si microwire photovoltaics,” *Energy Environ. Sci.*, vol. 4, pp. 866–871, 2011.

[160] K. Cho, D. J. Ruebusch, M. H. Lee, J. H. Moon, A. C. Ford, R. Kapadia, K. Takei, O. Ergen, and A. Javey, “Molecular monolayers for conformal, nanoscale doping of InP nanopillar photovoltaics,” *Appl. Phys. Lett.*, vol. 98, no. 20, p. 203101, 2011.

[161] K. Q. Peng, M. L. Zhang, A. J. Lu, N. B. Wong, R. Q. Zhang, and S. T. Lee, “Ordered silicon nanowire arrays via nanosphere lithography and metalinduced etching,” *Appl. Phys. Lett.*, vol. 90 , p. 163123, 2007.

[162] D. R. Kim, C. H. Lee, P. M. Rao, I. S. Cho, and X. L. Zheng, “Hibrid Si Microwire and planar solar cells: passivation and characterization,” *Nano Letters*, vol. 11, no. 7, pp. 2704–2708, 2011.

[163] H. W. Hillhouse and M. C. Beard, “Solar cells from colloidal nanocrystals: Fundamentals, materials, devices, and economics,” *Current Opinion in Colloid & Interface Science*, vol. 14, no. 4, pp. 245–259, 2009.

[164] K. C. Sahoo, M. K. Lin, E. Y. Chang, Y. Y. Lu, C. C. Chen, J. H. Huang and C. W. Chang, “Fabrication of antireflective sub-wavelength structures on silicon nitride using nano cluster mask for solar cell application,” *Nanosale Res. Lett.*, vol. 4, no. 7, pp. 680-683, 2009.

[165] H. Sai, H. Fujii, K. Arafune, Y. Ohshita, M. Yamaguchi, Y. Kanamori, and H. Yugami, “Antireflective subwavelength structures on crystalline Si fabricated using directly formed anodic porous alumina masks,” *Appl. Phys. Lett.*, vol. 88, no. 20, p. 201116, 2006.

[166] K. Park, H.T. Kim, D. Y. Kim, and N. E. Lee, “Formation of silicon nitride in dual-frequency capacitively coupled plasma and their application to Si nanopillar etching,” *J. Vac. Sci. Technol. A*, vol. 25, no. 4, pp. 1073-1077, 2007.

[167] V. Svrcek, J. L. Rehspringer, A. Slaoui, B. Pivac, and J. Muller, “Clustering/declustering of silicon nanocrystals in spin-on glass solutions,” *Semicond. Sci. Technol.*, vol. 20, no. 3, pp. 314-319, 2005.

[168] A. G. Nassiopoulos, S. Grigoropoulos, and D. Papadimitriou, “Electroluminescent device based on silicon nanopillars,” *Appl. Phys. Lett.*, vol. 69, no. 15, pp. 2267-2269, 1996.

[169] O. Bisi, S. Ossicini, and L. Pavesi, "Porous silicon: a quantum sponge structure for silicon based optoelectronics," *Surf. Sci. Rep.*, vol. 38, no. 1–3, pp. 1-126, 2000.

[170] G. C. John and V. A. Singh, "Porous silicon: theoretical studies," *Phys. Rep*., vol. 263, no. 2, pp. 93-151, 1995.

[171] M. Paxman, J. Nelson, B. Braun, J. Connolly, K. W. J. Barnham, C. T. Foxon, and J. S. Roberts, "Modeling the spectral response of the quantum well solar cell," *J. Appl. Phys*., vol. 74, no. 1, pp. 614-621, 1993.

[172] C. Tuovinen, A. Malinin, V. Ovchinnikov, and T. Toivola, "Properties of silicon nanopillar structures," *Physica Sccripta*, vol. T101, pp. 125-128, 2002.

[173] D. Glinka, S. H. Lin, and Y. Chen, "The photoluminescence from hydrogen-related species in composites of SiO2 nanoparticles," *Appl. Phys. Lett.*, vol. 75, no. 6, pp. 778, 1999.

[174] G. R. Lin, C. J. Lin, H. C. Kuo, H. S. Lin, and C. C. Kao, "Anomalous microphotoluminescence of high-aspect-ratio Si nanopillars formatted by dry-etching Si substrate with self-aggregated Ni nanodot mask," *Appl. Phys. Lett*., vol. 90, no. 14, p. 143102, 2007.

[175] J. Valenta, R. Juhasz, and J. Linnros, "Photoluminescence spectroscopy of single silicon quantum dots," *Appl. Phys. Lett.*, vol. 80, no. 6, pp. 1070-1072, 2002.

[176] M. G. Mauk, "Silicon solar cells: physical metallurgy principles," *J. Miner. Met. Mater. Soc*., vol. 55, no. 5, pp. 38–42, 2003.

[177] J. Zhu, Z. Yu, G. F. Burkhard, C. Hsu, S. T. Connor, Y. Xu, Q. Wang, M. McGehee, S. Fan, and Y. Cui,"Optical absorption enhancement in amorphous silicon nanowire and nanocone arrays," *Nano Lett*., vol. 9, no 1, pp. 279-282, 2008.

[178] C. Hsu, S. T. Connor, M. X. Tang, and Y. Cui, "Wafer scale silicon nanopillars and nanocones by langmuir-blodgett assembly and etching," *Appl. Phys. Lett*, vol. 93, no. 13, p. 133109, 2008.

[179] W. A. Nositschka, C. Beneking, O. Voigt, and H. Kurz,"Texturisation of multicrystalline silicon wafers for solar cells by reactive ion etching through colloidal masks," *Sol. Energ. Mat. Sol. C.*, vol. 76, no. 2, pp. 155–166, 2003.

[180] M. Mizuhata, T. Miyake, Y. Nomoto, and S. Deki, "Deep reactive ion etching (Deep-RIE) process for fabrication of ordered structural metal oxide thin films by the liquid phase infiltration method," *Miecroelec. Eng*., vol. 85, no. 2, pp. 355–364, 2008.

[181] G. S. Oehrlein and Y. Kurogi, "Sidewall Surface Chemistry in Directional Etching Processes," *Mater. Sci Eng*., vol. 24, no. 4, pp. 153–183, 1998.

[182] W. Graham, S. Guha, O. Gunawan, G. S. Tulevski, K. Wang, and Y. Zhang, "Nano/microwire solar cell fabricated by nano/microsphere lithography," US patent, 2010, Pub. No. US 20100221866A1.

[183] M. Farrokh-Baroughi and S.Sivoththaman,"A novel silicon photovoltaic cell using a low-temperature quasi-epitaxial silicon emitter," *IEEE Electron Device lett.*, vol.28, pp. 575-577, 2007.

[184] M. Law, J. Goldberger, and P. D Yang, "Semiconductor nanowires and nanotubes," *Ann. Rev. Mater. Res.*, vol. 34, pp. 83–122, 2004.

[185] J. Goldberger, A. I. Hochbaum, R. Fan, and P. D. Yang, "Silicon vertically integrated nanowire field effect transistors," *Nano Lett.*, vol. 6, pp. 973–977, 2006.

[186] Y. Cui, X. F. Duan, J. T. Hu, and C. M. Lieber, "Doping and electrical transport in silicon nanowires," *J. Phys. Chem. B*, vol. 104, pp. 5213–5216, 2000.

[187] R. Tu, L. Zhang, Y. Nishi, and H. J. Dai, "Measuring the capacitance of individual semiconductor nanowires for carrier mobility assessment", *Nano Lett*., vol. 7, pp. 1561–1565, 2007.

[188] O. Gunawan, L. Sekaric, A. Majumdar, M. Rooks, J. Appenzeller, J. W. Sleight, S. Guha and W. Haensch, "Measurement of carrier mobility in silicon nanowires," *Nano Lett.,* vol. 8, pp. 1566–1571, 2008.

[189] D. R. Khanal and J. Wu, "Gate coupling and charge distribution in nanowire field effect transistors," *Nano Lett.*, vol. 7, pp. 2778–2783, 2007.

[190] S. Roddaro, K. Nilsson, G. Astromskas, L. Samuelson, L. Wernersson, O. Karlström, and A. Wacker, "InAs nanowire metal-oxide semiconductor capacitors," *Appl. Phys. Lett.*, vol. 92, pp. 253509–253511, 2008.

[191] T. Minami, H. Sato, H. Nanto, and S. Takata, "Group III impurity doped zinc oxide thin films prepared by RF magnetron sputtering," *Jpn. J. Appl. Phys*., vol. 24, pp. L781–L784, 1985.

[192] J. Muller, G. Schope, O. Kluth, B. Rech, M. Ruske, J. Trube, B. Szyszka, Th. Hoing, X. Jiang, G. Brauer, "Texture-etched zinc oxide substrates for silicon thin film solar cells-from laboratory size to large areas," in *Photovoltaic Specialists Conference, 2000. Conference Record of the Twenty-Eighth IEEE,* Sep. 2000, pp. 758–761.

[193] O. Breitenstein, J. P. Rakotoniaina, M. H. Al Rifai, and M. Werner, "Shunt types in crystalline silicon solar cells," *Prog. Photovoltaics,* vol. 12, no. 7, pp. 529–538, 2004.

[194] D. Pysch, A. Mette, and S. W. Glunz, "A review and comparison of different methods to determine the series resistance of solar cells," *Sol. Energy Mater. Sol. Cells,* vol. 91, no. 18, pp. 1698–1706, 2007.

[195] H. Yoon, Y. A. Yuwen, C. E. Kendrick, G. D. Barber, N. J. Podraza, J. M. Redwing, T. E. Mallouk, C. R. Wronski, and T. S. Mayer, "Enhanced conversion efficiencies for pillar array solar cells fabricated from crystalline silicon with short minority carrier diffusion lengths," *Appl. Phys. Lett.*, vol. 96, no. 21, p. 213503, 2010.

[196] O. Gunawan and S. Guha, "Characteristics of vapor–liquid–solid grown silicon nanowire solar cells," *Sol. Energy Mater. Sol. Cells,* vol. 93, no. 8, pp. 1388–1393, 2009.

[197] Z. Yu, J. Xu, W. Xue, X. Li, and J. Li, "The preparation of AZO films with RF sputtering," in *Proc. of SPIE, International Symposium on Photoelectronic Detection and Imaging*, vol. 6624, 2007, p. 66241O.

[198] R. Singh, S. Sinha, R. P. S. Thakur, and P. Chou, "Some photoeffect roles in rapid isothermal processing," *Appl. Phys. Lett*., vol. 58, pp. 1217-19, 1991.

[199] D. L. King, M. E. Buck, "Experimental optimization of an anisotropic etching process for random texturization of silicon solar cells," 22nd IEEE Photovoltaics Specialists Conf, vol. 1, pp. 303, 1991.

[200] E. Vazsonyi, K. De Clercq, R. Einhaus, E. Van Kerschaver, K. Said, J. Poortmans, J. Szlufcik, J. Nijs, "Improved anisotropic etching process for industrial texturing of silicon solar cells," *Sol. Energy Mater. Sol. Cells,* vol. 57, pp. 179-188, 1999.

[201] C. Leguijt, P. Lölgen, J. A. Eikelboom, A. W. Weeber, F. M. Schuurmans, W. C. Sinke, P. F. A. Alkemade, P. M. Sarro, C. H. M. Marée, and L. A. Verhoef, "Low temperature surface passivation for silicon solar cells," *Sol. Ener. Mater. Sol. Cells*, vol. 40, pp. 297-345, 1996.

[202] W. P. Hirshman, G. Hering, M. Schmela, "Market survey, in: Cell & Module Production 2007: The Q Factor, Sharp and the Market," *Photon International,* pp. 140–174, March 2008.

[203] A. F. Mansour, "On enhancing the efficiency of solar cells and extending their performance life," *Polym. Test.*, vol. 22, no. 5, pp. 491-495, 2003.

[204] D. Z. Garbuzov, V. Bulovic, P. E. Burrows, and S. R. Forrest, "Photoluminescence efficiency and absorption of aluminum-tris-quinolate (Alq_3) thin films," *Chem. Phys.Lett.*, vol. 249, no. 5-6 , pp. 433-437, Feb. 1996.

[205] T. Jin, S. Inoue, K. Machida, and G. Adachi, "Photovoltaic cell characteristics of hybrid silicon devices with lanthanide complex phosphor-coating film," *J. Electrochem. Soc*., vol. 144, no. 11, pp. 4054–4058, Nov. 1997.

[206] E. Klampaftis, B. S. Richards, L. R. Wilson, K. R. McIntosh, A. Cole, K. Heasman, Improving spectral response of mc-Si cells via luminescent down-shifting of the incident spectrum, *Presented at the 4th PVSAT Conference*, Bath, UK, 2008.

[207] ASTM Standard G-173-03, <http://rredc.nrel.gov/solar/spectra/ >

[208] K.R. McIntosh, G. Lau, J. N. Cotsell, K. Hanton, D. L. Batzner, F. Bettiol, and B. S. Richards, "Increase in external quantum efficiency of encapsulated silicon solar cells from a luminescent down-shifting layer," *Prog. Photovolt: Res. Appl.*, vol. 17, no. 3, pp. 191-197, May 2009.

[209] A. Parretta, A. Sarno, P. Tortora, H. Yakubu, P. Maddalena, J. Zhao, and A. Wang, "Angle-dependent reflectance measurements on photovoltaic materials and solar cells," *Opt. Commun*., vol. 172, no. 1-6, pp. 139-151, Dec. 1999.

[210] M. Xu, Q. Huang, Q. Chen, P. Guo, and Z. Sun, "Synthesis and characterization of octadecylamine grafted multi-walled carbon nanotubes," *Chem. Phys. Lett*., vol. 375, no. 5-6, pp. 595-604, Jul. 2003.

[211] Y. Hwang, S. Shin, H. L. Park, S-H. Park, and D. Kim, "Effect of lattice contraction on the Raman shifts of CdSe quantum dots in glass matrices," *Phys. Rev. B,* vol. 54, no. 21, pp. 15120-15124, Dec. 1996.

[212] M. P. Chamberlain, C. Trallero-Giner, and M. Cardona, "Theory of one-phonon Raman scattering in semiconductor microcrystallites," *Phys. Rev. B*, vol. 51, no. 3, pp. 1680-1693, Jan. 1995.

[213] A. Leatherdale, W-K. Woo, F. V. Mikulec, and M. G. Bawendi, "On the absorption cross section of CdSe nanocrystal quantum dots," *J. Phys. Chem. B*, vol. 106, no. 31, pp. 7619-7622, Aug. 2002.

[214] M. Darbandi, R. Thomann, and T. Nann, "Single Quantum Dots in Silica Spheres by Microemulsion Synthesis," *Chem. Mater.*, vol. 17, no. 23, pp. 5720-5725, Oct. 2005.

[215] V. I. Klimov, "Nanocrystal quantum dots: from fundamental photophysics to multicolor lasing," *Los Alamos Science*, vol. 28, pp. 214–220, 2003.

[216] K. Osseo-Asare and F. J. Arriagada, "Preparation of SiO2 nanoparticles in a non-ionic reverse micellar system," *Colloids Surf.,* vol. 50, pp. 321-339, Feb. 1990.

[217] Y. P. Varshni, "Temperature dependence of the energy gap in semiconductors," *Physica (Amsterdam)*, vol. 34, no. 1, pp. 149-154, Jan. 1967.

[218] L. Landolt, R. Börnstein, K. H. Hellwege, W. Freyland, M. Schulz, and H. Weiss, *Landolt-Börnstein Numerical Data and Functional Relationship in Science and Technology*, New Series, Group III, vol. 17, Pt. B, Springer-Verlag, Berlin, 1982.

[219] L. G. Zhang, D. Z. Shen, X. W. Fan, and S. Z. Lu, "Exciton-Phonon Scattering in CdSe/ZnSe Quantum Dots," *Chin. Phys. Lett.*, vol. 19, no. 4, pp. 578-580, Apr. 2002.

[220] F. Gindele, K. Hild, W. Langbein, and U. Woggon, “Temperature-dependent line widths of single excitons and biexcitons,” *J. Lumin.,* vol. 87–89, pp. 381-383, May 2000.

[221] G. Cerullo, S. De Silvestri, and U. Banin, “Size-dependent dynamics of coherent acoustic phonons in nanocrystal quantum dots,” *Phys. Rev. B,* vol. 60, no. 3, pp. 1928-1932, July. 1999.

[222] J. Voigt, F. Spielgelberg, and M. Senoner, “Band parameters of CdS and CdSe single crystals determined from optical exciton spectra,” *Phys. Status Solidi B,* vol. 91, no. 1, pp. 189-199, Jan. 1979.

[223] T. Takagahara, “Electron-phonon interactions in semiconductor nanocrystals*,”J. Lumin.,* vol. 70, no. 1-6, pp. 129-143, Oct. 1996.

[224] C. Trallero-Giner, A. Debernardi, M. Cardona, E. Menendez- Proupin, and A. I. Ekimov, “Optical vibrons in CdSe dots and dispersion relation of the bulk material,” *Phys. Rev. B.,* vol. 57, no. 8, pp. 4664-4669, Feb. 1998.

[225] U. Banin, M. Bruchez, A. P. Alivisatos, T. Ha, S. Weiss, and D. S. Chemla, “Evidence for a thermal contribution to emission intermittency in single CdSe/CdS core/shell nanocrystals,” *J. Chem. Phys.* vol. 110, no. 2, pp. 1195-1201, Jan. 1999.

[226] Y. Ebenstein, T. Mokari, and U. Banin, “Fluorescence quantum yield of CdSe/ZnS nanocrystals investigated by correlated atomic-force and single-particle fluorescence microscopy,”*Appl. Phys. Lett.* , vol. 80, no. 21, pp. 4033-4035, Apr. 2002.

[227] M. Nirmal, B. O. Dabbousi, M. G Bawendi, J. J. Macklin, J. K. Trautman, T. D Harris, and L. E. Brus, “Fluorescence intermittency in single cadmium selenide nanocrystals,” *Nature,* vol. 383, no. 6603, pp. 802-804, Oct. 1996.

[228] M. Kuno, D. P. Fromm, H. F Hamann, A. Gallagher, and D. J. Nesbitt, “Nonexponential “blinking” kinetics of single CdSe quantum dots: A universal power law behavior,” *J. Chem. Phys*., vol. 112, no. 7, pp. 3117-3120, Dec. 1999.

[229] M. Jones, J. Nedeljkovic, R. J. Ellingson, A. J. Nozik, and G. Rumbles, “Photoenhancement of Luminescence in Colloidal CdSe Quantum Dot Solutions,” *J. Phys. Chem. B,* vol. 107, no. 41, pp. 11346-11352, Sep. 2003.

[230] M. Califano, A. Franceschetti, and A. Zunger, “Temperature Dependence of Excitonic Radiative Decay in CdSe Quantum Dots: The Role of Surface Hole Traps,” *Nano Lett.*, vol. 5, no. 12, pp. 2360-2364, Nov. 2005.

[231] S.A. Crooker, T. Barrik, J.A. Hollingsworth, and V. I. Kalimov, “Multiple temperature regimes of radiative decay in CdSe nanocrystal quantum dots: Intrinsic limits to the dark-exciton lifetime,” *Appl. Phys. Lett*., vol 82, no. 17, pp. 2793-2795, Mar. 2003.

[232] V. I. Klimov, A. A. Mikhailovsky, D. W. McBranch, C. A. Leatherdale, and M. G. Bawendi, “Quantization of Multiparticle Auger Rates in Semiconductor Quantum Dots,” *Sci.*, vol. 282, no. 5455, pp. 1011-1013, Feb. 2000.

[233] C. B. Murray, C. R. Kagan, and M. G. Bawendi, “Self-Organization of CdSe Nanocrystallites into Three-Dimensional Quantum Dot Superlattices,” *Sci.*, vol. 270, no. 5240, pp. 1335-1138, Nov. 1995.